TEL AVIV UNIVERSITY

RAYMOND AND BEVERLY SACKLER
FACULTY OF EXACT SCIENCES
SCHOOL OF PHYSICS & ASTRONOMY

אוניברסיטת תל-אביב

הפקולטה למדעים מדוייקים
ע''ש ריימונד ובברלי סאקלר
ביה''ס לפיסיקה ואסטרונומיה

Effects of Solvent Mediated Interactions on Electrolytes and Related Electrostatic Systems

Thesis submitted towards the degree
Doctor of Philosophy

by

Yoram Burak

Submitted to the Senate of Tel Aviv University

August 2004

This work was carried out under the supervision of

Professor David Andelman

Acknowledgments

I would like to thank my supervisor, Professor David Andelman, for his guidance, advice, and for everything that I have learned throughout my doctoral studies.

I had the very good fortune to collaborate with Professor Henri Orland, on the work presented in Chapter 4 and with Professor Roland Netz, on the work presented in chapter 6. Part of the work presented in chapter 5 was done with Gil Ariel, in a fruitful and enjoyable collaboration. This work benefited also from communication with Dr. Eric Raspaud, who provided us with experimental data and with many helpful remarks and suggestions. Dr. Jean-Louis Sikorav's comments were very helpful as well, and are gratefully acknowledged. The work in chapters 2-3 benefited greatly from many discussions with Professor Stjepan Marčelja.

This is a pleasant opportunity to thank my fellow students and friends in Tel-Aviv university: Gil Ariel, Itamar Borukhov, Haim Diamant, Oded Farago, Chai Goldenberg, Ido Golding, Uri Nevo, Yonathan Schwarzkopf, Orit Shefi, Ehud Schreiber, Adi Shafir, and Yoav Tsori.

Finally I would like to thank my parents Tamar and Itamar Burak, my sister Ruth Ecker, and my close friends – in particular, of those not already mentioned above – Eyal Rozenman, Hadar Malach, Danny Loya, Adee Matan, Uri Rom, and Guy Sagi.

Abstract

Ionic solutions are of central importance for the properties of charged macromolecules in solution. The fundamental problem, in this context, is to trace over the ionic degrees of freedom in order to obtain an effective electrostatic interaction, which acts between macromolecular objects. While the modern treatment of this problem dates back many decades ago, to the works of Debye, Hückel, Gouy and Chapman, its analytical treatment is possible only under strong simplifying assumptions, *e.g.*, small surface charges, simple macromolecular geometry, neglect of molecular details, neglect of ion-ion correlations, and other idealizations. Because charged macromolecules are abundant in nature (and especially in the aqueous environment of the living cell), taking these effects into account is of relevance for numerous systems, of theoretical and technological interest.

This thesis addresses four issues in the theory of charged macromolecular systems.

The first issue is concerned with discrete polar solvents such as water. The main objective is to study the consequences of solvent discreteness, as opposed to a continuous dielectric medium. Ion-ion interactions are taken as pairwise-additive, consisting of the usual Coulomb interaction in a dielectric medium and, in addition, a short-range contribution related to the solvent discreteness. In order to treat the short-range part of the interaction, a quadratic non-local term in the free energy is introduced, obtained using a virial expansion (which is performed in an inhomogeneous fluid). The long-range part of the interaction is treated using mean-field theory, as in the standard Poisson-Boltzmann (PB) approach. Two main effects of the solvent discreteness are investigated: the effect on the ion distribution near a single charged surface, and the effect on inter-surface forces. Both effects are found to be significant near highly charged surfaces. In particular, the force acting between identically charged surfaces is found to be attractive under certain conditions.

The second issue in this thesis is the theoretical treatment of ion-ion correlations, which are neglected in PB theory. A model is proposed, which takes into account ion-ion correlations in an approximated manner. Near an infinite, uniformly charged and planar surface (without added

salt) this model is shown to yield exact results in two opposing limits: the weak-coupling limit, in which the mean-field, PB theory is valid, and the strong coupling limit, in which exponential decay of the ion concentration was predicted by recent theoretical approaches. At intermediate coupling, the model interpolates between the exact results, showing semi-quantitative agreement with Monte-Carlo simulations. In addition, the model sheds light on the existence of a distance-dependent crossover, from exponential to algebraic decay.

The third issue is related to recent experiments on aggregation of rod-like, DNA segments, in the presence of multivalent counterions such as spermine and spermidine. The minimal amount of multivalent ions, required to induce aggregation, is considered theoretically. It is argued that this minimal amount must depend linearly on the DNA concentration, over a very large range of DNA concentrations. This result is shown to be in excellent agreement with recent experimental measurements. The two coefficients of the linear dependence are related in a simple manner to the distribution of ions near single DNA chains, at the onset of aggregation. Extracting them from the experimental data leads to interesting conclusions on the conditions prevailing at the onset of aggregation, and on the influence of short-range, ion specific interactions on the ion distribution. These effects are shown to be of particular importance when there is competition between monovalent and multivalent counterions.

The fourth issue is the charge regulation of weak, rod-like polyelectrolytes (PEs). In weak PEs the dissociation of charged groups is partial, and depends on parameters such as the pH and the salt concentration. Since all dissociation sites in a weak PE interact electrostatically with each other, the Hamiltonian for charge regulation is equivalent to a one dimensional Ising model with long-range interactions. A generalization of mean-field theory is proposed to treat this problem, allowing for two sub-lattice symmetry breaking. It is shown that this formalism performs much better than other commonly used approximations, when there is a plateau in the dissociation curve at intermediate pH values (signaling that there are strong anti-correlations between nearest-neighbor sites). A similar formalism is then used to study the interaction of a polyacid and a polybase.

Organization of the thesis

The four issues described in the Abstract are organized in five chapters: chapters 2–3 deal with discrete solvent effects, chapter 4 deals with ion-ion correlations, chapter 5 deals with DNA aggregation in the presence of monovalent and multivalent ions, and chapter 6 deals with charge regulation of weak polyelectrolytes. Each chapter has been published as one or more scientific papers and can be read independently of the others.

The division between chapters 2 and 3, which both deal with discrete solvent effects, is as follows: chapter 2 introduces the general formalism (which is the theoretical basis for both chapters), and proceeds to evaluate these effects near a single charged surface. In chapter 3 two interacting surfaces are considered. The main quantity of interest is the distance-dependent, inter-surface pressure.

Chapter 1 is a general theoretical introduction to inhomogeneous ionic solutions. The introduction is relatively extensive, which I believe is useful since there is currently no standard text that covers these topics in a unified manner. Sections 1–7 deal mainly with Poisson-Boltzmann theory whereas sections 8–9 deal with ion-ion correlation effects, which are not captured by mean-field theory (these two sections are of importance mainly to chapter 4).

The supplements to chapter 1 expand on several topics covered in the introduction. Some of them contain results that, to my knowledge, were not published elsewhere: the first one, in Supplement 1.B, concerns the boundary between attraction and repulsion of two oppositely charged surfaces. A previous result, due to Parsegian and Gingell (from the 1970s), is generalized beyond the linearized Debye-Hückel theory; Supplement 1.C considers the effective charge, far away from a charged cylinder in a salt solution. Numerical results are presented for this quantity. In addition, an analytical expression is derived in the limit of very small salt concentration, which differs from the commonly assumed expression coming from Manning condensation theory; in supplement 1.F the density functional of an inhomogeneous ionic liquid is systematically expanded in a loop expansion, relying on previous results of Netz and Orland.

Supplements 1.D and 1.E do not contain new results, but suggest a new perspective on the

ion distribution near a charged cylinder, which I hope will be useful for understanding this intricate topic.

Because the different chapters were written independently, they sometimes use different notation. For example, in chapters 1–3, e is the electron charge, so that a multivalent ion carries a charge ze where $z > 1$. In chapter 4, e is the counterion charge, which can be an integer multiple of the electron charge. This difference in notation has consequences also for the Bjerrum length l_B and for the Gouy-Chapman length. In order to facilitate the reading, a symbol legend was added at the end of each section. Symbol legends for chapters 2–3 are combined, since these chapters use identical notation.

Contents

Chapter 1

Introduction

This thesis deals with charged macromolecules in solution, and in the way that ionic solutions, surrounding these molecules, mediate interactions between them. The term *macromolecules* is used to describe objects that are small on macroscopic scale but contain many atomic or molecular subunits. Before giving specific examples, we briefly discuss why molecules (and macromolecules) often become charged in solution.

In vacuum or in air at room temperature the typical interaction energy, required to separate a positive ion from a negative one, is about 180 times the thermal energy – assuming a separation of $3\,\text{Å}$ at contact and monovalent ions. Hence, free charges exist in vacuum only at extremely low concentrations or high temperature. The situation changes dramatically in polar solvents such as water, where the dielectric screening reduces electrostatic interactions by a large factor, about 80 in water. Ionic bonds, now having interaction energies of order $k_B T$, can dissociate; dissociation is often favored due to the gain of entropy.

The dissociated ions typically form diffuse clouds around charged macromolecules, partially screening their electrostatic field. Consequently, interactions between different charged objects are not simply given by the bare Coulomb interaction. The ions play a central role, mediating an effective interaction that differs from the direct Coulomb interaction in magnitude and in range (in some situations, even in sign). In order to evaluate this effective interaction, a thermal average over ionic degrees of freedom is required. All problems studied in this thesis are concerned with such thermal averages in ionic solutions, and are within the realm of equilibrium statistical mechanics.

The following chapters deal, mainly, with highly idealized models, where macromolecules have simple geometrical shapes such as planes or cylinders. Several examples of real macromolecules, having different geometries are briefly discussed below. Many of the examples occur

within the context of cell biology, with water as the solvent.

Mica

Mica is a clay mineral that can be cleaved to obtain atomically flat sheets. Cleaved Mica surfaces are used in *surface force apparatus* [1] experiments, where the force acting across a solution between two such surfaces is accurately measured as a function of separation, with spatial resolution in the order of a few Angstroms. Mica is negatively charged, with a very high surface charge density of $0.33\,\mathrm{C/m^2}$ (corresponding $48\,\mathrm{\mathring{A}^2}$ per unit charge) at full dissociation of its K^+ ions.

Cell Membranes

Cell membranes are composed of *lipids*, molecules that have a hydrophobic hydrocarbon tail, covalently attached to a hydrophilic head group (either polar or charged). The competing tendency to prefer or to avoid contact with water molecules leads to self-assembly into various possible structures, in membranes – bilayers which conceal the hydrophobic tails from the aqueous environment (Fig. 1.1 a).

Cell membranes contain lipids of many different types, as well as numerous proteins such as ion channels, receptors, and enzymes; they can deform and bend, and their lipid components form a two-dimensional fluid. Nevertheless, from the electrostatic point of view, to first order they can be viewed as planar, charged interfaces. More refined theories must take into account their flexibility and heterogeneity.

In modeling of membranes as uniformly charged interfaces, the following physical parameters come into play. The surface charge density is about $500\text{-}1000\,\mathrm{\mathring{A}^2}/e$ (where e is the unit charge), assuming that 10–20% of the lipids are charged. The width of the lipid bilayer is about $30\text{–}50\,\mathrm{\mathring{A}}$. Ions are expelled from the inner part of the membrane due to its low dielectric constant.

Thermal undulations of lipid bilayers are smooth on cellular length scales [2], so that it is meaningful to think about them as two-dimensional interfaces, possibly with a certain curvature. In the outer cell membrane (as opposed to bilayers surrounding small organelles within a cell) the radius of curvature is often sufficiently large in order for the membrane to be considered as a flat interface. We note that at length scales of hundreds of nanometers or larger the shape and structure (as well as thermal undulations) are typically governed by the attachment to the cytoskeleton network.
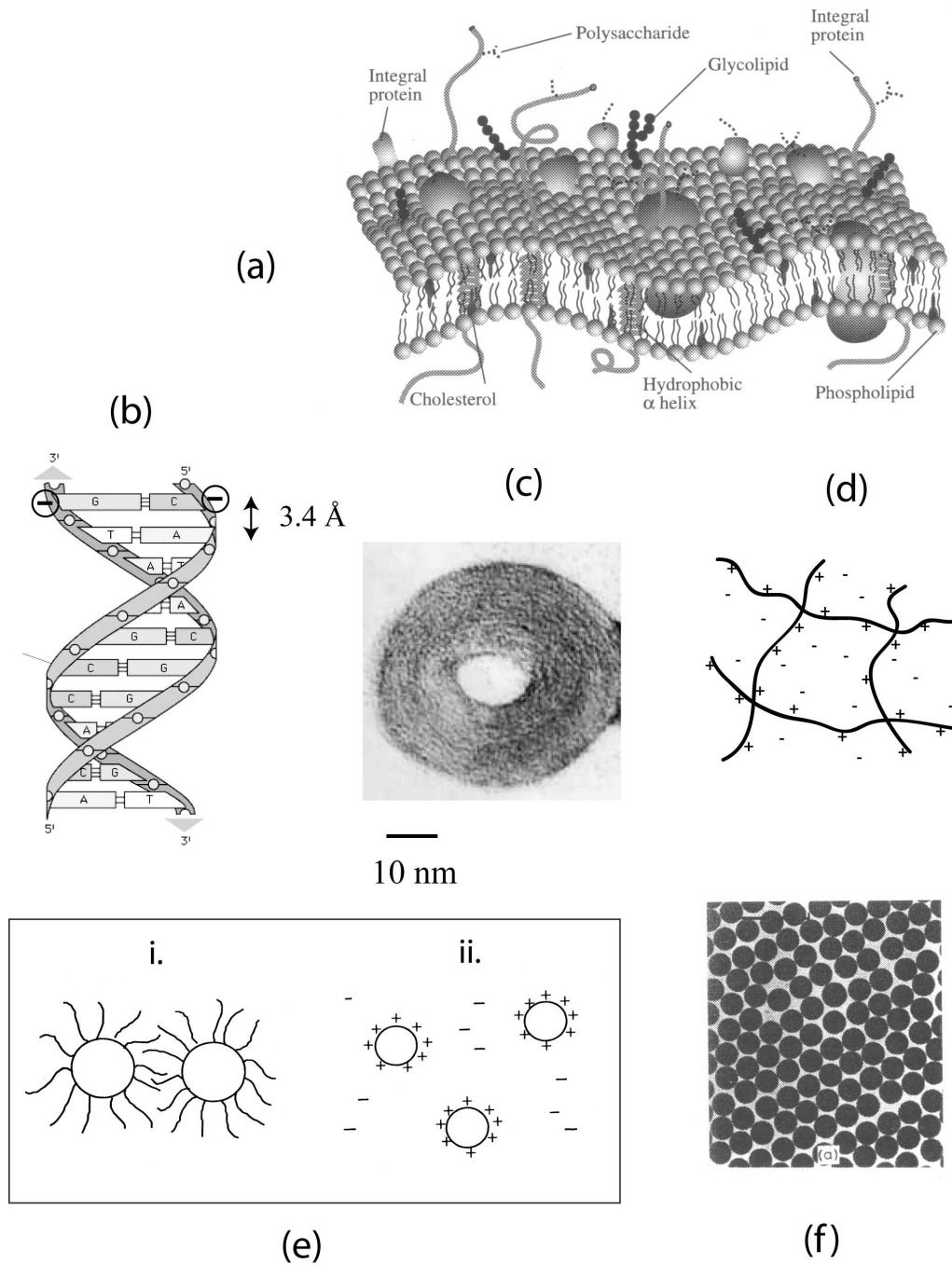
Figure 1.1: Charged macromolecules in solution. (a) Cell membrane (b) DNA structure (c) Electron micro-graph of DNA, collapsed into a toroidal structure in the presence of spermine (4+) ions (taken by J.L. Sikorav [4]) (d) Polyelectrolyte solution (e) Colloids: i. sterically stabilized ; ii. charge stabilized (f) Polystyrene latex particles in solution. Figures (a) and (f) are reproduced from Refs. [3] and [5], respectively.

Polyelectrolytes

Polyelectrolytes (PEs) are charged polymers, *i.e.*, long chains of molecular building blocks (monomers) that are chemically attached to each other. In comparison with neutral polymers, whose statistical mechanics is better understood, there are two main sources of difficulty in theoretical treatment of PEs. The first arises from the long-range nature of electrostatic interactions. The second source of difficulty is the coupling between PE conformation and the ionic solution, which can be easily treated within the linearized Debye-Hückel theory (discussed later on), but is difficult to treat when the Debye-Hückel theory is not valid (corresponding to highly charged PE and low salt concentrations). Here we consider stiff PEs, modeled as rigid, cylindrical rods. Even in this relatively simple case the distribution of ions involves subtle effects, due to the logarithmic decay of the electrostatic potential (discussed in Sec. 1.5).

Biological PEs

DNA (Fig. 1.1 b). Besides its fundamental function in storage of genetic information DNA is, physically, a highly charged polyelectrolyte. The charge is due to the phosphate groups (one per nucleotide), yielding a high packing of one unit charge per 1.7 Å (there are two nucleotides every 3.4 Å along the DNA axis). Other important physical parameters are the radius of DNA, about 10Å and the pitch, 34Å (exactly 10 nucleotide pairs). DNA is not simply a cylinder of radius 10 Å: small ions can easily penetrate the major and minor grooves.

DNA is a relatively stiff molecule. In physiological solution it is stiff, or rod-like, on length scales smaller than its *persistence length*, about 500 Å. Properties of extended DNA chains (long chains or short DNA segments) are extensively studied, motivated by the numerous technological and biomedical implications, as well as for pure scientific reasons. It is important to realize, however, that DNA does not assume an extended state in cells. Instead, it is wrapped around *histones*, positively charged proteins, to form a bead of roughly 11 nm in diameter. These interconnected beads, each containing about 150 base pairs, form the 30 nm thick chromatin fiber, and there can be several additional hierarchies of packing. In experiments involving extended DNA molecules, such as those discussed in chapter 5, the DNA is first separated from the packing agents and possibly cut into 150 base-pair strands. In a monovalent salt solution it can then be modeled as a rod-like or as a semi-flexible PE. As discussed in chapter 5, in presence of multivalent ions, DNA tends to aggregate or to collapse into compact toroidal structures (Fig. 1.1 c).

Other PEs in the cell environment. There are many other PEs within the living cell. For

example, many proteins are charged. Since they are heterogeneous (three of the amino acids are positively charged, two are negatively charged, and the rest are either polar or hydrophobic), and since they are usually folded in a native state, forming a compact three-dimensional object, their properties are quite different from those of stiff or semi-flexible PEs. Two important examples of rigid polymers in the cell are actin filaments and microtubules, both of which take part in affecting the cell's mechanical properties. Their high electric charge ($4.1\,e$/nm in actin filaments, $3.8\,e$/nm in microtubules) plays a prominent role in determining their interactions with other molecules, as well as the network structures that they form [6].

Colloids

The term *colloids* is used to describe particles of roughly spherical shape that are large on the atomic scale but are small on macroscopic scale.[1] In a macroscopic sample the number of colloids is typically very large – placing them, theoretically, within the subject matter of statistical mechanics [8]. Examples for colloids in solution (*colloidal suspensions*) include glues, paints, milk, blood, and latex particles in solution (Fig. 1.1 f).

In order to solubilize colloidal particles, short-range van der Waals and depletion interactions between them must be overcome: being relatively large on a microscopic scale, even weak attractive interactions between colloidal surfaces sum up to an attraction energy which is large compared to their translational entropy, of order $k_B T$. In the absence of stabilizing, repulsive forces colloids aggregate and precipitate from the solution.

There are two main methods to introduce a stabilizing, repulsive interaction (Fig. 1.1 e): (i) steric stabilization, using, *e.g.*, a polymer brush that is covalently attached to the colloidal surface, and (ii) charge stabilization, *i.e.*, a charging of the colloid surface, which leads to electrostatic repulsion. Sometimes these two methods are combined: for example, the casein micelles, which are the largest colloids in milk, are stabilized by a short brush of charged polymers.

Naturally, the class of colloids of relevance to this thesis are the charged ones. A typical charge for a colloid is between 100 and 10000 unit charges.

Ionic solutions

The most common ions in biological cells are the monovalent ions sodium (Na^+), chlorine (Cl^-) and potassium (K^+), and the divalent ions magnesium (Mg^{2+}) and calcium (Ca^{2+}). There are

---

[1] Although there is no clear-cut definition for what is considered a colloidal particle, this term is usually used for particle sizes ranging between a nanometer and a micron. For a discussion on physical properties of colloids that are relevant criteria for their definition, and for a general discussion on colloidal systems see Ref. [7].

also many small molecules of higher valency that, in some contexts can be viewed as small counterions, such as spermine (4^+) and spermidine (3^-), discussed in chapter 5.

Hydrogen (H^+) and hydroxyl (OH^-) ions play a special role in aqueous solutions since a water molecule can dissociate into a (H^+, HO^-) pair. Even pure water with no added salt contains some free ions: H^+ and HO^-, each of concentration 10^{-7} M (a tiny fraction of the water concentration, approximately 55 M). Addition of solutes that contribute hydrogen or hydroxyl ions, or associate with these ions, changes the concentrations of both H^+ and OH^- while keeping their product fixed, equal to the dissociation constant.[2]

From the electrostatic point of view, the most important property of an ion is its valency q. Because of the $qe\Phi$ form of the coupling to an external potential Φ, multivalent counterions are more closely bound to charged objects than monovalent ones. They tend to replace monovalent ions in the neutralizing layer even if their bulk concentration is very low: replacing q monovalent ions by one q-valent ion is rewarded by gain of translational entropy. Another important aspect of valency is that it controls the strength of interactions between ions. The larger the valency, the more important are correlations between ion positions. A host of experimental phenomena, theoretically attributed to ion-ion correlations effects, occur with multivalent ions – most notably, attraction of similarly charged objects; like-charge attraction is rarely seen with monovalent ions. Ion-ion correlation effects, near highly charged surfaces, are studied in chapter 4.

Changing the amount of added salt in a solution is an important method of tuning its electrostatic behavior, because of the Debye screening length's sensitivity to salt concentration (Sec. 1.2). The range of electrostatic interactions in water can vary between a few Angstroms (with added NaCl at saturation) up to hundreds of nanometers (with no added salt).

Specific (non-electrostatic) ion effects

At relatively high salt concentrations, where electrostatic interactions are highly screened, differences between ions of the same valency come into play. These differences are, for example, their size, the structure of the hydration (water) shell around them, and their different polarizabilities. An important example where different ions of the same valency differ in their experimental properties is the solubility of proteins (the *Hofmeister effect*) [9], where relatively large ion concentrations are involved. Specific ionic interactions are important also when there is competition between binding of different ion species to a charged macromolecule (as studied

---

[2]More precisely, the product of activities, divided by the activity of water, is fixed. Because water is at large excess over all other components this implies approximately a fixed product of the concentrations. The pH is defined as $-\log_{10} a_{H^+} \simeq -\log_{10}[H^+]$, where a_{H^+} is the hydrogen activity and $[H^+]$ is its concentration in M.

Figure 1.2: Potential of mean force between two sodium ions in water as a function of their distance, evaluated in a molecular-dynamics simulation. The insets show typical water configurations at the first local minimum and maximum (reproduced from Ref. [10]).
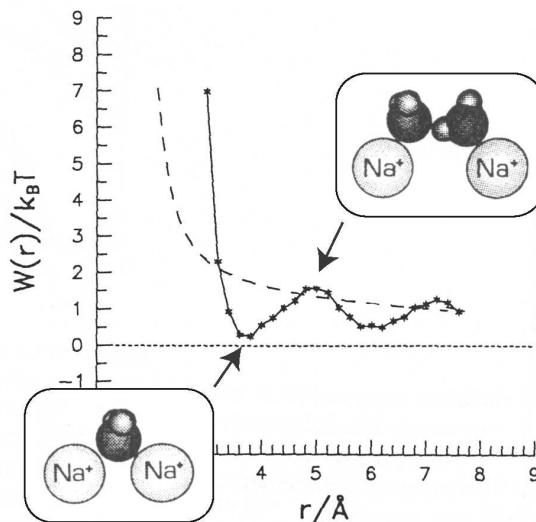
in chapter 5).

The solvent, assumed here to be water, is often considered as a continuous dielectric medium, $\varepsilon = 78$ in water at room temperature. This idealization, referred to as the *primitive model*, simplifies theoretical treatment but is not always justified. As an example for discrete solvent effects, Fig. 1.2 shows the potential of mean force between two sodium (Na^+) ions in water: $W(r) = -\ln Z(r)$ where $Z(r)$ is the partition function of two ions fixed at a distance r from each other, in a bath of water molecules.

Within the primitive model, $W(r) = l_B/r$, the monotonic dashed line in the figure. The solid line shows $W(r)$ as obtained in a molecular dynamics simulation [10]. Since $W(r)$ approaches l_B/r at large r, the difference $W(r) - l_B/r$ can be viewed as a short-range interaction acting between the ions in addition to their long-range Coulomb interaction. The oscillatory behavior of this short-range contribution reflects the arrangement of water molecules between the ions, and its range (roughly $10\,\text{Å}$) is governed by the size of a water molecule (about $3\,\text{Å}$). Solvent effects, beyond the primitive model, are studied in chapters 2 and 3.

Organization of the introduction

The rest of this chapter is a general theoretical introduction to inhomogeneous ionic solutions. It is organized in nine sections dealing with bulk electrolytes (1.1), ionic solutions near charged surfaces (1.2–1.6), and forces between charged objects in ionic solutions (1.7). The last two sections (1.8, 1.9) deal with ion correlation effects, beyond mean field theory. Throughout the introduction the solvent is treated within the primitive model as a continuous dielectric

medium.

The supplements expand on several topics, or include derivations of identities that are used in the introduction. Some of the supplements (1.B, 1.C, 1.F) contain new results that did not fit in any of the main chapters.

General introductions to soft condensed matter that include a discussion on electrostatic interactions can be found in Refs. [1, 11, 12].

1.1   Bulk electrolytes

In this thesis we deal mainly with highly inhomogeneous ionic solutions. We begin with a brief discussion on properties of bulk electrolytes, which typically form a reservoir to which the inhomogeneous ion distribution is coupled.

We consider a solution containing n species of ions of concentrations c_α and valencies q_α, where α is an index designating the ion species. It is first noted that charge neutrality must hold:

$$\sum_\alpha q_\alpha c_\alpha = 0, \tag{1.1}$$

otherwise the free energy is not extensive, and the thermodynamic limit does not exist. As a result of charge neutrality, the mean electrostatic potential must vanish: on the mean-field level, the free energy reduces to that of an ideal gas:

$$f_{\rm id} = \sum_\alpha c_\alpha \left[\ln(\lambda_\alpha^3 c_\alpha) - 1 \right] \tag{1.2}$$

where $f_{\rm id}$ is the free energy per unit volume and λ_α is the fugacity of ion species α.

In similarity to uncharged fluids, Eq. (1.2) represents the free energy of a sufficiently dilute ionic solution. A correction to this expression can be calculated for finite (non-zero) density. In marked difference from neutral fluids, the standard virial expansion, in powers of c_α, fails for charged fluids: the Mayer functions diverge due to the long range of the electrostatic interactions. In fact, the correction to Eq. (1.2) is not analytic at zero concentration, as will be demonstrated below.

A theory which takes ion-ion correlations into account was introduced by Debye and Hückel in 1923 [13], successfully explaining deviations from ideal gas properties of strong electrolytes. Below we follow the derivation of Landau and Lifshitz (Ref. [14], Sec. 78), which captures the most essential elements of Debye and Hückel's theory.

The electrostatic energy of the ionic solution, arising from correlations between ions, can be

written as follows:

$$E_{\text{corr}} = V \frac{1}{2} \sum_{\alpha} e q_\alpha c_\alpha \Phi_\alpha \tag{1.3}$$

where V is the volume and Φ_α is the electrostatic potential acting on an ion of type α due to the other ions in the system. Once an ion of species α is fixed at a certain position, the distribution of other ions around it leads to a non-vanishing electrostatic potential. To evaluate this distribution, suppose that the fixed ion is at the origin, and use the following approximation:

$$c_\alpha(r) = c_\alpha e^{-\beta q_\alpha e \Phi(r)} \tag{1.4}$$

where $\beta = 1/k_{\text{B}} T$ and $k_{\text{B}} T$ is the thermal energy; $\Phi(r)$ is the mean electrostatic potential in the presence of the fixed ion and $c_\alpha(r)$ is the average ion density of species α. Both $\Phi(r)$ and $c_\alpha(r)$ are radially-symmetric. The prefactor in Eq. (1.4) is determined by requiring that $c_\alpha(r) \to c_\alpha$ far away from the fixed ion, where $\Phi(r) \to 0$.

The potential $\Phi(r)$ is related to $c_\alpha(r)$ by the Poisson equation:

$$\nabla^2 \Phi(r) = -\frac{4\pi}{\varepsilon} e \sum_{\alpha} q_\alpha c_\alpha(r) \tag{1.5}$$

where ε is the dielectric constant. Equations (1.4) and (1.5) yield together a non-linear self-consistent equation for $\Phi(r)$, which is known as the Poisson-Boltzmann equation.

For a sufficiently dilute solution, where interactions between ions are weak, we can assume that $\beta e q_\alpha \Phi(r)$ is small and linearize Eq. (1.4). We then obtain for $\Phi(r)$:

$$- \left[\nabla^2 + \kappa^2 \right] \Phi = 0 \tag{1.6}$$

where

$$\kappa^2 = \frac{4\pi \beta e^2}{\varepsilon} \sum_{\alpha} c_\alpha q_\alpha^2 \tag{1.7}$$

and the length κ^{-1} is known as the Debye screening length. It is now straightforward to solve for $\Phi(r)$:

$$\Phi(r) = \frac{e q_0}{\varepsilon} \frac{e^{-\kappa r}}{r} \tag{1.8}$$

where q_0 is the valency of the fixed charge. In the immediate vicinity of the fixed charge the field must approach the Coulomb field of a point charge $q_0 e$. This requirement sets the prefactor in Eq. (1.8).

According to Eq. (1.8) the electrostatic field of a point charge is screened exponentially by the other ions, with a characteristic decay length equal to κ^{-1}. Note that κ increases with

increase of c_α and vanishes when $c_\alpha \to 0$. Hence for small density we can expand Eq. (1.8) in powers of κ:

$$\Phi(r) = \frac{eq_0}{\varepsilon} \left[\frac{1}{r} - \kappa + \cdots \right] \qquad (1.9)$$

The first term is the electrostatic potential due to the fixed charge, and does not enter in Eq. (1.3). The second term is the lowest order contribution to the electrostatic potential exerted by the other ions. We thus obtain from Eq. (1.3):

$$E_{\text{corr}} = -V e^3 \sqrt{\frac{\beta\pi}{\varepsilon^3}} \left(\sum_\alpha c_\alpha q_\alpha^2 \right)^{3/2} = -\frac{V\kappa^3}{8\pi\beta} \qquad (1.10)$$

In order to evaluate the free energy we integrate the identity $E = (\partial/\partial\beta)(\beta V f)$ to find:

$$f = f_{\text{id}} - \frac{1}{12\pi\beta}\kappa^3 \qquad (1.11)$$

(using the fact that $f \to f_{\text{id}}$ as $\beta \to 0$). Note that the first order correction to f_{id} goes like the density to power $(3/2)$, in contrast to the quadratic form that is typical to uncharged fluids. The pressure follows from Eqs. (1.11) and (1.7):

$$P = k_B T \left(\sum_\alpha c_\alpha - \frac{\kappa^3}{24\pi} \right) \qquad (1.12)$$

Using Eq. (1.12) it is easy to assess at what concentrations ion-ion correlation effects are important. Comparing the two terms in this equation we see these effects are important if the Debye length κ^{-1} is small compared to the typical ion-ion distance. In order to obtain a more quantitative criterion, let us consider a q:1 salt of concentration c_s. Concentrations of the multivalent and monovalent ions are then c_s and qc_s, respectively. The ratio between the second and first terms in Eq. (1.12) is equal to:

$$\frac{|P_{\text{corr}}|}{P_{\text{id}}} = \frac{\pi}{9}(q+1)q^3 l_B^3 c_s \qquad (1.13)$$

where $l_B = e^2/(\varepsilon k_B T)$, the Bjerrum length, is the distance at which the interaction between two unit charges is equal to the thermal energy. Since the typical distance between neighboring ions in a 1:1 salt is of order $c_s^{-1/3}$, the ratio in Eq. (1.13) is small as long as the electrostatic interaction between neighboring ions is small compared to the thermal energy.

In water at room temperature $l_B \simeq 7\,\text{Å}$ and $l_B^{-3} \simeq 0.0029\text{Å}^{-3} \simeq 4.8\,\text{M}$. For a 1:1 salt correlation effects are thus important for concentrations of order $1\,\text{M}$ or larger. At salt concentrations in the order of $0.1\,\text{M}$ or smaller they can be safely neglected. Note that for multivalent salts correlation effects are important at much smaller concentrations, as can be appreciated from the dependence on q in Eq. (1.13).

At sufficiently low temperature an ionic solution phase-separates into coexisting ion-rich and ion-poor phases. In order to understand this phase separation, it is essential to take the finite size of ions into account. This topic is briefly discussed in Supplement 1.A for completeness, although its relevance to aqueous ionic solutions is minor: the critical temperature is well below the freezing point of water.[3]

1.2 Electrolytes near charged surfaces

In contrast to the situation in bulk solutions, near charged interfaces there is a non-vanishing electrostatic potential. Evaluation of this potential using mean-field theory is often adequate in order to evaluate quantities such as the ion density profile near the interface or the force acting between two charged objects, as mediated by the ionic solution. Limitations of mean-field theory are discussed later on, in Sections 1.8 and 1.9.

Before proceeding to discuss mean-field theory, we note that there are situations where an ionic solution is non-homogeneous, but the leading correction to ideal-gas behavior still comes from correlation effects beyond mean-field theory, as in a bulk solution. An important example is a neutral interface between an ionic solution and a low-dielectric medium, such as a water-oil or a water-air interface. Because the interface is neutral, the average electrostatic potential is zero and the ion density is uniform on the mean field level. In fact, there is a depletion of positive and negative ions from the interface due to their repulsion from the dielectric discontinuity. The relevant interaction energy, naively a coulomb interaction with the image charge, is screened by the ionic solution (and thus involves ion-ion correlations in an essential manner). The depletion of ions from the surface is related, through the Gibbs adsorption equation (Ref. [14], Sec. 157), to an increase of the interfacial energy. Hence addition of salt usually increases the surface tension of polar solvents such as water. This increase was calculated by Onsager and Samaras [15] (see also Ref. [14], Sections 157–158).

1.2.1 Mean-field theory

Figure 1.3 shows a group of charged objects immersed in an ionic solution. For simplicity we assume that the dielectric constant is uniform, and that the only non-electrostatic interaction is an exclusion of ions from a certain region of space – for example, the interior of a colloidal

---

[3]Demixing of the liquid phase, below the critical temperature, is not to be confused with the first order, liquid–solid phase transition. Phase separation in an aqueous solution of NaCl occurs above a saturation concentration of about 6 M at room temperature.
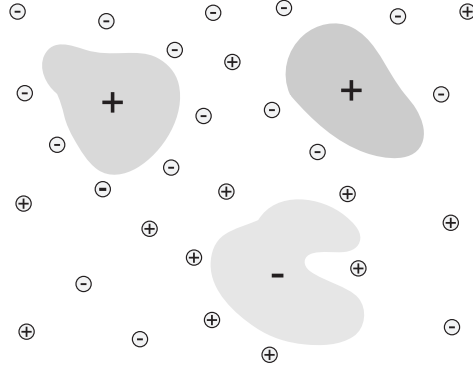
Figure 1.3: Fixed charged objects, immersed in ionic solution. The fixed charge density due to these objects is denoted $n_e(\mathbf{r})$ (in units of e, the unit charge). An excluded volume function $\Theta(\mathbf{r})$ is equal to zero in regions that the ions cannot penetrate (such as the interior of the fixed objects), and to unity elsewhere.

particle. The electrostatic potential is related to the charge density by the Poisson equation,

$$-\frac{1}{4\pi l_B}\nabla^2\phi(\mathbf{r}) = \sum_\alpha q_\alpha n_\alpha(\mathbf{r}) + n_e(\mathbf{r}) \tag{1.14}$$

where ϕ, the *reduced electrostatic potential*, is dimensionless and equal to the electrostatic potential Φ multiplied by $e/(k_B T)$, $l_B = e^2/(\varepsilon k_B T)$ is the Bjerrum length, q_α is the valency of the ion of species α, n_α is its local number concentration, and $n_e(\mathbf{r})$ is a fixed charge distribution coming from the charged objects, expressed in units of the unit charge e per unit volume.

A second, mean-field equation is obtained by treating the ions as if they interact with an external potential ϕ which is not influenced by their own presence:

$$n_\alpha(\mathbf{r}) = c_\alpha \Theta(\mathbf{r}) \exp\left[-q_\alpha \phi(\mathbf{r})\right] \tag{1.15}$$

where c_α is the fugacity of the ion species α [also equal to its bulk density on the mean field level, as in Eq. (1.4)] and $\Theta(\mathbf{r})$ is equal to zero in the excluded volume where ions cannot be present and to unity everywhere else. Combining these two equations yields a non-linear equation for ϕ:

$$-\frac{1}{4\pi l_B}\nabla^2\phi = \sum_\alpha q_\alpha c_\alpha \Theta(\mathbf{r}) \exp\left[-q_\alpha \phi(\mathbf{r})\right] + n_e(\mathbf{r}) \tag{1.16}$$

This is known as the Poisson-Boltzmann (PB) equation.

Linearized theory

Much of the practical difficulty in solving the PB equation (1.16) arises from its non-linearity. For weakly charged objects [corresponding to sufficiently small $n_e(\mathbf{r})$] the PB equation can be

linearized, leading to a considerable simplification:

$$\frac{1}{4\pi l_B}\left[-\nabla^2 + \kappa^2\right]\phi(\mathbf{r}) = n_e(\mathbf{r}) \tag{1.17}$$

where

$$\kappa^2 = 4\pi l_B \sum_\alpha q_\alpha^2 c_\alpha \tag{1.18}$$

and κ^{-1} is the Debye screening length, introduced already in Sec. 1.1. For a 1:1 salt of concentration c_s, $\kappa^2 = 8\pi l_B c_s$. Equation (1.17) was first derived by Debye and Hückel within the context of the bulk properties of electrolytes (Eq. 1.6) and is therefore called the Debye-Hückel equation. Its solution can be written in terms of the Green's function:[4]

$$v_{\mathrm{DH}}(\mathbf{r}, \mathbf{r}') = \frac{l_B \mathrm{e}^{-\kappa|\mathbf{r}-\mathbf{r}'|}}{|\mathbf{r} - \mathbf{r}'|} \tag{1.19}$$

Since the theory is linear, Eq. (1.19) leads to exponential screening of the interaction between any two charged objects. The importance of Eqs. (1.17) and (1.19) goes, in fact, far beyond the linearized theory. Far away from any charged object the electrostatic potential is small and Eq. (1.17) describes the ion distribution. Consequently, even interactions between highly charged objects can be described using Debye-Hückel theory as long as the distance between them is large compared to the Debye length. The price that has to be paid is that the surface charge is renormalized due to non-linearities close to the surfaces.

To close this section we note that the screening length itself is modified at high ion concentrations ($\kappa l_B \gtrsim 1$), due to corrections to the Debye-Hückel theory [20] (see also Sec 1.1). Throughout this thesis we assume that the bulk ionic solution is sufficiently dilute that these effects are insignificant.

1.2.2 Free energy

The exact partition function reads, in the grand-canonical ensemble,

$$Z_G = \sum_{N_+, N_- = 0}^\infty \lambda_0^{N_+ + N_-} Z_{N_+, N_-} \tag{1.20}$$

where we assume, for simplicity, a 1:1 salt (the generalization to other combinations of ion species is straightforward). In the above expression $\lambda_0 = \mathrm{e}^{\beta\mu_c}/\lambda_T^3$ is the fugacity, μ_c is the chemical potential, λ_T is the de Broglie thermal wave-length, and Z_{N_+, N_-} is the partition

---

[4]This form of v_{DH} holds only in the translationally invariant situation where ions can access the whole space, $\Theta(\mathbf{r}) = 1$ for all $\mathbf{r}$. Inhomogeneities in Θ or in the dielectric constant modify the Green's function [16–19].

function in the canonical ensemble,

$$
\begin{aligned}
Z_{N_+,N_-} \;=\; & \frac{1}{N_+!N_-!}\prod_i\left(\frac{1}{\lambda_T^3}d\mathbf{r}_i\Theta(\mathbf{r}_i)\right) \\
& \times\;\exp\left[-\frac{1}{2}\int d\mathbf{r}\,d\mathbf{r}'\,\hat{n}_c(\mathbf{r})v_c(\mathbf{r}-\mathbf{r}')\hat{n}_c(\mathbf{r}')+\frac{1}{2}(N_++N_-)v_c(0)\right]
\end{aligned} \tag{1.21}
$$

where

$$
v_c(\mathbf{r},\mathbf{r}')=\frac{l_B}{|\mathbf{r}-\mathbf{r}'|} \tag{1.22}
$$

is the coulomb interaction in units of the thermal energy, and $\hat{n}_c$ is the local charge density operator,[5]

$$
\hat{n}_c(\mathbf{r})=\hat{n}_+(\mathbf{r})-\hat{n}_-(\mathbf{r})+n_e(\mathbf{r}) \tag{1.23}
$$

in which

$$
\hat{n}_\pm(\mathbf{r})=\sum_{i=1}^{N_\pm}\delta(\mathbf{r}-\mathbf{r}_i^\pm) \tag{1.24}
$$

The first term within the exponential in (1.21) includes an infinite self energy, $\sum_i v_c(\mathbf{r}_i,\mathbf{r}_i)$, which is canceled by the second term.

One way to derive the mean-field equation (1.16) is through the Gibbs variational principle (Ref. [21], Sec. 10.4) where the solution of the PB equation minimizes a variational free energy. Another, more systematic method is to re-express the partition function as a field theory [22–24]:

$$
Z_G=\frac{1}{Z_v}\int\mathcal{D}\varphi\exp\left\{-\frac{1}{l}\int d\mathbf{r}\left[\frac{1}{8\pi l_B}(\nabla\varphi)^2+in_e\varphi-2\lambda\Theta\cos\varphi\right]\right\}. \tag{1.25}
$$

where $\mathcal{D}\varphi$ denotes a functional integral over a fluctuating field φ. In this expression $\lambda=\lambda_0 e^{v_c(0)/2}$ is a renormalized fugacity and the constant Z_v is the partition function of the Coulomb interaction, $Z_v=\sqrt{\det(v_c)}$. The prefactor $1/l$ is equal to one, but formally it is convenient to include this prefactor and to expand in powers of l (the so-called loop expansion parameter). To leading order in l the functional integral is dominated by the stationary point of the functional in the square brackets:

$$
l\mathcal{F}=-\ln Z=\mathcal{F}_0+l\mathcal{F}_1+\dots \tag{1.26}
$$

The zeroth-order term in Eq. (1.26), F_0, is the mean-field free energy, equal to

$$
\mathcal{F}_0=\max_{\phi(\mathbf{r})}\int d\mathbf{r}\left\{-\frac{1}{8\pi l_B}(\nabla\phi)^2+n_e\phi-2\lambda\Theta\cosh\phi\right\} \tag{1.27}
$$

and written in units of the thermal energy, where $\phi=i\varphi$ is the electrostatic potential. We omit the infinite but constant contribution coming from the prefactor Z_v. It is easy to verify

---

[5]The term *operator* and the ˆ superscript are used to distinguish $\hat{n}(\mathbf{r})$, which depends on the microscopic degrees of freedom, from $n(\mathbf{r})$, its thermodynamic average.

that $\mathcal{F}_0$ is a maximum at its extremum if ϕ is restricted to be real. In the complex plane the functional in Eq. (1.25) has neither a maximum or a minimum, but is instead a saddle point. The corrections to the mean-field free energy $(\mathcal{F}_1, \mathcal{F}_2, \ldots)$ arise from fluctuations around the saddle point and are discussed in Sec. 1.8.2.

Truncating the loop expansion at the mean-field term can be justified, of course, only if the other terms are small. In the case of a planar interface without salt, rescaling all spatial coordinates by the Gouy-Chapman length μ (defined in Sec. 1.3), leads to a natural dimensionless parameter that can be viewed as the loop parameter [Sec. 1.8.2, Eqs. (1.126) and (1.128)].

The mean-field free energy can also be expressed as a minimum of a functional of the local densities $n_\alpha(\mathbf{r})$ ($\alpha = \pm 1$ for a $1:1$ salt):

$$\mathcal{F}_0 = \min_{n_\alpha(\mathbf{r})} \left\{ \int d\mathbf{r} \sum_\alpha n_\alpha(r) \left[\ln \frac{n_\alpha(r)}{\lambda_\alpha} - 1 \right] + \frac{1}{2} \int d\mathbf{r} \, d\mathbf{r}' \, n_c(\mathbf{r}) v_c(\mathbf{r}, \mathbf{r}') n_c(\mathbf{r}') \right\} \qquad (1.28)$$

where $n_c = n_+ - n_- + n_e$. It is straightforward to show that this form for $\mathcal{F}_0$ is indeed a minimum at its extremum.[6]

It is interesting to note that, while both expressions (1.27) and (1.28) have the same value at their extremum, one is a minimum while the other is a maximum. This observation can be used to obtain bounds, from below and above, to the mean-field free energy. A slightly different form for F_0, combining these two expressions, is found by defining $\phi(\mathbf{r}) = \int d\mathbf{r}' v_c(r, r') n_c(\mathbf{r}')$ and using the Poisson equation to re-express the second term in Eq. (1.28):

$$\mathcal{F}_0 = \min_{n_\alpha(\mathbf{r})} \int d\mathbf{r} \left\{ \frac{1}{8\pi l_B} (\nabla \phi)^2 + \sum_\alpha n_\alpha(r) \left[\ln \frac{n_\alpha(r)}{\lambda_\alpha} - 1 \right] \right\} \qquad (1.29)$$

where ϕ is regarded here as a functional of n_α. Formally the relation between ϕ and n_α can be imposed using a Lagrange multiplier $\Lambda(\mathbf{r})$. This procedure yields a functional of ϕ, n_α, and Λ from which both the expressions (1.28) and (1.27) can be obtained (see chapter 2).

Using a free energy functional as a starting point for the theoretical treatment has several benefits. First, it is sometimes convenient to solve the PB equation numerically by minimizing or maximizing a free energy functional. Second, the free energy approach lends itself easily to extensions and generalizations, introduced by adding terms to the free energy functional, whose origin may be phenomenological or systematic. The value of the free energy itself is important – for example, the force acting on a charged object is found from the variation of the free energy with respect to a change in its position.

---

[6] As discussed in Sec. 1.8.1, a density functional $\tilde{\mathcal{F}}[n_\alpha]$ has a precise formal meaning that is not restricted to approximations such as mean-field theory. The functional that is minimized in Eq. (1.28) is, in fact, the zeroth order term in a loop expansion of $\tilde{\mathcal{F}}[n_\alpha]$ in powers of l. this result is derived in Supplement 1.F, showing also that corrections can be obtained to this expression in a systematic manner.

1.3   Planar case

The Poisson-Boltzmann equation can be solved analytically in a few simple geometries. The most simple case, and a very important one, is an infinite planar surface with a uniform surface charge σ:

$$n_e(\mathbf{r}) = \frac{\sigma}{e}\delta(z) \tag{1.30}$$

where z is the coordinate perpendicular to the plane. We assume also that $\Theta(\mathbf{r}) = 0$ at $z < 0$ and $\Theta(\mathbf{r}) = 1$ at $z > 0$, *i.e.*, ions can be present only on one side of the plane.[7] The treatment of this problem, the *planar electric double layer*, dates back to the pioneering works of Gouy [25] and Chapman [26].

The planar wall introduces a natural length scale into the problem, being the distance at which the bare interaction of an ion with the plane increases by $k_B T$,

$$\mu = \frac{e}{2\pi l_B |\sigma|} \tag{1.31}$$

This distance, which is inversely proportional to the surface charge, is called the *Gouy-Chapman length* [27]. From here on we assume that σ is negative, so that counterions carry a positive charge. For a 1:1 salt of concentration c_s, the solution of the PB equation reads (assuming negative σ):

$$\phi(z) = -2\ln\left(\frac{1 + \gamma e^{-\kappa z}}{1 - \gamma e^{-\kappa z}}\right) \tag{1.32}$$

where $\kappa^2 = 8\pi l_B c_s$ [Eq. (1.18)],

$$\gamma = \sqrt{(\kappa\mu)^2 + 1} - \kappa\mu \tag{1.33}$$

and the densities of positive and negative ions are

$$n_\pm(z) = c_s\left(\frac{1 \pm \gamma e^{-\kappa z}}{1 \mp \gamma e^{-\kappa z}}\right)^2 \tag{1.34}$$

If σ is positive the sign of ϕ should be reversed. Note that as $z \to \infty$ all quantities tend to their bulk values, $\phi \to 0$ and $n_\pm \to c_s$. At contact with the surface, $d\phi/dz = -2/\mu = 4\pi l_B \sigma/e$ – as it should be considering the surface charge at $z = 0$ and noting that the electric field vanishes at $z < 0$, since there are no ions in this region.[8] Two limits of the solution are of special interest:

---

[7]This is the relevant situation for membranes, because the low dielectric constant within the membrane prevents the penetration of ions. Neglect of the image forces (due to the dielectric discontinuity), which is inherent to the mean-field approach, can often be justified for monovalent ions.

[8]Only half of the reduced electrostatic field at contact, $2\pi l_B \sigma/e$, is directly due to the surface charge. The other half comes from the ions at $z > 0$.

Linear screening

When $\kappa\mu \gg 1$, corresponding to large ion concentration or small surface charge, $\gamma \simeq 2/(\kappa\mu) \ll 1$ and $\phi(z)$ tends to the solution of the linear Debye-Hückel equation (1.17),

$$\phi(z) = -\frac{2}{\kappa\mu}\exp(-\kappa z) \tag{1.35}$$

In this limit $|\phi(z)| \ll 1$ everywhere, and ion densities deviate only slightly from their bulk value: $n_\pm(z) \simeq c_s\left[1 \pm 2\exp(-\kappa z)/(\kappa\mu)\right]$. In contrast to the ion densities that decay to c_s as $\mathrm{e}^{-\kappa z}$, we note that the charge density $[n_+(z) - n_-(z)]$ decays to zero more rapidly, as $\mathrm{e}^{-2\kappa z}$. The reason for this faster decay is that the deviations of n_+ and n_- from c_s cancel each other to first order in ϕ.

Limit of no salt

The opposite limit, $\kappa\mu \to 0$, corresponds to $c_s \to 0$ or large surface charge. Let us consider the formal limit $c_s = 0$. In this limit $\gamma \simeq 1 - \kappa\mu$ and the solution in Eqs. (1.32)–(1.34) tends to the following result:

$$\begin{aligned} \phi(z) &\rightarrow -2\ln\left[\frac{2}{\kappa(z+\mu)}\right] \\ n_+(z) &\rightarrow \frac{1}{2\pi l_B(z+\mu)^2} \end{aligned} \tag{1.36}$$

where we assumed that $\kappa z \ll 1$ in addition to $\kappa\mu \ll 1$. Despite the vanishing concentration of ions in the bulk, the density of counterions (positive ions in our case) is not zero. In fact, these ions completely neutralize the charged plate as can be verified by integrating $n_+(z)$ from $z = 0$ to infinity. The co-ion density, $n_-(z)$, vanishes to leading order and scales as κ^3 for small κ.

The fact that all counterions are bound to the surface in the extreme limit of zero salt concentration is special to the infinite planar case considered here, being a consequence of the linear bare potential created by a charged surface of infinite extent (see also the discussion in Sec. 1.4). Note that there is no need for salt in order for counterions to exist - the very fact that the surface is charged implies that it has released counterions into the solution.

An alternative way to obtain Eqs. (1.36) is to solve the PB equation for only one species of ions:

$$-\frac{1}{4\pi l_B}\nabla^2\phi = c_0\Theta(\mathbf{r})\mathrm{e}^{-\phi(\mathbf{r})} + n_e(\mathbf{r}) \tag{1.37}$$

imposing a boundary condition of zero field at infinity (which is equivalent, in this case, to the requirement of overall charge neutrality). The constant c_0 has dimensions of concentration

but its value can be chosen arbitrarily: changing it only shifts the electrostatic potential by a constant. Indeed, Eq. (1.37) is invariant to the transformation: $c_0 \rightarrow \alpha c_0$; $\phi(\mathbf{r}) \rightarrow \phi(\mathbf{r}) + \ln \alpha$.

In the limit of no salt the ionic layer is very diffuse since the counterion density decays algebraically with z. The width of the ionic layer is characterized by μ: half the counterions are present between $z = 0$ and $z = \mu$. Beyond $z = \mu$ the distribution can be seen as corresponding to a charged surface at $z = \mu$ having half the surface charge of the plane at $z = 0$ or, equivalently, a twofold Gouy-Chapman length. This observation demonstrates that the ionic layer becomes more and more diffuse with increasing distance from the charged plate. In fact, all the moments $\langle z^n \rangle$ ($n \geq 1$) diverge, in marked contrast to the case of added salt.

Crossover to linear screening

When $\kappa\mu \ll 1$ but is not identically zero, the density profile follows the no-salt solution close to the charged plate, but crosses over to exponential decay at large z. This can be seen from Eq. (1.32): the equation cannot be linearized with respect to $\gamma e^{-\kappa z}$ close to the plate because $\gamma \simeq 1$ is not small, but it can be linearized for $\kappa z \gg 1$,

$$\phi(z) \simeq 4\gamma e^{-\kappa z} \tag{1.38}$$

Comparing with Eq. (1.35) shows that $\phi(z)$ has the same form as in the case of linear screening, but having an effective surface charge

$$\sigma_{\text{eff}} = 2\kappa\mu\gamma \cdot \sigma \tag{1.39}$$

and $|\sigma_{\text{eff}}| < |\sigma|$. The effective surface charge is smaller in magnitude than the nominal one due to the non-linear screening close to the charged plane. In the limit where non-linear effects are large, $\kappa\mu \ll 1$ and $\sigma_{\text{eff}}/\sigma \simeq 2\kappa\mu \ll 1$. Equation (1.39) applies for any value of $\kappa\mu$; in the opposite limit $\kappa\mu \gg 1$, $\sigma_{\text{eff}} \rightarrow \sigma$.

To summarize, even for highly charged surfaces where non-linear effects are important, linear screening applies beyond a distance of about κ^{-1}, the Debye length, from the charged surface. This important result applies also to non-planar charged objects. A few simple cases are discussed in the following sections.

Contact theorem

The contact density of ions is given, from Eq. (1.34), by

$$n_+(0) + n_-(0) = \frac{1}{2\pi l_B \mu^2} + \frac{\kappa^2}{4\pi l_B} = 2\pi l_B \left(\frac{\sigma}{e}\right)^2 + 2c_s \tag{1.40}$$

This identity, called the Grahame equation, has a simple interpretation, relating the ion pressure directly at the planar interface with the ion pressure in the bulk. The pressure exerted by ions on the charged plate can be written as a sum of two terms: the electrostatic force per unit area acting between the ions and the plate, $-2\pi l_B(\sigma/e)^2$, and an osmotic term, $n_+(0) + n_-(0)$ (see, also, Sec. 1.7.1). This pressure must be equal to $2c_s$, the pressure far away from the plate, because the ionic solution is in thermodynamic equilibrium, in agreement with Eq. (1.40).

Because the electrostatic field of an infinite charged plane is uniform, Eq. (1.40) can be generalized beyond mean-field theory, yielding an exact identity, known as the contact theorem [1, 28],

$$n_+(0) + n_-(0) = 2\pi l_B \left(\frac{\sigma}{e}\right)^2 + P_{\text{bulk}} \tag{1.41}$$

where P_{bulk} is the pressure in the bulk ionic solution. In particular, in the limit of zero salt concentration, $P_{\text{bulk}} = 0$ and Eq. (1.41) determines the contact density of counterions in a closed form: a derivation of Eq. (1.41) in this limit is given in Appendix 4.D. Furthermore, Eq. (1.41) is exact even if there are non-electrostatic interactions between the ions, in addition to their electrostatic interaction , but not if there is an ion-surface interaction. There are other exact sum rules that can be derived for ionic solutions in the planar case [29].

Validity of the mean-field approach

We note that the density profile's form depends only on the length scales μ and κ^{-1} (and in fact only their dimensionless ratio μ/κ^{-1} is important). Notably l_B, which is an independent length scale in the problem, does not influence the form of the density profile – a result of the mean-field approximation. This result is valid only when l_B is small compared to μ as well as to κ^{-1}. If any of these two inequalities is not obeyed, correlation effects beyond mean field are important. The case $l_B > \mu$ is discussed in Sections 1.8.2, 1.9 and in chapter 5.

1.4 Other geometries

General considerations

To what extent is the planar solution relevant to non-planar geometries? It should first be noted that regions of a charged surface, separated from each other by a distance large compared to κ^{-1}, are decoupled from each other. Consequently, if a surface is planar on this scale, the planar solution can be applied locally.[9]

---

[9]Similarly, if the surface charge is not uniform on a length scale that is large compared to κ^{-1}, the planar solution can be applied locally.

Let us consider now the ion distribution without salt, Eq. (1.36). In the no-salt limit (when κ^{-1} tends to infinity), there are substantial differences between ion distributions near objects of different geometry – an important observation that will be discussed in more detail below. Despite these differences, the planar solution without salt is relevant to curved objects in some situations. Consider a surface that is characterized by a radius of curvature R. If the Gouy-Chapman length μ is much smaller than R, there exists a window of salt concentrations:

$$\mu \ll \kappa^{-1} \ll R \tag{1.42}$$

where the counterions distribution, close to the charged object, is similar to the one obtained from the planar case. For example, near a colloid of radius $1000\,\text{Å}$ and with $\mu = 10\,\text{Å}$, Eq. (1.42) holds for $10^{-5}\,\text{M} \ll c_s \ll 0.1\,\text{M}$ (see, also, Supplement 1.6).

A similar statement can be made on the relevance of the cylindrical solution (Sec. 1.5) to semi-flexible PEs: if the persistence length is large compared to the Debye length, the infinite rod limit is relevant locally (see, for example, a comment on this issue in the concluding remarks of Ref. [30]).

Zero salt limit

At low salt concentrations, surfaces of different geometries differ fundamentally in the way counterions distribute around them. Consider a single charged sphere, and a single ion interacting with this sphere. The probability to find the ion, of charge qe, at a finite distance from the sphere, of charge Qe and radius a, is zero because the weight

$$4\pi \int_a^\infty r^2 \mathrm{d}r \exp\left(-\frac{Qql_B}{r}\right) \tag{1.43}$$

diverges. Consequently, a charged sphere does not bind any ions, whereas a charged plane is completely neutralized by its counterions, as discussed in Sec. 1.3. In the case of a charged sphere the entropy of an ion at a distance r from the sphere, scaling as $\ln(r^2)$, overcomes the electrostatic attraction which decays to zero at large r. In the case of a charged plane the situation is reversed. A special case is that of an infinite charged cylinder, where both the entropy and electrostatic interaction depend logarithmically on the ion-cylinder distance. The counterpart of Eq. (1.43),

$$2\pi \int_a^\infty r \mathrm{d}r \exp\left[-2ql_B\rho\ln(r)\right] \tag{1.44}$$

can be finite or, alternatively, diverge at $ql_B\rho > 1$ or $ql_B\rho < 1$, respectively.

We consider the charged cylinder in the following section. The charged sphere is discussed in Sec. 1.6.

1.5 Charged cylinder

The cylindrical case is of great importance due to its relevance to charged polymers (polyelectrolytes). In this section we discuss the predictions of mean-field (Poisson-Boltzmann) theory.

Throughout this section we assume that the cylinder is infinite in extent and is uniformly charged at its surface. The number of unit charges per unit length of the cylinder is designated by ρ, and the sign of the surface charge is taken to be negative:

$$n_e(\mathbf{r}) = -\frac{1}{2\pi a}\rho\delta(r-a) \tag{1.45}$$

where $\rho > 0$, a is the cylinder radius, and r is the radial coordinate (the cylinder axis is at $r = 0$). We assume that ions cannot penetrate the cylinder, so that $\Theta(\mathbf{r}) = 0$ for $r < a$.

1.5.1 Single cylinder without salt

In the most simple situation of a single, uniformly charged cylinder, no salt, and assuming monovalent counterions ($q = 1$) the ion distribution is

$$n(r) = \begin{cases} 0 & , \quad l_B\rho < 1 \\ \dfrac{1}{2\pi l_B r^2}\dfrac{(l_B\rho-1)^2}{[(l_B\rho-1)\ln(r/a)+1]^2} & , \quad l_B\rho > 1 \end{cases} \tag{1.46}$$

where r is the radial distance from the cylinder and a is the cylinder radius (for details on the PB equation in this geometry see Supplement 1.D). If $l_B\rho$ is smaller than unity, all the counterions escape to infinity. If, on the other hand, $l_B\rho$ is larger than unity some counterions are bound. A charge $1/l_B$ remains unneutralized, as can be verified by integrating the charge distribution from a to infinity.

The partial neutralization of charged cylinders is of central importance for polyelectrolytes (PEs). It is common to assume that highly charged PEs, having a linear charge density larger than $1/l_B$, are neutralized by a condensed layer of ions, resulting in an effective charge that is equal to $1/l_B$. This assumption was introduced by Manning [30] and Oosawa [31] in the late 1960's (see also, [32]), and remains very influential until this day. Its consequences and limits of validity are examined below in several contexts: the number of counterions near a PE, the effective charge of a PE in a salt solution, the excess of counterions, and the osmotic pressure (Sec. 1.7.4). Chapter 4 deals with a situation in which there is more than one species of counterions in the solution.

Bound ions

For some purposes it is important to know how many counterions are present near the charged cylinder. For example, these counterions may mediate an effective interaction between two polyelectrolytes.

We first note that a sets the scale in Eq. (1.46). As $a \to 0$ the layer of bound ions reduces to an infinitely dense, line charge distribution. However in practice, due to the logarithmic dependence in Eq. (1.46), a part of the condensed layer is very diffuse. This can be seen as follows: a fraction f of the condensed ions are present up to the radius

$$a \exp \left[\frac{f}{(l_B\rho - 1)(1 - f)} \right].$$

$$(1.47)$$

Therefore, roughly speaking, only a fraction $(l_B\rho - 1)/(l_B\rho)$ of the ions are present up to a distance of order a from the cylinder. The rest of the ionic layer is extremely diffuse, since for larger values of f the argument in the exponential [Eq. (1.47)] is large compared to unity. If $l_B\rho$ is not much larger than unity (the typical situation, even for highly charged PEs such as DNA), this very diffuse part of the ionic layer contains a significant fraction of the condensed ions.

The situation is different if $(l_B\rho - 1) \gg 1$. In this case almost all the condensed layer is within a distance of order a from the cylinder. This situation can be achieved in practice with multivalent ions, where the parameter $l_B\rho$ is replaced with $ql_B\rho$.

Usually there is salt in the solution (a situation that is discussed in more detail below). As long as $\kappa a \ll 1$ salt has a relatively small influence on the ion distribution close to the cylinder, and the above considerations are still valid.

1.5.2   Cylinder in a salt solution

Rescaling the spatial coordinate by the cylinder radius a, $\mathbf{r} \to \tilde{\mathbf{r}} = \mathbf{r}/a$, $\nabla \to \tilde{\nabla} = a\nabla$, yields the following equation (a 1:1 salt is assumed)

$$\tilde{\nabla}^2\phi = \kappa^2 a^2 \sinh\phi \quad ; \quad \left.\frac{\partial \phi}{\partial \tilde{r}}\right|_{\tilde{r}=1} = 2l_B\rho \quad ; \quad \left.\frac{\partial \phi}{\partial \tilde{r}}\right|_{\tilde{r}\to\infty} = 0 \qquad (1.48)$$

Hence the only independent dimensionless parameters in the problem are $l_B\rho$ and κa. An analytical solution to Eq. (1.48) is not known,[10] but important observations can be made.

It is instructive to see, first, how the concept of partial neutralization, obtained in the no-salt limit, remains relevant in the presence of salt. Far away from the cylinder, exponential

---

[10]An analytic expression for the case $\kappa a \to 0$ and $l_B\rho \leq 1$ was recently obtained by Tracy and Widom [33], expressed as an infinite sum of terms, each one the trace of an integral operator. Another recent treatment of the small κa limit can be found in Ref. [34].

screening results in complete neutralization of the cylinder by the ionic solution. This happens on the scale of the Debye length κ^{-1}. It should be clear then, that partial neutralization is a meaningful concept only if there is separation of scales: the Debye length κ^{-1} (over which complete neutralization occurs) must be large compared to a, the cylinder radius.

The importance of the limit $\kappa a \to 0$ can also be understood as follows. The potential difference between a position r, close to the cylinder, relative to infinite distance from the cylinder is obtained from the linear DH equation:

$$\phi(r) = 2l_B\rho K_0(\kappa r) \tag{1.49}$$

where K_0 is the zeroth order modified Bessel function of the second kind and we ignore, for the moment, possible nonlinear screening close to the cylinder.

Let us assume that the electrostatic potential follows the linearized theory up to contact with the cylinder. The ion density at contact with the cylinder is then

$$c_0\mathrm{e}^{-\phi(a)} = \frac{\kappa^2}{4\pi l_B}\mathrm{e}^{-\phi(a)} \simeq \frac{1}{4\pi l_B a^2}(\kappa a)^{2-2l_B\rho} \tag{1.50}$$

where in the last identity $K_0(\kappa a)$ was replaced by its asymptotic behavior for small κa, $K_0(\kappa a) \simeq -\ln(\kappa a)$. If $l_B\rho < 1$ this density vanishes when $\kappa a \to 0$. Consequently, there is no accumulation of ions near the cylinder, despite the fact that the electrostatic potential is large. If, on the other hand, $l_B\rho > 1$ the density in Eq. (1.50) diverges, signaling that there is a condensed layer of ions close to the cylinder.

Effective charge

At large distance from the cylinder the electrostatic potential is proportional to the solution of the linearized Debye-Hückel equation,

$$\phi(r) = 2l_B\rho_{\mathrm{eff}}\frac{K_0(\kappa r)}{\kappa a K_1(\kappa a)} \tag{1.51}$$

The effective charge ρ_{eff} determines the interactions between polyelectrolytes in a sufficiently dilute solution, as well as the interaction between different rod-like segments of a single PE, provided that the distance between them is large compared to the Debye length.

Despite the importance of this quantity, its exact values are not reported in the literature (as far as we know), whereas it is common to assume that

$$l_B\rho_{\mathrm{eff}} = \begin{cases} l_B\rho & , \quad l_B\rho < 1 \\ 1 & , \quad l_B\rho > 1 \end{cases} \tag{1.52}$$

This issue is addressed in Supplement 1.C, where we show that Eq. (1.52) is over-simplified for several important reasons. The main results are summarized below, and more details can be found in the supplement.

The following identity is derived in the supplement,

$$\lim_{\kappa a \to 0} l_B \rho_{\text{eff}} = \frac{2}{\pi} \cdot \begin{cases} \sin\left(\dfrac{\pi l_B \rho}{2}\right) & , \quad l_B \rho < 1 \\ 1 & , \quad l_B \rho > 1 \end{cases} \tag{1.53}$$

relying on previous results of Tracy and Widom [33] and Ramanathan [35]. Equation (1.53) is an asymptotic expression, valid only in the limit $\kappa a \ll 1$. In this limit, $l_B \rho_{\text{eff}}$ is a constant when $l_B \rho > 1$, as in Eq. (1.52), but the constant is equal $2/\pi \simeq 0.64 < 1$. There is also a difference between the Eqs. (1.53) and (1.52) when $l_B \rho < 1$. In particular, an equality of $l_B \rho_{\text{eff}}$ and $l_B \rho$ is found in Eq. (1.53) only when $l_B \rho \ll 1$.

We recall that the effective charge characterizes the electrostatic potential only far away from the cylinder, at distances that are large compared to the Debye length. Since the Debye length diverges as $\kappa a \to 0$, Eq. (1.53) is useful only when there is some salt in the solution, so that κ^{-1} is finite but is still large compared to a. From the general considerations in the beginning of this section we may expect to find small corrections to Eq. (1.53) as long as $\kappa a \lesssim 1$.

The actual effect of added salt (non-zero κa) is studied in Supplement 1.C using numerical solution of the PB equation, leading to two main conclusions. First, the approach to the asymptotic limit (1.53) is very slow. At small, but realistic values of κa, there are significant corrections to (1.53). Despite these corrections the main qualitative outcome of Eq. (1.53), that $l_B \rho_{\text{eff}}$ depends very weakly on $l_B \rho$ when $l_B \rho > 1$, remains valid. Second, when $\kappa a \gtrsim 1$ Eq. (1.53) is not relevant at all. In particular, $l_B \rho_{\text{eff}}$ strongly depends on $l_B \rho$ when $l_B \rho > 1$.

The very slow, logarithmic, convergence to asymptotic limits in the cylindrical problem is one of the reasons for the difficulty to develop scaling theories for highly charged PEs. Another example for such slow convergence is found in the zero salt limit, when finite PE concentration effects are considered (discussed in Sec. 1.5.3).

Excess of bound ions

In addition to the effective charge, there is another important quantity for cylindrical macromolecules that are sufficiently dilute (separated by distances large compared to the Debye length). This quantity is the excess of each counterion species per unit length of the cylinder,

$$\rho_\alpha = 2\pi \int_0^\infty r \mathrm{d}r \, [n_\alpha(r) - c_\alpha] \tag{1.54}$$

Due to charge neutrality,

$$-\rho + \sum_{\alpha} q_{\alpha}\rho_{\alpha} = 0 \tag{1.55}$$

where ρ is the number of negative unit charges per unit length of the cylinder. The excess is important for several reasons:

- For a single charged rod in salt solution, the excess is related to a derivative of the free energy:

$$\rho_{\alpha} = \left.\frac{\partial}{\partial\mu_{\alpha}}\left(f - f_0\right)\right|_{T,V,\mu_{\alpha}} \tag{1.56}$$

  where f is the free energy per unit length, and f_0 is the free energy per unit length in the absence of the PE, in the ensemble where chemical potentials of the ion species are specified.

  For a dilute solution of PEs, the excess free energy $f - f_0$ of a single PE is related to the Gibbs free energy (or, equivalently, the chemical potential of PEs expressed through all the other intensive parameters), of importance for equilibrium processes in which the PE is involved.

- In a dilute PE solution the pressure is dominated by the concentration of ions far away from the PE. This bulk concentration is different from the average ion concentration, which takes into account the distribution of ions close to the PEs and is typically controlled experimentally. The bulk and average concentrations are related to each other through the excess. This is further discussed in Sec. 1.7.4.

- The excess ρ_{α} is a measure of the number of bound ions, up to a distance of order κ^{-1} from the PE.

An exact identity within mean-field theory, derived in Supplement 1.E, relates the sum $\sum_{\alpha}\rho_{\alpha}$ to the density of ions at contact with the cylinder (see, also, Sec. 1.7.4 for an application of this identity). The behavior of ρ_{α} in a solution containing competing species of monovalent and multivalent counterions is studied in chapter 5.

1.5.3 Finite volume: charged cylinder in a cylindrical cell

We return now to discuss the salt-free situation. As will be demonstrated below, the limit of a single, isolated cylinder can be applied without modification only at extreme dilution of a PE solution. In evaluating the influence of finite volume on the ion distribution, a standard
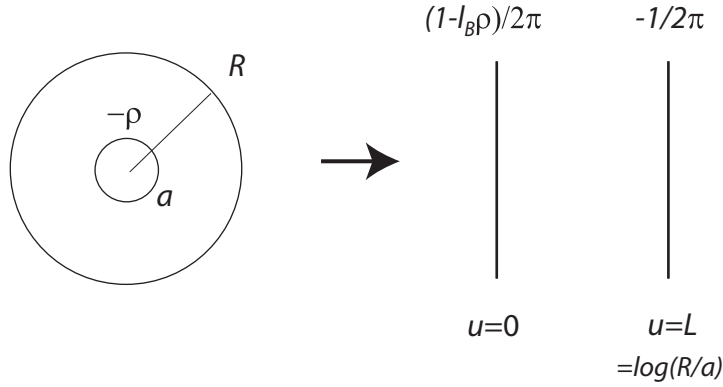
Figure 1.4: The problem of an infinite charged cylinder of radius a and linear charge density $-\rho$ ($\rho > 0$), enclosed in a cell of radius R is analogous, within mean-field theory, to that of two infinite, uniformly charged planes separated by a distance $L = \ln(R/a)$. Their surface charge densities are $(1 - l_B\rho)/2\pi$ and $-1/2\pi$ (choosing the units in the planar problem such that $l_B = 1$).

theoretical model is the *cell model* [37], where each PE is placed at the axis of a cylindrical cell of radius R. The volume of this cylinder is the inverse of the PE density:

$$\pi R^2 a_m c_m = 1 \tag{1.57}$$

where c_m is the monomer concentration and a_m is the distance between monomers along the PE backbone (equal to $1/\rho$ if each monomer carries a unit charge). Charge neutrality within the cell implies that $\partial \phi / \partial r$ must be zero at the cell boundary.[11]

A solution of the PB equation in a cylindrical cell was obtained by Fuoss, Katchalsky and Lifson in 1951 [39]. Le Bret and Zimm [40] clarified the relation between this solution and Manning's condensation theory. Here we present the Fuoss-Katchalsky-Lifson solution from a slightly different perspective, which makes the relation to the single cylinder situation more transparent. For more details see Supplement 1.D.

As shown in the Supplement, a transformation to the variable

$$u = \ln\frac{r}{a} \tag{1.58}$$

maps the problem into a more familiar one: that of two charged plates separated by a distance $L = \ln(R/a)$ (Fig 1.4). The plate at $u = L$ has a surface charge equal to $-1/2\pi$ (in rescaled units), so it always attracts the positively charged ions. The plate at $u = 0$, corresponding to the surface of the charged cylinder, has a surface charge $(1 - l_B\rho)/2\pi$.

---

[11]The case of extremely dilute, rod-like PEs without salt, was recently studied in Ref. [38]. Assuming that PE distances are much larger than the PE length, the cell model is modified by embedding a cylindrical cell within a larger, spherical cell that surrounds each PE.

There are two distinct situations: if $l_B \rho < 1$ $(1 - l_B \rho > 0)$, the plate at $u = 0$ repels the ions. As L is increased towards infinity all the ions follow the second plate and escape to infinity; the ion concentration at any finite u vanishes. If $l_B \rho > 1$, the plate at $u = 0$ is negatively charged. This negative charge is neutralized by a layer of bound ions ($l_B \rho - 1$ ions per unit length), even as $L \to \infty$. The rest of the ions escape to infinity with the second plate. In the asymptotic limit $L \to \infty$ the density profile of ions near the cylinder becomes a single plate profile, Eq. (1.36), with a Gouy-Chapman length $(l_B \rho - 1)^{-1}$. Mapping back to the cylindrical coordinates yields Eq. (1.46).

When L is finite and $l_B \rho > 1$ there is a layer of bound ions near $u = 0$ and another layer near $u = L$. Because there is no screening by salt these two layers are coupled to each other. The relative magnitude of the two single-plate profiles is sufficient in order to obtain a rough estimate for the magnitude of finite volume effects, although the density profile is not a simple superposition of the single-plate profiles. For example, at large $\ln(R/a)$ the ion density at contact with the cylinder scales as

$$\frac{1}{2\pi l_B a^2} \left\{ (l_B \rho - 1)^2 + \frac{\pi^2}{[1 + \ln(R/a)]^2} \right\} \tag{1.59}$$

as expected from simple superposition, but the prefactor π^2 can only be found from the exact solution in the two-plate case. Equation (1.59) is an example for the very slow decay of finite concentration effects with dilution of the PE solution (See also Sec. 1.7.4).

We finally note that the mapping of the cylindrical problem to a planar one is restricted to mean-field theory, and cannot be performed in the exact theory.

1.6 Charged sphere

In the case of a charged sphere, there are no bound ions in the no-salt limit. Hence the main quantity of interest is the effective charge of a sphere in a salt solution, defined through the behavior of the electrostatic potential far away from the sphere:

$$\phi(\mathbf{r}) = Q_{\text{eff}} \frac{l_B}{(1 + \kappa a)} \frac{e^{-\kappa(r-a)}}{r} \tag{1.60}$$

where r is the distance from the sphere's center. Many of the concepts discussed in the section on cylinders are relevant also to the sphere. The discussion here will be more brief, since this thesis does not deal directly with spherical objects.

We will assume that the sphere is highly charged, in the sense that the effective Gouy-

Chapman length is small compared to the sphere radius:

$$\frac{\mu}{a} = \frac{2a}{l_B Q} \ll 1 \tag{1.61}$$

where Qe is the total charge of the spherical particle, assumed to be uniformly distributed on its surface. We note that the nominal valency Q is usually not known, whereas Q_{eff} is often a fit parameter in analysis of experimental data.

Despite the absence of bound ions in the absolute limit of zero salt concentration, a small amount of salt is sufficient in order to maintain a layer of ions near the sphere, which renormalizes its charge. In order to understand why this happens, note that the potential at the cylinder boundary, $-Ql_B/a$, is very large and is not influenced by salt (on the Debye-Hückel level) if $\kappa a \ll 1$. Even if c_s is very small the concentration at the sphere surface,

$$c_s \exp\left(\frac{Ql_B}{a}\right) \tag{1.62}$$

can be very large, indicating that there is accumulation of counterions near the sphere.[12]

The effective charge of a sphere, in the case $\kappa a \ll 1$, was evaluated by Ramanathan [96]. To leading order in κa he found:

$$Q_{\text{eff}} = 2\frac{a}{l_B}\ln\left[\frac{4}{\kappa a}\ln\left(\frac{1}{\kappa a}\right)\right] \tag{1.63}$$

which implies, using Eq. (1.62), that ions accumulate at the surface of the sphere until their concentration, at the boundary of the bound layer, reduces to about $1/l_B a^2$ (up to a prefactor of order unity). Note that the effective charge, Eq.(1.63), does not depend on Q: it is a saturated value, which does not apply if Q or κa are very small.[13]

So far we discussed the effective charge only at low (but not extremely low) salt concentration. Spanning the whole possible range of salt concentrations, one finds that there are five different regimes:

1. $\boldsymbol{\kappa a < \exp(-Ql_B/2a)}$. At extremely small salt concentration the effective charge is equal to the nominal charge. Due to the exponential dependence, this regime is accessible in practice only for relatively small and weakly charged colloids.

---

[12]It is interesting to compare Eq. (1.62) with the parallel quantity in the cylindrical case, Eq. (1.50). Near a charged cylinder having $l_B\rho < 1$ there is no accumulation of ions, a situation that persists even with addition of salt, as long as $\kappa a \ll 1$.

[13]The variational approach of Netz and Orland [36] leads to a slightly different estimate, which depends weakly on the colloid charge,

$$Q_{\text{eff}} = 2\frac{a}{l_B}\ln\left(\frac{1}{\kappa a}\sqrt{\frac{Ql_B}{a}}\right)$$

We use Ramanathan's result in this discussion, because it is obtained using a more systematic approach than the variational one, and because it is supported by our numerical results, obtained from solution of the PB equation.

2. $\exp(-Ql_B/2a) < \kappa a \ll 1$. Here the effective charge is equal to the saturated value of Eq. (1.63).

3. $\kappa a \simeq 1$. Crossover between small and large κa. When κa is of order unity it is difficult to obtain an analytical estimate for Q_{eff} [96].

When $\kappa a \gg 1$, the curvature of the sphere is irrelevant on the scale of the Debye length. The renormalized charge can then be obtained from the planar case, using Eq. (1.39):[14]

4. $1 \ll \kappa a \ll a/\mu$. Using the expansion of γ for small $\kappa\mu$ one obtains:

$$Q_{\text{eff}} = Q \left(2\kappa\mu - 2\kappa^2\mu^2 + \ldots\right) = \frac{4\kappa a^2}{l_B} \left(1 - \kappa\mu + \ldots\right) \tag{1.64}$$

Note that Q_{eff} does not depend on Q to leading order.

5. $a/\mu \ll \kappa a$. Here the linearized Debye-Hückel equation is valid and to leading order $Q_{\text{eff}} = Q$. Using the expansion of γ for large $\kappa\mu$:

$$Q_{\text{eff}} = Q \left(1 - \frac{1}{4\kappa^2\mu^2} + \ldots\right) \tag{1.65}$$

The four latter regimes are easily accessible experimentally.

Figure 1.5 shows the effective charge of a colloid having $a/\mu = 35$. For a colloid of radius $a = 200\,\text{Å}$ this ratio corresponds (in aqueous solution) to $Q = 2000$ – matching, roughly, the structural charge of a polystyrene latex particle of this size. Regimes (2)–(4) can be seen in the plot, whereas regime (1) occurs at unrealistically small salt concentrations. With $a = 200\,\text{Å}$ the accessible range of salt concentrations $10^{-7}\,\text{M}$ (water with no added salt) up to $5\,\text{M}$ (close to saturation of NaCl) corresponds, roughly, to $\kappa a = 10^{-2}$ up to 10^2.

To summarize this section, the charge Q of a colloidal particle is typically renormalized in the presence of salt. Furthermore, there is a wide range of salt concentrations where the renormalized charge is almost independent on Q: if the salt concentration is kept fixed and Q is gradually increased, Q_{eff} quickly saturates at a value that depends only on the salt concentration and on the particle size.

In colloid suspensions inter-colloid separations are often large compared to the Debye length. The relevance of Debye-Hückel theory with a renormalized charge, in these situations, was experimentally verified to a very high degree of accuracy in colloidal suspensions confined to a two dimensional layer. Using several techniques involving video microscopy, it was possible to extract the pair correlation function between spheres and to deduce the pairwise-additive interaction energy [97, 98].

---

[14]Similar asymptotic expressions apply to charged cylinders at large κa but are seldom of practical relevance for PEs.
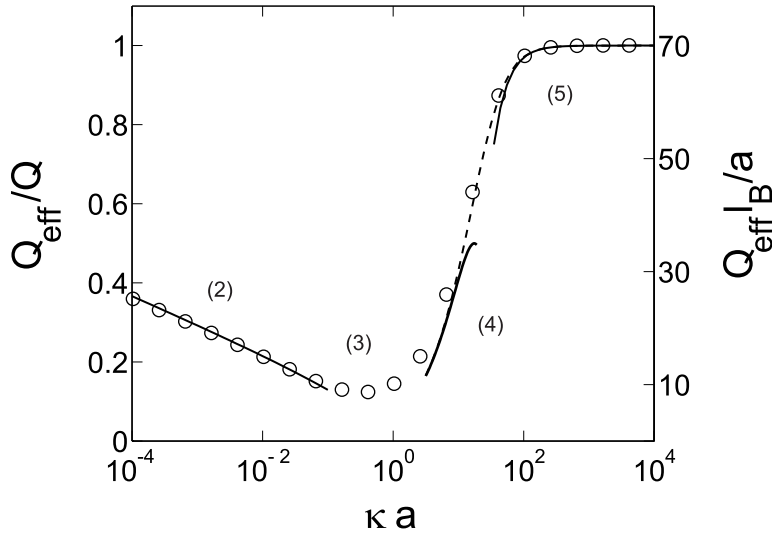
Figure 1.5: Effective charge, Q_{eff}, of a spherical particle in a salt solution as a function of κa. The ratio $a/\mu = 35$. Different regimes (described in the text) are designated by the numbers (2)–(5). The solid lines are the analytical expressions in the regimes (2), (4), and (5), Eqs. (1.63)–(1.65), while the dashed line is obtained from the planar solution without any further approximations (thus being valid in both regimes (4) and (5), as well as in the crossover region between them). The symbols were obtained from numerical solution of the PB equation in spherical coordinates. The right axis shows the ratio $Q_{\text{eff}} l_B/a$, which is independent on the structural charge Q in regimes (2) and (4), being there a function only of κa.

Finite colloid concentration

Historically, the notion of charge renormalization in colloids was introduced by Alexander et al. in 1984 [99]. They considered colloidal suspensions in the limit of no salt, but at non-zero colloid concentration. Despite the absence of salt it was proposed that, far away from a colloid, the potential is given by the Debye-Hückel form with a suitably matched effective charge.

The main idea behind Alexander et al's estimate for the effective charge is that the free ions (those that do not renormalize the colloid charge) form a reservoir, similar to a salt solution, of concentration

$$c_s = Q_{\text{eff}} c_c \tag{1.66}$$

where c_c is the colloid concentration. The effective charge of the colloid can then be estimated from Eq. (1.63):

$$Q_{\text{eff}} = \frac{a}{l_B} \ln \left(\frac{1}{Q_{\text{eff}} c_c v} \right). \tag{1.67}$$

where, up to a logarithmic prefactor,

$$v \sim l_B a^2. \tag{1.68}$$

Alexander et al used, in their estimate, a much smaller value for v than (1.68), equal to the excluded volume of a single counterion. This does not necessarily make a dramatic difference for Q_{eff} since v appears inside the logarithm (we note, however, that choosing v to be the volume of a counterion is difficult to justify from first principles). The outcome is that Q_{eff} depends very weakly on Q, and is considerably smaller than Q for highly charged colloids.

Critical evaluation of the estimate (1.67)

In order for the free ions to form a reservoir of constant density, and in order for the concept of effective charge to be meaningful in the presence of neighboring colloids, the typical distance between colloids, $R = c_c^{-1/3}$, must be large compared to the effective Debye length:

$$1 \ll \kappa^2 R^2 = 4\pi l_B Q_{\text{eff}} c_c^{1/3} = \frac{4\pi l_B Q_{\text{eff}}}{R} \qquad (1.69)$$

For this inequality to hold, we must have

$$R \ll 4\pi l_B Q_{\text{eff}} \simeq 4\pi a \qquad (1.70)$$

where Eq. (1.67) was used. This condition never holds, meaning that the coupling between neighboring colloids is always large. Thinking of their interactions in terms of the Debye-Hückel interaction is thus an unjustified idealization [100]. Moreover, it is difficult to justify the use of Debye-Hückel theory when there are only counterions in the solution: the leading term in the linearization of the exponent $\exp(-\phi)$ (appearing in the Poisson-Boltzmann equation for a single ion species) is a constant, rather than a linear term in ϕ.

On the qualitative level the estimate of Eq. (1.67) is important, since it complements the result for the case of added salt, leading to the following conclusions:

- A layer of neutralizing counterions exists almost invariably near a highly charged colloid (obeying $a/\mu \gg 1$). This layer can disappear only if the salt concentration is extremely low and, simultaneously, the colloidal solution is extremely dilute.

- Far away from such a colloid, the ion distribution depends very weakly on the colloid charge Q (or in other words saturates) once Q crosses a certain threshold. At low salt concentrations ($\kappa a \ll 1$) the threshold is of order a/l_B, with a logarithmic dependence on the colloid concentration or the concentration of added salt.

We comment, in this context, that charged colloidal suspensions at low salt concentration are not well understood, due to the coupling of ion distributions near different colloids and the non pairwise-additivity of colloid-colloid interactions [100].

1.7   Forces between charged objects in solution

There are several types of forces acting between charged surfaces in solution, in addition to the electrostatic interaction [1]. These include dispersion forces [56], solvation and depletion forces [1], and steric forces between undulating objects such as membranes and polymers [11, 57]. Recently it has been realized that ion-surface dispersion forces can have an important contribution, especially at high salt concentrations where electrostatic interactions are strongly screened [58,59]. In this section we discuss only the force mediated directly by the ionic solution, treating the solvent as a continuum and assuming that the only interactions on the Hamiltonian level are: (i) ion-ion electrostatic interactions, (ii) ion-surface electrostatic interactions, and (iii) excluded volume interactions, restricting the ions from penetrating certain regions in space. The modern theoretical treatment of these forces, together with the contribution of attractive dispersion forces, was pioneered by Verwey and Overbeek [60] and, independently, by Derjaguin and Landau [61], and is known as the DLVO theory.

1.7.1   The planar case

We begin with two uniformly charged, parallel plates. Due to symmetry, the reduced electrostatic potential ϕ depends in this case only on the normal coordinate z. The PB equation can be solved analytically in the absence of salt (see Supplement 1.B for details), whereas in the presence of salt z can be expressed a function of ϕ, in terms of an elliptic integral [27].

We first discuss how the pressure is evaluated in the planar problem assuming, for simplicity, that both plates are identically charged. The more general case of two different surface charges is considered in Supplement 1.B.

We imagine that the plates are immersed in a solution that exerts pressure on both sides of each plate. The pressure exerted in the inner side is found from the variation of the free energy with respect to a small change in d:

$$P_{\text{in}} = -k_B T \frac{\delta \mathcal{F}}{\delta d} \tag{1.71}$$

whereas the pressure P_{bulk}, acting on the external side of the plates, is equal to the free energy per unit volume in the bulk solution. Within mean-field theory it is simply

$$P_{\text{bulk}} = k_B T \sum_{\alpha} c_{\alpha} \tag{1.72}$$

where c_{α} is the bulk concentration of the ion species α. The pressure required to maintain the two plates at their position is equal to $P = P_{\text{in}} - P_{\text{bulk}}$. The variation in (1.71) can be evaluated

by inserting a thin slice of width δd at an arbitrary position z_0 between the plates – leading, within mean-field theory to the result,

$$\frac{P}{k_B T} = -\frac{1}{8\pi l_B} \left(\frac{\mathrm{d}\phi}{\mathrm{d}z}\right)\bigg|_{z_0} + \sum_\alpha \left[n_\alpha(z_0) - c_\alpha\right] \tag{1.73}$$

where $n_\alpha(z_0)$ is the local concentration of ion species α at z_0. The first term is the electrostatic force acting between the two sides of the plane z_0, and the second term is the excess osmotic pressure exerted by ions at this plane, relative to the bulk. A derivation of this identity, in a more general case where there are also ion-ion interactions, is presented in Appendix 3.A. As expected, P does not depend on z_0, as can be verified using the PB equation.

Equation (1.73) has a particularly simple form at the mid-plane, where $\mathrm{d}\phi/\mathrm{d}z = 0$ from symmetry, so that

$$P = \sum_\alpha \left[n_\alpha(d/2) - c_\alpha\right] \tag{1.74}$$

It also has a simple form at contact with the plane, where $\mathrm{d}\phi/\mathrm{d}z$ is fixed by the boundary condition, leading to the result

$$-2\pi l_B \left(\frac{\sigma}{e}\right)^2 + \sum_\alpha n_\alpha(0) = \sum_\alpha n_\alpha(d/2) \tag{1.75}$$

where σ is the surface charge concentration on the plates. Equation (1.75) is the contact (or Graham) equation for two parallel, identically charged plates.

It can be easily proved that the pressure, Eq. (1.74), is positive: surfaces with charge of the same sign repel each other on the mean-field level (see also, Sec. 1.9). Note that at the mid-plane the electrostatic interaction between the two halves of the system is identically zero, and the repulsion is purely due to the osmotic pressure of a dilute solution of ions.

The important limits in the behavior of $P(d)$ are briefly discussed, assuming a symmetric 1:1 salt of concentration c_s. More details can be found in Ref. [27]. When $\boldsymbol{\kappa d \gg 1}$ the two plates are decoupled from each other: the mid-plane potential is small and equal to twice the potential at a distance $d/2$ from a single plate.

1. If, furthermore, $\boldsymbol{\kappa\mu \gg 1}$, the linearized Debye-Hückel theory is valid, and

$$\frac{P}{k_B T} \simeq c_0 \phi^2(d/2) = 8\pi l_B \left(\frac{\sigma}{e}\right)^2 \mathrm{e}^{-\kappa d} \tag{1.76}$$

2. More generally, an equation similar to (1.76) holds, with σ replaced by the effective surface charge that takes into account nonlinearities near the surfaces, Eq. (1.39). In the limit $\boldsymbol{\kappa\mu \ll 1}$, $\sigma_{\mathrm{eff}} \simeq \kappa/(\pi l_B)$ does not depend on μ (or, equivalently, on σ) and

$$\frac{P}{k_B T} \simeq \frac{8\kappa^2}{\pi l_B} \mathrm{e}^{-\kappa d} \tag{1.77}$$

When $\boldsymbol{\kappa d} \ll 1$ the potential is not simply a superposition of the single-plate potentials. There are three important limits:

3. If $\boldsymbol{d} \gg \boldsymbol{\mu}$ (*Gouy-Chapman limit*),

$$\frac{P}{k_B T} \simeq \frac{\pi}{2 l_B d^2} \tag{1.78}$$

This result is related to the single plate profile without salt: at $z \gg \mu$ the density is independent on σ, scaling as $1/(l_B z^2)$. The coupling between the two plates only affects the prefactor in (1.78), which is found from the analytical solution for two plates and no salt. It is easy to check that the identity $\kappa d \ll 1$ ensures that the mid-plane density is large compared to c_s, justifying the neglect of salt in the Gouy-Chapman limit.

4. If $\boldsymbol{d} \ll \boldsymbol{\mu}$ and $\boldsymbol{\kappa^2 d\mu} \ll 1$ (*ideal gas limit*) the influence of salt can still be neglected, but there are no longer distinct profiles near the two plates. To leading order in d/μ,

$$\frac{P}{k_B T} \simeq \frac{1}{\pi l_B \mu d} = \frac{1}{d} \frac{2|\sigma|}{e} \tag{1.79}$$

5. Finally, if $\boldsymbol{d} \ll \boldsymbol{\mu}$ but $\boldsymbol{\kappa^2 d\mu} \gg 1$, Debye-Hückel theory is valid, and it is found that

$$\frac{P}{k_B T} \simeq \frac{2}{\pi l_B \mu d} \frac{1}{\kappa^2 \mu d} \tag{1.80}$$

From cases 2 and 3 it follows that for sufficiently large σ the pressure saturates at a value that depends on κ and d but does not depend on the actual surface charge.

Oppositely charged plates

Two plates having charge of opposite sign can attract or repel each other. Repulsion is due to the osmotic pressure of counterions that are squeezed between the plates, and occurs at small separation – unless the two surfaces charges exactly balance each other. An underlying assumption in reaching this conclusion is that the surface charge is neutralized completely within the gap between the two plates. This is often the case with membranes due to their low dielectric constant. The boundary separation between attraction and repulsion is derived in Supplement 1.B.

1.7.2   Electrostatic stress tensor

In this section we discuss how the expression for the pressure in the planar geometry, Eq. (1.73), can be generalized to objects of arbitrary shape. Fig. 1.6 shows a charged object in an ionic
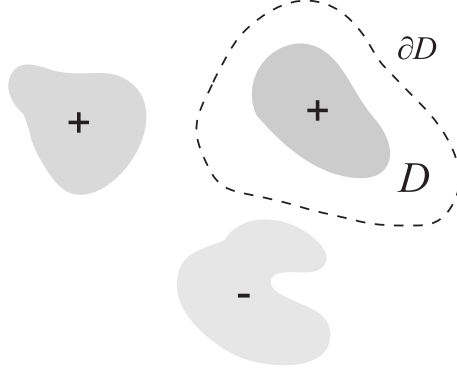
Figure 1.6: A volume element D in an ionic solution, surrounding a charged object. ∂D is the boundary surface.

solution, surrounded by a volume element D. The electrostatic force acting on the volume element can be written as

$$\vec{F}_e = -k_B T \int_D \mathrm{d}^3\mathbf{r}\, n_c(\mathbf{r}) \nabla\phi(\mathbf{r}) \tag{1.81}$$

where ϕ is the reduced electrostatic potential (in units of $k_B T/e$) and $n_c(\mathbf{r})$ is the charge density (in units of e, the unit charge), taking into account both the ionic solution and the fixed charge distribution. This integral can be transformed into a surface integral:

$$
\begin{aligned}
\vec{F}_{e,i} &= -k_B T \int_D \mathrm{d}^3\mathbf{r}\, n_c \partial_i \phi = \frac{k_B T}{4\pi l_B} \int_D \mathrm{d}^3\mathbf{r}\, (\partial_j \partial_j \phi)(\partial_i \phi) \\
&= \frac{k_B T}{4\pi l_B} \int_D \mathrm{d}^3\mathbf{r}\, \partial_j \left[(\partial_j \phi)(\partial_i \phi) - \frac{1}{2}\delta_{ij}(\partial_k \phi)(\partial_k \phi) \right]
\end{aligned}
\tag{1.82}
$$

where $\vec{F}_{e,i}$ is the i-th component of $\vec{F}_e$ and Einstein's summation convention is used. Since the integrand is a divergence, Green's theorem can be applied, to obtain:

$$\vec{F}_{e,i} = \int_{\partial D} \mathrm{d}^2 s\, \hat{\mathbf{n}}_i \mathbf{T}_{e,ij} \tag{1.83}$$

where $\mathbf{T}_e$ is the *electrostatic stress tensor*:

$$\mathbf{T}_{e,ij} = \frac{k_B T}{4\pi l_B} \left[(\partial_i \phi)(\partial_j \phi) - \frac{1}{2}\delta_{ij}(\partial_k \phi)(\partial_k \phi) \right], \tag{1.84}$$

∂D is the boundary surface of the volume element and $\hat{n}$ is the unit normal to the surface, pointing from the volume element outwards. Equation (1.81) represents the electrostatic force acting on the volume element D at any particular configuration of the ions. A statistical average over this expression yields the average electrostatic force.

On the mean-field level a statistical average over (1.81) can be replaced by separate averages over each occurrence of ϕ, which in turn can be replaced by the solution of the Poisson-

Boltzmann equation. The total force acting on the volume element is then expressed as follows:

$$\vec{F_i} = \int_{\partial D} \mathrm{d}^2 s \, \hat{\mathbf{n}}_i \mathbf{T}_{ij} \tag{1.85}$$

where $\mathbf{T}$ the full stress tensor, equal to:

$$\mathbf{T}_{ij}(\mathbf{r}) = -\delta_{ij} k_B T \sum_{\alpha} n_{\alpha}(\mathbf{r}) + \mathbf{T}_{e,ij} \tag{1.86}$$

The first term is the momentum transfer due to ions crossing the boundary of D. This result can be derived from the change in free energy, Eq. (1.29), due to an infinitesimal translation of the volume element D. A similar derivation, albeit in a simple planar geometry, is presented in Appendix 3.A

The tensor $\mathbf{T}$ is divergence free: $\partial_j \mathbf{T}_{ij} = 0$, a result that follows from the Poisson-Boltzmann equation. Hence the force acting on the charged object surrounded by D does not depend on the choice of the surrounding surface. Note also that the force is zero if the volume element does not contain any charged object, as it should be since the ionic solution is at thermodynamic equilibrium.

We finally note that the relevance of Eq. (1.85) goes beyond mean-field theory. It is in fact an exact expression for the force, for the case of point-like ions. A statistical average should be placed over all the terms in (1.84) and n_{α} are the average concentrations. In Sec. 1.8.2 we show that the stress tensor (1.86) is indeed divergence-free in the exact theory.

1.7.3   The Derjaguin approximation

As noted in Sec. 1.4, when the radius of curvature of a surface is large relative to the Debye length, the planar case can be used locally to describe the ion distribution close to the surface. Similarly, the force acting between two such curved objects can be approximated by locally treating them as parallel planes, summing up the contributions from the planar-like local patches. This summation yields a surprising result (outlined below): the force acting between two curved objects is proportional to the *free energy* associated with two planar surfaces of the same separation.

We consider first a sphere of radius R interacting with a plane, and assume that the gap D between the sphere and the plane is much smaller than R. As long as $\kappa^{-1} \ll R$ the force can be approximated as follows (Fig. 1.7),

$$F(D) \simeq \int 2\pi r \mathrm{d}r \, P\left[d(r)\right] \tag{1.87}$$
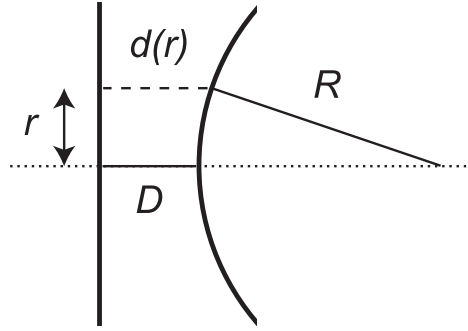
Figure 1.7: The sphere-plane geometry considered in Eqs. (1.87)–(1.89).

where r is the radial coordinate perpendicular to the symmetry axis, $d(r)$ is the local distance between the plane and the sphere:

$$d(r) = D + R - \sqrt{R^2 - r^2} \tag{1.88}$$

and $P(d)$ is the force per unit area (pressure) between two parallel planes at a distance d from each other. This approximation, known as the *Derjaguin approximation*, can be applied with any interaction whose range is very small compared to R, and relies heavily on this requirement (as noted above, another requirement is that $D \ll R$).

The integration in Eq. (1.87) yields the following simple result:

$$F(D) = 2\pi R W(D) \tag{1.89}$$

where $W(D)$ is the interaction free energy, per unit area, of two planes.[15]

More generally [1], for two spheres of radii R_1 and R_2 the force is given by

$$F(D) = 2\pi \left(\frac{1}{R_1} + \frac{1}{R_2} \right) W(D) \tag{1.90}$$

and for two crossed cylinders of radii R_1 and R_2, whose symmetry axes are oriented in perpendicular directions,

$$F(D) = 2\pi \sqrt{R_1 R_2} W(D) \tag{1.91}$$

This equation provides the necessary link between surface-force apparatus measurements, typically using crossed cylinders, to the planar model. Use of the Derjaguin approximation is justified since the crossed radii R_1 and R_2, being in order of magnitude of a centimeter, are

---

[15]more precisely, it is the free energy difference relative to infinite separation. Note that in the presence of salt this difference is finite.

much larger than κ^{-1} – even at very low salt concentrations. The Derjaguin approximation [Eq. (1.90)] is useful also for colloids, at sufficiently high salt concentrations and small inter-colloid separations.

1.7.4   Cell model and osmotic pressure in a PE solution

The osmotic pressure in a PE solution is almost always dominated by the small ions, because of the small translational entropy of the PEs. The situation is very different from that of neutral polymer solutions, in which the polymers are the sole component.

The nomenclature in this topic is confusing, because the terms *osmotic pressure* and the related *osmotic coefficient* are each used to describe two different quantities. The first is the excess pressure of the ionic solution, relative to pure solvent [30,37,62,63]. This is the pressure acting across a (real or imaginary) semi-permeable membrane that allows only the solvent to flow through, such that one side contains solvent while the other one contains solvent, PE, and ions. The second quantity, also commonly called the osmotic pressure [64–66], is the pressure acting across a membrane that is permeable to solvent as well as small ions, but not to the PE – a common setup in experiments. This is the excess pressure relative to a solution of salt, having the same chemical potential as in the PE solution. We call the latter quantity the *excess osmotic pressure* [67] in order to distinguish it from the former quantity.

To be more concrete, we first show how these quantities are calculated within the cell model – a useful theoretical framework for their study, introduced already in Sec. 1.5.

Cell model

Within the cell model, each PE is enclosed within a cylindrical cell of radius R, given by Eq. (1.57). The electrostatic potential obeys a Neumann boundary condition at the cell boundary:

$$\left.\frac{\partial \phi}{\partial R}\right|_R = 0 \tag{1.92}$$

The ionic contribution to the pressure is found from the derivative of the free energy F [Eq. (1.29)] with respect to volume,

$$\frac{\Pi}{k_B T} = -\frac{\delta \mathcal{F}}{\delta V} = -\frac{\delta}{\delta V}\left[N_m a_m f(R)\right] = -\frac{1}{2\pi R}\frac{\delta f(R)}{\delta R} \tag{1.93}$$

where N_m is the number of PE monomers in the cell, $f(R)$ is the free energy per unit length of the cell (in units of $k_B T$), and Eq. (1.57) is used in the last identity (in which $c_m = N_m/V$). Evaluation of this derivative is similar to the pressure evaluation at the mid-plane between two

identical planar surfaces, yielding:

$$\Pi = k_B T \sum_\alpha n_\alpha(R) \tag{1.94}$$

that is, the osmotic pressure is proportional to the ion density at the cell boundary.

The excess osmotic pressure, which we denote $\tilde\Pi$, is equal to

$$\tilde\Pi = k_B T \sum_\alpha [n_\alpha(R) - c_\alpha] \tag{1.95}$$

where c_α are the reservoir concentrations with which the ions in the cell are at equilibrium. For a symmetric 1:1 salt $c_+ = c_- \equiv c_s$.

An important relation for PE solutions (at least, within the cell model), is summarized by the following relation, obtained from Eqs. (1.18) and (1.57),

$$\kappa^2 R^2 = 8l_B \rho \frac{c_s}{c_m} \tag{1.96}$$

where ρ is number of unit charges per unit length of the cylinder. This equation shows that the following two conditions are related: decoupling of neighboring PEs by electrostatic screening, and the number ratio of salt ions to that of counterions coming from the PE. Assume first that $l_B \rho$ is of order unity. If κR is large (decoupled PEs), most of the ions in the solution come from the salt ($c_s \gg c_m$). Conversely, if κR is small, most of the ions are counterions ($c_s \ll c_m$). A large value of $l_B \rho$ does not change this conclusion because of the nonlinear condensation close to each PE. The only exception is a very weakly charged PE ($l_B \rho \ll 1$), in which case it is possible to have $\kappa R \ll 1$ and at the same time have salt as the main source of ions in the solution.

Osmotic pressure in dilute solutions

Consider a container of fixed volume, which holds a PE solution of monomer concentration c_m, and salt of concentration c_s (for simplicity we assume a symmetric 1:1 salt). Let us assume also that the PEs are sufficiently dilute that their typical distance is large compared to the Debye length.

Because the PEs are dilute, the electrostatic potential far away from the PEs is exponentially small, and the ion concentration at the cell boundary is equal to $2c_0$. Since in our scenario the experimentally known ion concentration is c_s, we need to evaluate the difference between c_s and c_0. As shown in Supplement 1.E,

$$2c_0 = 2c_s + \frac{c_m}{\rho}(\rho - \rho_+ - \rho_-) \tag{1.97}$$

where $\rho_\pm$ is the excess of positive or negative ions per unit length of the PE. Because we assume that each monomer carries a unit charge, $1/\rho = a_m$ is the axial distance between monomers and $\rho_\pm/\rho$ is the excess of positive or negative ions per monomer.

An exact identity, proved in Supplement 1.E, relates $\rho_+ + \rho_-$ to the density of ions at contact with the cylinder. This contact density is weakly affected by salt, and to leading order may be taken from the salt-free case – leading to the following result (see the supplement for details),

$$\frac{\Pi}{k_B T} = 2c_0 = 2c_s + \frac{c_m}{l_B \rho} \times \begin{cases} l_B \rho \left[1 - \frac{l_B \rho}{2} \right] & , \quad l_B \rho < 1 \\ \frac{1}{2} & , \quad l_B \rho > 1 \end{cases} \tag{1.98}$$

up to a correction term that tends to zero in the limit of vanishing salt concentration, $\kappa a \to 0$. This result is useful as long as:

$$a \ll \kappa^{-1} \ll R \tag{1.99}$$

If R is estimated using the cell model,[16] this requirement can also be written as follows:

$$\frac{1}{8 l_B \rho} c_m \ll c_s \ll \frac{1}{8 \pi l_B a^2} \tag{1.100}$$

The *osmotic coefficient* is defined as follows:

$$\phi = \frac{\Pi}{k_B T (c_m + 2c_s)} \tag{1.101}$$

and is thus equal to:

$$\phi = \begin{cases} 1 - \dfrac{l_B \rho}{2} \dfrac{X}{X + 2} & , \quad l_B \rho < 1 \\ \left(2 + \dfrac{X}{2 l_B \rho} \right) \dfrac{1}{X + 2} & , \quad l_B \rho > 1 \end{cases} \tag{1.102}$$

where $X \equiv c_m/c_s$. This result is identical to the one obtained by Manning in Ref. [30], using several simple assumptions and without direct reference to the ion distribution. The derivation presented here shows that the same result is rigorous within PB theory.[17] We emphasize that the PEs must be decoupled (having separation large compared to κ^{-1}), an assumption that is also made in [30].

The *salt exclusion factor* is defined as follows

$$\Gamma = \frac{c_0 - c_s}{c_m} = \begin{cases} \dfrac{1}{2} \left[1 - \dfrac{l_B \rho}{2} \right] & , \quad l_B \rho < 1 \\ \dfrac{1}{4 l_B \rho} & , \quad l_B \rho > 1 \end{cases} \tag{1.103}$$

where Eq. (1.98) was used. This result is also in agreement with Manning's derivation [30].

---

[16]Note that the cell model is not required for any other ingredient of the calculation.
[17]This derivation was also obtained by Anderson and Record [68] and by Ramanathan [69].

No salt limit

In the no-salt limit, there are only counterions contributing to the osmotic pressure. Within the cell model, their contribution can be obtained from the Fuoss-Katchalsky-Lifson solution (Sec 1.5.3). A particularly simple result is obtained if $\ln(R/a) \gg 1$: it is then possible to use the limiting values for $n(R)$, Eqs. (1.200) and (1.201). We then find that

$$\phi = \begin{cases} 1 - \dfrac{l_B \rho}{2} & , \quad l_B \rho < 1 \\[3mm] \dfrac{1}{2 l_B \rho} & , \quad l_B \rho > 1 \end{cases} \tag{1.104}$$

It is interesting to note that Eq. (1.102) crosses over smoothly to (1.104) when $c_s \to 0$ ($X \to \infty$). We note, however, that when R is not large compared to κ^{-1} adjacent PEs are usually coupled. Finite distance effects decay very slowly through $\ln(R/a)$ and are not taken into account in Eq. (1.104).

Excess osmotic pressure

Although Eq. (1.104) is the zero salt limit of Eq. (1.102), these equations represent two distinct physical situations. This becomes clear when the excess osmotic pressure is considered.

Within Manning's derivation [30] the excess osmotic pressure is identically zero. This is easily verified by evaluating $(\Pi - 2c_0)$ using Manning's expressions for ϕ and Γ [which are identical to Eqs. (1.102) and (1.103)]. In fact, the derivation of these equations here uses the equation $\Pi = 2c_0$ as its starting point.

In reality, the excess osmotic pressure is not zero, but is exponentially small in κR. In order to evaluate it the exponentially small electrostatic potential, at the cell boundary, must be found. This can be done using the PB equation within the cell model or using Manning's two-phase model [32] , but is completely beyond the scope of the derivation leading to Eqs. (1.102) and (1.103).

In the context of experiments that measure the excess osmotic pressure an osmotic coefficient is usually defined as follows:[18]

$$\tilde{\phi} = \frac{\tilde{\Pi}}{k_B T c_m} \tag{1.105}$$

In similarity to $\tilde{\Pi}$, $\tilde{\phi}$ is exponentially small when $\kappa R \gg 1$.

In the opposite limit of $\kappa R \ll 1$ there are typically many more counterions than salt ions, and the difference between $\tilde{\Pi}$ and Π is small. It is then tempting to use Eq. (1.104) as an

---

[18]This quantity is usually designated by ϕ. We use $\tilde{\phi}$ in order to distinguish it from ϕ, Eq. (1.101).

estimate for the osmotic coefficient $\tilde{\phi}$. However, Eq. (1.104) is a limiting expression that is seldom valid since it requires both $\kappa R \ll 1$ and $\ln(R/a) \gg 1$.
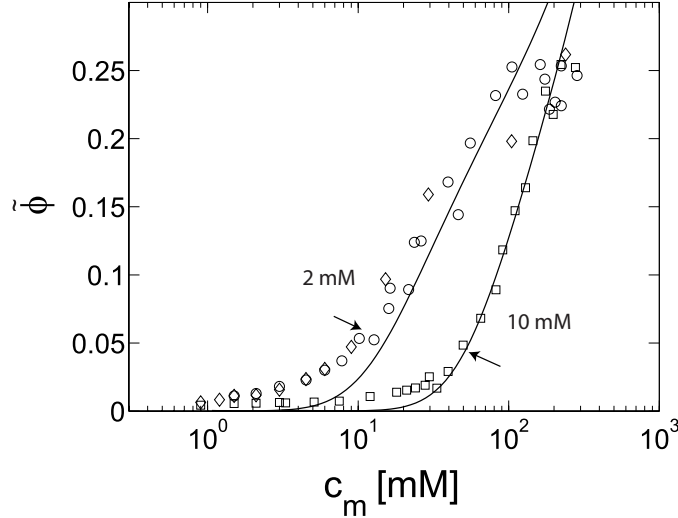
Figure 1.8: Excess osmotic coefficient, Eq. (1.105), in a PE solution, as a function of PE monomer concentration. Symbols: experimental results of Raspaud et al. [65] with short (150 base pair) rod-like DNA segments ($l_B \rho = 4.2$). Squares - with 10 mM TE. Circles - 2 mM NaCl. Diamonds - 2 mM TE. Solid lines are obtained from numerical solution of the PB equation in a cell. The DNA is modeled as a rigid cylinder of radius $a = 10\,\text{Å}$. The arrows designate the DNA concentration at which $\kappa R = 2.5$. Below this value there is large deviation between the cell model prediction and experimental data, as well as between the cell model prediction and the approximation of Eq. (1.106).

As an example, Fig. 1.8 shows recent measurements of the excess osmotic pressure in a solution of rod-like DNA segments [65], as a function c_m, at two different salt concentrations: 2 mM (circles and diamonds) and 10 mM (squares). The solid lines show the cell model prediction, obtained from numerical solution of the PB equation. It is clear that the cell model itself works well for small κR (large c_m). On the other hand equation (1.104), which for DNA ($l_B \rho = 4.2$) yields $\phi = 0.12$, is clearly not valid.

In Ref. [66] it was demonstrated that an analytical approximation can be used to evaluate $\tilde{\Pi}$, yielding very good agreement with the experimental data. The idea is based on the classical notion of Donnan equilibrium [70]. However, instead of treating the ions as uniformly distributed within the cell, it is assumed that the charge distribution $n_+ - n_-$ is governed by the zero-salt solution. The ion concentration at the cell boundary is then found from the two equations

$$n_+(R) - n_-(R) \quad \simeq \quad n_{\text{FKL}}(R)$$

$$n_+(R) \cdot n_-(R) = c_0^2 \qquad (1.106)$$

where n_{FKL} is the analytic Fuoss-Katchalsky-Lifson expression. The second equation is exact, since the Boltzmann factors $\mathrm{e}^{\pm\phi}$ cancel each other. We note that the same derivation was obtained by Oosawa (Ref. [31], Chapter 7, Sec. IV).

It should be stressed that the above approximation is valid only for $\kappa R \lesssim 1$. At large κR (small c_m) it yields much larger $\tilde{\phi}$ values than the exponentially small result predicted by full numerical solution of the PB equation with salt. Incidentally, these larger results agree quite well with the experimental data [66]. We believe that this apparent agreement is only a coincidence. The measured osmotic pressure cannot be a simple ionic contribution within the cell model, and must be attributed to PE-PE interactions.[19]

Finally, for very weakly charged PEs it is possible to have both small κR and a comparable number of salt ions and counterions. The ions (both counterions and salt ions) are then almost uniformly distributed within the PE solution, leading to the result

$$\tilde{\phi} = \sqrt{1 + \frac{4}{X^2}} - \frac{2}{X} \qquad (1.107)$$

where $X = c_m/c_s$. This result is similar to that of Eq. (1.106), if n_{FKL} is replaced by c_m.

1.8 Beyond mean-field theory

1.8.1 Liquid-state theory approaches

There is a large class of approximate methods used to treat fluids in the liquid state. All of these methods involve some kind of uncontrolled approximation, making them less rigorous than perturbation methods, but much more successful at the relatively high concentrations that are characteristic of liquids. All liquid-state theory approaches concentrate on the evaluation of correlation functions of various orders and the relations between them. Thus, in the context of charged fluids, they offer a possibility to take into account ion-ion correlations, beyond mean-field theory.

---

[19]This interpretation was also suggested in Ref. [65]. By PE-PE interactions we mean configurations other than the dispersed, parallel configuration assumed by the cell model. In the extreme limit of large screening, the problem becomes that of rigid rods having an effective radius determined by the Debye length. As shown by Onsager in a classical treatment of this problem [71], the second term in the virial expansion is the main contribution to the pressure or, in other words, the pressure is dominated by two-body rod-rod interactions. On the other hand, the statistical mechanics of charged rods with moderate screening (such as the lower concentrations in Fig. 1.8), is not well understood theoretically.

Integral equation methods

Integral equation theories [41] introduce a certain approximate relation between two correlation functions. One possible starting point is the exact Bogolyubov-Born-Green-Kirkwood-Yvon (BBGKY) hierarchy of equations,

$$
\begin{aligned}
-k_B T \nabla_{\mathbf{r}_1} \rho_n(\mathbf{r}_1, \ldots, \mathbf{r}_n) & = \sum_{j=2}^{n} \nabla_{\mathbf{r}_1} v(\mathbf{r}_1, \mathbf{r}_j) \rho_n(\mathbf{r}_1 \ldots \mathbf{r}_n) \\
& + \int d\mathbf{r}_{n+1} \nabla_{\mathbf{r}_1} v(\mathbf{r}_1, \mathbf{r}_{n+1}) \rho_{n+1}(\mathbf{r}_1 \ldots \mathbf{r}_{n+1})
\end{aligned}
\tag{1.108}
$$

written here for a homogeneous fluid (with no applied external field), and assuming that there are only pairwise-additive interactions between the particles: the Hamiltonian is $H = k_B T \sum_{i>j} v(\mathbf{r}_i, \mathbf{r}_j)$. This equation relates the n-particle and the $(n+1)$-particle density functions, whose definition is,

$$
\rho_n(\mathbf{r}_1 \ldots \mathbf{r}_n) = \frac{N!}{(N-n)!} \frac{\int e^{-\beta H} d\mathbf{r}_{n+1} \cdots d\mathbf{r}_N}{\int e^{-\beta H} d\mathbf{r}_1 \cdots d\mathbf{r}_N},
\tag{1.109}
$$

where N is the total number of particles (in the canonical ensemble). A related quantity, the n-particle correlation function g_n is conventionally defined such that $g_k = \rho_k / n^k$ where $n = \rho_1$ is the (one-particle) density. Eq. (1.108) is easily obtained by differentiation of Eq. (1.109).

The most simple approximation is based on the first BGGKY equation, relating ρ_2 to ρ_3. A second, approximate, relation between ρ_2 and ρ_3 is introduced, allowing one to solve for ρ_2:

$$
g_3(\mathbf{r}_1, \mathbf{r}_2, \mathbf{r}_3) = g_2(\mathbf{r}_1, \mathbf{r}_2) g_2(\mathbf{r}_2, \mathbf{r}_3) g_2(\mathbf{r}_1, \mathbf{r}_3)
\tag{1.110}
$$

This equation is called the *Kirkwood superposition approximation*.

Several widely used approximations [41] consider only the two-particle correlation function g_2 [which, for a bulk fluid, is a function of a single coordinate: $g_2(\mathbf{r}_1, \mathbf{r}_2) = g(\mathbf{r}_1 - \mathbf{r}_2)$]. Instead of relating $g(\mathbf{r})$ to a higher order correlation function, an approximate relation is introduced between $g(\mathbf{r})$ and the *direct correlation function* $c(\mathbf{r})$, defined as follows (the *Ornstein-Zernike* equation):

$$
g(\mathbf{r}) - 1 = c(\mathbf{r}) + [c * n \cdot (g - 1)](\mathbf{r})
\tag{1.111}
$$

where n is the density and $c * n \cdot (g - 1)$ is the convolution of c and $n \cdot (g - 1)$. In the *Hypernetted-Chain* (HNC) approximation, the approximate relation is:

$$
g(\mathbf{r}) = \exp\{-v(\mathbf{r}) + [g(\mathbf{r}) - 1] - c(\mathbf{r})\}
\tag{1.112}
$$

where $v(\mathbf{r})$ is the interaction potential appearing in the Hamiltonian. This equation, together with Eq. (1.111), can be solved in Fourier space to obtain $g(\mathbf{r})$. Since we do not motivate

Figure 1.9: Interaction pressure between two planar, charged plates with divalent counterions. Anisotropic-hypernetted-chain results (solid line) are compared with Monte-Carlo simulations (full circles). The surface charge corresponds to $1/60\,e/\text{Å}^2$ and counterions are spheres of diameter $4.25\,\text{Å}$ (reproduced from Ref. [45]).
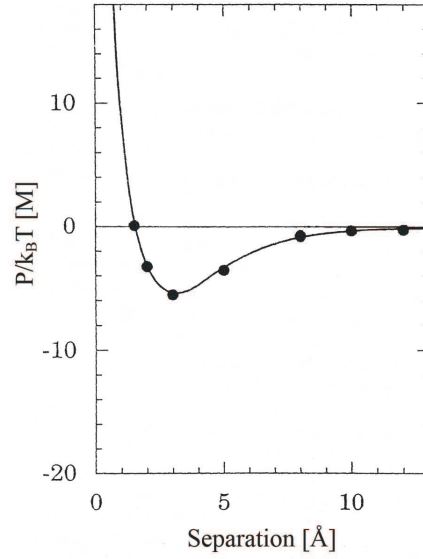
Eq. (1.112) (and similar relations) within this short introduction, we will only mention by name two other widely used relations [41]: the Percus-Yevick approximation and the mean spherical approximation (MSA). Generally speaking, the HNC approximation is more successful than the Percus-Yevick and MSA in treating long range interactions [42, 43], and is therefore commonly used with charged fluids.

The HNC approximation can be related to the virial expansion, which is the exact expansion in powers of the density. It is equivalent to partial summation of the diagrams appearing in the perturbative expansion, while neglecting a certain class of diagrams called the bridge diagrams. A refinement is obtained by reintroducing the bridge diagrams, taking their contribution from a reference system such as that of hard-core particles [44].

The AHNC approximation

Integral equation methods can also be formulated in anisotropic systems [42]. A generalization of the HNC approximation yields equations similar to (1.111) and (1.112), with g and c being functions of $\mathbf{r}_1$ and $\mathbf{r}_2$ (not simply of their difference), and n being a non-uniform function of $\mathbf{r}$ (a third equation relates the $\mathbf{r}$ dependent n to g, c, and the external potential responsible to the anisotropy [43]).

The *Anisotropic-Hypernetted-Chain* (AHNC) approximation [43, 46], has been very successful in describing ionic solutions in contact with uniformly charged planar walls. For such a planar system it can be derived also in the following way [46]. First, the coordinate z per-

pendicular to the charged interfaces is discretized. Then, by considering ions at different z values as different species, the inhomogeneous three-dimensional problem is transformed into a homogeneous two-dimensional problem with many species. The HNC approximation is then applied to this two-dimensional problem, requiring also that all "species" have the same value of the chemical potential.

An example for an AHNC calculation is shown in Fig. 1.9, where the AHNC prediction for the pressure between highly charged plates ($60\,\text{Å}^2$ per unit charge) is compared with Monte-Carlo simulation results, showing excellent agreement. In the presence of divalent counterions the pressure is attractive at close separations, in contrast to mean-field predictions. The AHNC approach was one of the first to predict this effect in a quantitative manner [47].

Solving the AHNC equations is computationally-intensive, since it requires a two-dimensional Fourier (Hankel) transform for each pair of discrete coordinates z_1, z_2, at each iteration of the solution of the nonlinear equations. In practice, only planar systems were treated in the AHNC approximation.

Density functional theories

The formal basis for *density functional* theories is the existence of a thermodynamic potential, whose natural variable is the local density $n(\mathbf{r})$. To show that such a potential exists, imagine a system under the influence of an external field $h(\mathbf{r})$ (in units of the thermal energy), in equilibrium with a particle reservoir. From the partition function it then follows directly that

$$\frac{\delta \mathcal{F}}{\delta h(r)} = n(\mathbf{r}) \tag{1.113}$$

where $\mathcal{F}$ is the grand potential, considered here as a functional of $h(\mathbf{r})$, and n is the local particle concentration. A Legendre transform with respect to $h(\mathbf{r})$ yields a functional of $n(\mathbf{r})$,

$$\tilde{\mathcal{F}}[n(\mathbf{r})] = \mathcal{F}[h(\mathbf{r})] - \int d\mathbf{r}\, n(\mathbf{r}) h(\mathbf{r}) \tag{1.114}$$

that must obey

$$\frac{\delta \tilde{\mathcal{F}}}{\delta n(\mathbf{r})} = -h(\mathbf{r}) \tag{1.115}$$

or vanish in the absence of an external field.

The density functional approach is very well suited for the treatment of inhomogeneous problems. Deriving an expression for the density functional can proceed using perturbational methods or a virial expansion (as in Supplement 1.F and Chapter 2), as well as heuristic or approximate relations, in similarity to integral equation methods [48].

In *Local density functional theories* (LDFTs) the density functional is approximated by an integral over a function of the local density:

$$\tilde{\mathcal{F}}[n(\mathbf{r})] = \int \mathrm{d}\mathbf{r}\, f[n(\mathbf{r})] \tag{1.116}$$

where $f(n)$ is the free energy per unit volume of a bulk system having density n. Naturally, this approach is suited for problems where the concentration varies slowly [49, 50].

1.8.2 Field theory methods

The field theory formulation of the partition function, Eq. (1.25), is a starting point for a perturbative expansion in the loop expansion parameter l [24]. We consider here the case of only counterions in the solution. The partition function is then similar to Eq. (1.25), with $2\cos\varphi$ replaced by $\mathrm{e}^{-i\varphi}$ [24]:

$$Z_G = \frac{1}{Z_v} \int \mathcal{D}\varphi \exp\left\{ -\frac{1}{l} \int \mathrm{d}\mathbf{r} \left[\frac{1}{8\pi l_B} (\nabla\varphi)^2 + i n_e \varphi - \lambda\Theta(\mathbf{r}) \mathrm{e}^{-i\varphi(\mathbf{r}) - h(\mathbf{r})} \right] \right\} \tag{1.117}$$

The field $h(\mathbf{r})$ is introduced in order to facilitate evaluation of the average local density, using a term in the Hamiltonian of the form $\int \mathrm{d}\mathbf{r}'\, h(\mathbf{r}')\hat{n}(\mathbf{r}') = \sum_i h(\mathbf{r}_i)$. It follows that the local density is

$$\langle n(\mathbf{r}) \rangle = -l \left. \frac{\delta \ln Z_G}{\delta h(\mathbf{r})} \right|_{h=0} . \tag{1.118}$$

From the way $h(\mathbf{r})$ enters in Eq. (1.117) it is seen that

$$\langle n(\mathbf{r}) \rangle = \lambda\Theta(\mathbf{r}) \langle \mathrm{e}^{-i\varphi(\mathbf{r})} \rangle \tag{1.119}$$

Before discussing the loop expansion, we make a few comments on the field theory formu-

lation. First, the following equation is exact:[20]

$$-\frac{1}{4\pi l_B}\langle \nabla^2 i\varphi\rangle = \lambda\Theta(\mathbf{r})\langle e^{-i\varphi(\mathbf{r})}\rangle + n_e(\mathbf{r}) \tag{1.120}$$

which demonstrates that mean-field theory is valid when $\langle e^{-i\varphi}\rangle = e^{-i\langle\varphi\rangle}$. Eq. (1.120) is the field-theory version of the Poisson equation. A second comment is related to the fugacity λ which is introduced, in the grand canonical ensemble, as a conjugate variable to the total number of ions. In the special case where there are only counterions in the system, the field theory has the peculiar property that λ has no influence on the ion distribution. This is seen by noting that the integrand in (1.117) is invariant to the transformation

$$\lambda \to \alpha\lambda \quad ; \quad \varphi(\mathbf{r}) \to \varphi(\mathbf{r}) - i\ln\alpha \tag{1.121}$$

which leaves the ion density, Eq. (1.119), unaffected. In fact, the total number of ions in the system is controlled by the boundary condition imposed on φ, as seen by integration of Eq. (1.120). On the formal level, a boundary condition must be defined when inverting the Coulomb operator, in the transformation from Eqs. (1.20) and (1.21) to the field theory (1.25). Typically, this boundary condition is of the Neumann type, $\nabla\phi \cdot \hat{\mathbf{n}} = 0$, a requirement of vanishing electrostatic field in the perpendicular direction to the boundary of the region in which the problem is defined. Using Eq. (1.120), this boundary condition implies overall charge neutrality if the problem is defined within a finite region (which can be arbitrarily large).

A third, related comment is that, if the boundary condition is imposed at infinity, charge neutrality is not guaranteed. Indeed, for a single charged sphere or a cylinder below the Manning threshold and on the mean-field level, all ions "escape" to infinity. More precisely, the system

---

[20]This identity can be derived as follows. The field φ is first shifted by defining: $-i\tilde\varphi = -i\varphi - h$. By doing so, h is eliminated form the exponent in Eq. (1.117) but three new terms are generated:

$$-\frac{1}{l}\int d\mathbf{r}\left[\frac{i}{4\pi l_B}\nabla\tilde\varphi\cdot\nabla h - \frac{1}{8\pi l_B}(\nabla h)^2 - n_e h\right]$$

Taking the functional derivative of $\ln Z$ with respect to h then yields,

$$-\left.\frac{\delta\ln Z_G}{\delta h(\mathbf{r})}\right|_{h=0} = -\frac{i}{4\pi l_B}\langle\nabla^2\varphi(\mathbf{r})\rangle - n_e(\mathbf{r})$$

where integration by parts is used to evaluate the contribution of the first term in Eq. (20). Comparison with Eq. (1.119) yields Eq. (1.120).

If $\nabla\varphi(\mathbf{r}')$ is first inserted in front of the exponential in (1.117), a similar derivation yields the identity

$$-\frac{i}{4\pi l_B}\langle\nabla\varphi(\mathbf{r}')\nabla^2\varphi(\mathbf{r})\rangle = \lambda\langle\nabla\varphi(\mathbf{r}')e^{-i\phi(\mathbf{r})}\rangle$$

where we restrict ourselves to points in space where there is no fixed electric charge, $n_e = 0$ and where $\Theta = 1$. Using this identity it is straightforward to show that the stress tensor [Eqs. (1.84), (1.86)] is divergence free,

$$\partial_j\langle\mathbf{T}_{e,kj} - k_B T\lambda e^{-i\varphi}\rangle = 0$$

is charge-neutral if it is enclosed in a finite cell, but all the ions are bound to the cell boundary and disappear as this boundary is taken to infinity. Charge neutrality is guaranteed in the exact theory only within a finite volume, or if there is salt in the solution.

Returning to discuss the loop expansion, up to linear order in l the free energy reads:

$$l\mathcal{F} = \mathcal{F}_0 + \frac{l}{2}\ln\left[\det G^{-1}\right] + \dots \tag{1.122}$$

where F_0 is the mean-field free energy. The first-order correction is obtained from a Gaussian integral over the quadratic term in the expansion of the field-theory Hamiltonian around its saddle point at $\varphi_0 \equiv -i\phi_{\mathrm{PB}}$: G^{-1} is the operator

$$G^{-1} = -\frac{\nabla^2}{4\pi l_B} + \Theta\lambda\mathrm{e}^{-\phi_{\mathrm{PB}}-h} = v_c^{-1} + n_{\mathrm{PB}} \tag{1.123}$$

Higher order terms in l can be obtained, in principle, in a diagrammatic expansion [24].

The outcome of the loop expansion is an expansion, in l, of observables such as the electrostatic potential and the ion density:

$$\begin{aligned}
\langle\phi(\mathbf{r})\rangle &= \phi_0(\mathbf{r}) + l\phi_1(\mathbf{r}) + \dots \\
\langle n(\mathbf{r})\rangle &= n_0(\mathbf{r}) + ln_1(\mathbf{r}) + \dots
\end{aligned} \tag{1.124}$$

where $\phi = i\varphi$, ϕ_0 is the PB potential and n_0 is the PB density.

The equations determining the first order terms were obtained explicitly in Ref. [24] and are presented, from a slightly different perspective, in Supplement 1.F.

Single charged plate

In the case of single plate of charge density σ and no salt,

$$n_e(\mathbf{r}) = \frac{\sigma}{e}\delta(z), \tag{1.125}$$

the leading order correction to mean-field theory was evaluated explicitly [24].

The mean-field density profile is characterized by a single length scale, the Gouy-Chapman length μ. There is only one more independent length scale in the problem, l_B, and the importance of correlations is determined by the dimensionless ratio $\Xi = l_B/\mu$. This can be seen by rescaling all coordinates by μ, $\mathbf{r} \to \tilde{\mathbf{r}} = \mathbf{r}/\mu$, $\nabla \to \tilde{\nabla} = \mu\nabla$ after which the partition function, Eq. (1.117) is

$$Z_G = \frac{1}{Z_v}\int \mathcal{D}\varphi \exp\left\{-\frac{1}{\Xi}\int \mathrm{d}\tilde{\mathbf{r}}\left[\frac{1}{8\pi}(\tilde{\nabla}\varphi)^2 + \frac{i}{2\pi}\varphi(\tilde{\mathbf{r}})\delta(\tilde{z}) - \tilde{\lambda}\Theta\mathrm{e}^{-i\varphi(\tilde{\mathbf{r}})}\right]\right\} \tag{1.126}$$
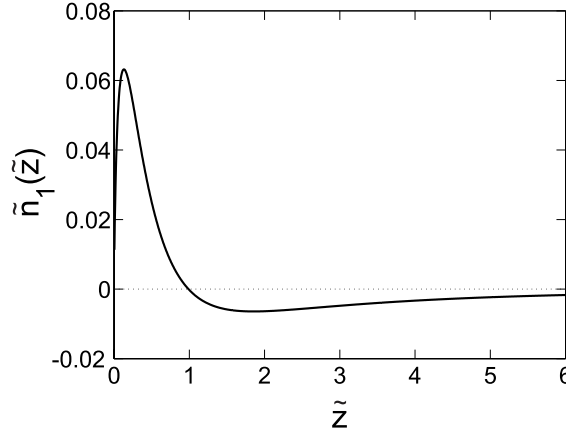
Figure 1.10:   The first order correction in the loop expansion to the PB density profile, $\tilde{n}_1(\tilde{z})$, appearing in Eq. (1.129).

where

$$\tilde{\lambda} = l_B \mu^2 \lambda \tag{1.127}$$

Therefore, Ξ (called the coupling parameter) plays the role of the loop parameter, that was introduced in Sec. 1.2.2 only as a formal expansion parameter. When Ξ is small, mean-field theory is expected to be exact, while correlation effects become increasingly important with increase of Ξ. We note that

$$\Xi = \frac{l_B}{\mu} = \frac{2\pi e^3 \sigma}{(\varepsilon k_B T)^2} \tag{1.128}$$

and that for multivalent ions of valency q, e is replaced by qe. Therefore Ξ increases with increase of the surface charge, decrease of the temperature and increase of the ion valency.

A loop expansion, using Ξ as the expansion parameter, yields an expansion for the ion density:

$$\langle n(z) \rangle = \frac{1}{2\pi l_B \mu^2} \left[\tilde{n}_0(\tilde{z}) + \Xi \tilde{n}_1(\tilde{z}) + \ldots \right] \tag{1.129}$$

where $\tilde{z} = z/\mu$. The zeroth order term is the Poisson-Boltzmann density profile, $\tilde{n}_0(\tilde{z}) = 1/(\tilde{z}+1)^2$.

The function $\tilde{n}_1(\tilde{z})$ was calculated in Ref. [24] and is reproduced in Fig. 1.10 (the analytical expression for n_1 is rather lengthy and is not reproduced here). We note that $\tilde{n}_1(0) = 0$, as it must be due to the contact theorem. Because the ions neutralize completely the charged plate,

$$\int_0^\infty \mathrm{d}\tilde{z}\, \tilde{n}_1(\tilde{z}) = 0 \tag{1.130}$$

The ion density is increased close to the charged plate, relative to mean-field theory. The physical reason for this increase is discussed in chapter 5. Roughly speaking, an ion close to

the plate is attracted more strongly to the plate than predicted by mean-field theory. Due to Eq. (1.130), an increase in the ion density close to the plate must be compensated by a decrease further away.

Being a perturbative approach, the loop expansion is useful only for small values of Ξ. Comparison with MC results [52] shows that truncation at the one-loop level is useful for Ξ of order unity or smaller, where the one-loop term is a small correction to the PB term. Since obtaining higher order terms in the loop expansion is difficult technically, the loop expansion is not useful for higher values of Ξ.

1.8.3 Other theoretical approaches

To conclude this section on theoretical treatments beyond mean-field theory, we mention two recent theoretical approaches. The first, *Strong coupling theory* [51, 52], is an expansion in the limit $\Xi \gg 1$. It turns out that a virial expansion can be used in this limit because, in the rescaled coordinates $\tilde{\mathbf{r}} = \mathbf{r}/\mu$, the ionic solution becomes dilute as $\Xi \to \infty$. To leading order in the virial expansion,

$$n(\mathbf{r}) \propto \exp[-u(\mathbf{r})] \tag{1.131}$$

where $u(r)$ is the bare ion-macroion interaction. One conclusion from this expansion is that, near a planar, highly charged surface, the ion density decays exponentially instead of the algebraic decay predicted by mean-field theory. Other results, related to forces between macroions, are discussed in Sec. 1.9.

The second approach, also treating the case of large Ξ, approximates the free energy of ions close to the charged surface by that of a two-dimensional one-component plasma [53, 54]. One of the important observations made in these works is that in the presence of salt (a z:1 salt or z-valent counterions and monovalent 1:1 salt) the surface charge can be overcompensated by z-valent counterions, leading to sign reversal of the effective charge [55].

1.9 Correlation induced attraction

Mean-field theory predicts a repulsive force between like-charged objects. This was seen in Sec. 1.7.1 for the planar case, but the same conclusion can be reached for other geometries, as was recently proved rigorously by Neu [72] and by Sader and Chan [73]. Limitations of mean-field theory were realized only in the past 15 years or so, and this subject continues to attract theoretical interest. In particular, it is now realized that like-charged objects can attract each other – as was demonstrated in simulation [52, 74–77], and using liquid state theory approaches

[45, 47, 75], field theory [23, 51] and other theoretical approaches [22, 49, 54, 78, 79]. There is also ample experimental evidence for this phenomenon [80–84]. In particular, aggregation of DNA and other PEs in presence of multivalent ions (discussed in chapter 4) is interpreted in this context as related mainly to electrostatic interactions.

Here we discuss the most simple possible model system: two parallel and uniformly charged plates having the same surface charge, without salt. The only interactions are the Coulomb interactions, and an excluded volume interaction that confines ions to the gap between the plates. The main purpose of the discussion is to elucidate why correlation-induced attraction can occur. Some of the ideas presented here are due to Safran and Pincus [79], Perel and Shklovskii [53, 54], and especially Moreira and Netz [51, 52].

1.9.1   Planar model

The model has the following parameters: σ, the surface charge density of each plate; qe, the ion charge where $z > 1$ for multivalent ions; d, the plate separation, the thermal energy $k_B T$; and ε, the dielectric constant.

In order to evaluate the pressure we pass a dividing plane at $z = z_0$, and write the force per unit area acting between the two sides of this dividing plane:

$$P = k_{\mathrm{B}} T n(z_0) + P_e \tag{1.132}$$

where P_e is the electrostatic force acting between the two sides of the plane. The first and second terms correspond, respectively, to the first and second terms in Eq. (1.86). For the present discussion it is convenient to express P_e as a volume integral:

$$P_e = \frac{1}{A} \left\langle \int_{z=-d/2}^{z_0} \mathrm{d}\mathbf{r} \int_{z'=z_0}^{d/2} \mathrm{d}\mathbf{r}' \, n_c(\mathbf{r}) \frac{\partial v_c \left(|\mathbf{r} - \mathbf{r}'| \right)}{\partial z} n_c(\mathbf{r}') \right\rangle \tag{1.133}$$

where $v_c(r) = e^2/(\varepsilon r)$, n_c is the charge density, A is the area, and the brackets denote a statistical average.

On the mean-field level the statistical average in Eq. (1.133) can be replaced by a statistical average over $n_c(\mathbf{r})$ and a separate average over $n_c(\mathbf{r}')$. In the particular choice of $z_0 = 0$, P_e must vanish, being the electrostatic force between two charge-neutral slabs: from symmetry each half of the system is charge-neutral. The remaining contribution to the pressure, $k_B T n(z_0)$, is positive.

Note that in the stress tensor language P_e is equal to $\langle \partial_z \phi \partial_z \phi / 2 - \partial_x \phi \partial_x \phi - \partial_y \phi \partial_y \phi \rangle$. On the mean-field level $\left\langle (\partial_i \phi)^2 \right\rangle = \langle \partial_i \phi \rangle^2$; all the derivatives vanish at the mid-plane from sym-

Figure 1.11: Two plates, each with a uniform charge density $-\sigma$, in the regime: $d \ll (2\sigma)^{-1/2} \ll z^2 l_B$. The amount of charge within the gray region is $-\sigma A$ on the right side of the dividing line, and $+\sigma$ on its left side.
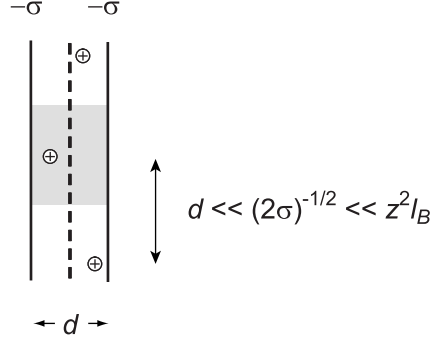
metry. This line of reasoning is the basis for more general theorems [72,73] applicable to other geometries and to the presence of salt.

Let us now focus our attention on the situation shown in Fig. 1.11. The typical lateral distance between neighboring ions is (i) large compared to d and (ii) small compared to $z^2 l_B$. According to (ii), electrostatic interactions between neighboring ions are much larger than $k_B T$, enforcing strong correlation in their lateral positions.

In the neighborhood of a particular ion, highlighted in Fig. 1.11, there is only a small probability to find another ion. Neglecting this small probability altogether, we find that there are charges of opposite sign on the two sides of the dividing plane. In the figure, a charge $-\sigma A$ on the right side coming from the charged surface (A is the area). On the left side, a total charge of $+\sigma A$: $-\sigma A$ coming from the charged surface and $+2\sigma A$ coming from the ion, since the number of ions per unit area is equal to 2σ from charge neutrality. The charges are reversed (but still opposite) if the ion crosses to the other side of the dividing plane.

From this discussion, it is seen that the electrostatic interaction across the plane z_0 is attractive: the pressure $P_e < 0$. Its magnitude is estimated as follows: a uniform electric field $-2\pi k_B T l_B \sigma / e^2$, exerted by the charge plate in the vacant side, acts on a charge σA in the opposite side, so that

$$P_e \simeq -2\pi k_B T l_B (\sigma/e)^2 \qquad (1.134)$$

The osmotic term can also be estimated easily. The force acting on an ion in the z direction is almost zero, because the contribution of the charged walls vanishes, while the contribution of the other ions is very small, due to the large lateral separation. As a result the probability distribution in the z direction is almost uniform (a statement that is made more precise in
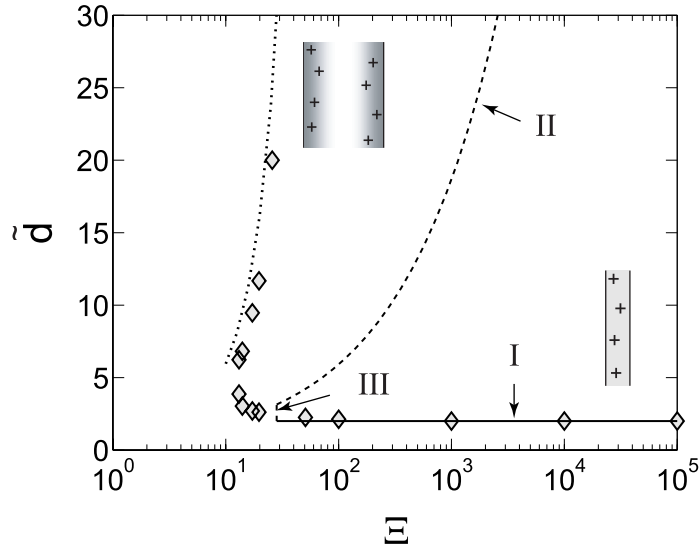
Figure 1.12:   Dividing line between attraction and repulsion for two interacting plates, as obtained from numerical simulation (diamonds, adapted from [52]). The lines I, II, III and the dotted line are discussed in the text.

chapter 5):

$$k_B T n(z_0) \simeq \frac{2\sigma}{ed} \tag{1.135}$$

An overall attraction is thus expected if

$$2\pi z l_B(\sigma/e)d > 2 \tag{1.136}$$

The estimates (1.134) and (1.135) are relevant only in the situation of Fig. 1.11, where the typical lateral distance between ions obeys:

$$d \lesssim \sqrt{\frac{q}{2\sigma}} \lesssim q^2 l_B \tag{1.137}$$

An overall attraction between the two plates is thus expected in the range of parameters bounded by the inequalities (1.136) and, up to prefactors of order unity, (1.137). This region is shown in Fig. 1.12 in terms of the two independent dimensionless parameters in the problem, $\tilde{d} = d/\mu$ and the coupling parameter Ξ [Eq. (1.128)].

   Using $\tilde{d}$ and Ξ, equation (1.136) reads:

$$\tilde{d} > 2 \qquad\qquad \text{(I)} \tag{1.138}$$

This relation is shown as a solid line. The two other requirements, correct only up to a prefactor of order unity, are shown using dashed lines (a prefactor $\alpha = 3$ is chosen in the figure): the

small separation requirement $d < \sqrt{q/2\sigma}$ translates into:

$$\tilde{d} \lesssim \alpha^{-1}\sqrt{\pi\Xi} \qquad \text{(II)} \qquad\qquad (1.139)$$

while the requirement of strong lateral correlation, $\sqrt{q/2\sigma} < q^2 l_B$ reads:

$$\Xi \gtrsim \alpha^2\pi \qquad \text{(III)} \qquad\qquad (1.140)$$

The region bounded by Eqs. (1.138)-(1.140) is compared with recent results from Monte-Carlo simulations [52]. Symbols, corresponding to zero pressure, trace the boundary separating attraction from repulsion in the simulation. There is excellent agreement with Eq. (1.138), showing that the estimates (1.134) and (1.135) are almost exact close to line (I).

Another conclusion from the simulation results is that attraction is possible beyond the boundary II, at much larger plate separations. The situation of large $\tilde{d}$, where there is a distinct layer of counterions near each plate, was considered in several theoretical studies [22, 79, 85–87], emphasizing the role of correlated fluctuations in the two layers. These fluctuations can generate an attraction that overcomes the osmotic repulsion in Eq. (1.132). The physics of attraction in this regime is different from the small separation situation, and requires a separate discussion.

Attraction at large separation

We consider a relatively simple model, studied by Pincus and Safran [79], where each plate has an associated two-dimensional layer of counterions. The counterions are modeled as a liquid with a bulk modulus χ, which characterizes the energy cost of density fluctuations around the average density σ. The final result for the electrostatic pressure [Eq. (1.133)] is expressed as an integral over the wave-vector k of lateral fluctuations:

$$P_e = -k_B T \int_0^\infty \frac{\mathrm{d}k}{2\pi} \frac{k^2}{\left[\mathrm{e}^{2kd}\left(1+k\lambda\right)^2 - 1\right]} \qquad\qquad (1.141)$$

where $\lambda = \chi/(2\pi l_B)$. The surface charge σ enters this expression through the value of χ: if the non-electrostatic part of the 2-d layer's free energy is simply its ideal gas entropy, $\chi \sim e/\sigma$.

Equation (1.141) has an interesting feature: when $d \gg \lambda$ the pressure is dominated by fluctuations on length scales larger than d ($kd \lesssim 1$), and is completely independent of λ (or, equivalently, on σ):

$$P_e = -\frac{\zeta(3)}{8\pi}\frac{k_B T}{d^3} \qquad\qquad (1.142)$$

where ζ is the Riemann zeta function, $\zeta(3) \simeq 1.2$. In fact, this expression is identical to the van der Waals interaction between two conductors at large separation, where the zero frequency term dominates [56].

A more elaborate calculation was performed by Attard, Mitchell, and Ninham [85], and by Podgornik and Zeks [22,86]. They considered the contribution to the free energy of fluctuations around the mean-field solution, up to quadratic (one loop) order. The leading order for $d \gg \mu$ is similar to (1.142), with a logarithmic prefactor:

$$P_e \simeq -\frac{\pi}{2}\frac{k_B T}{d^3}\ln\left(\frac{d}{\mu}\right) \tag{1.143}$$

The logarithmic prefactor is related to the very weak decay of the mean-field ion density profile, which leads to the presence of a three-dimensional distribution of ions between the plates [87].

To check the possibility of overall attraction, Eq. (1.143) should be compared with the mean field mid-plane density. In similarity to (1.143), this density is almost independent on σ for $d \gg \mu$ [Eq. (1.78)]. The fluctuation pressure is the larger term if

$$d < \frac{1}{2\pi}l_B\ln\left(\frac{d}{\mu}\right) \tag{1.144}$$

or in the rescaled parameters,

$$\Xi > 2\pi\frac{\tilde{d}}{\ln\tilde{d}} \tag{1.145}$$

However, these expressions are only valid for $\tilde{d} \gg 1$ [at smaller separations the fluctuation pressure is much smaller than (1.143), while the density is larger]. This means that Ξ must be large compared to unity, whereas the derivation itself is valid only for small Ξ, since it considers small fluctuations around the mean-field solution. The outcome is that Eq. (1.145), while suggesting the possibility of fluctuation-induced attraction at large Ξ, cannot be taken too seriously in this regime.

We briefly discuss the situation close to the dotted line, assuming that Ξ is large. It was recently found, in theoretical treatments of the one-plate distribution, that ions are then much more localized near the charged plate than predicted by mean-field theory (Refs. [51–54, 88] and chapter 5). As discussed in chapter 5, the ion density decays exponentially as $\exp(-\tilde{d})$ up to a rescaled distance of, roughly, $\tilde{z} = \sqrt{\Xi}$ from the charged plate. Assuming that the rest of the ions are uniformly distributed between the two plates, a rough estimate for the mid-plane density is:

$$n(d/2) \sim \frac{1}{2\pi l_B \mu^2}\frac{\exp(-\sqrt{\Xi})}{\tilde{d}} \tag{1.146}$$

The presence of two very localized ion layers near each plate brings us back to the derivation of Eq. (1.142). This equation is obtained in the regime where long wavelength fluctuations $(k^{-1} \gg d)$ dominate, whose contribution is insensitive to the bulk modulus of the two dimen-

sional layer. This suggests that the $1/d^3$ dependence [Eq. (1.142)] applies for two-dimensional ion layers with large Ξ, provided that the distance between them is sufficiently large.[21]

Using Eq. (1.146) for the mid-plane density and Eq. (1.142) for P_e leads to zero pressure along the line:

$$\tilde{d}^2 = \frac{\zeta(3)}{8}\Xi\exp(\sqrt{\Xi}), \tag{1.147}$$

shown as a dotted line in Fig. 1.12. Because the mid-plane density is much smaller than the PB prediction, attraction is possible at larger distances than in Eq. (1.145). We stress that the estimates (1.142) and (1.146) for the pressure ingredients, in the regime where $\Xi \gg 1$ and $\tilde{d} \gg \sqrt{\Xi}$, are rather speculative: a systematic theoretical treatment of this regime is still missing.

On the other hand, at small separations, close to line I, strong coupling (SC) theory (Sec. 1.8.3) can be used to evaluate the pressure. The leading term in the SC free energy expansion involves the partition function of a single ion, sandwiched between the charged objects, leading to the same pressure estimate as in Eqs. (1.134) and (1.135). In addition to interacting planar surfaces, this theory was also used to study forces between cylindrical and spherical objects [89].

To summarize this section, there is a smooth crossover in Fig. 1.12 between two different mechanisms for attraction. Close to line I the electrostatic attraction is a low-temperature effect: P_e is independent on the temperature, equal to its value in the limit of $T = 0$. The repulsive term, scaling as $k_B T \sigma / d$, arises from the lateral pressure exerted by a single layer of counterions which are squeezed between the two plates.

Close to the dotted line there are separate, distinct layers of ions near the two plates; electrostatic attraction arises from long-wavelength, correlated fluctuations within these layers. Because this attraction arises from thermal fluctuations around a charge-neutral state, it increases in magnitude with increase of the temperature. We note, however, that so does the repulsive, osmotic term. The increase of the osmotic term more than compensates for the increase in P_e, so the region of attraction shrinks with increase of temperature in both of its boundaries. The situation near the critical point, at $\Xi \simeq 10$, cannot be described precisely by either of the above pictures.

We note, finally, that only line I corresponds to a minimum of the free energy, whereas the other boundary of attraction (near the dotted line) corresponds to an unstable configuration.

---

[21] In rescaled coordinates the distance between neighboring ions scales as $\sqrt{\Xi}$. If $\tilde{d} \gg \sqrt{\Xi}$ P_e is dominated by fluctuations on length scales much larger than this lateral distance, and the derivation of Ref. [79] may be applicable. In other words, it is reasonable to assume that the two ion layers interact as if they were conducting plates.

Consequently, within an aggregated state of macromolecules the mechanism of attraction is expected to be similar to the situation near line I, more than the situation near the dotted line. There is one important reservation regarding line I: at small inter-molecule separations, non-electrostatic interactions such as dispersion forces, hydration forces, finite ion size, and other short-range interactions are important, and must contribute to the balance between attraction and repulsion. The model discussed here is thus only a crude approximation for aggregation of real macromolecules, intended to highlight the role of electrostatic correlations.

Supplements to chapter 1

1.A   Critical behavior in electrolytes

This supplement is included for completeness of the discussion on bulk properties (Sec. 1.1). It is largely based on the reviews [90] and [91].

The free energy in Eq. (1.11) has a negative second derivative with respect to the salt concentration c_s, when c_s is sufficiently large, at $c_s > (2/\pi)l_B^{-3}$ for a 1:1 salt. This behavior of the free energy is unphysical since it leads, at any temperature, to collapse of the electrolyte to zero volume at sufficiently large concentration. In order to understand the global phase behavior of electrolytes the finite size of ions must be taken into account, although it affects the free energy in a different way than in uncharged fluids.

Let us consider ions modeled as hard spheres of radius a and assume, for simplicity, that they are monovalent. The derivation leading to Eq. (1.11) can then be modified, allowing screening ions to be present only outside a spherical shell of radius $2a$ around the fixed ion. The calculation is straightforward and leads to the following expression for the free energy [13]:

$$f = f_{\text{id}} - \frac{k_B T}{4\pi a^3} \left[\ln(\kappa a + 1) - \kappa a + (\kappa a)^2/2 \right] \tag{1.148}$$

where κ is given by Eq. (1.7) and is equal to $(8\pi l_B c_s)^{1/2}$ for a monovalent salt. Note that as $\kappa a \to 0$ (corresponding to small ion density) this expression approaches the previous result of Eq. (1.11).

Since the model discussed here involves three independent length scales: l_B, κ^{-1} (or, alternatively, $c_s^{-1/3}$), and a, there are two independent dimensionless parameters. Following Ref. [90] we choose these two parameters to be a dimensionless concentration, the volume fraction

$$\rho = 2a^3 c_s, \tag{1.149}$$

and a dimensionless temperature:

$$\tilde{T} = \frac{a\varepsilon}{e^2} k_B T = \frac{a}{l_B} \tag{1.150}$$
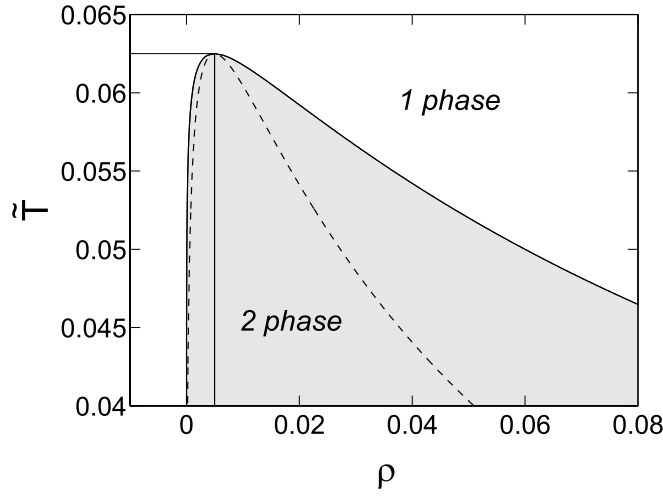
Figure 1.13:   Phase diagram of a symmetric electrolyte in the ρ-$\tilde{T}$ plane (dimensionless concentration and temperature, Eqs. (1.149) and (1.150)), as obtained from the free energy of Eq. (1.148) which takes into account the finite size of ions.   The critical point is at $\tilde{T}_c = 0.0625$ and $\rho_c = 0.00497$. Within the gray-shaded region of the phase diagram the ionic solution separates into a dense and dilute phase. The spinodal is represented by a dashed line: within the region bounded by this line the homogeneous solution is unstable to small fluctuations.

The free energy (1.148) leads to phase separation below a critical temperature $\tilde{T}_c$. The phase diagram can be easily calculated and is shown in Fig. 1.13. The critical point is at

$$\tilde{T}_c = \frac{1}{16} = 0.0625 \quad ; \quad \rho_c = \frac{1}{64\pi} \simeq 0.00497 \tag{1.151}$$

Note that correlations play an important role at the critical point, according to the estimate of Eq. (1.13): $l_B^2 c_s = \rho/(2\tilde{T}^3) = 10.2 \gg 1$. The parameters $\tilde{T}_c$ and ρ_c agree in order of magnitude with estimates from simulation; a theoretical improvement that yields semi-quantitative agreement with experiment is briefly discussed in the following section.

Several comments are in order. First, a ratio $a/l_B = 0.0625$ or smaller cannot be achieved in water: this requires a reduction of the temperature below the freezing temperature, because a is at least in the order of a few Angströms and $l_B = 7$ Å in water at room temperature. A practical way to observe criticality in ionic liquids is to replace water by a solvent of lower dielectric constant [92].

Second, below $\tilde{T}_c$ the concentrated phase is not stabilized directly by hard core interactions between ions, as in a van der Waals fluid. The ion size enters in a more subtle way, through the structure of ionic clouds. Indeed, Eq. (1.148) does not take into account the hard-core ion-ion interactions. Including their contribution – through a quadratic term in the density, or

through excluded volume (as in the van der Waals theory), shifts the critical parameters only slightly [90]. This can be expected because the volume fraction of ions is small at the critical temperature: $2\rho_c \simeq 0.01 \ll 1$

Finally, the criticality class of the hard sphere ionic solution is not yet clear, neither theoretically or experimentally, an issue that is beyond the scope of the present discussion.

Bjerrum pairing

Let us return the derivation of Eq. (1.11). Since the ions were considered as point-like, the linearization [Eq. (1.9)] cannot be justified sufficiently close to the fixed ion. This problem occurs also in the derivation of Eq. (1.148), if a is sufficiently small. In fact, as $a \to 0$, ions are expected to form tightly bound neutral ion pairs, since the integral $\int \mathrm{d}^3\mathbf{r} \exp(l_B/r)$ diverges at small r; linearization strongly underestimates the weight of such configurations if $a/l_B \ll 1$.

A crude, but useful approximation is to treat closely bound configurations of a positive and negative ion as a distinct component, coexisting with the free ions. This idea, dating back to Bjerrum, is similar in spirit to the two-phase models used in treatment of Manning condensation. Another way to think about it is that some salt molecules are not dissociated. Although the number of associated pairs is very small in strong electrolytes at room temperature, association becomes more important at lower temperatures, close to the critical temperature.

The density of associated pairs is related to the square of the free ion density through a law of mass action, involving the free energy of a bound positive–negative ion pair. The free energy (1.148) can be modified to take into account these bound pairs in several levels of refinement. The most simple level is to treat bound pairs as neutral particles that do not interact electrostatically with free ions. A more refined theory [90, 93] takes into account dipole-ion interactions of the bound pairs with free ions, leading to semi-quantitative agreement in the coexistence curve with Monte-Carlo simulations [90].

1.B   Two interacting planes

In this supplement the mean-field interaction of two surfaces of arbitrary sign is considered. After presenting the PB equation's solution in the case of no added salt, we consider plates having surface charge of opposite sign. The boundary separation between attraction and separation is derived, generalizing a result of Parsegian and Gingell [94] that was obtained within the linearized Debye-Hückel approximation.

We begin with the case of no salt, where the PB equation can be solved analytically.

1.B.1   No salt

The PB equation is:

$$-\frac{1}{4\pi l_B}\frac{\mathrm{d}^2\phi}{\mathrm{d}z^2} = \lambda \mathrm{e}^{-\phi} \tag{1.152}$$

with boundary conditions:

$$-\frac{1}{4\pi l_B}\left.\frac{\mathrm{d}\phi}{\mathrm{d}z}\right|_{z=0} = \frac{\sigma_1}{e} \quad ; \quad -\frac{1}{4\pi l_B}\left.\frac{\mathrm{d}\phi}{\mathrm{d}z}\right|_{z=d} = -\frac{\sigma_2}{e} \tag{1.153}$$

where σ_1 and σ_2 can be positive or negative. Since we assumed that counterions are positive, only the case:

$$\sigma_1 + \sigma_2 \leq 0 \tag{1.154}$$

is considered. Changing λ only shifts ϕ by a constant, and can be used to set ϕ to zero at an arbitrary position.

Multiplying Eq. (1.152) by $\mathrm{d}\phi/\mathrm{d}z$, it is seen that $(-1/8\pi l_B)(\phi')^2 + \lambda \mathrm{e}^{-\phi}$ is a constant, that we identify as the pressure p between the two plates (divided by $k_B T$):

$$-\frac{1}{8\pi l_B}\left(\frac{\mathrm{d}\phi}{\mathrm{d}z}\right)^2 + \lambda \mathrm{e}^{-\phi} = p \tag{1.155}$$

This equation can be integrated once more to obtain $\phi(z)$. There are three types of solutions, corresponding to positive, zero, and negative p.

Because $\lambda \mathrm{e}^{-\phi}$ is positive, ϕ' can be zero only if $p > 0$. If both σ_1 and σ_2 are negative, ϕ' must vanish between 0 and d, as seen from the two boundary condition. The solution must then belong to the class of solutions with $p > 0$. A general solution can be written as follows,

$$\phi = \ln\left\{\frac{\lambda}{p}\cos^2\left[(2\pi l_B p)^{1/2}(z - z_0)\right]\right\} \tag{1.156}$$

where z_0 is the coordinate where $\phi' = 0$. The density at this position, $\lambda \mathrm{e}^{-\phi(z_0)}$, is equal to p, in agreement with Eq. (1.155). To simplify notation we chose $\lambda = p$ [so that $\phi(z_0) = 0$], and

define $K \equiv (2\pi l_B p)^{1/2}$:

$$\phi = \ln \cos^2 \left[K(z - z_0) \right] \tag{1.157}$$

The parameters z_0 and K are determined from the two boundary conditions, noting that

$$\frac{\mathrm{d}\phi}{\mathrm{d}z} = -2K \tan \left[K(z - z_0) \right] \tag{1.158}$$

In the symmetric case $\sigma_1 = \sigma_2 \equiv -e/(2\pi l_B \mu)$, $z_0 = d/2$ from symmetry, and $p = K^2/2\pi l_B$ is determined from the transcendental equation,

$$K\mu \tan \left(\frac{Kd}{2} \right) = 1 \tag{1.159}$$

Surface charges of opposite sign

The parameter z_0 in Eq. (1.156) can be outside the interval $[0,d]$, in which case the surfaces at $z = 0$ and $z = d$ have charges of opposite sign. The coordinate z_0 is then the position where the electric field would vanish, had the solution been continued outside the interval $[0, d]$. It is also possible that such a position does not exist at all, in which case the parameter $p \leq 0$, corresponding to attraction between oppositely charged plates.

The general solution of Eq. (1.155) with $p < 0$ is:

$$\phi = \ln \left\{ \frac{\lambda}{|p|} \sinh^2 \left[(2\pi l_B |p|)^{1/2} (z - z_0) \right] \right\} \tag{1.160}$$

and the parameters z_0, p are found from the two boundary conditions. Note that here z_0 is a singular point that must be outside the interval $[0,d]$.

We next investigate the boundary between attraction and repulsion in the phase space of σ_1, σ_2 and d. Without loss of generality, assume that $\sigma_1 = -\sigma_-$ is negative and $\sigma_2 = \sigma_+$ is positive. We define $\sigma_1 = -e/2\pi l_B \mu_-$ and $\sigma_2 = e/2\pi l_B \mu_+$, so that

$$\left. \frac{\mathrm{d}\phi}{\mathrm{d}z} \right|_{z=0} = \frac{2}{\mu_-} \quad ; \quad \left. \frac{\mathrm{d}\phi}{\mathrm{d}z} \right|_{z=d} = \frac{2}{\mu_+} \tag{1.161}$$

Keeping σ_- fixed, the boundary between attraction and repulsion corresponds to the density profile at zero pressure; this profile is the same as for a single charged plate, as given by Eq. (1.36):

$$\frac{\mathrm{d}\phi}{\mathrm{d}z} = \frac{2}{z + \mu_1} \tag{1.162}$$

Hence the pressure is zero (see Fig. 1.14) if:

$$\frac{2}{d + \mu_-} = \frac{2}{\mu_+}. \tag{1.163}$$
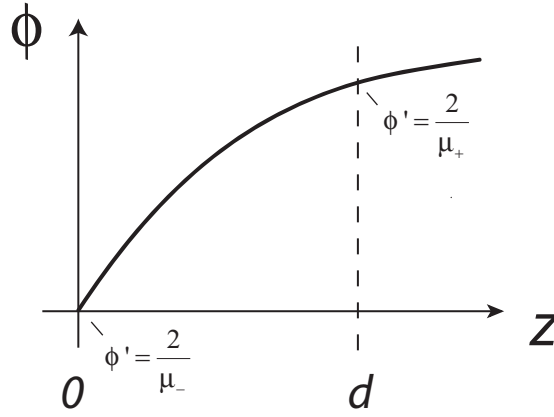
Figure 1.14:   The mean-field interaction between a negatively charged plate and a positively charged plate can be either attractive or repulsive.   The solid line shows schematically the electrostatic potential ϕ between the two plates. If the pressure vanishes, the potential is the same as if there is a charged plate only at $z = 0$.

To check which side of the equality corresponds to attraction, we note that in the limit $\mu_+ \to \infty$ the electrostatic field vanishes at $z = d$, and the pressure must be positive. Hence the two plates attract each other if

$$\mu_+ - \mu_- < d \tag{1.164}$$

a result that was obtained also in Ref. [95] [note that μ_+ must be larger than μ_- due to Eq. (1.154)]. Equation (1.164) can be written as follows,

$$\frac{2\pi l_B}{e^2}\sigma_+\sigma_- > \frac{\sigma_- - \sigma_+}{ed} \tag{1.165}$$

This expression demonstrates that the boundary between attraction and repulsion is the result of competition between electrostatic attraction (left hand side) and osmotic repulsion coming from the counterions (right hand side).

Using Eq. (1.164), and without assuming that $\sigma_- - \sigma_+ > 0$, the requirement for attraction can be written as follows,

$$\left| \frac{1}{\sigma_+} - \frac{1}{\sigma_-} \right| < \frac{1}{\sigma_d} \tag{1.166}$$

where

$$\sigma_d = \frac{e}{2\pi l_B d} \tag{1.167}$$

This region is shown in Fig. 1.15.
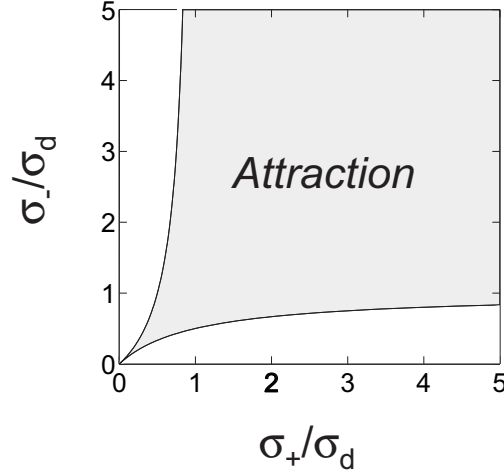
Figure 1.15: Regions of attraction (gray) and repulsion (white) for a positively charged plate interacting with a negatively charged plate, in the case of no added salt. The axes show $\sigma_\pm/\sigma_d$ where $\sigma_\pm$ are the charge densities and σ_d is defined in Eq. (1.167).

1.B.2 Added salt

In the case of two charged plates and added salt the PB equation reads,

$$\frac{\mathrm{d}^2\phi}{\mathrm{d}z^2} = \kappa^2\sinh\phi \tag{1.168}$$

where we assumed a 1:1 salt of concentration c_s ($\kappa^2 = 8\pi l_B c_s$) and the boundary conditions are the same as in the no-salt case [Eq. (1.153)]. In similarity to the no-salt case, this equation can be integrated once to obtain

$$-\frac{1}{8\pi l_B}\left(\frac{\mathrm{d}\phi}{\mathrm{d}z}\right)^2 + 2c_s\cosh\phi = p_{\mathrm{in}} \tag{1.169}$$

where p_{in} is the pressure acting on the inner side of the plates, divided by $k_B T$. The total pressure acting on the plates, divided by $k_B T$, is equal to

$$p = p_{\mathrm{in}} - p_{\mathrm{bulk}} = p_{\mathrm{in}} - 2c_s \tag{1.170}$$

(see, also, Sec. 1.7.1). A second integration of Eq. (1.169) yields an expression for z as a function of ϕ, in terms of an elliptic integral:

$$z = \kappa^{-1}\int_{\phi_0}^{\phi} \frac{\mathrm{d}\phi'}{\sqrt{2\cosh\phi' - p_{\mathrm{in}}/c_s}} \tag{1.171}$$

where ϕ_0 is a free parameter, determined together with p_{in} from the boundary conditions.

In general, a simple analytical expression for $\phi(z)$ cannot be obtained from Eq. (1.171). However, a full analytical solution is available in the case of zero pressure ($p_{\mathrm{in}}/c_s = 2$), being the expression for a single charged plate [Eqs. (1.32)–(1.33)]. This expression is sufficient in order to find the boundary between attraction and repulsion, on similar lines as in the no-salt case.

We first note that in the presence of salt there is no restriction on $\sigma_1 + \sigma_2$, which can be either positive or negative with the same form for the PB equation. We define,

$$\gamma_- = \sqrt{(\kappa\mu_-)^2 + 1} - \kappa\mu_- \tag{1.172}$$

Using the derivative of Eq. (1.32), the pressure is zero if

$$\left.\frac{\mathrm{d}\phi}{\mathrm{d}z}\right|_{z=d} = \frac{4\mathrm{e}^{\kappa d}\kappa\gamma_-}{\mathrm{e}^{2\kappa d} - \gamma_-^2} = \frac{2}{\mu_+} \tag{1.173}$$

We next define

$$\gamma_+ = \sqrt{(\kappa\mu_+)^2 + 1} - \kappa\mu_+; \tag{1.174}$$

re-expressing (1.173) using γ_+ yields a particularly simple result,

$$\gamma_+ = \gamma_-/\mathrm{e}^{\kappa d} \tag{1.175}$$

When $\gamma_+ \to 0$ (vanishing surface charge at $z = d$), the two plates must repel each other. Therefore the parameter range for attraction is

$$\mathrm{e}^{-\kappa d} < \frac{\gamma_+}{\gamma_-} < \mathrm{e}^{\kappa d} \tag{1.176}$$

where the inequality on the right hand side is found by reversing the signs and positions of σ_+ and σ_-. The outcome is that γ_+ and γ_- must be sufficiently similar to each other to have attraction. Attraction at contact ($d \to 0$) is possible only if they are identical.

Eq. (1.176) is a generalization of a result obtained by Parsegian and Gingell, only in the linearized theory [94]. Indeed, using the definition (1.39), Eq. (1.176) can be re-written in terms of the effective surface charges $\sigma_{+,\mathrm{eff}}$, $\sigma_{-,\mathrm{eff}}$:

$$\mathrm{e}^{-\kappa d} < \frac{\sigma_{+,\mathrm{eff}}}{\sigma_{-,\mathrm{eff}}} < \mathrm{e}^{\kappa d} \tag{1.177}$$

In agreement with Parsegian and Gingell's result for small surface charges, where $\sigma_{\pm,\mathrm{eff}} \simeq \sigma_\pm$.

Since Eq. (1.176) is valid even when the PB equation cannot be linearized, it includes as a special case the zero salt limit of Eq. (1.164). This can be verified by using the expansion of γ for small $\kappa\mu$, $\gamma \simeq 1 - \kappa\mu$, and requiring in addition to $\kappa\mu_\pm \ll 1$ also that $\kappa d \ll 1$.

1.C Effective charge of a cylinder in a salt solution

In this supplement we consider the effective charge of an infinite charged cylinder, having a negative linear charge density ρ and radius a, and immersed in a salt solution of concentration c_s. Far away from the cylinder, the solution of the PB equation is proportional to that of the linearized Debye-Hückel equation, making it possible to define an effective linear charge density ρ_{eff}, as in Eq. (1.51). This effective charge characterizes the electrostatic potential far away from the cylinder, at distances that are large compared to the Debye length.

As the salt concentration tends to zero, the effective charge becomes relevant at increasingly larger and larger distances from the cylinder. Nevertheless, it remains a well-defined quantity that can be considered even in the formal limit of vanishing c_s, as will be done below. In practice the effective charge is a useful quantity only at non-vanishing salt concentrations which may, nevertheless, be small.

As discussed in Sec. 1.5.2, the only dimensionless parameters in the problem are $l_B\rho$ and κa [see Eq. (1.48)]. By small salt concentrations we mean that κa is small compared to unity. We first derive an analytic expression for the effective charge in the limit $\kappa a \to 0$, using a recent analytic result of Tracy and Widom [33]. The situation of finite κa values is then studied numerically.

1.C.1 The limit $\kappa a \to 0$

In this limit the denominator in Eq. (1.51) is unity, so that

$$\phi = 2l_B\rho_{\text{eff}}K_0(\kappa r) \tag{1.178}$$

Tracy and Widom derived an analytical expression for the potential ϕ in the limit $\kappa a \to 0$, which applies only for $l_B\rho \leq 1$ and reads,

$$\phi(\kappa r) = 4\sum_{j=0}^{\infty} \frac{\lambda^{2j+1}}{2j+1}\text{Tr}\left(K^{2j+1}\right) \tag{1.179}$$

where K is the integral operator on $[0,\infty]$ with the kernel

$$\frac{\exp\left[-(\kappa r/2)(x+1/x)\right]}{x+y} \tag{1.180}$$

and

$$\lambda = \frac{1}{\pi}\sin\frac{\pi l_B\rho}{2} \tag{1.181}$$

In Ref. [33] this expression was used to evaluate the free energy and structure factor of the ion density profile. Here we note that it can also be used to evaluate $l_B\rho_{\text{eff}}$, as follows. For large r

only the first term in Eq. (1.179) is important, because $\text{Tr}(K^n) = O(e^{-n\kappa r})$ as $\kappa r \to \infty$ [33]. The first term can be easily evaluated:

$$\text{Tr}(K) = \int_0^\infty dx \, \frac{\exp\left[-(\kappa r/2)(x + 1/x)\right]}{2x} = K_0(\kappa r) \tag{1.182}$$

and comparison with (1.178) leads to the conclusion that

$$l_B \rho_{\text{eff}} = \frac{2}{\pi} \sin\left(\frac{\pi l_B \rho}{2}\right). \tag{1.183}$$

For $l_B \rho = 1$, $l_B \rho_{\text{eff}} = \pi/2 \simeq 0.64$.

Beyond the threshold $l_B \rho = 1$, $l_B \rho_{\text{eff}}$ must be equal to its value at the threshold:

$$\lim_{\kappa a \to 0} l_B \rho_{\text{eff}} \bigg|_{l_B \rho > 1} = \lim_{\kappa a \to 0} l_B \rho_{\text{eff}} \bigg|_{l_B \rho = 1} \tag{1.184}$$

This statement was proved by Ramanathan [35]. Combining this result with Eq. (1.183) leads to an expression for $l_B \rho_{\text{eff}}$ for all values of $l_B \rho$, Eq. (1.53).

1.C.2   Numerical results with added salt

Despite the importance of ρ_{eff}, as far as we know its exact values are not reported in the literature, whereas it is very common to assume simply that $l_B \rho_{\text{eff}} = 1$ when $l_B \rho \geq 1$, and that $l_B \rho_{\text{eff}} = l_B \rho$ when $l_B \rho < 1$. Figure 1.16 a shows $l_B \rho_{\text{eff}}$ for five different values of κa: 10^{-4}, 10^{-2}, 10^{-1}, 1, and 5, obtained from numerical solution of the PB equation. Several conclusions are reached: first, if κa is small compared to unity, $l_B \rho_{\text{eff}}$ is (approximately) constant for $l_B \rho > 1$. Second, in the limit of very small κa this constant is smaller than unity, in agreement with Eq. (1.53). The asymptotic limit $2/\pi \simeq 0.64$ (dotted line) is reached numerically only at extremely small values of κa (not shown in the plot). As can be appreciated from the plot, the approach to the asymptotic limit as $\kappa a \to 0$ is very slow. Finally, when κa is of order unity or larger the effective charge has very little to do with the Manning prediction.

Figure 1.16 b shows $l_B \rho_{\text{eff}}$ as function of κa for fixed $l_B \rho = 0.5$, 1, and 4.2 (solid lines, top to bottom). The last value corresponds to DNA in aqueous solution. Note that when $\kappa a \gg 1$, $l_B \rho_{\text{eff}}$ approaches the nominal value $l_B \rho$ in all cases. For some purposes it is more relevant to define the effective charge as if the electrostatic potential is due to a line charge distribution, concentrated at $r = 0$:

$$\phi(r) = 2 l_B \tilde{\rho}_{\text{eff}} K_0(\kappa r) \tag{1.185}$$

This effective charge, which can be considerably larger than $l_B \rho_{\text{eff}}$ [Eq. (1.51)], is shown for DNA (dashed line). At 10 mM salt ($\kappa a \simeq 0.3$) $l_B \tilde{\rho}_{\text{eff}}$ is equal to about 1.7, almost twice the

Figure 1.16: Effective charge $l_B\rho_{\text{eff}}$ of a charged cylinder in salt solution, obtained from numerical solution of the PB equation:
(a) $l_B\rho_{\text{eff}}$ as a function of $l_B\rho$, for $\kappa a = 10^{-4}$, 10^{-2}, 0.1, 1, and 5. The dashed line is the Manning prediction, $l_B\rho_{\text{eff}} = 1$ for $l_B\rho > 1$ and $l_B\rho_{\text{eff}} = l_B\rho$ for $l_B\rho < 1$. The dotted line is the asymptotic limit at $\kappa a \to 0$, Eq. (1.53).
(b) $l_B\rho_{\text{eff}}$ as a function of κa, with fixed $l_B\rho = 0.5$, 1.0, and 4.2 (solid lines, bottom to top). The dashed line shows the effective charge $l_B\tilde{\rho}_{\text{eff}}$, defined to match the Debye-Hückel potential of a cylinder of zero radius [Eq. (1.185)], for $l_B\rho = 4.2$.
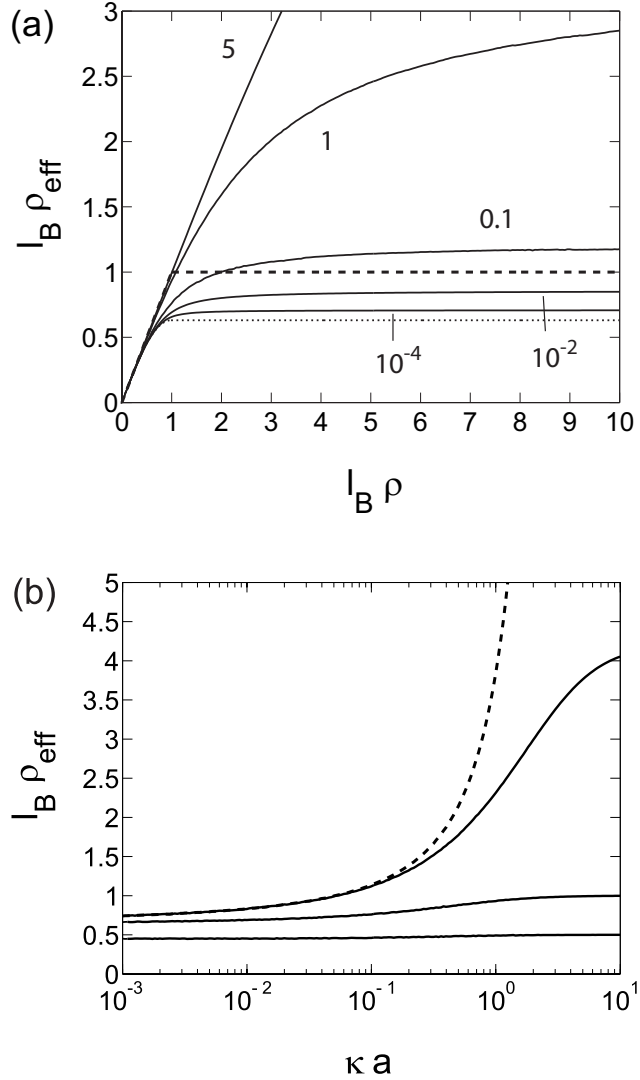
Manning prediction. At physiological salt solution ($c_s = 100$ mM, $\kappa a \simeq 1$) $l_B\tilde{\rho}_{\text{eff}}$ jumps to 4.0, while at extremely low salt concentration ($c_s = 10^{-4}$ mM, corresponding to water with no added salt), it is about 25 percent smaller than unity (the Manning prediction).

Recently, a variational scheme was suggested for evaluating the renormalized charge of surfaces having arbitrary shape [36]. In highly symmetric cases (single plane, cylinder, or sphere) this scheme yields a transcendental equation that can be solved numerically to obtain the variational effective charge. Numerical values presented in [36] for a cylinder agree quite well with the exact numerical values that are presented here.[22]

---

[22]However, an asymptotic analysis leads, in Ref. [36], to the conclusion that the effective charge at $l_B\rho \geq 1$ is equal to unity when $\kappa a \to 0$, in disagreement with our results.

1.D   Mapping between the cylindrical and planar problems

An analytic solution of the PB equation in a cell geometry without salt was obtained by Fuoss, Katchalsky and Lifson [39]. Here we present this solution from a slightly different perspective, which makes the relation to the single cylinder solution relatively transparent.

We consider a uniformly, negatively charged cylinder of radius a, in contact with its counterions. The number of negative unit charges per unit length is ρ, and we assume for simplicity that counterions are monovalent, carrying each a charge e. The counterions are point-like and can be present only between the radius a and an outer radius R.

Assuming that the cylinder is negatively charged and the counterions are positively charged, the Poisson-Boltzmann equation, written in cylindrical coordinates, reads:

$$-\frac{1}{4\pi l_B}\left[\frac{\mathrm{d}^2}{\mathrm{d}r^2} + \frac{1}{r}\frac{\mathrm{d}}{\mathrm{d}r}\right]\phi = \lambda\mathrm{e}^{-\phi} \tag{1.186}$$

where

$$\left.\frac{\mathrm{d}\phi}{\mathrm{d}r}\right|_{r=a} = 4\pi l_B\sigma = \frac{2l_B\rho}{a} \quad ; \quad \left.\frac{\mathrm{d}\phi}{\mathrm{d}r}\right|_{r=R} = 0 \tag{1.187}$$

Changing to the variable

$$u = \ln\left(\frac{r}{a}\right) \tag{1.188}$$

yields the equation

$$-\frac{1}{4\pi}\frac{\mathrm{d}^2\phi}{\mathrm{d}u^2} = \tilde{\lambda}\mathrm{e}^{-\phi+2u} \tag{1.189}$$

where

$$\tilde{\lambda} = l_B a^2\lambda \tag{1.190}$$

and boundary conditions are at $u = 0$ and at $u = L \equiv \ln(R/a)$. It is now possible to shift the variable ϕ:

$$\psi = \phi - 2u \tag{1.191}$$

leading to our final form for the equation (see, also, Fig. 1.4):

$$-\frac{1}{4\pi}\frac{\mathrm{d}^2\psi}{\mathrm{d}u^2} = \tilde{\lambda}\mathrm{e}^{-\psi} \tag{1.192}$$

with the boundary conditions

$$\left.\frac{\mathrm{d}\psi}{\mathrm{d}u}\right|_{u=0} = 2(l_B\rho - 1) \quad ; \quad \left.\frac{\mathrm{d}\psi}{\mathrm{d}u}\right|_{u=L} = -2 \tag{1.193}$$

This equation describes the distribution of positive ions between two charged planes (using units in which $l_B = 1$): a first plane at $u = 0$ with a surface charge $(1 - l_B\rho)/2\pi$ and a second

plane at $u = L$ with a surface charge $-1/2\pi$. The density of ions in this equivalent planar system corresponds to the density of ions in the cylindrical problem, in the following sense:

$$2\pi \int_{r_1}^{r_2} r\mathrm{d}r\, n(r) = \frac{2\pi}{l_B} \int_{u_1}^{u_2} \mathrm{d}u\, \tilde{n}(u) \tag{1.194}$$

where $n(r) = \lambda \exp[-\phi(r)]$ and $\tilde{n}(u) = \tilde{\lambda}\exp[-\psi(u)]$.

In the planar system to which we have mapped our problem, the charged plane at $u = L$ attracts ions since it is negatively charged, while the charged plane at $u = 0$ can be positively or negatively charged, depending on $l_B\rho$. If $l_B\rho < 1$ the plate at $u = 0$ is positively charged and repels the counterions. As $L \to \infty$ all the counterions go to infinity together with the second plate. If, on the other hand $l_B\rho > 1$ the first plate is negatively charged; a fraction of the ions, which neutralize this plate remain bound to it as L is increased. When $L \to \infty$ the ion distribution becomes that of a single charged plate, Eq. (1.36):

$$\tilde{n}(u) = \frac{1}{2\pi(u + \mu)^2} \tag{1.195}$$

where

$$\mu = (l_B\rho - 1)^{-1} \tag{1.196}$$

In the original, cylindrical problem this result maps into Eq. (1.46).

Bound counterions neutralize the charged cylinder only partially: their number, per unit length, is equal to $\rho - l_B^{-1}$. The Gouy-Chapman length of the planar problem, Eq. (1.196), determines the characteristic radius in which ions are bound: exactly half the ions are present up to the radius

$$r_{1/2} = a \exp\left[\frac{1}{l_B\rho - 1}\right] \tag{1.197}$$

When $l_B\rho \gg 1$, $r_{1/2} - a \simeq a/(l_B\rho)$. This is precisely the Gouy-Chapman length corresponding to a surface charge $\sigma = \rho/(2\pi a)$. On the other hand, when $l_B\rho \to 1$, $r_{1/2}$ diverges exponentially.

In the planar problem there is also a layer of ions that are bound to the plate at $u = L$ or, in other words, are not bound to the plate at $u = 0$. In similarity to the bound ions, their distribution approaches a single-plate density profile as $L \to \infty$ (only in the case $l_B > 1$), with a Gouy-Chapman length $\mu = 1$:

$$\tilde{n}_{\text{unbound}}(u) = \frac{1}{2\pi(L - u + 1)^2} \tag{1.198}$$

which maps in the cylindrical problem into

$$n_{\text{unbound}}(r) = \frac{1}{2\pi l_B r^2} \frac{1}{[\ln(R/r) + 1]^2} \tag{1.199}$$

Note that the unbound ions are not uniformly distributed within the cell area. Therefore it is an oversimplification to view them as an ideal gas of free ions. A uniform distribution occurs only if there is salt in the solution, beyond a distance of the Debye length from the cylinder.

A second conclusion from Eq. (1.199) is that, when $L \to \infty$, the ion density at $r = R$ is

$$n(R) = \frac{1}{\pi R^2} \cdot \frac{1}{2l_B} \tag{1.200}$$

This is half the density obtained by uniformly distributing the free ions (of linear concentration $1/l_B$) within the cell area. This result has important implications for the osmotic pressure of a polyelectrolyte solution, discussed in Sec. 1.7.4.

In the case $l_B\rho < 1$, the ion density at $r = R$ (in the limit $R \to \infty$) can be found as follows. In the equivalent planar problem, the contact density at $u = 0$ is zero, so the pressure is equal to $-(1 - l_B\rho)^2/2\pi$. This must also be equal to $-1/2\pi + \tilde{n}(L)$, which is the pressure evaluated at $u = L$. Mapping the result to the cylindrical problem yields

$$n(R) = \frac{\tilde{n}(L)}{l_B R^2} = \frac{\rho}{\pi R^2}\left(1 - \frac{l_B\rho}{2}\right) \tag{1.201}$$

For small $l_B\rho \ll 1$ this is equal to the density obtained by distributing all the counterions uniformly within the cell [note that $\rho/(\pi R^2) = c_m$].

Equations (1.200) and (1.201) were obtained in the limit $L \to \infty$. In practice, $L = \ln(R/a)$ is usually not a very large number, even for dilute polyelectrolyte solutions, because of the logarithmic dependence on R. For finite L the ion distributions near $u = 0$ and near $u = L$ are not decoupled, leading to significant corrections to the ion density profile, Eq. (1.46), and to Eqs. (1.200) and (1.201). These effects are further discussed in the following subsection and in Sec. 1.7.4.

1.D.1   Analytical solution for finite R

As discussed in Sec. 1.B.1, the solution to the PB equation can be written analytically for the case of two charged plates and no salt. Recall that here we are interested in a charged plate with surface charge $(1 - l_B\rho)/2\pi$ at $u = 0$ and a charged plate with surface charge $1/2\pi$ at $u = L$. Mapping the analytical solution for this case back to the cylindrical coordinates yields the Fuoss-Katchalsky-Lifson solution [39],

$$n(r) = \frac{1}{2\pi l_B r^2} \times \begin{cases} \dfrac{B^2}{\sinh^2\left[B\ln(r/R) - \tanh^{-1}B\right]} & \rho < \rho^* \\[2ex] \dfrac{1}{\left[\ln(R/r) + 1\right]^2} & \rho = \rho^* \\[2ex] \dfrac{B^2}{\sin^2\left[B\ln(r/R) - \tan^{-1}B\right]} & \rho > \rho^* \end{cases} \tag{1.202}$$

where

$$l_B \rho^* = \frac{\ln(R/a)}{\ln(R/a) + 1} \tag{1.203}$$

and B is obtained from the boundary conditions,

$$l_B \rho = \begin{cases} 1 - B\coth\left[B\ln(R/a) + \tanh^{-1}B\right] & \rho < \rho^* \\ 1 - B\cot\left[B\ln(R/a) + \tan^{-1}B\right] & \rho > \rho^* \end{cases} \tag{1.204}$$

The solution is written here using similar notation to that of Fuoss, Katchalsky, and Lifson. The three different analytical forms in Eq. (1.202) correspond to the cases of negative, zero, and positive pressure p in the analogous planar problem: Eqs. (1.160), (1.36), and (1.156), respectively, with the following relation between the parameters B and p,

$$p = \begin{cases} -B^2/(2\pi l_B) & \rho < \rho^* \quad (B < 0) \\ 0 & \rho = \rho^* \quad (B = 0) \\ B^2/(2\pi l_B) & \rho > \rho^* \quad (B > 0) \end{cases} \tag{1.205}$$

We stress that p, the pressure in the analogous planar problem, should not be confused with the real pressure in the cylindrical cell, which is always positive.

The value of the threshold ρ^*, where the analytical solution changes its analytical behavior, can be found as follows. At the threshold, $p = 0$ and the density profile between the two plates is the same as though there is only one plate at $u = L$, Eq. (1.199). The value of ρ^* is thus easily obtained from this equation:

$$2(l_B \rho^* - 1) = \left.\frac{d\psi}{du}\right|_{u=0} = -\left.\frac{d\ln n_0}{du}\right|_{u=0} = -\frac{2}{L+1} \tag{1.206}$$

where Eq. (1.199) was used for $n_0(u)$, so that

$$l_B \rho^* = \frac{L}{L+1} = \frac{\ln(R/a)}{\ln(R/a) + 1}. \tag{1.207}$$

as in Eq. (1.203). This is equivalent to the boundary between attraction and repulsion $d = |\mu_+ - \mu_-|$ [Eq. (1.164)], with $\mu_+ = 1$, $\mu_- = (l_B \rho - 1)^{-1}$, and $d = \ln(R/a)$.

1.E   Contact identity for a charged cylinder with salt

Consider a single cylinder immersed in a salt solution. In this section we develop an exact
identity relating the concentration of ions at contact with the cylinder, to the excess of ions,
per unit length, adsorbed on the cylinder. This identity is useful for evaluation of the osmotic
pressure in a dilute PE solution, discussed in Sec. 1.7.4. Some of the details of this derivation
are presented here.

The parameters of the problem are defined as follows. The cylinder, of radius a, is confined
in a cylindrical cell of radius R and carries a negative charge per unit length ρ. The cylindrical
cell contains a salt solution including several species of ions. We imagine that the solution is
in equilibrium with a large reservoir where the concentration of the species α, of valency q_α, is
equal to c_α. Due to charge neutrality

$$\sum_\alpha q_\alpha c_\alpha = 0 \tag{1.208}$$

A mapping to a one dimensional problem, in similarity to Eq. (1.189) can be performed, leading
to the following equation:

$$-\frac{1}{4\pi}\frac{\mathrm{d}^2\phi}{\mathrm{d}u^2} = \sum_\alpha q_\alpha l_B c_\alpha a^2 \exp(-q_\alpha\phi + 2u) \tag{1.209}$$

with the following boundary conditions:

$$\left.\frac{\mathrm{d}\phi}{\mathrm{d}u}\right|_{u=0} = 2l_B\rho \quad ; \quad \left.\frac{\mathrm{d}\phi}{\mathrm{d}u}\right|_{u=L} = 0 \tag{1.210}$$

where $L = \ln(R/a)$ and $u = \ln(r/a)$.

In contrast to the no-salt case, shifting ϕ is not useful in Eq. (1.209), because it can cancel
the $2u$ term within the exponential only for one of the ion species. Equation (1.209) describes
ions interacting with a charged plate at $u = 0$, subject also to a linear external potential $2u$.
This external potential cannot be interpreted as an electrostatic force because it has the same
(repulsive) form for all ion species. Nevertheless, Eq. (1.209) can be used to obtain a useful
exact identity in the limit of a large cell $(R \gg \kappa^{-1})$.

Multiplying Eq. (1.209) by $\mathrm{d}\phi/\mathrm{d}u$ and integrating from $u = 0$ to $u = L$ leads to following
result:

$$\begin{aligned}
-\frac{1}{8\pi}\left(\frac{\mathrm{d}\phi}{\mathrm{d}u}\right)^2\Bigg|_0^L &= -l_B a^2 \sum_\alpha c_\alpha \exp(-q_\alpha\phi + 2u)\Bigg|_0^L \\
&+ 2l_B a^2 \sum_\alpha \int_0^L \mathrm{d}u\, c_\alpha \exp(q_\alpha\phi + 2u)
\end{aligned} \tag{1.211}$$

This equation can be interpreted as an equality of the pressure evaluated at $u = 0$ and at $u = L$ in the one dimensional system. Returning to the cylindrical coordinates and using the boundary conditions (1.210), Eq. (1.211) maps into the following result:

$$\frac{1}{2\pi}(l_B\rho)^2 = -l_B \sum_\alpha \left[R^2 n_\alpha(R) - a^2 n_\alpha(a) \right] + 2l_B \sum_\alpha \int_a^R r\, dr\, n_\alpha(r) \qquad (1.212)$$

where the integration is within the cell area and $n_\alpha(r)$ is the local concentration of ion species α.

Consider now the limit $R \to \infty$. The concentrations $n_\alpha(R)$ are then equal to c_α (the difference between these two quantities decays exponentially with κR). It is then straightforward to obtain from Eq. (1.212) our final result:

$$\sum_\alpha n_\alpha(a) = \frac{1}{2\pi l_B a^2}(l_B\rho)^2 - \frac{1}{\pi a^2}\sum_\alpha \rho_\alpha \qquad (1.213)$$

where

$$\rho_\alpha \equiv 2\pi \int_0^R r\, dr\, [n_\alpha(r) - c_\alpha] \qquad (1.214)$$

is the excess number of ions of species i, per unit length, compared to the bulk solution, and $n_\alpha(r) = 0$ for $r < a$.

This identity was also derived by Anderson and Record [68] (see, also, Ref. [69]). It should be noted that, in contrast to the planar contact theorem, the identity derived here is restricted to mean-field theory and is not valid if there are short-range ion-ion interactions.

1.E.1 An application: Osmotic pressure in a dilute PE solution

We consider a symmetric 1:1 salt. The number of positive and negative ions, per unit volume, can be written as follows:

$$\begin{aligned}
c_s &= c_0 + c_m \rho_+/\rho \\
c_m + c_s &= c_0 + c_m \rho_-/\rho
\end{aligned} \qquad (1.215)$$

where $\rho_\pm$ is the excess of positive or negative ions per unit length of the PE. For example, in the second line the left hand side is the number of counterions contributed by PE monomers and salt. The right hand side is the contribution of the bulk concentration c_0 (the concentration far away from the PEs), plus a correction which is proportional to the PE concentration. The proportionality factor, ρ_m/ρ, is the excess of adsorbed counterions per monomer (we assume, for simplicity, that each monomer carries a unit charge, so that $1/\rho_m = a_m$ is the distance

between monomers). From these two equations,

$$2c_0 = 2c_s + \frac{c_m}{\rho}(\rho - \rho_+ - \rho_-) \tag{1.216}$$

Using the identity (1.213) for $\rho_+ + \rho_-$,

$$2c_0 = 2c_s + \frac{c_m}{l_B\rho}\left\{ l_B\rho - \frac{1}{2}(l_B\rho)^2 + \pi a^2 l_B \sum_\alpha n_\alpha(a) \right\} \tag{1.217}$$

As long as κ^{-1} is large compared to a, the contact density of ions is close to its value without salt,

$$\sum_\alpha n_\alpha(a) \simeq \left\{ \begin{array}{ll} 0 & , \quad l_B\rho < 1 \\ \frac{1}{2l_B}(l_B\rho - 1)^2 & , \quad l_B\rho > 1 \end{array} \right. + \frac{1}{l_B a^2}o(1) \tag{1.218}$$

where Eq. (1.46) was used. The notation $o(1)$ indicates that the correction term tends to zero in the limit of vanishing salt concentration, $\kappa a \to 0$.[23] We thus obtain:

$$2c_0 = 2c_s + \frac{c_m}{l_B\rho} \times \left\{ \begin{array}{ll} l_B\rho\left[1 - \frac{l_B\rho}{2}\right] & , \quad l_B\rho < 1 \\ \frac{1}{2} & , \quad l_B\rho > 1 \end{array} \right. + o(1) \tag{1.219}$$

which is the expression for the osmotic pressure, Eq. (1.98).

---

[23]This statement is proved in Ref. [35].

1.F Loop expansion of the density functional

In this section we develop the loop expansion of the density functional, for a charged fluid of point-like ions. We consider first the case of only counterions and no salt, where Z_G is given by Eq. (1.117). We define

$$\mathcal{F}[h] = -\ln Z_G \tag{1.220}$$

and perform the Legendre transformation from $\mathcal{F}[h]$ to $\tilde{\mathcal{F}}[n]$, discussed in Sec. 1.8.1 [Eqs. (1.113)–(1.115)], to obtain an expansion in l of the density functional. For simplicity we assume that $\Theta(\mathbf{r}) = 1$ for all $\mathbf{r}$.[24]

The partition function's invariance with respect to a constant shift in h, which occurs only when there is no salt, requires special attention. Due to this invariance, when inverting the dependence of n on h – to express h in terms of n, there is freedom to choose h up to a constant. This freedom will be used in the following derivation. On the other hand, not all choices of n are valid: assuming that the problem is defined within a finite volume and that Neumann boundary conditions are imposed on φ, Eq. (1.120) imposes charge neutrality:

$$\int d\mathbf{r} \, [\langle n(\mathbf{r}) \rangle + n_e(\mathbf{r})] = 0 \tag{1.221}$$

The argument of $\tilde{\mathcal{F}}[n]$ should obey this relation.

We will evaluate the first two terms in the expansion,

$$l\tilde{\mathcal{F}} = \tilde{\mathcal{F}}_0 + l\tilde{\mathcal{F}}_1 + \ldots \tag{1.222}$$

Only the two leading terms of $\mathcal{F}[h]$ are required, which are given by [24]:

$$\mathcal{F}_0 = \int d\mathbf{r} \left[\frac{1}{8\pi l_B} (\nabla\varphi)^2 + i\varphi n_e - \lambda e^{-i\varphi - h} \right] \tag{1.223}$$

and

$$\mathcal{F}_1 = \frac{1}{2}\ln \det G^{-1} \tag{1.224}$$

where

$$G^{-1} = -\frac{\nabla^2}{4\pi l_B} + \lambda e^{-i\varphi_{\text{PB}} - h} = -\frac{\nabla^2}{4\pi l_B} + n_0 \tag{1.225}$$

in which φ_{PB} is the saddle point of $\mathcal{F}_0$.

Using Eq. (1.118) n is expressed in terms of h. Up to first order in l:

$$n(\mathbf{r}) = n_0(\mathbf{r}) + l n_1(\mathbf{r}) + \ldots \tag{1.226}$$

---

[24]Having a nonuniform $\Theta(\mathbf{r})$ is equivalent to an external field $h_{\text{ex}}(\mathbf{r})$ equal to zero wherever $\Theta = 1$ and to infinity wherever $\Theta = 0$. It follows that the only modification to $\tilde{\mathcal{F}}[n]$ is the addition of a term $\int d\mathbf{r} \, h_{\text{ex}}(\mathbf{r}) n(\mathbf{r})$.

The result of this evaluation is [24]:

$$n_0(\mathbf{r}) = \frac{\delta \mathcal{F}_0}{\delta h(\mathbf{r})} = \lambda e^{-i\varphi_{\mathrm{PB}}(\mathbf{r}) - h(\mathbf{r})} \tag{1.227}$$

and

$$\begin{aligned} n_1(\mathbf{r}) &= \frac{\delta \mathcal{F}_1}{\delta h(\mathbf{r})} \\ &= -\frac{1}{2}G(\mathbf{r}, \mathbf{r})n_0(\mathbf{r}) + \frac{1}{2}\int d\mathbf{r}' G(\mathbf{r}', \mathbf{r}')G(\mathbf{r}', \mathbf{r})n_0(\mathbf{r}')n_0(\mathbf{r}) \end{aligned} \tag{1.228}$$

The next step is to invert this relation to express h in terms of n. We re-express Eq. (1.226) as follows,

$$\lambda e^{-i\varphi_{\mathrm{PB}} - h(\mathbf{r})} + ln_1 = n \tag{1.229}$$

Because n_1 is multiplied by l we can replace every occurrence of n_0 by n in the expression for n_1, Eq. (1.228). This yields:

$$\lambda e^{-i\varphi_{\mathrm{PB}} - h} = n(1 + l\eta) \tag{1.230}$$

where

$$\eta(\mathbf{r}) = \frac{1}{2}G(\mathbf{r}, \mathbf{r}) - \frac{1}{2}\int_{\mathrm{d}} \mathbf{r}' \, G(\mathbf{r}', \mathbf{r}')G(\mathbf{r}', \mathbf{r})n(\mathbf{r}') \tag{1.231}$$

in which G is now defined using n instead of n_0:

$$G^{-1} = -\frac{\nabla^2}{4\pi l_B} + n \tag{1.232}$$

and

$$h(\mathbf{r}) = -i\varphi_{\mathrm{PB}}(\mathbf{r}) - \ln\left[\frac{n(\mathbf{r})}{\lambda}\right] - l\eta(\mathbf{r}) \tag{1.233}$$

In order to express φ_{PB} using n we first express it using n_0 and then use Eq. (1.230), written as follows: $n_0 = n(1 + l\eta)$. To express φ_{PB} using n_0 we use the Poisson equation:

$$-\frac{i}{4\pi l_B}\nabla^2 \varphi_{\mathrm{PB}} = n_0 + n_e \tag{1.234}$$

which can be inverted as follows:

$$i\varphi_{\mathrm{PB}}(\mathbf{r}) = \int d\mathbf{r}' \, v_c(\mathbf{r}, \mathbf{r}') \left[n_0(\mathbf{r}') + n_e(\mathbf{r}')\right] + \phi_0 \tag{1.235}$$

The presence of a constant ϕ_0 is special to the case of no salt (in the presence of salt the potential must decay to zero at infinity). We now recall that there is freedom in $F[h]$ to shift h by a constant, which leads to a shift in $i\varphi_{PB}$ but does not affect the value of n. Using this freedom we set $\phi_0 = 0$, which corresponds to a particular choice of the additive constant in h.

The remaining steps (whose details are skipped) are to express the terms of F_0 using n. In F_1 the definition of G, Eq. (1.225), can be replaced by Eq. (1.232), which is a replacement of n_0 by n. This is allowed because F_1 is multiplied by l, so the difference between the two definitions contributes only to higher orders in the expansion of F. The final result for $\tilde{F}$ is very simple:

$$
\begin{aligned}
\tilde{\mathcal{F}}[n] &= \int \mathrm{d}\mathbf{r}\, n(\mathbf{r}) \left[\ln \frac{n(\mathbf{r})}{\lambda} - 1 \right] \\
&+ \frac{1}{2} \int \mathrm{d}\mathbf{r}\mathrm{d}\mathbf{r}'\, [n(\mathbf{r}) + n_e(\mathbf{r})]\, v_c(\mathbf{r}, \mathbf{r}')\, [n(\mathbf{r}') + n_e(\mathbf{r}')] \\
&+ \frac{l}{2} \ln \det \left[-\frac{\nabla^2}{4\pi l_B} + n \right]
\end{aligned}
\tag{1.236}
$$

The constraint of charge neutrality should be imposed on $\int \mathrm{d}\mathbf{r}\, n(\mathbf{r})$, which can be included as a Lagrange multiplier. In practice this means that λ is replaced by a constant that is determined from the constraint, at each order of the loop expansion.

Density equation

From Eq. (1.236) the first order correction in l to n and ϕ is obtained as follows. Requiring $\delta \tilde{\mathcal{F}} / \delta n = 0$ yields,

$$
\ln \frac{n}{\lambda} + \int \mathrm{d}\mathbf{r}'\, v_c(\mathbf{r}, \mathbf{r}')\, [n(\mathbf{r}') + n_e(\mathbf{r}')] + \frac{l}{2} G(\mathbf{r}, \mathbf{r}) = 0
\tag{1.237}
$$

where

$$
G^{-1} = -\frac{\nabla^2}{4\pi l_B} + n
\tag{1.238}
$$

and the identity:

$$
\frac{\delta \ln \det A}{\delta A_{ij}} = A_{ji}^{-1}
\tag{1.239}
$$

was used. Note that $G(\mathbf{r}, \mathbf{r})$ is infinite, but the difference $G(\mathbf{r}, \mathbf{r}) - v_c(0)$ is finite.

Salt

In the case of a monovalent 1:1 salt, the derivation is similar to the previous case, but there are two fields $h_+(\mathbf{r})$, $h_-(\mathbf{r})$, coupled to the positive and negative ions. The partition function is similar to Eq. (1.25), with the inclusion of h_+ and h_-:

$$
Z = \frac{1}{Z_v} \int \mathcal{D}\varphi \exp \left\{ -\frac{1}{l} \int \mathrm{d}\mathbf{r} \left[\frac{1}{8\pi l_B} (\nabla \varphi)^2 + i n_e \varphi - \lambda \Theta e^{-i\varphi - h_+} - \lambda \Theta e^{i\varphi - h_-} \right] \right\}
\tag{1.240}
$$

The final result for the density functional is:

$$\tilde{\mathcal{F}}[n_+, n_-] \;=\; \sum_{\alpha=+,-} \int \mathrm{d}\mathbf{r}\, n_\alpha \left[\ln \frac{n_a}{\lambda} - 1\right]$$

$$+ \;\; \frac{1}{2} \int \mathrm{d}\mathbf{r}\mathrm{d}\mathbf{r}'\, n_c(\mathbf{r}) v_c(\mathbf{r}, \mathbf{r}') n_c(\mathbf{r}')$$

$$+ \;\; \frac{l}{2} \ln \det G^{-1} \tag{1.241}$$

where $n_c(\mathbf{r}) = n_e(\mathbf{r}) + n_+(\mathbf{r}) - n_-(\mathbf{r})$ and

$$G^{-1} = -\frac{\nabla^2}{4\pi l_B} + n_+ + n_- \tag{1.242}$$

More generally, for several ion species of valencies q_α $\tilde{\mathcal{F}}$ has a similar form as Eq. (1.241), with $n_c(\mathbf{r}) = n_e(\mathbf{r}) + \sum_\alpha q_\alpha n_\alpha(\mathbf{r})$ and

$$G^{-1} = -\frac{\nabla^2}{4\pi l_B} + \sum_\alpha q_\alpha^2 n_\alpha \tag{1.243}$$

The first order correction coming from the loop expansion is the generalization, for a nonuniform fluid, to the correlation free energy that was calculated by Debye and Hückel (Sec. 1.1). Indeed, in a bulk fluid with constant densities n_α the first two terms are the ideal gas free energy per unit volume (in the grand canonical ensemble), and

$$G^{-1} = \frac{1}{4\pi l_B} \left[-\nabla^2 + \kappa^2\right] \tag{1.244}$$

so that G obeys the differential equation

$$\frac{1}{4\pi l_B} \left[-\nabla^2 + \kappa^2\right] G(\mathbf{r}, \mathbf{r}') = \delta(\mathbf{r} - \mathbf{r}') \tag{1.245}$$

whose solution is $G(\mathbf{r}, \mathbf{r}) = l_B e^{-\kappa R}/R$ where $R = |\mathbf{r} - \mathbf{r}'|$, and

$$G(\mathbf{r}, \mathbf{r}) = v_c(0) - l_B \kappa + \ldots \tag{1.246}$$

The derivative of $\ln \det G$ with respect to κ is

$$\frac{\mathrm{d}}{\mathrm{d}\kappa} \frac{1}{2} \ln \det G \;=\; \frac{\kappa}{4\pi l_B} G(\mathbf{r}, \mathbf{r}) = \frac{\kappa}{4\pi l_B} \left[v_c(0) - l_B \kappa + \ldots\right] \tag{1.247}$$

and by integration with respect to κ,

$$\frac{1}{2} \ln \det G = \frac{1}{2} \sum_\alpha z_\alpha^2 v_c(0) - \frac{1}{12\pi} \kappa^3 + \ldots \tag{1.248}$$

The first term is the Coulomb self energy of the ions, which renormalizes the fugacity of each ion species, while the second term is the same as in Eq. (1.11) (see, also, [23]).

Finally, the equations that n_α obey in an inhomogeneous solution are obtained from functional differentiation of $\tilde{\mathcal{F}}$ with respect to n_α:

$$\ln\frac{n_\alpha}{\lambda_\alpha} + q_\alpha \int \mathrm{d}\mathbf{r}'\, v_c(\mathbf{r},\mathbf{r}')n_c(\mathbf{r}') + l\frac{q_\alpha^2}{2}G(\mathbf{r},\mathbf{r}) = 0 \qquad (1.249)$$

which is equivalent to the following set of equations:

$$-\frac{1}{4\pi l_B}\nabla^2\phi(\mathbf{r}) = n_e(\mathbf{r}) + \sum_\alpha q_\alpha n_\alpha(\mathbf{r})$$

$$n_\alpha(\mathbf{r}) = \lambda_\alpha\exp\left[-q_\alpha\phi(\mathbf{r}) - \frac{l}{2}G(\mathbf{r},\mathbf{r})\right]$$

$$\left[-\frac{1}{4\pi l_B}\nabla^2 + \sum_\alpha q_\alpha^2 n_\alpha(\mathbf{r})\right]G(\mathbf{r},\mathbf{r}') = \delta(\mathbf{r}-\mathbf{r}') \qquad (1.250)$$

Symbol Legend (Chapter 1)

α	Ion species index.
ε	Dielectric constant.
Φ	Electrostatic potential.
ϕ	Reduced electrostatic potential, $\phi = e\Phi/(k_B T)$.
φ	Fluctuating field.
$\phi, \tilde{\phi}$	Osmotic coefficient and excess osmotic coefficient (Sec. 1.7.4).
γ	Eq. (1.33).
κ	Inverse Debye length, Eq. (1.17).
λ	Fugacity.
μ	Gouy-Chapman length, Eq. (1.31).
μ_c	Chemical potential.
$\Pi, \tilde{\Pi}$	Osmotic pressure and excess osmotic pressure.
ρ	PE charge [negative unit charge per unit length].
ρ_α	Number excess per unit length of ion species α, Eq. (1.54).
ρ_{eff}	Effective PE charge [negative unit charge per unit length].
σ	Surface charge [electric charge per unit area].
$\Theta(\mathbf{r})$	Excluded volume function.
$\mathcal{F}$	Free energy (in units of thermal energy).
f	Free energy per unit volume (sec.) or length (Sec.).
F	Force.
Ξ	Coupling parameter, Eq. (1.128).
a	Radius of PE or colloid.
a_c	Distance between unit charges along a PE backbone, $a_c = 1/\rho$.
c_α	Bulk concentration of ion species α.
c_m	PE monomer concentration.
c_s	Concentration of a 1:1 salt.
c_0	Concentration of a 1:1 salt in a PE solution, far away from the PEs.
d	Inter-plate separation.
e	Unit (electron) charge.
$k_B T$	Thermal energy.
l	Loop expansion parameter (Sec. 1.2.2).
l_B	Bjerrum length, $l_B = e^2/(\varepsilon k_B T)$.
M	Molar (Mol/Liter).
n_α	Local number density of ion species α.
P	Pressure.
P_e	Electrostatic pressure, Eq. (1.133).
q_α	Valency of ion species α.
Q	Colloid valency.
R	Cylindrical cell radius.
$W(r)$	Potential of mean force (in units of the thermal energy).
z	Normal coordinate to charged plane.
Z, Z_G	Partition function.

Bibliography

[1] J. Israelachvili, *Intermolecular and Surface Forces*, 2nd ed., Academic Press: New York, 1991.

[2] D. Boal, *Mechanics of the Cell*, Cambridge Univ. Press: Cambridge, 2002.

[3] I. W. Hamley, *Introduction to Soft Matter. Polymers, Colloids, Amphiphiles, and Liquid Crystals*, Wiley: Chichester, 2000.

[4] W. M. Gelbart, R. F. Bruinsma, P. A. Pincus, and V. A. Parsegian, *Phys. Today* **53** (2000) 38 .

[5] D. H. Everett, *Basic Principles of Colloid Science*, Royal Society of Chemistry: Cambridge, 1988.

[6] P. Janmey, in *Handbook of Physics of Biological Systems*, edited by R. Lipowsky and E. Sackmann, Elsevier Science: Amsterdam, 1994, Vol. I, Chap. 17, p. 805.

[7] D. Frenkel, in *Soft and fragile matter*, M.E. Cates and M.R. Evans (eds.), SUSSP Publications: Edinburgh, 2000.

[8] D. F. Evans and H. Wennerström, *The Colloidal domain*, VCH Publishers: New-York, 1994.

[9] For several review articles on this topic, and a translation of Hofmeister's original papers, see *Curr. Opin. Coll. Interface Sci.*, special issue dedicated to Hofmeister phenomena, to appear in 2004.

[10] E. Guàrdia, R. Rey, and A. Padró, *J. Chem. Phys.* **95** (1991) 2823.

[11] S. A. Safran, *Statistical Thermodynamics of Surfaces, Interfaces, and Membranes*, Addison-Wesley: Reading, MA, 1994.

[12] T. Witten, *Structured Fluids. Polymers, Colloids, Surfactants*, Oxford Univ. Press: Oxford, 2004.

[13] P. Debye and E. Hückel, *Physik. Z.* **24** (1923) 185. An English translation is published in: *The collected works of Peter J.W. Debye*, Interscience: New York, 1954.

[14] L. D. Landau and E. M. Lifshitz, *Statistical Physics, 3rd edition, Part 1*, Pergamon Press: New York, 1980.

[15] L. Onsager and N. N. T. Samaras, *J. Chem. Phys.* **2** (1934) 528.

[16] R. R. Netz, *Phys. Rev. E* **60** (1999) 3174.

[17] R. R. Netz, *Eur. Phys. J. E* **3** (2000) 131.

[18] M. Borkovec, J. Daicic, and G. J. Koper, *Physica A* **298** (2002) 1.

[19] Y. Burak and R. R. Netz, *J. Phys. Chem. B* **108** (2004) 4840.

[20] See, for example, D. J. Mitchell and B. W. Ninham, *Chem. Phys. Lett.* **53** (1978) 397; R. Kjellander and D. J. Mitchell, *J. Chem. Phys.* **101** (1994) 603; R. Kjellander and J. Ulander, *Mol. Phys.* **95** (1998) 495.

[21] K. Huang, *Statistical Mechanics, 2nd edition*, Wiley: New York, 1987.

[22] R. Podgornik and B. Žekš, *J. Chem. Soc., Faraday Trans. 2* **84**, 611 (1988).

[23] R. R. Netz and H. Orland, *Europhys. Lett.* **45** (1999) 726.

[24] R. R. Netz and H. Orland, *Eur. Phys. J. E* **1** (2000) 203.

[25] G. Gouy, *J. Phys. (Paris)* **9** (1910) 457; G. Gouy, *Ann. Phys.* **7** (1917) 129.

[26] D. L. Chapman, *Philos. Mag.* **25** (1913) 475.

[27] D. Andelman, in *Handbook of Physics of Biological Systems*, R. Lipowsky and E. Sackmann (eds.), Elsevier Science: Amsterdam, 1994, Vol. I, Chap. 12, p. 603.

[28] S. L. Carnie and D. Y. C. Chan, *J. Chem. Phys.* **74** (1981) 1293.

[29] See, for example, Ph. A. Martin, *Rev. Mod. Phys.* **60** (1988) 1075.

[30] G. S. Manning, *J. Chem. Phys.* **51** (1969) 924.

[31] F. Oosawa, *Polyelectrolytes*, Marcel Dekker: New-York, 1971.

[32] G. S. Manning, *Biophys. Chem.* **7** (1977) 95.

[33] C. A. Tracy and H. Widom, *Physica A* **244** (1997) 402.

[34] I. Shkel, O. V. Tsodikov, and M. T. Record, Jr., *Proc. Natl. Acad. Sci. (USA)* **99** (2002) 2597.

[35] G. V. Ramanathan, *J. Chem. Phys.* **78** (1983) 3223; G. V. Ramanathan and C. P. Woodbury, Jr., *J. Chem. Phys.* **82** (1985) 1482.

[36] R. R. Netz and H. Orland, *Eur. Phys. J. E* **11** (2003) 301.

[37] R. A. Marcus, *J. Chem. Phys.* **23** (1955) 1057.

[38] A. Deshkovski, S. Obukhov, and M. Rubinstein, *Phys. Rev. Lett.* **86** (2001) 2341.

[39] R. M. Fuoss, A. Katchalsky, and S. Lifson, *Proc. Natl. Acad. Sci. (USA)* **37** (1951) 579.

[40] M. Le Bret and B. H. Zimm, *Biopolymers* **23** (1984) 287.

[41] J. P. Hansen and I. R. McDonald, *Theory of Simple Liquids*, 2nd ed., Academic Press: London, 1986.

[42] D. Henderson, in *Fundamentals of Inhomogeneous Fluids*, D. Henderson (ed.), Marcel Dekker: New York, 1992, Chap. 6, p. 177.

[43] R. Kjellander, *J. Chem. Phys.* **88** (1988) 7129.

[44] Y. Rosenfeld and N. W. Ashcroft, *Phys. Rev. A* **20** (1979) 1208.

[45] R. Kjellander, *Ber. Bun. Phys. Chem.* **100** (1996) 894.

[46] R. Kjellander and S. Marčelja, *J. Chem. Phys.* **82** (1985) 2122.

[47] R. Kjellander and S. Marčelja, *Chem. Phys. Lett.* **112** (1984) 49; **114** (1985) 124(E).

[48] For a review see, R. Evans, in *Fundamentals of Inhomogeneous Fluids*, D. Henderson (ed.), Marcel Dekker: New York, 1992, Chap. 6, p. 85.

[49] An example where LDFT is used to study correlation effects in ionic solutions is: M. J. Stevens and M. O. Robbins, *Europhys. Lett.* **12** (1990) 81.

[50] An example where LDFT is used to study finite ion size effects is: I. Borukhov, D. Andelman, and H. Orland, *Phys. Rev. Lett.* **79** (1997) 435.

[51] R. R. Netz, *Eur. Phys. J. E* **5** (2001) 557.

[52] A. G. Moreira and R. R. Netz, *Eur. Phys. J. E* **8** (2002) 33.

[53] V. I. Perel and B. I. Shklovskii, *Physica A* **274** (1999) 446.

[54] B. I. Shklovskii, *Phys. Rev. E* **60** (1999) 5802.

[55] A. Y. Grosberg, T. T. Nguyen, and B. Shklovskii, *Rev. Mod. Phys.* **74** (2002) 329.

[56] J. Mahanty and B. W. Ninham, *Dispersion Forces*, Academic: London, 1976; A more recent treatment is due to appear in 2005: A. Parsegian, *Van der Waals Forces, A Handbook for Biologists, Chemists, Engineers, and Physicists*, Cambridge Univ. Press: Cambridge, 2005.

[57] P.-G. de Gennes, *Scaling Concepts in Polymer Physics*, Cornell Univ. Press: Ithaca, 1979.

[58] B. W. Ninham and V. Yaminsky, *Langmuir* **13** (1997) 2097.

[59] S. A. Edwards and D. R. M. Williams, *Phys. Rev. Lett.* **92** (2004) 248303 and references therein.

[60] E. J. W. Verwey and J. Th. G. Overbeek, *Theory of the Stability of Lyophobic Colloids*, Elsevir: New York, 1948.

[61] B. V. Derjaguin and L. Landau, *Acta Physicochim. URSS* **14** (1941) 633.

[62] S. Lifson and A. Katchalsky, *J. Polym. Sci.* **XIII** (1954) 43.

[63] C. F. Anderson and M. T. Record, Jr., *Annu. Rev. Phys. Chem.* **33** (1982) 191.

[64] A. V. Dobryinin, R. H. Colby, and M. Rubinstein, *Macromolecules* **28** (1995) 1859.

[65] E. Raspaud, M. da Conceiçao, and F. Livolant, *Phys. Rev. Lett.* **84** (2000) 2533.

[66] P. L. Hansen, R. Podgornik, and V. A. Parsegian, *Phys. Rev. E* **64** (2001) 021907.

[67] M. Deserno and C. Holm, in *Electrostatic Effects in Soft Matter and Biophysics*, C. Holm et al. (eds.), Kluwer: Dordrecht, 2001.

[68] C. F. Anderson and M. T. Record, Jr., *Biophys. Chem.* **11** (1980) 353.

[69] G. V. Ramanathan, *J. Chem. Phys.* **85** (1986) 2957.

[70] F. G. Donnan, *Chem. Rev.* **1** (1924) 73.

[71] L. Onsager, *Phys. Rev.* **62** (1942) 558; L. Onsager, *Ann. New York Acad. Sci.* **51** (1949) 627.

[72] J. C. Neu, *Phys. Rev. Lett.* **82** (1999) 1072.

[73] J. E. Sader and D. Y. C. Chan, *J. Coll. Interface Sci.* **213** (1999) 268; *Langmuir* **16** (2000) 324.

[74] L. Guldbrand, B. Jönsson, H. Wennerström, and P. Linse, *J. Chem. Phys.* **80** (1984) 2221.

[75] R. Kjellander, T. Åkesson, B. Jönsson, and S. Marčelja, *J. Chem. Phys.* **97** (1992) 1424.

[76] N. Grønbech-Jensen, R. J. Mashl, R. F. Bruinsma, and W. M. Gelbart, *Phys. Rev. Lett.* **78** (1997) 2477.

[77] M. Deserno, A. Arnold, and C. Holm, *Macromolecules* **36** (2003) 249.

[78] B. Y. Ha and A. J. Liu, *Phys. Rev. Lett.* **79** (1997) 1289.

[79] P. A. Pincus and S. A. Safran, *Europhys. Lett.* **42** (1998) 103.

[80] R. Kjellander, S. Marčelja, and J. P. Quirk, *J. Coll. Interface Sci.* **126** (1988) 194.

[81] V. A. Bloomfield, *Biopolymers* **31** (1991) 1471.

[82] D. C. Rau and A. Parsegian, *Biophys. J.* **61** (1992) 246; D.C. Rau and A. Parsegian, *Biophys. J.* **61** (1992) 260.

[83] P. Kékicheff, S. Marčelja, T. J. Senden, and V. E. Shubin, *J. Chem. Phys.* **99** (1993) 6098.

[84] E. Raspaud, M. O. de la Cruz, J. L. Sikorav, and F. Livolant, *Biophys. J.* **74** (1998) 381.

[85] P. Attard, D. J. Mitchell, and B. W. Ninham, *J. Chem. Phys.* **88** (1988) 4987.

[86] R. Podgornik, *J. Phys. A* **23** (1990) 275.

[87] D. B. Lukatsky and S. A. Safran, *Phys. Rev. E* **60** (1999) 5848.

[88] A. W. C. Lau, D. B. Lukatsky, P. Pincus, and S. A. Safran, *Phys. Rev. E* **65** (2002) 051502.

[89] A. Naji and R. Netz, *Eur. Phys. J. E* **13** (2004) 43.

[90] M. E. Fisher, *J. Stat. Phys.*, and references therein. **75** (1994) 1.

[91] Y. Levin, *Rep. Prog. Phys.* **65** (2002), 1577.

[92] See, for example, K. S. Pitzer, *J. Phys. Chem.* **99** (1995) 13070.; *Acc. Chem. Res.* **23** (1990) 333; J. M. H. L. Sengers and J. A. Given, *Mol. Phys.* **80** (1993) 899.

[93] M. E. Fisher and Y. Levin, *Phys. Rev. Lett.* **71** (1993) 3826.

[94] V. A. Parsegian and D. Gingell, *Biophys. J.* **12** (1972) 1192.

[95] A. W. C. Lau and P. Pincus, **10** (1999) 175.

[96] G. V. Ramanathan, *J. Chem. Phys.* **88** (1988) 3887.

[97] J. Crocker and D. Grier, *Phys. Rev. Lett.* **77** (1996) 1897.

[98] S. H. Behrens and D. G. Grier, *Phys. Rev. E* **64** (2001) 050401.

[99] S. Alexander, P. M. Chaikin, P. Grant, J. Morales, and P. Pincus, *J. Chem. Phys.* **80** (1984) 5776.

[100] L. Belloni, *Colloid Surf. A* **140** (1998) 227.

Chapter 2

Hydration interactions: Aqueous solvent effects in electric double layers

The following two chapters deal with short-range, solvent mediated interactions between ions, and their influence on ion-distributions near highly charged macromolecules. Chapter 2 introduces the theoretical framework and then concentrates on the situation of a single planar surface. In chapter 3 the implications for inter-surface interactions are investigated.

In the present chapter,[1] a model for ionic solutions with an attractive short-range pair interaction between the ions is presented. The short-range interaction is accounted for by adding a quadratic non-local term to the Poisson-Boltzmann free energy. The model is used to study discrete solvent effects in a planar electric double layer (an aqueous solvent and sodium counterions are assumed). The counter-ion density is found to increase near the charged surface, as compared with the Poisson-Boltzmann theory, and to decrease at larger distances. The ion density profile is studied analytically in the case where the ion distribution near the plate is dominated by counter-ions. It is shown that far away from the plate the density distribution can be described using a Poisson-Boltzmann theory, with an effective surface charge that is smaller than the actual one.

2.1 Introduction

Electrolytes, in contact with charged surfaces or macro-ions, play an important role in determining the properties of many biological and chemical systems. One of the most widely used tools for studying ions in aqueous solutions is the Poisson-Boltzmann (PB) theory (Chapter

---

[1]The material presented in this chapter was published in Ref. [1].

1 and Refs. [2–7]). The mathematical and conceptual simplicity of this theory makes it very appealing both for numerical computation [8], and for gaining insight into the underlying physical principles. Although the theory contains important simplifications, it has proven to be a useful and accurate tool in the study of systems such as colloidal dispersions [9, 10], biological membranes [7], polyelectrolytes [11] and complex systems, *e.g.*, proteins or DNA interacting with charged membranes [12–14].

The Poisson-Boltzmann theory is obtained by making two simplifying approximations. The first approximation is the treatment of the electrostatic interactions on a mean-field level. The ions are treated as independent charged particles interacting with an external electrostatic potential, derived self-consistently from the mean charge density distribution. Thus, correlations between the ion positions are not taken into account. The second approximation is the treatment of the ions as point-like objects, interacting only through the electrostatic interaction in a dielectric medium. In reality, ions in aqueous solutions have more intricate interactions [6]. These include a non-Coulombic interaction between ion pairs, which is mainly a short-range steric repulsion, interactions with the polar solvent molecules and short-range interactions with the confining charged surfaces.

Various models have been proposed for the inclusion of effects not accounted for by the PB theory. These include liquid state theory approaches [15–19], field theory expansions [20, 21], computer simulations [22–24] and other modifications to the PB theory [25–28]. Most of these models remain within the framework of the so-called "primitive model", in which the interaction between the ions is modeled as a purely repulsive hard-core interaction. On the other hand, relatively few works have addressed explicitly the discrete nature of the solvent molecules [19, 29–31]. Clearly, the replacement of the solvent by a continuous medium cannot be precise when the inter-ion distance is comparable to the solvent molecular size. Therefore, when the ions reach high densities the discreteness of the solvent is expected to have an important effect on the ionic distribution. This is of particular importance for water. Due to its high polarity, the strong screening of the electrostatic interaction (represented by the dielectric constant) is modified at small ion separations.

Using the surface force apparatus [6], it is possible to measure precisely the force between charged mica plates. These measurements supply evidence for the importance of the solvent structure in aqueous solutions [32, 33]. At inter-plate separations below approximately $20\,\text{Å}$ significant deviations are found from the prediction of the Derjaguin-Landau-Verwey-Overbeek (DLVO) theory [9, 34]. The measured force is oscillatory or consists of a series of steps, with
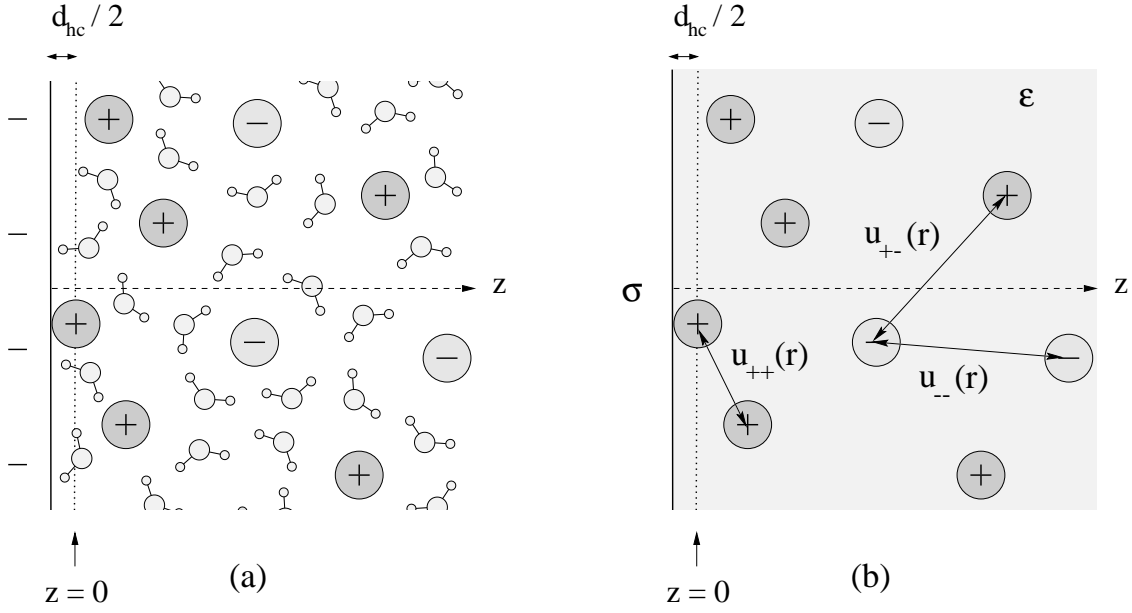
Figure 2.1: Schematic description of the aqueous pair potential model. An aqueous ionic solution in contact with a charged plate in (a) is replaced in (b) by ions in a continuum dielectric medium having a dielectric constant ε, with electrostatic and short-range interactions $u_{ij}(r) = u_{ij}(|\mathbf{r}|)$. The z coordinate designates the distance from the charged plate, with $z = 0$ corresponding to the distance of closest approach of the ions to the plate. The distance of closest approach is equal to $d_{\mathrm{hc}}/2$, where d_{hc} is the hard-core diameter of the ions.

a period corresponding to the water molecular size. Oscillatory forces are known to arise as a result of the solvent structuring in layers between surfaces [6]. However, a repulsive contribution is found in addition to the oscillatory force at plate separations below several nanometers [32,33]. This repulsive force is often referred to as the "hydration force" [6,32], and its origin is not yet completely understood [30].

2.1.1 Aqueous pair potential model

Recently [35,36], an aqueous pair potential model has been proposed for electrolytes, in which the effect of the solvent on the ions is described as a short-range two-body interaction between the ions. The solvent is replaced by a continuum dielectric medium as in PB theory, but the ions also interact through a two-body short-range hydration interaction [35]. This is shown schematically in Fig. 2.1.

This aqueous pair potential model [35,36], involves several simplifying assumptions. One is that the effect of the solvent can be represented as a linear superposition of two-body potentials between all ion pairs. Another simplification is that the effective potential between the ions

is taken as the effective potential in the bulk, regardless of the ion concentration, and of the geometry imposed by the charged surfaces. Finally, a short-range surface-ion effective potential should be included in addition to the ion-ion effective potential. Despite of the simplifications made in the aqueous pair potential model, it offers a first step towards a qualitative understanding of solvent effects on the ion distribution, in particular near highly charged surfaces.

2.1.2   Effective ion pair interaction

For the short-range ion-ion interaction, the so-called potential of mean force between ions in solution can be used. Potentials of mean force are defined as $-k_B T \ln g_{ij}(\mathbf{r})$ where $g_{ij}(\mathbf{r})$ are the ion-ion radial distribution functions for ion pairs of species i and j. The radial distribution functions have been calculated numerically for a single ion pair immersed in an aqueous solution using molecular dynamics techniques [37–39].

An alternative approach has been proposed in Refs. [40,41]. In this approach, a Hamiltonian consisting of a pairwise effective potential between the ions is obtained using the so-called "reverse Monte-Carlo" approach. The ion-ion radial distribution functions are first calculated using a molecular dynamics simulation for a system including solvent molecules and a finite concentration of ions. The ion-ion effective potential in the system without the solvent is then adjusted iteratively until the same distribution functions are obtained using Monte-Carlo simulations.

The different available calculations of potentials of mean force differ in their quantitative predictions. This may be a result of high sensitivity of the models to detailed features used for the water molecules and for the inter-molecular interactions [37]. However, all the potentials of mean force as well as the effective potentials [40] are qualitatively similar [42]. Thus, for the purpose of the present work, aiming at a qualitative understanding of solvent effects, any one of these potentials may be used.

At large ionic separations the ion-ion effective potential is well approximated by a screened electrostatic interaction, with the water dielectric constant in the continuum limit. At short ionic separation, the difference between the total effective potential and the screened electrostatic interaction is a short-range potential reflecting the structure of water molecules in the ion vicinity. Fig. 2.2 shows the short-range contribution (excluding the screened electrostatic part) to the effective potential calculated between Na^+ - Na^+ pairs in the reverse Monte-Carlo approach [40]. Below about $3\,\text{Å}$, the electrostatic repulsion between the ions becomes unscreened. Therefore it is much larger than the screened repulsion in the dielectric medium, and the effective potential is strongly repulsive. The unscreened electrostatic potential leads to an
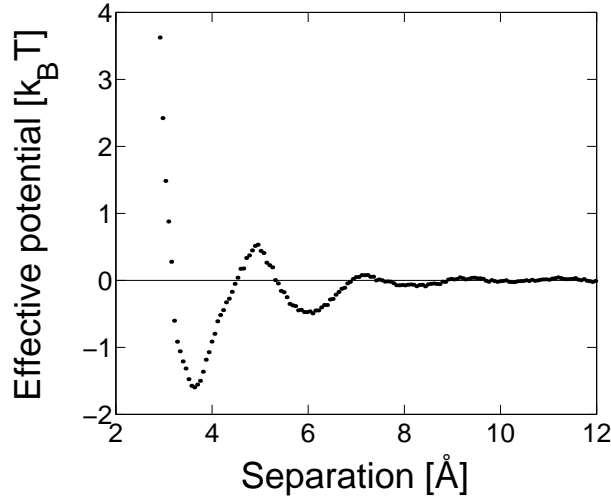
Figure 2.2: Short-range effective potential between Na^+ ion pairs, adapted from Ref. [40] using simulations in a bulk NaCl solution of concentration $0.55\,M$, at room temperature [44]. The potential is shown in units of k_BT, as a function of the distance between the ion centers. For ion separations smaller than $2.9\,Å$ a hard core interaction was assumed. The Coulomb interaction is subtracted to show only the short-range hydration effect due to the water molecules.

effectively enlarged hard-core separation between the ions, relative to a hard-core diameter of about $2.3\,Å$ used in the short-range part of the bare ion-ion potential. At larger separations, the effective potential is oscillatory, and mainly attractive. It has a distinct minimum at an ion-ion separation of about $3.6\,Å$, followed by a maximum and a second minimum at approximately $6\,Å$.

2.1.3 The present work

The replacement of the discrete solvent by a continuum medium, with electrostatic and short range interactions between the ions, is a considerable simplification. Still, the statistical mechanical treatment of an electrolyte solution in this model is difficult, and requires the use of further approximations, or simulations.

The Anisotropic Hyper-Netted Chain approximation (AHNC) [16] was previously used to calculate the effects of hydration interactions in the aqueous pair potential model [42, 43]. When the ion concentration is large enough, *e.g.*, near a highly charged surface, the hydration interaction is found to have a significant effect on the distribution of ions in the solution. It was also proposed that the so-called repulsive "hydration forces" between surfaces arise from the ionic structure near highly charged surfaces. According to this description, at large distances from the plate, the ion distribution follows a PB profile with a reduced effective surface charge.

When two plates approach each other, the ions near the surfaces come into contact giving rise to an apparent new repulsive force.

In the present work a simple description for ions interacting through electrostatic and short-range attractive interactions as mediated by the solvent molecules is introduced. We apply this description to the aqueous pair potential model. Our aim is limited to describe the important effects of the short-range interaction, and not to provide an accurate tool for their calculation. Therefore our model follows the PB theory as closely as possible, and describes the short-range interaction using a simplified term added to the free energy. The advantage of this approach over more elaborate treatments such as the AHNC [42, 43], is that it provides relatively simple equations that can be treated numerically and analytically with relative ease as well as allowing extensions to non-planar geometries. In a planar geometry, we show that the effect of the ion-ion hydration interaction can be understood as a perturbation over the PB results. An increase in the concentration of counter-ions near the charged surface is found, and it results in an apparent surface charge which is reduced relatively to the PB theory.

The outline of the chapter is as follows. Section 2.2 presents the model. In section 2.3 we apply the model to a single charged plate, present numerical results for the ion density profile and discuss the modifications to the PB theory due to the addition of short-range interactions. In section 2.4 we present analytical results in the low salt limit. We calculate the effective PB surface charge and the effect of the hydration interaction on the density profile of counter-ions in a system with no added salt.

2.2   The Model

2.2.1   Free energy

We start from an approximated free energy, written as a functional of the various ion densities. We choose the electrostatic boundary conditions to be of fixed surface charge densities and write the free energy as a sum of the usual PB term and a correction term, due to hydration, as will be explained below:

$$\Omega = \Omega_{\mathrm{PB}} + \Delta\Omega \tag{2.1}$$

We discuss first how the PB free energy is obtained, and then generalize this result to include the short-range hydration interaction.

Poisson-Boltzmann free energy

The Hamiltonian of the system is:

$$H = \frac{1}{2} \sum_i \int_V d^3\mathbf{r} \, e_i \rho_i(\mathbf{r}) \phi(\mathbf{r}) + \frac{1}{2} \oint_{\partial V} d^2\mathbf{r}_s \, \sigma(\mathbf{r}_s) \phi(\mathbf{r}_s) \tag{2.2}$$

where V is the volume occupied by the electrolyte solution, $\sigma(\mathbf{r}_s)$ is the surface charge density of immobile charges on the boundaries ∂V, and e_i is the charge of the ith ion species. The ion densities $\rho_i(\mathbf{r})$ are:

$$\rho_i(\mathbf{r}) \equiv \sum_{j=1}^{N_i} \delta(\mathbf{r} - \mathbf{r}_i^j) \tag{2.3}$$

where $\mathbf{r}_i^j$ is the position of the jth ion of the ith species, and the electrostatic potential $\phi(\mathbf{r})$ is a function the different ion positions:

$$\phi(\mathbf{r}) = \sum_j \int_V d^3\mathbf{r}' \, \frac{e_j \rho_j(\mathbf{r}')}{\varepsilon \, |\mathbf{r} - \mathbf{r}'|} + \oint_{\partial V} d^2\mathbf{r}_s \, \frac{\sigma(\mathbf{r}_s)}{\varepsilon \, |\mathbf{r} - \mathbf{r}_s|} \tag{2.4}$$

where $\varepsilon = 78$ is the dielectric constant of water. The PB theory is obtained by using a mean-field approximation for the electrostatic interaction. The Hamiltonian (2.2) is first replaced by a mean-field Hamiltonian, where the electrostatic potential $\phi(\mathbf{r})$ is replaced by an external field $\Psi(\mathbf{r})$. In the thermodynamic limit the free energy can then be written as a functional of the mean densities of the ion species, $c_i(\mathbf{r}) = \langle \rho_i(\mathbf{r}) \rangle_{\mathrm{MF}}$, as follows:

$$\begin{aligned} \Omega_{\mathrm{MF}} &= k_B T \int_V \sum_i c_i \left[\ln \frac{c_i}{\zeta_i} - 1 \right] d^3\mathbf{r} \\ &+ \frac{1}{2} \int_V \sum_i e_i \Psi(\mathbf{r}) c_i(\mathbf{r}) d^3\mathbf{r} + \frac{1}{2} \oint_{\partial V} \sigma(\mathbf{r}_s) \Psi(\mathbf{r}_s) \end{aligned} \tag{2.5}$$

where $k_B T$ is the thermal energy, and ζ_i is the fugacity of the ith ion species. The mean-field approximation is obtained by requiring that the external potential $\Psi(\mathbf{r})$ is the thermodynamical average of (2.4) in the system with the mean-field Hamiltonian, $\Psi(\mathbf{r}) = \langle \phi(\mathbf{r}) \rangle_{\mathrm{MF}}$, *i.e.*:

$$\Psi(\mathbf{r}) = \sum_i \int_V d^3\mathbf{r}' \, \frac{e_i c_i(\mathbf{r}')}{\varepsilon \, |\mathbf{r} - \mathbf{r}'|} + \oint_{\partial V} d^2\mathbf{r}_s \, \frac{\sigma(\mathbf{r}_s)}{\varepsilon \, |\mathbf{r} - \mathbf{r}_s|} \tag{2.6}$$

This relation is equivalent to the Poisson equation:

$$\nabla^2 \Psi = -\frac{4\pi}{\varepsilon} \sum_i e_i c_i \tag{2.7}$$

supplemented by the boundary condition:

$$\nabla\Psi \cdot \hat{\mathbf{n}}|_{\mathbf{r_s}} = -\frac{4\pi}{\varepsilon}\sigma(\mathbf{r_s}) \qquad \text{on the charged surfaces} \tag{2.8}$$

where the normal vector $\hat{\mathbf{n}}$ points away from the charged surfaces into the volume occupied by the ionic solution. Using this boundary condition and Eq. (2.7), the second and third terms of Eq. (2.5) can be re-expressed as:

$$\frac{1}{2}\int_V \sum_i e_i\Psi(\mathbf{r})c_i(\mathbf{r})\mathrm{d}^3\mathbf{r} + \frac{1}{2}\oint_{\partial V} \sigma(\mathbf{r}_s)\Psi(\mathbf{r}) = \frac{\varepsilon}{8\pi}\int_V (\nabla\Psi)^2\mathrm{d}^3\mathbf{r} \tag{2.9}$$

Substituting this relation in Eq. (2.5) we obtain the PB free energy:

$$\begin{aligned}
\Omega_{\mathrm{PB}} &= \frac{\varepsilon}{8\pi}\int(\nabla\Psi)^2\mathrm{d}^3\mathbf{r} + k_BT\int\sum_i c_i\left[\ln\frac{c_i}{\zeta_i} - 1\right]\mathrm{d}^3\mathbf{r} \\
&\quad + \int\lambda(\mathbf{r})\left(\nabla^2\Psi + \frac{4\pi}{\varepsilon}\sum_i e_ic_i\right)\mathrm{d}^3\mathbf{r}
\end{aligned} \tag{2.10}$$

The first term in Ω_{PB} is the electrostatic free energy and the second term is the entropy of the ions. The fugacity ζ_i, in the second term, is equal in PB theory to the bulk concentration $c_{\mathrm{b},i}$ of the ith ion species, $\zeta_i = c_{\mathrm{b},i}$, as for an ideal gas. For more generalized free energies, a different relation may exist between the fugacity of each ion species and its respective bulk concentration. The electrostatic potential Ψ is a functional of the ion densities c_i, and is determined by the Poisson equation (2.7) and the boundary conditions (2.8) imposed by the surface charges. Alternatively, in Eq. (2.10) Ψ is regarded as an independent field and a third term containing a Lagrange multiplier $\lambda(\mathbf{r})$ is added to Ω_{PB}. The PB equilibrium mean densities $c_i(\mathbf{r})$ result from minimizing Ω_{PB}. With the introduction of $\lambda(\mathbf{r})$ the minimization is equivalent to requiring an extremum of Ω_{PB} with respect to the three fields c_i, Ψ and λ, subject to the boundary condition (2.8). By requiring first an extremum of Ω_{PB} with respect to Ψ and c_i the following relations are obtained:

$$\lambda = \frac{\varepsilon}{4\pi}\Psi \tag{2.11}$$

and:

$$c_i = \zeta_i\exp\left(-\beta e_i\Psi\right) \tag{2.12}$$

where $\beta = 1/(k_BT)$ and $\zeta_i = c_{\mathrm{b},i}$. The extremum condition with respect to λ gives the Poisson equation:

$$\nabla^2 \Psi = -\frac{4\pi}{\varepsilon} \sum_i e_i c_i \tag{2.13}$$

Combining these relations we obtain the PB equation:

$$\nabla^2 \Psi = -\frac{4\pi}{\varepsilon} \sum_i \zeta_i e_i \mathrm{e}^{-\beta e_i \Psi} \tag{2.14}$$

Alternatively, the first two relations, obtained from the extremum condition with respect to Ψ and c_i, can be substituted into Eq. (2.10). Formally, this gives Ω_{PB} as a functional of λ. Using Eq. (2.11), the expression obtained for Ω_{PB} can be written as a functional of Ψ:

$$\Omega_{\mathrm{PB}} = -\frac{\varepsilon}{8\pi} \int_V (\nabla \Psi)^2 \mathrm{d}^3\mathbf{r} + \oint_{\partial V} \sigma \Psi \mathrm{d}^2\mathbf{r}_s - k_B T \int_V \mathrm{d}^3\mathbf{r} \sum_i \zeta_i \mathrm{e}^{-\beta e_i \Psi} \tag{2.15}$$

where the second integration is over the charged surfaces. Requiring an extremum of this functional with respect to Ψ is another way to obtain the Poisson-Boltzmann equation (2.14).

A more formal derivation of the mean field, PB free energy, and a discussion on its generalization to systems with non-electrostatic interactions is presented in Ref. [45]. The PB free energy (2.10) can also be derived by formulating the problem using field theory methods. In this approach the mean-field approximation is obtained as the saddle point of the functional integral, and corrections due to ion-ion correlations can be obtained in a systematic expansion [20, 21].

Inclusion of the hydration interaction

As discussed in the introduction, our starting point is a model in which the hydration interaction, arising from solvent effects, is described as an effective ion-pair interaction. We denote this short-range potential between ions of species i and j at distance $\mathbf{r}$ as $u_{ij}(\mathbf{r})$. The potential is taken as the short-range effective potential between ions immersed in a *bulk* ionic solution having a specific, constant concentration. Therefore, $u_{ij}(\mathbf{r})$ is assumed to be isotropic and does not depend on the ion positions or the confining geometry.

Our aim is to treat the long range electrostatic interaction on the mean-field level, as in PB theory. Thus, we begin by considering the free energy of a system placed in some *arbitrary* field $\Psi(\mathbf{r})$, where the ions interact with each other only through the two-body potential $u_{ij}(\mathbf{r})$. Due to the short-range nature of the hydration interaction, the free energy can be obtained from a virial expansion of the grand canonical partition function. Since we will be interested in highly inhomogeneous systems, we perform an expansion in the inhomogeneous ion density. The derivation is given in Appendix 2.A. Including terms up to the quadratic order in the expansion we obtain:

$$\Omega_h = k_B T \int \sum_i c_i \left[\ln \frac{c_i}{\zeta_i} - 1 \right] \mathrm{d}^3 \mathbf{r} + \int \sum_i e_i c_i \Psi \, \mathrm{d}^3 \mathbf{r}$$
$$+ \frac{k_B T}{2} \sum_{i,j} \int c_i(\mathbf{r}) U_{ij}(\mathbf{r} - \mathbf{r}') c_j(\mathbf{r}') \, \mathrm{d}^3 \mathbf{r} \mathrm{d}^3 \mathbf{r}' \tag{2.16}$$

where $\Psi(\mathbf{r})$ is an external field, coupled to the ith ion charge density $e_i c_i$. The short-range weighted potential U_{ij} in the third term of Ω_h is defined as:

$$U_{ij} = 1 - \mathrm{e}^{-\beta u_{ij}(|\mathbf{r} - \mathbf{r}'|)} \tag{2.17}$$

where u_{ij} is the nominal short-range interaction potential between ions of species i and j. This form of describing the short-range interaction is a rather crude approximation, valid only in the low density limit. Its advantage is its simplicity. The free energy Ω_h amounts to setting the direct correlation function $c_2(|\mathbf{r} - \mathbf{r}'|)$ to be equal to $-U(|\mathbf{r} - \mathbf{r}'|)$, and all higher order direct correlation functions to zero [46].

Having found the hydration free energy Ω_h, the electrostatic interaction can be treated on the mean-field level. This is done by considering $\Psi(\mathbf{r})$ as the electrostatic potential and imposing the self-consistency requirement of the Poisson equation (2.7). This is essentially the approximation we used to derive the PB equation (2.14), with the difference that the free energy of a dilute, non-interacting ion distribution is replaced by the free energy Ω_h of Eq. (2.16). The result is the free energy of Eq. (2.1), with $\Delta\Omega$ defined as follows:

$$\Delta\Omega = \frac{k_B T}{2} \sum_{i,j} \int c_i(\mathbf{r}) U_{ij}(\mathbf{r} - \mathbf{r}') c_j(\mathbf{r}') \, \mathrm{d}^3 \mathbf{r} \mathrm{d}^3 \mathbf{r}' \tag{2.18}$$

We conclude this section with some remarks on the approach presented above. Important solvent effects are already introduced in the PB theory by using an electrostatic interaction with a dielectric constant $\varepsilon = 78$ of water, instead of the bare electrostatic interaction. In the modified model a more precise effective potential between the ions is used. The separation of this potential into a long-range electrostatic term and a short-range hydration term allows each of these two interactions to be treated in a simple though approximated form. The virial expansion is a standard choice for approximating short-range interactions. Such an expansion fails for the electrostatic interaction due to its long-range [47]. On the other hand, the wide success of PB theory demonstrates that the electrostatic interaction can be treated quite well in the mean-field approximation. Therefore we use this approximation for the long-range part of the interaction, and in this respect we remain within the framework of PB theory.

The free energy (2.1) can also be obtained by rewriting the grand canonical partition function as a field-theory partition function. The short-range part of the interaction can be separated from the electrostatic interaction and a different expansion can be performed for each of these interactions. By using a density expansion for the short-range interaction and a loop expansion for the electrostatic interaction, Eq. (2.1) is obtained up to second order in the density expansion and first order in the electrostatic potential [48].

The simplicity of our approach can lead to elegant analytical results, but has several limitations. The use of only the second term in the virial expansion implies that we are using a low density approximation. The validity of such an approximation for a bulk fluid can be assessed by considering $k_B T B_2 c$, where B_2 is the second virial coefficient in the expansion of the pressure, and c is the ion density. Qualitatively, if $B_2 c$ is small compared to unity, the correction to the ideal gas behavior is small and truncating the virial expansion after the second term is sensible. For non-homogeneous cases, the corresponding quantity is $(1/2) \sum_j \int d\mathbf{r}' \, c(\mathbf{r}') U_{ij}(\mathbf{r} - \mathbf{r}')$. For relatively high surface charges considered here this integral approaches values of order unity near the charged surfaces, indicating that the approximation should only be expected to give qualitative results. Another deficiency of the virial expansion to second order can be seen from the fact that the direct correlation function is simply $-U_{ij}(\mathbf{r})$. This implies that the hard core interaction is not described accurately in our treatment. A faithful description would require the vanishing of the pair correlation function $h_2(\mathbf{r})$ for separations smaller than the hard-core diameter. Hence, it should be kept in mind that our main concern is to study the effects of a short-range interaction with a dominant attractive part. Finally, the fact that we describe the electrostatic interaction in the mean-field approximation implies that ion-ion correlations are ignored, as they are in PB theory. When our approach is applied for the aqueous pair potential model, these approximations should also be kept in mind. In particular, we follow Ref. [35] and do not include an effective ion-surface potential [49].

2.2.2 Density equations

The mean density distribution is obtained by minimizing the total free energy $\Omega = \Omega_{\mathrm{PB}} + \Delta\Omega$. From equations (2.1), (2.10) and (2.18) we have:

$$
\begin{aligned}
\Omega \;=\;& \frac{\varepsilon}{8\pi} \int (\nabla \Psi)^2 \mathrm{d}^3\mathbf{r} + k_B T \int \sum_i c_i \left(\ln \frac{c_i}{\zeta_i} - 1 \right) \mathrm{d}^3\mathbf{r} \\
& + \frac{k_B T}{2} \sum_{i,j} \int c_i(\mathbf{r}) U_{ij}(\mathbf{r} - \mathbf{r}') c_j(\mathbf{r}') \, \mathrm{d}^3\mathbf{r}\mathrm{d}^3\mathbf{r}'
\end{aligned}
$$

$$+ \int \lambda(\mathbf{r}) \left(\nabla^2 \Psi + \frac{4\pi}{\varepsilon} \sum_i c_i e_i \right) d^3\mathbf{r} \tag{2.19}$$

where μ_i and $\zeta_i = \exp(\beta\mu_i)/\lambda_T^3$ are the chemical potential and the fugacity of the ion species i, respectively. The thermal de Broglie wavelength, λ_T, is equal to $h/(2\pi m k_B T)^{1/2}$, where h is the Planck constant and m is the ion mass. Requiring an extremum of Ω with respect to Ψ gives: $\lambda = (\varepsilon/4\pi)\Psi$ as in Eq. 2.11. Taking the variation with respect to c_i then gives:

$$\ln \frac{c_i(\mathbf{r})}{\zeta_i} + \sum_j \int c_j(\mathbf{r}')U_{ij}(\mathbf{r} - \mathbf{r}') d^3\mathbf{r}' + \beta e_i \Psi(\mathbf{r}) = 0 \tag{2.20}$$

This equation is supplemented by the Poisson equation (2.7). Since Eq. (2.20) is an integral equation, the c_i cannot be written as a simple function of Ψ as in the PB case. Therefore, a single equation for Ψ, analogous to the PB equation, cannot be obtained, and we are left with the two coupled integro-differential equations (2.20) and (2.7). These equations should be solved together to obtain the electrostatic potential and density profiles. In the case $U \to 0$, Eq. (2.20) reduces to the Boltzmann relation $c_i = \zeta_i \exp(-\beta e_i \Psi)$ with $\zeta_i = c_{b,i}$. Combining this relation with Eq. (2.7) reproduces the PB equation (2.14).

In order to simplify the set of equations, we assume the same short-range interaction between the different pairs of ion species. Assuming that the charged surfaces are negatively charged, we choose: $u_{ij}(\mathbf{r}) = u_{++}(\mathbf{r}) \equiv u(\mathbf{r})$, where $u_{++}(\mathbf{r})$ is the short-range effective potential between the (positive) counter-ions. This assumption is not exact for the effective potentials of ions in water [40]. However, since only the counter-ions reach high densities, close to the oppositely charged surfaces, and the co-ions are repelled from the surface neighborhood, the exact choice of the potentials $u_{+-}(\mathbf{r})$ and $u_{--}(\mathbf{r})$ is expected to be of only minor significance.

We now consider an electrolyte of valency $z_+ : z_-$, *i.e.*, a solution of positive and negative ions of charges $e_\pm = \pm z_\pm e$, where e is the electron charge. We designate the surface charge density on the plate as a constant σ and the bulk densities of the positive and negative ions as $c_b \equiv c_{b,+}$ and $c_{b,-}$, respectively. Due to charge neutrality in the bulk, $c_{b,-} = (z_+/z_-)c_b$ and similarly, $\zeta_- = (z_+/z_-)\zeta$ where $\zeta \equiv \zeta_+$. Equation (2.20) can then be written as follows:

$$c_\pm(\mathbf{r}) = \zeta_\pm e^{\mp \beta e z_\pm \Psi} \exp\left[-\int c(\mathbf{r}')U(\mathbf{r} - \mathbf{r}') d^2\mathbf{r}' \right] \tag{2.21}$$

where $c(\mathbf{r}) = c_+(\mathbf{r}) + c_-(\mathbf{r})$ is the total ion density, and $U(\mathbf{r}) = U_{++}(\mathbf{r})$ is obtained from $u(\mathbf{r})$ using Eq. (2.17). From the Poisson equation (2.7) we obtain:

$$\nabla^2 \Psi = -\frac{4\pi e}{\varepsilon}(z_+ c_+ - z_- c_-)$$

$$= \frac{4\pi e}{\varepsilon}\zeta z_+ \left(e^{\beta e z_- \Psi} - e^{-\beta e z_+ \Psi}\right)\exp\left[-\int c(\mathbf{r'})U(\mathbf{r}-\mathbf{r'})\,\mathrm{d}^3\mathbf{r'}\right] \qquad (2.22)$$

Note that in addition to the explicit dependence on the ion valencies $z_\pm$ in equations (2.21) and (2.22), in a more realistic model the details of the potential $u(\mathbf{r})$ should also depend on the type of counter-ion species present in the problem.

2.3 Single charged plate

2.3.1 Density equations

After presenting the general formalism let us consider, as an example, a single negatively charged planar surface (Fig. 2.1). The charged surface is in contact with an electrolyte of valency $z_+:z_-$. We designate the axis perpendicular to the plate as the z axis, and consider the ion solution in the region $z > 0$. For simplicity we consider positive and negative ions of the same hard-core diameter d_{hc}. The coordinate of closest approach of the ions to the plate is designated as $z = 0$. Hence the "real" surface lies at a distance of one ion radius $d_{\mathrm{hc}}/2$ from the actual $z = 0$ plate position, as shown in Fig. 2.1 (a). When we refer to conventional PB results, however, the ions are point-like and the plate should be understood to be positioned exactly at $z = 0$.

Due to the one-dimensional symmetry imposed by the uniformly charged planar plate, the integration in Eq. (2.21) can be performed over the $x-y$ plane, leaving us with profiles depending only on z, the distance from the plate:

$$c_\pm(z) = \zeta_\pm e^{\mp\beta e z_\pm \Psi}\exp\left[-\int_0^\infty c(z')B(z-z')\,\mathrm{d}z'\right] \qquad (2.23)$$

where $c(z) = c_+(z) + c_-(z)$ is the total ion density and $B(z)$ is the integral of $U(\mathbf{r})$ in the plane of constant z. Using cylindrical coordinates:

$$B(z) = 2\pi\int_0^\infty \rho\,\mathrm{d}\rho\, U\left(\sqrt{z^2 + \rho^2}\right) \qquad (2.24)$$

and the Poisson equation (2.22) reads:

$$\begin{aligned}
\frac{\mathrm{d}^2\Psi}{\mathrm{d}z^2} &= \frac{4\pi e}{\varepsilon}\zeta z_+ \left(e^{\beta e z_- \Psi} - e^{-\beta e z_+ \Psi}\right) \\
&\quad \times \exp\left[-\int_0^\infty c(z')B(z-z')\,\mathrm{d}z'\right]
\end{aligned} \qquad (2.25)$$

Equations (2.23) and (2.25) are supplemented by the boundary conditions:

$$\left.\frac{\mathrm{d}\Psi}{\mathrm{d}z}\right|_{z=0} = -\frac{4\pi}{\varepsilon}\sigma \quad ; \quad \left.\frac{\mathrm{d}\Psi}{\mathrm{d}z}\right|_{z\to\infty} = 0 \qquad (2.26)$$

Finally, the relation between ζ and the bulk density c_b can be obtained from Eq. (2.23). As $z \to \infty$, Ψ becomes zero, and $c_{\pm}$ assume their asymptotic constant, bulk values. Thus the integrand inside the exponential can be replaced by $-(1 + z_+/z_-)c_b B(z - z')$. Recalling that $c_+ = c_b$ and $c_- = (z_+/z_-)c_b$, we obtain:

$$c_b = \zeta \exp\left[-\left(1 + \frac{z_+}{z_-}\right)B_t c_b\right] \tag{2.27}$$

where:

$$B_t \equiv \int_{-\infty}^{\infty} dz\, B(z) = \int d^3\mathbf{r}\, U(\mathbf{r}) \tag{2.28}$$

is also equal to $2B_2$, the second virial coefficient. Note that $B(z)$ and B_t are negative for an attractive interaction. The limit $B_t c_b \to 0$ is the limit in which the short-range interaction becomes negligible in the bulk. In this limit the relation between the bulk density and fugacity of Eq. (2.27) tends to the ideal gas relation $c_b = \zeta = \exp(\beta\mu)/\lambda_T^3$.

Two special cases will be of particular interest in the following sections. The first is the case of a monovalent 1:1 electrolyte, where we have:

$$\begin{aligned}
c_{\pm}(z) &= \zeta e^{\mp\beta e\Psi} \exp\left[-\int_0^{\infty} c(z')B(z - z')\, dz'\right] \\
\frac{d^2\Psi}{dz^2} &= = -\frac{4\pi}{\varepsilon}c(z)
\end{aligned} \tag{2.29}$$

and:

$$c_b = \zeta \exp\left(-2B_t c_b\right) \tag{2.30}$$

The second case is that of no added salt. The solution contains only monovalent counter-ions ($z_+ = 1$, $z_- = 0$). This case can be obtained by taking formally the limit $\zeta \to 0$ of Eq. (2.29), or by repeating the derivation from Eq. (2.19) with only one type of ions, of charge e. The term $-k_B T \int d^3\mathbf{r}\, c \ln(\zeta)$ in Ω is then a Lagrange multiplier added to impose the condition: $\int_0^{\infty} dz\, ec(z) = |\sigma|$. The following equations are then obtained:

$$\begin{aligned}
c(z) &= \zeta_0 e^{-\beta e\Psi} \exp\left[-\int_0^{\infty} c(z')B(z - z')\, dz'\right] \\
\frac{d^2\Psi}{dz^2} &= -\frac{4\pi e}{\varepsilon}c(z)
\end{aligned} \tag{2.31}$$
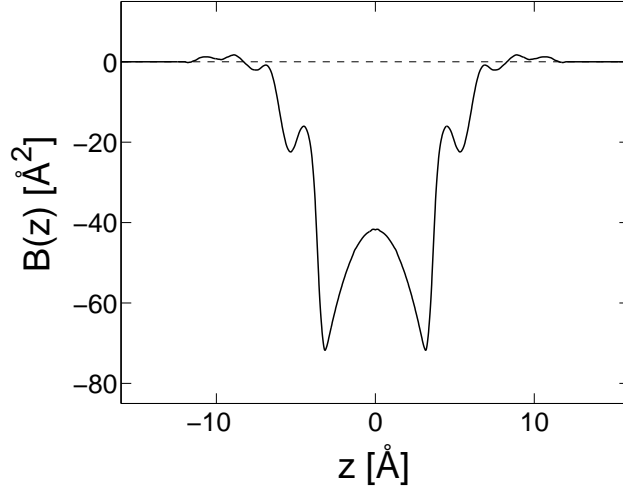
Figure 2.3: The effective interaction in a planar geometry $B(z)$ obtained from the potential of Fig. 2.2, using Eq. (2.24). The oscillating structure of the radial potential shown in Fig. 2.2 is apparent in the secondary minima of $B(z)$.

where ζ_0 is an arbitrary reference fugacity. The choice of ζ_0 determines the (arbitrary) position in which Ψ is zero. Note that the electrostatic potential Ψ diverges in the bulk. This divergence exists also in the usual PB theory, because the system is effectively one dimensional with no screening by added salt. Although $\Psi(z)$ has a weak logarithmic divergence, the density of counter-ions decays to zero, $\lim_{z\to\infty} c(z) = 0$ as it should.

2.3.2 Parameters and length scales

For the ion-ion potential $u(\mathbf{r} - \mathbf{r}')$ we use an effective potential between Na$^+$ - Na$^+$ ion pairs. The potential was calculated using a Monte-Carlo simulation [40] for an NaCl ionic solution of concentration $0.55\,\mathrm{M}$, at room temperature. The electrostatic interaction between the ions is subtracted, and the net short-range potential is shown in Fig. 2.2. For ion-ion separations below $2.9\,\mathrm{\mathring{A}}$ a hard core interaction is assumed. Fig. 2.3 shows the function $B(z)$, derived from this potential, using Eq. (2.24). Note that $B(z)$ has several local maxima and minima. These correspond to the local maxima and minima of $u(\mathbf{r})$. Thus the structure of $B(z)$ reflects the oscillatory behavior of the effective potential.

We use the effective potential calculated for $c_b = 0.55\,\mathrm{M}$, regardless of the actual bulk ion concentration in the system. Since the important effects occur near the charged surface, where the ion concentration is much larger than c_b, it seems reasonable to use an effective potential calculated in the presence of a rather high salt concentration. The choice of $c_b = 0.55\,\mathrm{M}$ is still

somewhat arbitrary, and we rely on the fact that the dependence of the effective potential on the ion concentration is weak [40].

It is useful to employ two length scales that characterize the PB density profiles [7]. The *Gouy-Chapman length*, defined as $b = \varepsilon k_B T/(2\pi e|\sigma|)$, characterizes the width of the diffusive counter-ion layer close to a single plate charged with a surface charge σ, in the absence of added salt. The *Debye-Hückel screening length*, $\lambda_D = (8\pi c_b e^2/\varepsilon k_B T)^{-1/2}$, equal to $19.6\,\text{Å}$ for $c_b = 0.025\text{M}$ at room temperature characterizes the decay of the screened electrostatic interaction in a solution with added salt. The strength of the electrostatic interaction can also be expressed using the *Bjerrum length*, $l_B = e^2/(\varepsilon k_B T)$. This is the distance at which the electrostatic interaction between two unit charges becomes equal to the thermal energy. The Bjerrum length is equal to about $7\,\text{Å}$ in water at room temperature.

The inclusion of hydration interactions introduces additional length scales in the system. For the interaction shown in Figs. 2.2 and 2.3, the range of the interaction d_{hyd} can be seen to be approximately $7\,\text{Å}$, over twice the hard core diameter $d_{\text{hc}} = 2.9\,\text{Å}$. The strength of the hydration interaction is characterized by $B_t \simeq -(7.9\,\text{Å})^3$, as is calculated from Eq. (2.28).

2.3.3 Numerical results

Equations (2.23) and (2.25) are a set of three nonlinear integro-differential equations. We treat them numerically using an iterative scheme, based on the assumption that the positive ion density profile is dominated by the electrostatic interaction. We start with the analytically known PB profile close to a single charged plate and calculate iteratively corrections to this profile, as result from equations (2.23) and (2.25). For a 1:1 electrolyte we iteratively solve the equation:

$$\frac{\mathrm{d}^2\Psi^{(n)}}{\mathrm{d}z^2} = \frac{8\pi e}{\varepsilon}\zeta \sinh\left(\beta e\Psi^{(n)}\right)\exp\left[-\int_0^\infty c^{(n-1)}(z')B(z-z')\,\mathrm{d}z'\right] \tag{2.32}$$

where $c(z) = c_+(z) + c_-(z)$ is the total ion density and the superscript n stands for the nth iteration. For $n > 0$:

$$c_\pm^{(n)}(z) \equiv \zeta \mathrm{e}^{\mp\beta e\Psi^{(n)}}\exp\left[-\int_0^\infty c^{(n-1)}(z')B(z-z')\,\mathrm{d}z'\right] \tag{2.33}$$

and the zeroth order densities $c_\pm^{(0)}$ are taken as the density profiles generated by the PB equation (2.14). The boundary conditions (2.26) are satisfied by the electrostatic potential $\Psi^{(n)}$ in all the iterations. Note that using our iterative scheme, Eq. (2.32) is an inhomogeneous differential equation, because the integral in the exponential is a known function of z, calculated numerically

in the $(n-1)$ iteration. A similar iterative scheme, based on Eq. (2.31) can be used when only counter-ions are present in the solution.
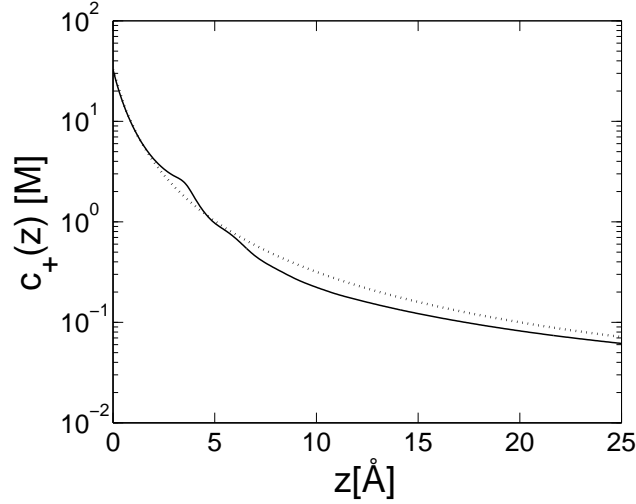
Figure 2.4: Counter-ion density profile (solid line) obtained from numerical solution of Eq. (2.31) with the hydration interaction as of Fig. 2.3, plotted on a semi-log plot. No salt is present in the solution. The surface charge is $|\sigma| = 0.333\,\mathrm{C/m^2}$. The dielectric constant is $\varepsilon = 78$ and the temperature is $T = 298\,\mathrm{K}$. The dotted line shows the corresponding density profile obtained from the PB equation.

Figure 2.4 shows the calculated density profile of the counter-ions on a semi-logarithmic scale, for a charged plate with a surface charge, $|\sigma| = 0.333\,\mathrm{C/m^2}$, corresponding to an area of approximately $48\,\text{Å}^2$ per unit charge. This is a typical high surface charge obtained with mica plates. It corresponds to a Gouy-Chapman length $b = 1.06\,\text{Å}$, at a temperature of 298K, with $\varepsilon = 78$. No salt is present in the solution. The calculated density profile (solid line) is compared to the PB prediction (dotted line). The short-range attraction favors an increased concentration of counter-ions in the vicinity of the charged plate. This results in an increase of the concentration relative to the PB prediction. For a surface charge as in Fig. 2.4, an increase of the concentration is seen at distances from the plate up to approximately $4.5\,\text{Å}$. The overall number of counter-ions is fixed by the requirement of charge neutrality. Therefore, the increase in the density of counter-ions *near* the plate is balanced by a reduced concentration *further* away.

When salt is present in the solution, the short-range attraction draws additional ions from the bulk solution to the diffuse electrical layer near the plate. This can be seen in Fig. 2.5, in a comparison of counter-ion profiles for different values of the bulk concentration c_b. For each salt concentration, the figure shows the ratio between the counter-ion density and the density

Figure 2.5: The ratio c_+/c_+^{PB} between the positive ion density obtained from Eq. (2.29) and the value obtained from PB theory, for a surface charge $|\sigma| = 0.333\,\mathrm{C/m^2}$ and several values of c_b. Other parameters are as in Fig. 2.4. The three values of c_b: $0.1\,\mathrm{M}$, $0.025\,\mathrm{M}$ and $0.00625\,\mathrm{M}$ correspond to Debye-Hückel screening lengths $\lambda_D \simeq 9.8\,\text{Å}$, $19.6\,\text{Å}$ and $39.2\,\text{Å}$, respectively.

predicted by PB theory, as a function of the distance from the plate. The dotted line shows the result in the no-salt limit. As the salt concentration increases, the counterion concentration increases relative to the PB concentration at all distances from the charged plate. Qualitatively, however, the hydration effect on the counter-ion profile is similar in all the curves. As long as the Debye-Hückel screening length is large compared to the Gouy-Chapman length, $b = 1.06\,\text{Å}$, the density profile in the vicinity of the plate is dominated by the balancing counter-ions and the salt has only a small effect.

The effect of the hydration interaction is strongly dependent on the surface charge σ. As σ is increased, the ion density near the surface increases too. The exponential in Eq. (2.31) deviates more strongly from unity, leading to a larger deviation from PB theory. The dependence on σ is demonstrated in Fig. 2.6. The ratio of the positive ion density to its PB value is shown for three values of the surface charge. The effect of the hydration potential is very minor for small surface charge, $|\sigma| = 0.0333\,\mathrm{C/m^2}$ (dotted line), where the deviation from PB is less than 2% at its maximum, and considerable for a surface charge of $0.333\,\mathrm{C/m^2}$ (dashed line), where the deviation from PB reaches almost 40%.

The numerical scheme, described above, requires several iterations to converge fully. It is interesting to note, though, that the first iteration captures most of the effect of the short range interaction. This indicates that the density profile is dominated, as we assumed, by the electrostatic interaction, and assures that the convergence of the iterative scheme is good with
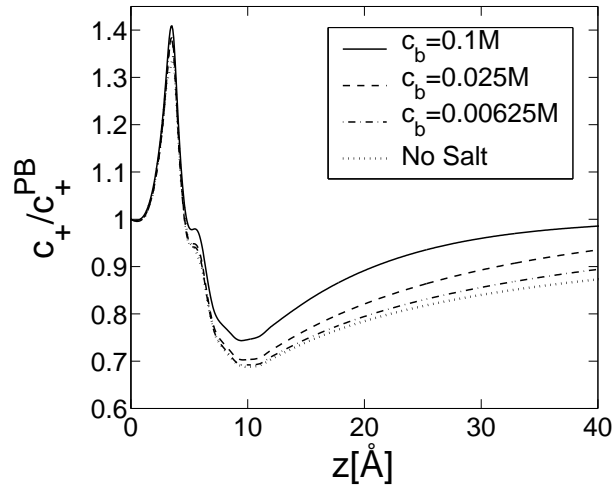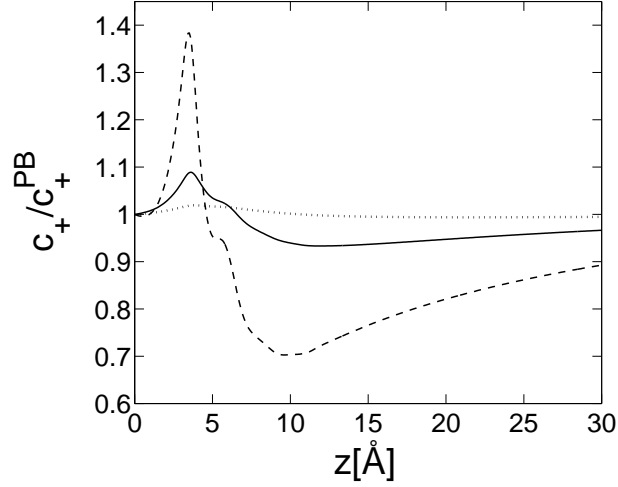
Figure 2.6: The ratio c_+/c_+^{PB} between the positive ion density obtained from Eq. (2.29) and the value obtained from PB theory, for surface charges $|\sigma| = 0.333\,\mathrm{C/m^2}$ (dashed line), $0.1\,\mathrm{C/m^2}$ (solid line) and $0.0333\,\mathrm{C/m^2}$ (dotted line). The bulk salt concentration c_b is $0.025\,\mathrm{M}$. Other parameters are as in Fig. 2.4.

the PB density profile as the zero-th order approximation. On the theoretical level it indicates that the effect of the hydration interaction can be seen as a perturbation over the PB results. The fact that the first iteration provides a good approximation to the full iterative result can lead to further analytical approximations. For example, the corrections to the density profiles, in the no added salt limit, are studied analytically in the next section, based on this observation.

As an example for the results of the first iteration, we compare, in Fig. 2.7, the correction to the counter-ion density profile obtained in the first iteration (dashed line), with the full iterative result (solid line). We use a high surface charge of $0.333\,\mathrm{C/m^2}$, where the differences between the exact profile and that of the first iteration are relatively pronounced. The two density profiles differ by at most 3.2 percent, where the ion density deviates from the PB value by 30 percent. For smaller surface charge the results obtained in the first iteration are even better.

2.3.4 Contact density and the contact theorem

The contact density of the ions is barely modified as compared with the PB prediction. This is evident in Figs. 2.4–2.6. As long as the Debye-Hückel screening length is large compared to the Gouy-Chapman length, or the hydration interaction is negligible in the bulk, the modification remains small. This result can be obtained from a generalization of the PB contact theorem [6, 50]:
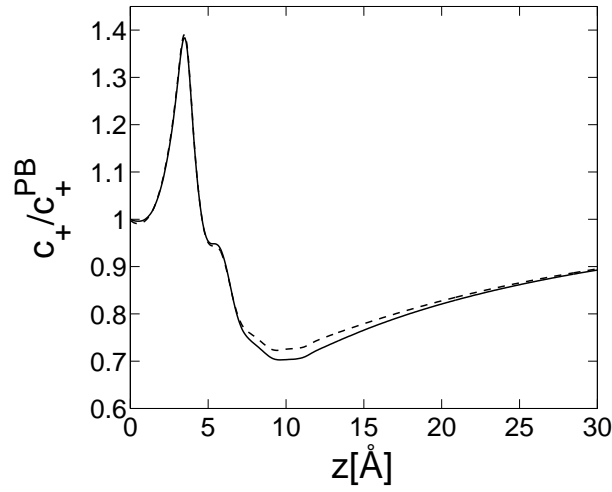
Figure 2.7: The positive ion density profile obtained after one iteration of Eq. (2.32) (dotted line), compared to the full solution of Eq. (2.29) (solid line). Parameters are as in Fig. 2.5. The maximal deviation between the two density profiles is 3.2 percent, where the deviation from PB is approximately 30 percent.

$$\sum_i c_i(0) - \frac{2\pi\beta}{\varepsilon}\sigma^2 = P_{\text{bulk}} \qquad (2.34)$$

where P_{bulk} is the bulk pressure of the ionic solution. Equation (2.34) is derived in detail for the free energy used in our model in Chapter 3. It is obtained from the equality of the internal pressure in the electrolyte solution at different distances from the charged plate. Far away from the charged plate the pressure must be equal to the bulk pressure of the ionic solution, because the densities approach their bulk values and the electrostatic potential becomes constant. At the contact plane between the plate and the solution, the pressure involves only an electrostatic contribution and an osmotic contribution, as in PB theory. This is due to the fact that in our model no short range interaction between the plate and the ions is included. Equating the pressure at the contact plane and far away from the plate results in Eq. (2.34).

The contact density, as expressed by Eq. (2.34), differs from the PB prediction only due to the change in the actual value of P_{bulk}. This change is negligible if the short-range interaction is not of importance in the bulk. In addition, if the surface charge is high, such that $b \ll \lambda_D$, P_{bulk} is negligible compared to the second term in the left hand side of Eq. (2.34). Thus the contact density remains very close to the PB prediction. In the no-salt limit P_{bulk} is zero and the contact density coincides exactly with the PB result, $c_+(0) = (2\pi\beta/\varepsilon)\sigma^2$.

2.4   Analytical solutions

The simplicity of the model makes it possible to obtain various analytical results. The effect of the hydration on the ion distribution can be characterized by several quantities, such as the magnitude of the deviation from the PB result and the effective PB surface charge density seen at a distance from the plate. Using several simplifying assumptions it is possible to obtain analytical expressions for these quantities.

First we assume that the hydration interactions can be neglected in the bulk, *i.e.*, $B_t c_b \ll 1$. In this case, the effect of the hydration potential is significant only in the vicinity of the charged surface, where the ion density becomes large. In addition, the Debye-Hückel screening length, λ_D, is taken to be large compared to the Gouy-Chapman length $b = e/(2\pi l_B |\sigma|)$. Since $\lambda_D \gg b$, the negative co-ion density near the negatively charged surface can be neglected compared to the positive counter-ion density. Far away from the charged plate, the system is well described using the PB equation, with an effective surface charge density σ_{eff} different from the actual charge density σ. The result of the above two simplifying assumptions is that the salt is of minor importance in the region where the effective surface charge is determined. The effective surface charge can then be inferred by considering the case in which only counter-ions are present in the solution (no added salt).

Equation (2.31) can now be recast in a simpler form, by considering $\eta \equiv \ln(c/\zeta_0)$, as expressed by Eq. (2.31), and taking its second derivative:

$$\frac{\mathrm{d}^2\eta}{\mathrm{d}z^2} = \frac{4\pi}{\varepsilon}\beta e^2 \zeta_0 \mathrm{e}^\eta - \int_0^\infty \zeta_0 \mathrm{e}^{\eta(z')}\frac{\mathrm{d}^2 B(z-z')}{\mathrm{d}z^2}\,\mathrm{d}z' \tag{2.35}$$

The PB density profile, $c_{\text{PB}}(z) \equiv \zeta_0 \mathrm{e}^{\eta_0(z)}$, for the same surface charge, satisfies the equation $d^2\eta_0/dz^2 = (4\pi\beta e^2 \zeta_0/\varepsilon)\exp(\eta_0)$. Its exact solution is known to be:

$$c_{\text{PB}}(z) = \zeta_0 \mathrm{e}^{\eta_0(z)} = \frac{1}{2\pi l_B} \cdot \frac{1}{(z+b)^2} \tag{2.36}$$

Note that only in the PB equation $\eta(z)$ is the reduced electrostatic potential $e\Psi(z)/k_B T$. From the generalized contact theorem (2.34), the surface density in the no added salt case and in the presence of one plate is $c(0) = 2\pi\beta\sigma^2/\varepsilon$, as in PB theory. Therefore:

$$\eta(z=0) = \eta_0(z=0) \tag{2.37}$$

From the derivative of $c(z)$, Eq. (2.31), we find:

$$\frac{\mathrm{d}\eta}{\mathrm{d}z} = -\beta e \frac{\mathrm{d}\Psi}{\mathrm{d}z} - \int_0^\infty \mathrm{d}z'\, c(z') \frac{\mathrm{d}B(z-z')}{\mathrm{d}z} \tag{2.38}$$

and using the boundary condition (2.26):

$$\left.\frac{\mathrm{d}\eta}{\mathrm{d}z}\right|_{z=0} = \left.\frac{\mathrm{d}\eta_0}{\mathrm{d}z}\right|_{z=0} + \int_0^\infty \mathrm{d}z'\, c(z') \frac{\mathrm{d}B(z')}{\mathrm{d}z} \tag{2.39}$$

where the odd parity of $\mathrm{d}B/\mathrm{d}z$ has been used. This relation can be used together with Eq. (2.37) as a second boundary condition at $z = 0$, instead of the boundary condition of vanishing $\mathrm{d}\eta/\mathrm{d}z$ at infinity.

Linearizing Eq. (2.35) with respect to:

$$w \equiv \eta - \eta_0 = \ln(c/c_{\mathrm{PB}}) \tag{2.40}$$

which is valid for relatively small deviations from the PB profile, results in the following equation:

$$\begin{aligned}
&\frac{\mathrm{d}^2 w}{\mathrm{d}z^2} - \frac{4\pi}{\varepsilon}\beta e^2 c_{\mathrm{PB}}(z)w(z) \\
&= -\int_0^\infty \mathrm{d}z'\,(1 + w(z'))c_{\mathrm{PB}}(z') \frac{\mathrm{d}^2 B(z-z')}{\mathrm{d}z^2}
\end{aligned} \tag{2.41}$$

This equation can be further simplified by omitting $w(z')$ from the integrand in the right hand side. This approximation was motivated in Sec. 2.3.3 and is equivalent to stopping the iterative scheme (2.32) after the first iteration. The density profile is then replaced by the PB density profile in the term that involves the hydration interaction $B(z)$. This results in the equation:

$$\frac{\mathrm{d}^2 w}{\mathrm{d}z^2} - \frac{4\pi}{\varepsilon}\beta e^2 c_{\mathrm{PB}}(z)w(z) + \Gamma(z) = 0 \tag{2.42}$$

where $\Gamma(z)$ is the convolution integral:

$$\Gamma(z) = \frac{1}{2\pi l_B} \int_0^\infty \mathrm{d}z'\, \frac{1}{(z'+b)^2} \frac{\mathrm{d}^2 B(z-z')}{\mathrm{d}z^2} \tag{2.43}$$

The corresponding boundary conditions, obtained from equations (2.37) and (2.39) using the same approximations, are:

$$\begin{aligned}
w(z=0) &= 0 \\
\left.\frac{\mathrm{d}w}{\mathrm{d}z}\right|_{z=0} &= \int_0^\infty \mathrm{d}z'\, c_{\mathrm{PB}}(z') \frac{\mathrm{d}B(z')}{\mathrm{d}z}
\end{aligned} \tag{2.44}$$

Equation (2.42) is a second order linear differential equation for $w(z)$ and can be solved analytically. The solution, given in detail in Appendix 2.B, is expressed in terms of the convolution integral $\Gamma(z)$ of Eq. (2.43). The effective surface charge and the effect of the hydration on the density profile can then be calculated in several limits, described in detail in Appendix 2.B. Here we outline the main results.

2.4.1 Slowly varying density: $b \gg d_{\mathrm{hyd}}$

In the limit $b \gg d_{\mathrm{hyd}}$, the PB distribution varies slowly on the scale of the hydration interaction, described by $B(z)$, and the theory becomes effectively a local density functional theory. The specific form of $B(z)$ is not important, and all the results simply depend on $B_t = \int_{-\infty}^{\infty} B(z)\,\mathrm{d}z$. The deviation of the effective Gouy-Chapman length b_{eff} from the actual Gouy-Chapman length b depends linearly on B_t and on the surface charge $\sigma \sim 1/b$. This can be expected since we use a linearized equation. Thus we have, on dimensional grounds, $b_{\mathrm{eff}} - b \sim B_t/l_B b$. The detailed calculation gives the numerical prefactor:

$$b_{\mathrm{eff}} - b \cong \frac{-B_t}{4\pi l_B}\frac{1}{b} \tag{2.45}$$

Since B_t is negative b_{eff} is larger than b and the effective surface charge, σ_{eff}, is smaller than the actual surface charge σ. This result should be expected. The short range interaction attracts counterions to the vicinity of the charged plate and the surface charge is screened more effectively than in the PB equation.

The correction to the counter-ion density profile, described by $w(z) = \ln[c(z)/c_{\mathrm{PB}}(z)]$, is found to be:

$$w(z) = \frac{-B_t}{2\pi l_B}\left\{\frac{3}{2(z+b)^2} - \frac{1}{b(z+b)}\right\} \tag{2.46}$$

The density profile is increased relative to PB theory for distances smaller than $b/2$, and decreased for larger distances. The deviation from PB, $w(z)$, is maximal at $z = 0$, where it is equal to $-B_t/(4\pi l_B b^2)$, and minimal at $z = 2b$, where it is equal to $B_t/(12\pi l_B b^2)$.

Figure 2.8 shows the approximated function $w(z)$ of Eq. (2.46) for $b = 21.2$ Å, corresponding to $b/d_{\mathrm{hyd}} \approx 3$ (dotted line). The approximation is compared with the function $w(z)$ obtained from the exact solution of equation (2.31) for the case of no added salt (solid line). Although b is not much larger than d_{hyd}, the approximation describes well the correction to the PB profile. Note that $w(z)$, as expressed by Eq. (2.46) is maximal at $z = 0$, whereas according to the contact theorem $w(0)$ should be zero. This apparent inconsistency results from neglecting the

Figure 2.8: The logarithm of the ratio between the counter-ion density obtained with the inclusion of the hydration interaction and its value in PB theory, $w(z)$, as a function of the distance from a charged plate, with no added salt in the solution. The solid line shows the function $w(z)$ obtained from the exact solution, for $b = 21.2\,\text{Å}$. The dotted line shows the approximated curve obtained from the linearization with respect to w, Eq. (2.42), in the limit $b \gg d_{\text{hyd}}$, Eq. (2.46).

range of the hydration potential relative to b. In the precise solution of Eq. (2.31) $w(0)$ is zero, as it should be. The prediction of Eq. (2.46) is valid only for distances $z \gtrsim d_{\text{hyd}}$, as can be seen in Fig. 2.8.

The range of validity of the linearization procedure can be found by requiring that the minimal and maximal values of $w(z)$ are small compared to unity:

$$\frac{-B_t}{4\pi l_B b^2} \ll 1 \tag{2.47}$$

2.4.2 Surface layer limit: $b \ll d_{\text{hyd}}$

In the limit in which $b \ll d_{\text{hyd}}$, the ion density effectively becomes a dense layer concentrated at $z = 0$ on the scale of the hydration interaction. The effective Gouy-Chapman length has the same form as in the limit of slowly varying density, $b \gg d_{\text{hyd}}$, but having a different prefactor:

$$b_{\text{eff}} - b \cong \frac{-B_t}{12\pi l_B} \frac{1}{b} \tag{2.48}$$

The effective surface charge is, therefore, smaller than the actual surface charge. Note that b_{eff} depends on $B(z)$, in this limit, only through B_t. The linear dependence on $\sigma \sim 1/b$ follows from the linearization leading to Eq. (2.42), as in the previous limit.
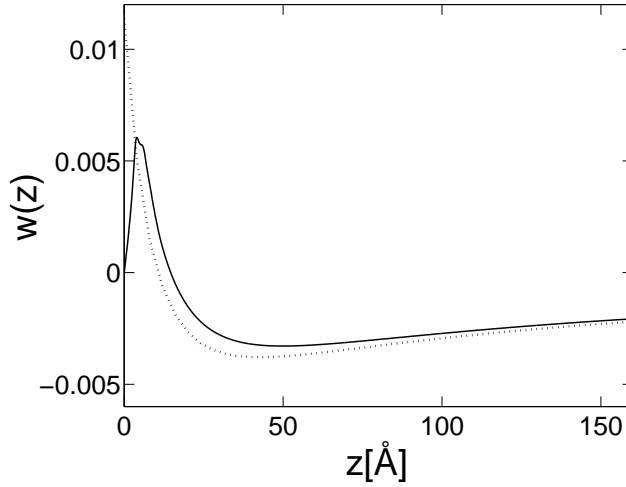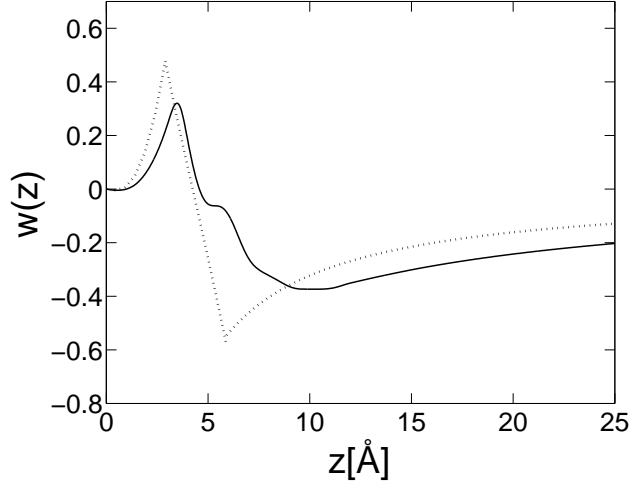
Figure 2.9: The logarithm of the ratio between the counter-ion density obtained with the inclusion of the hydration interaction and its value in PB theory, $w(z)$, as a function of the distance from a charged plate, with no added salt in the solution. The solid line shows the function $w(z)$ obtained from the exact solution, for $b = 1.06$ Å. The dotted line shows the approximated curve obtained from the linearization with respect to w, Eq. (2.42), in the limit $b \ll d_{\mathrm{hyd}}$, Eq. (2.77).

It should be stressed that although b is small compared to d_{hyd} we still assume that b is large enough for the linearization to be valid, *i.e.*, we assume that $w(z)$ is small compared to unity. Furthermore, the counter-ion density should be small enough that we can sensibly use only the quadratic term in the virial expansion. To check the validity of these assumptions, the correction to the density profile should be considered.

The form of $w(z)$ depends, in the surface layer limit, on the specific form of $B(z)$. In order to study $w(z)$ analytically, we use an approximated form of $B(z)$, described in Appendix 2.B. A typical form of the approximated $w(z)$, obtained using this approximation [Eq. (2.77)], is shown in Fig. 2.9 (dotted line). The Gouy-Chapman length is $b = 1.06$ Å, corresponding to $b/d_{\mathrm{hyd}} \approx 0.15$. In addition, the function $w(z)$ obtained from the exact solution of equation (2.31) is shown for comparison (solid line). The approximated curve captures well the qualitative behavior of the correction to the PB profile. Note that the discrepancy between the approximated and actual profiles results not only from the linearization and small b limit, but also from the loss of detail due to the use of an approximated form for $B(z)$.

The deviation from the PB profile, $w(z)$, can be qualitatively described as follows. For $z < d_{\mathrm{hc}}$, $w(z)$ increases from zero quadratically (with an additional term of the form $z^2 \ln z$) to its value at $z = d_{\mathrm{hc}}$. It then decreases from its maximum positive value to a minimum, negative value, on a scale of the range of the attractive part of $B(z)$. This minimum value is equal to

approximately $B_t/6\pi l_B b d_{\mathrm{hyd}}$. For distances larger than the interaction range, $w(z)$ assumes the form $w(z) \sim 1/z$, characterizing a PB profile with a modified, effective surface charge. For finite values of b, we can expect the above behavior to be smoothed over a scale of order b.

The validity of the linearization can be found by requiring that $|w(z)| \ll 1$. This requirement results in the following condition:

$$\frac{-B_t}{6\pi l_B b d_{\mathrm{hyd}}} \ll 1 \tag{2.49}$$

The validity of stopping the virial expansion at the quadratic order can be shown to have the same condition. For the hydration potential of Fig. 2.2, the condition expressed in Eq. (2.49) implies that the various approximations we use start to break down when b becomes smaller than approximately $1\,\text{Å}$, or $\sigma \gtrsim 0.022\,e/\text{Å}^2$. When b is of this order, it is well below d_{hyd}, making the surface layer limit a sensible approximation.

2.4.3   Effective surface charge

In the two limits described above, the effective Gouy-Chapman length was found to be of the form $b_{\mathrm{eff}} - b \sim -B_t/l_B b$, with different prefactors in the two limits. For intermediate values of b, the effective charge depends on the specific structure of the function $B(z)$. In order to study this dependence, we use a simple approximated form for $B(z)$, described in Appendix 2.B. Using this approximation, an analytical expression can be obtained for the effective Gouy-Chapman length for all values of b.

Figures 2.10 (a) and (b) show the predicted b_{eff} and $b_{\mathrm{eff}} - b$, respectively (solid lines) as a function of b, together with the asymptotic limits (2.45) and (2.48) (dotted lines). As the surface charge increases from zero (and b decreases from infinity), the effective charge $|\sigma_{\mathrm{eff}}|$ increases too (but is always smaller than the actual surface charge). When b reaches a certain value b^{min}, b_{eff} starts increasing with further reduction of b, i.e., the effective charge decreases with increasing surface charge above $|\sigma|^{\mathrm{max}} = e/(2\pi l_B b^{\mathrm{min}})$. The value of b^{min} depends on the structure of the function $B(z)$, but can be estimated to be between the values predicted by the asymptotic expressions (2.45) and (2.48). From the condition $\mathrm{d}b_{\mathrm{eff}}/\mathrm{d}b|_{b=b^{\mathrm{min}}} = 0$ we find:

$$\sqrt{\frac{-B_t}{12\pi l_B}} < b^{\mathrm{min}} < \sqrt{\frac{-B_t}{4\pi l_B}} \tag{2.50}$$

and:

$$b_{\mathrm{eff}}^{\mathrm{min}} \simeq 2b^{\mathrm{min}} \tag{2.51}$$
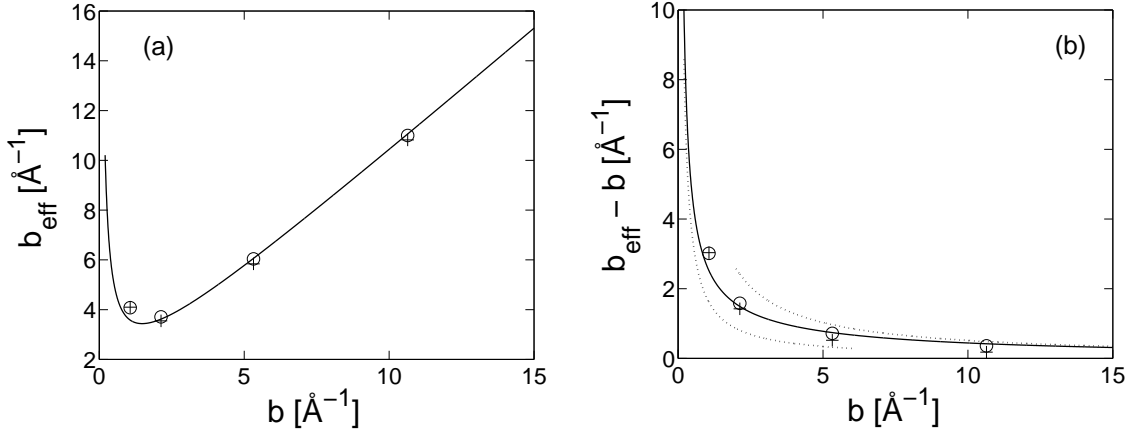
Figure 2.10: The effective Gouy-Chapman length b_{eff} (a) and $\Delta b = b_{\text{eff}} - b$ (b), as a function of the Gouy-Chapman length b. The solid lines show the behavior predicted by Eq. (2.79), with $B_t = -500\,\text{Å}^3$, $d_{\text{hc}} = 2.9\,\text{Å}$ and $B_0 = 41.8\,\text{Å}^2$. The dotted lines show the asymptotic limits of equations (2.45) and (2.48). The symbols show results extracted from numerical solutions of Eq. (2.29), using $B(z)$ of Fig. 2.3, with salt concentrations of $10^{-7}\,\text{M}$ (circles) and $0.1\,\text{M}$ (crosses). The salt has a very small effect.

For the hydration interaction of Fig. 2.2, B_t is approximately $-500\,\text{Å}^3$. The value of b^{min} is then between $1.36\,\text{Å}$ and $2.35\,\text{Å}$, corresponding to a surface charge density between $0.15\,\text{C/m}^2$ and $0.26\,\text{C/m}^2$. The values obtained from the approximated curve, shown in Fig. 2.10, are $b^{\text{min}} \simeq 1.5\,\text{Å}$ and $b_{\text{eff}}^{\text{min}} \simeq 3.4\,\text{Å}$.

For small enough values of b, the effective surface charge $|\sigma_{\text{eff}}|$ should increase again with an increase of $|\sigma|$ and become larger than $|\sigma|$. This effect cannot be predicted by our model because of the low density approximation used for the hard core interaction. In particular, the hard core of the ions should cause the density to saturate at the close packing density, leading to a reduced screening of the surface charge relative to PB theory [26,27,51]. In our model, as in the PB theory, the counterion density near the surface is not bounded, and increases indefinitely as σ is increased. Although our model includes the steric repulsion between ions, this repulsion is "softened", and is always outweighed by the attractive part of the ion-ion interaction.

In addition to the prediction obtained using the linearized approximation, Figure 2.10 shows values of b_{eff} extracted from numerical solutions of the full equation (2.29), using the original interaction $B(z)$. The equation was solved with two different salt concentrations: $10^{-7}\,\text{M}$ (circles) and $0.1\,\text{M}$ (crosses). The value of b_{eff} was estimated from the positive ion density at large distances from the plate, by finding the value of b that would result in the same calculated values of the density in a solution of the PB equation. Note that for both salt concentrations,

b_{eff} is very close to its predicted value, meaning that the salt has a very small effect on σ_{eff}. This result is not obvious for the high salt concentration of $0.1\,\mathrm{M}$. The Debye-Hückel screening length is approximately $9.6\,\text{Å}$, not much larger than the range of the hydration interaction, $d_{\mathrm{hyd}} \simeq 7\,\text{Å}$, and comparable to the Gouy-Chapman length at the large b region of the plot.

2.5   Conclusions and Outlook

In this chapter we have studied the effects due to the discreteness of the solvent in aqueous ionic solutions. Hydration interactions are found to have a significant effect on the structure of the diffusive layer near highly charged surfaces. The counter-ion density is increased in the vicinity of the charged surface, relative to the PB prediction, and decreased further away. The distance from the charged plate in which the density is increased, and the magnitude of the deviation from the PB density, depend strongly on the surface charge, and on the parameters of the short-range hydration interaction between ion pairs.

The ion-ion hydration interaction can be described roughly using two parameters. The first parameter is the range of the hydration interaction, d_{hyd}, equal to approximately $7\,\text{Å}$ for Na^+-Na^+ pairs. The second parameter, B_t has dimensions of volume and characterizes the strength of the hydration interaction. It is equal to approximately $-500\,\text{Å}^3$ for Na^+-Na^+ pairs. Two limits can be considered, where the Gouy-Chapman length, $b \sim 1/\sigma$, is small or large compared to the range of the hydration interaction d_{hyd}. In both of these limits we assume that the Debye-Hückel screening length, λ_D, is large compared to b and d_{hyd}.

In the limit $b \gg d_{\mathrm{hyd}}$, the counter-ion density becomes depleted, relative to the PB prediction, starting at a distance $z \simeq b/2$ from the charged plate. The maximum absolute value of $w(z) = \ln[c(z)/c_{\mathrm{PB}}(z)]$ scales as $-B_t/l_B b^2$. In the limit $b \ll d_{\mathrm{hyd}}$, the distance from the plate, where the counter-ion density becomes lower than the PB prediction, is between $z = d_{\mathrm{hc}}$ and $z = d_{\mathrm{hyd}}$. The maximum absolute value of $w(z)$ scales as $-B_t/l_B d_{\mathrm{hyd}} b$.

Far away from the charged plate, the density profile can be well described using the PB theory with an effective surface charge that can be calculated analytically. The correction to the Gouy-Chapman length in the two limits $b \gg d_{\mathrm{hyd}}$ and $b \ll d_{\mathrm{hyd}}$ is always positive and scales as $-B_t/l_B b$, but has different numerical prefactors. When the surface charge on the plate is increased, the effective surface charge, σ_{eff}, is found to reach a certain maximal value. Above this maximal value σ_{eff} decreases with further increase of the actual σ on the plate. The various approximations we use start to break down when b is smaller than approximately $-B_t/6\pi l_B d_{\mathrm{hyd}}$, corresponding to $b \lesssim 1\,\text{Å}$.

An important outcome of this work is that the correction of the PB ion density due to the hydration interaction is significant near highly charged surfaces. The electrostatic interaction dominates the ionic distribution and the hydration interaction can be seen as a perturbation. For a high surface charge density of, say, one unit charge per $48\,\text{Å}^2$ the counterion density deviates from its Poisson Boltzmann value by at most 30 percent. The effective change in the surface charge is more significant, from $1\,e/48\,\text{Å}^2$ to about $1\,e/13\,\text{Å}^2$.

The formalism we present can be readily generalized to other geometries. This could lead to an estimation of the aqueous solvent effects on phenomena such as the Manning condensation on cylindrical polyions [52], and charge renormalization of spherical micelles or colloids [10]. In this respect our formalism offers an advantage over the AHNC approximation which was applied so far only in a planar geometry. Another interesting extension of this work would be to consider the combination of fluctuation and hydration effects. This is particularly important for ionic solutions with divalent counter-ions, where fluctuation effects become large [22, 23, 25].

2.A   Inhomogeneous virial expansion

We consider an inhomogeneous system of particles with a short-range two-body interaction, and aim to express the free energy of the system in the low density limit as a functional of the density distribution. For simplicity we consider only one species of particles. The inhomogeneity of the system arises from the inclusion of an external field $\varphi(\mathbf{r})$, or from the boundary conditions imposed on the system. We begin by considering the grand canonical ensemble. The grand canonical partition function is:

$$Z_G = \sum_N \frac{1}{N!} \left(\frac{e^{\beta\mu}}{\lambda_T^3} \right)^N Q_N \tag{2.52}$$

where μ is the chemical potential, λ_T is the de Broglie thermal wavelength and Q_N is:

$$Q_N = \int \prod_{i=1}^N \mathrm{d}^3\mathbf{r}_i \, e^{-\beta U_N(\{\mathbf{r}_i\})} \tag{2.53}$$

$$U_N(\{\mathbf{r}_i\}) = \sum_i \varphi(\mathbf{r}_i) + \frac{1}{2} \sum_i \sum_{j\neq i} u\left(|\mathbf{r}_i - \mathbf{r}_j|\right) \tag{2.54}$$

We proceed on similar lines as the usual virial expansion in a bulk fluid, expanding $\ln Z_G$ in powers of the activity. Up to second order we have:

$$\ln Z_G = \left(\frac{e^{\beta\mu}}{\lambda_T^3} \right) Q_1 + \frac{1}{2} \left(\frac{e^{\beta\mu}}{\lambda_T^3} \right)^2 (Q_2 - Q_1^2) = \left(\frac{e^{\beta\mu}}{\lambda_T^3} \right) \int \mathrm{d}^3\mathbf{r} \, e^{-\beta\varphi(\mathbf{r})}$$

$$+\frac{1}{2}\left(\frac{e^{\beta\mu}}{\lambda_T^3}\right)^2\int d^3\mathbf{r}\int d^3\mathbf{r}'\,e^{-\beta(\varphi(\mathbf{r})+\varphi(\mathbf{r}'))}\left(e^{-\beta u(|\mathbf{r}-\mathbf{r}'|)}-1\right) \qquad (2.55)$$

This can be seen as an expansion in powers of the field $\exp\left[\beta\left(\mu-\varphi(\mathbf{r})\right)\right]/\lambda_T^3$. The local density $c(\mathbf{r})$ can be expressed in a similar expansion:

$$
\begin{aligned}
c(\mathbf{r}) &= -\frac{1}{\beta}\frac{\delta\ln Z_G}{\delta\varphi(\mathbf{r})}=\left(\frac{e^{\beta\mu}}{\lambda_T^3}\right)e^{-\beta\varphi(\mathbf{r})}\\
&\quad+\left(\frac{e^{\beta\mu}}{\lambda_T^3}\right)^2 e^{-\beta\varphi(\mathbf{r})}\int d^3\mathbf{r}'e^{-\beta\varphi(\mathbf{r}')}\left(e^{-\beta u(|\mathbf{r}-\mathbf{r}'|)}-1\right)
\end{aligned}
\qquad (2.56)
$$

This relation can be inverted to obtain an expansion of $\exp\left[\beta\left(\mu-\varphi(\mathbf{r})\right)\right]/\lambda_T^3$ in powers of $c(\mathbf{r})$. Up to the second order:

$$\frac{e^{\beta(\mu-\varphi(\mathbf{r}))}}{\lambda_T^3}=c(\mathbf{r})+c(\mathbf{r})\int d^3\mathbf{r}'\,c(\mathbf{r}')\left(1-e^{-\beta u(|\mathbf{r}-\mathbf{r}'|)}\right) \qquad (2.57)$$

and by substituting this relation in Eq. (2.55) $\ln Z_G$ can be expressed as an expansion in c. Up to the second order:

$$\ln Z_G=\int d^3\mathbf{r}\,c(\mathbf{r})+\frac{1}{2}\int d^3\mathbf{r}\int d^3\mathbf{r}'\,c(\mathbf{r})c(\mathbf{r}')\left(1-e^{-\beta u(|\mathbf{r}-\mathbf{r}'|)}\right) \qquad (2.58)$$

The grand canonical potential can be obtained from the relation $\Omega=-k_BT\ln Z_G$, with $\ln Z_G$ given by Eq. (2.58). In this expression, $c(\mathbf{r})$ is the mean density profile for the imposed external field $\varphi(\mathbf{r})$ and a given chemical potential μ. We would like to express Ω as a functional of a general ion density $c(\mathbf{r})$, whose minimization with respect to $c(\mathbf{r})$ would give the equilibrium mean density. Regarding $-k_BT\ln Z_G$ as a functional of $\chi(\mathbf{r})\equiv\varphi(\mathbf{r})-\mu$, we have:

$$-k_BT\frac{\delta\ln Z_G}{\delta\chi(\mathbf{r})}=c(\mathbf{r}) \qquad (2.59)$$

The Legendre transform of this relation can be obtained by defining:

$$\Theta=-k_BT\ln Z_G-\int d^3\mathbf{r}\,c(\mathbf{r})\chi(\mathbf{r}) \qquad (2.60)$$

and expressing $\ln Z_G$ and χ as functionals of $c(\mathbf{r})$. We have already expressed $\ln Z_G$ as a functional of $c(\mathbf{r})$ in Eq. (2.58). An expression for $\chi(\mathbf{r})$ as a functional of $c(\mathbf{r})$ can be obtained from Eq. (2.57). Up to first order in c we have :

$$
\begin{aligned}
\beta[\varphi(\mathbf{r})-\mu] &= -\ln\left\{\lambda_T^3 c(\mathbf{r})\left[1+\int d^3\mathbf{r}'\,c(\mathbf{r}')\left(1-e^{-\beta u(|\mathbf{r}-\mathbf{r}'|)}\right)\right]\right\}\\
&= -\ln\left[\lambda_T^3 c(\mathbf{r})\right]-\int d^3\mathbf{r}'\,c(\mathbf{r}')\left(1-e^{-\beta u(|\mathbf{r}-\mathbf{r}'|)}\right)+O(c^2)
\end{aligned}
\qquad (2.61)
$$

Using this relation and Eq. (2.58) we obtain, up to second order in c:

$$
\begin{aligned}
\beta\Theta(\{c(\mathbf{r})\}) \;=\;& \int d^3\mathbf{r}\, c(\mathbf{r}) \left[\ln(\lambda_T^3 c(\mathbf{r})) - 1\right] \\
& + \frac{1}{2} \int d^3\mathbf{r} \int d^3\mathbf{r}'\, c(\mathbf{r})c(\mathbf{r}') \left(1 - e^{-\beta u(|\mathbf{r}-\mathbf{r}'|)}\right)
\end{aligned}
\tag{2.62}
$$

The functional Θ of $c(\mathbf{r})$ has the property that:

$$
\frac{\delta\Theta}{\delta c(\mathbf{r})} = -\chi(\mathbf{r}) = -\left[\varphi(\mathbf{r}) - \mu\right]
\tag{2.63}
$$

or equivalently:

$$
\frac{\delta}{\delta c(\mathbf{r})} \left\{ \Theta + \int d^3\mathbf{r}\, c(\mathbf{r}) \left[\varphi(\mathbf{r}) - \mu\right] \right\} = \frac{\delta\Omega(\{c(\mathbf{r})\})}{\delta c(\mathbf{r})} = 0
\tag{2.64}
$$

Thus, using Eq. (2.62), we obtain:

$$
\begin{aligned}
\Omega(\{c(\mathbf{r})\}) \;=\;& k_B T \int d^3\mathbf{r}\, c(\mathbf{r}) \left(\ln \frac{c(\mathbf{r})}{\zeta} - 1 \right) + \int d^3\mathbf{r}\, c(\mathbf{r})\varphi(\mathbf{r}) \\
& + \frac{1}{2} k_B T \int d^3\mathbf{r} \int d^3\mathbf{r}'\, c(\mathbf{r})c(\mathbf{r}') \left(1 - e^{-\beta u(|\mathbf{r}-\mathbf{r}'|)}\right)
\end{aligned}
\tag{2.65}
$$

where $\zeta = \exp(\beta\mu)/\lambda_T^3$.

The derivation of Eq. (2.65) can be readily generalized to the case of several ion species of different charges and different pair interactions $u_{ij}(\mathbf{r})$, resulting in Eq. (2.16).

A similar, more elaborate diagrammatic expansion of the thermodynamic potentials in the presence of an external field is presented in Ref. [53]. A variational principal for the grand canonical potential Ω is obtained in which Ω is expressed as a functional of the mean density $c(\mathbf{r})$ and the pair correlation function $h_2(\mathbf{r}_1, \mathbf{r}_2)$. This expression is equivalent to Eq. (2.65) up to the second order in the cluster expansion.

2.B Details of analytical results

In this appendix we present details of the analytical approximations of Sec. 2.4.

We consider first the analytical solution of Equation (2.42). This equation is a second order linear differential equation for $w(z)$. Note that the function $c_{PB}(z)$ is a known function of z, given by Eq. (2.36). The solution of Eq. (2.42), with the boundary conditions of Eq. (2.44) is:

$$
w(z) = \frac{1}{z+b} \int_0^z dz_2\, (z_2 + b)^2 \int_{z_2}^{\infty} \frac{dz_1}{(z_1 + b)} \Gamma(z_1)
\tag{2.66}
$$

where $\Gamma(z)$ is the convolution integral, defined by Eq. (2.43). By writing $\Gamma(z)$ as:

$$\Gamma(z) = \int_0^\infty \mathrm{d}z' \, \Gamma(z')\delta(z - z') \tag{2.67}$$

$w(z)$ can be rewritten in the following form:

$$
\begin{aligned}
w(z) &= -\frac{1}{z+b}\left\{\frac{b^3}{3}\int_0^\infty \mathrm{d}z' \frac{\Gamma(z')}{z'+b} - \frac{1}{3}\int_0^z \mathrm{d}z' \,(z'+b)^2\Gamma(z')\right\} \\
&\quad +\frac{(z+b)^2}{3}\int_z^\infty \mathrm{d}z' \frac{\Gamma(z')}{z'+b}
\end{aligned}
\tag{2.68}
$$

The effective charge σ_{eff} (or equivalently, the effective Gouy-Chapman length b_{eff}) can be calculated from the coefficient of z^{-1} in $w(z)$, as z approaches infinity:

$$w(z) \sim \frac{2\,(b - b_{\mathrm{eff}})}{z}, \quad z \to \infty \tag{2.69}$$

We thus find:

$$b_{\mathrm{eff}} - b = \frac{1}{6}\int_0^\infty \mathrm{d}z \left[\frac{b^3}{z+b} - (z+b)^2\right]\Gamma(z) \tag{2.70}$$

A simple form for the convolution integral $\Gamma(z)$ can be obtained in the limits in which b is small or large relative to d_{hyd}, the characteristic range of the hydration potential.

2.B.1   Slowly varying density: $b \gg d_{\mathrm{hyd}}$

In the limit $b \gg d_{\mathrm{hyd}}$, the PB distribution varies slowly on the scale of the hydration interaction. The convolution integral $\Gamma(z)$ of Eq. (2.43) can then be approximated in the following way:

$$
\begin{aligned}
\Gamma(z) &= \frac{1}{2\pi l_B}\int_{-\infty}^\infty \mathrm{d}z' \frac{H(z')}{(z'+b)^2}\frac{\mathrm{d}^2 B}{\mathrm{d}z^2}(z - z') \\
&= \frac{1}{2\pi l_B}\int_{-\infty}^\infty \mathrm{d}z' \left[\frac{1}{b^2}\frac{\mathrm{d}\delta(z)}{\mathrm{d}z} - \frac{2}{b^3}\delta(z) + \frac{6H(z)}{(z+b)^4}\right]B(z - z') \\
&\simeq \frac{B_t}{2\pi l_B}\cdot\left[\frac{1}{b^2}\frac{\mathrm{d}\delta(z)}{\mathrm{d}z} - \frac{2}{b^3}\delta(z) + \frac{6H(z)}{(z+b)^4}\right]
\end{aligned}
\tag{2.71}
$$

where $H(z)$ is the Heaviside function ($H(z) = 0$ for $z < 0$ and $\mathrm{H(z)} = 1$ for $z > 0$). Inserting this expression in Eq. (2.70) we obtain Eq. (2.45) for the effective Gouy-Chapman length. By substituting equation (2.71) in Eq. (2.68), the form of $w(z)$, given in Eq. (2.46), is obtained.

2.B.2 Approximated form for $B(z)$

Some of the following results depend on the specific structure of the hydration interaction, characterized by the function $B(z)$. In order to obtain analytical expressions, we use a simple approximated form, $B^{\text{app}}(z)$, instead of $B(z)$. Assuming that the hydration interaction consists of a hard core interaction and a short-range attractive part, the function $B(z)$ has some general characteristics that should be present in $B^{\text{app}}(z)$. For $z < d_{\text{hc}}$, $B(z)$ always has the parabolic form $-(B_0 + \pi z^2)$, where $B_0 = -B(z = 0)$. We assume that the attractive part of the interaction dominates over the short-range repulsion so that B_0 is positive. For z larger than some finite value $d_{\text{hc}} + \Delta$, $B(z)$ is practically zero due to the short range of the interaction. For $d_{\text{hc}} < z < d_{\text{hc}} + \Delta$, $B(z)$ varies from $-(B_0 + \pi d_{\text{hc}}^2)$ to zero in a functional form that depends on the details of the attractive potential. The most simple way to model this behavior of $B(z)$ is to have a linear increase of $B^{\text{app}}(z)$ between $z = d_{\text{hc}}$ and $z = d_{\text{hc}} + \Delta$, and to set B^{app} to be zero for z larger than $d_{\text{hc}} + \Delta$:

$$B^{\text{app}}(z) = \begin{cases} -(B_0 + \pi z^2) & |z| \leq d_{\text{hc}} \\ -\left(B_0 + \pi d_{\text{hc}}^2\right) \dfrac{(d_{\text{hc}} + \Delta - z)}{\Delta} & d_{\text{hc}} < |z| \leq d_{\text{hc}} + \Delta \\ 0 & d_{\text{hc}} + \Delta < |z| \end{cases} \tag{2.72}$$

The parameters in this expression should be chosen to match, approximately, the form of $B(z)$. Setting d_{hc} to be the hard core diameter of the real potential and setting $B_0 = -B(0)$ ensures that $B(z)$ and $B^{\text{app}}(z)$ are identical for $z < d_{\text{hc}}$. The width Δ can then be set such that $B_t^{\text{app}} = B_t$:

$$2B_0 d_{\text{hc}} + \frac{2}{3}d_{\text{hc}}^3 + \Delta \left(B_0 + \pi d_{\text{hc}}^2\right) = -B_t \tag{2.73}$$

This is desirable in light of equations (2.45) and (2.48), since the effective surface charge depends only on B_t in these limits. Figure 2.11 shows $B(z)$ and $B^{\text{app}}(z)$ for the hydration potential of Fig. 2.2.

2.B.3 Surface layer limit: $b \ll d_{\text{hyd}}$

In the limit $b \ll d_{\text{hyd}}$, the convolution integral in Eq. (2.43) becomes:

$$\Gamma(z) \simeq \frac{|\sigma|}{e} \frac{\mathrm{d}^2 B(z)}{\mathrm{d}z^2} = \frac{1}{2\pi l_B b} \frac{\mathrm{d}^2 B(z)}{\mathrm{d}z^2} \tag{2.74}$$

The prefactor of $\Gamma(z)$ in Eq. (2.70) is $-\frac{1}{6}z^2 + O(b)$ and therefore the effective Gouy-Chapman length is:
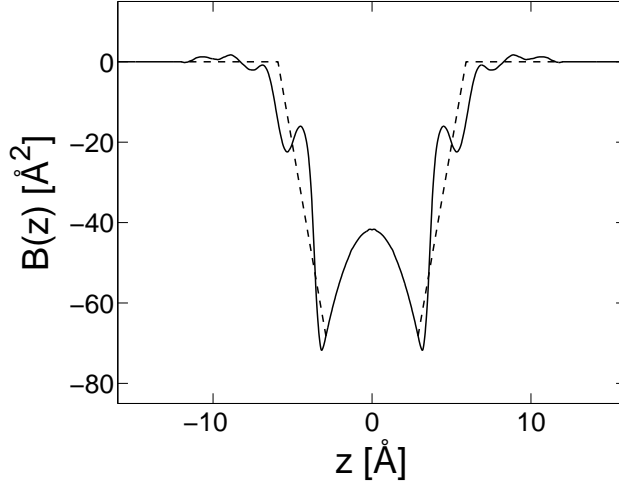
Figure 2.11: The effective interaction in a planar geometry, $B(z)$, obtained from the potential of Fig. 2, and the corresponding approximated function $B^{\text{app}}(z)$, defined by Eq. (2.72) (dashed line). The parabolic dependence for $|z| < d_{\text{hc}}$ is identical in the two curves.

$$b_{\text{eff}} - b \cong \frac{-1}{12\pi l_B b} \int_0^\infty \mathrm{d}z \, z^2 B''(z) = \frac{-B_t}{12\pi l_B} \frac{1}{b} \tag{2.75}$$

This result is independent on the specific form of $B(z)$.

To obtain $w(z)$, the deviation of the density profile relative to PB theory, Eq. (2.74) can be substituted in Eq. (2.68). Up to leading order in b the following expression is obtained:

$$w(z) = \frac{1}{6\pi l_B b} \frac{1}{z} \int_0^z \mathrm{d}z' \, B''(z') z'^2 + \frac{1}{6\pi l_B b} z^2 \int_z^\infty \mathrm{d}z' \, \frac{1}{z'} B''(z') \tag{2.76}$$

Using $B^{\text{app}}(z)$, the approximated form of $B(z)$ presented in the previous subsection, this gives:

$$w(z) = \begin{cases} \dfrac{1}{6\pi l_B b} z^2 \left(\dfrac{4\pi}{3} + \dfrac{B_0 + \pi d_{\text{hc}}^2}{d_{\text{hc}}(d_{\text{hc}} + \Delta)} - 2\pi \ln \dfrac{d_{\text{hc}}}{z} \right) , & |z| \le d_{\text{hc}} \\[2em] \dfrac{1}{6\pi l_B b} \left[d_{\text{hc}}^2 \left(\dfrac{4\pi}{3} d_{\text{hc}} + \dfrac{B_0 + \pi d_{\text{hc}}^2}{\Delta} \right) \dfrac{1}{z} \right. \\ \left. \qquad\qquad - \dfrac{B_0 + \pi d_{\text{hc}}^2}{\Delta(d_{\text{hc}} + \Delta)} z^2 \right] , & d_{\text{hc}} < |z| \le d_{\text{hc}} + \Delta \\[2em] \dfrac{B_t}{6\pi l_B b} \dfrac{1}{z} , & d_{\text{hc}} + \Delta < |z| \end{cases} \tag{2.77}$$

The minimal, negative value of $w(z)$ is assumed at $z = d_{\text{hc}} + \Delta$ and is equal to:

$$w(d_{\text{hc}} + \Delta) = \frac{B_t}{6\pi l_B b(d_{\text{hc}} + \Delta)} \simeq \frac{B_t}{6\pi l_B b d_{\text{hyd}}} \tag{2.78}$$

This results in the condition (2.49) for the validity of the linearization in the surface layer limit.

Using only the quadratic term in the virial expansion is sensible if $\int_0^\infty dz'\, c(z')B(z-z')$ is small compared to unity. In the surface layer limit, this integral is simply: $(|\sigma|/e)B(z) = B(z)/(2\pi l_B b)$. Estimating the maximum value of $|B(z)|$ to be approximately $-B_t/(2d_{\mathrm{hyd}})$ we obtain the requirement: $-B_t/(4\pi l_B b d_{\mathrm{hyd}}) \ll 1$, which is analogous to (2.49).

2.B.4 Effective Gouy-Chapman length

Using $B^{\mathrm{app}}(z)$ in equations (2.43) and (2.70) we find the following approximation for the effective Gouy-Chapman length:

$$
\begin{aligned}
b_{\mathrm{eff}} - b \;=\; & \frac{1}{12\pi l_B b}\left\{-B_t^{\mathrm{app}} - \pi d_{\mathrm{hc}}^2 b + 2\pi d_{\mathrm{hc}} b^2 + 2B_0 \ln\left(\frac{b + d_{\mathrm{hc}} + \Delta}{b}\right) b \right. \\
& - \frac{2}{\Delta}\left(\pi d_{\mathrm{hc}}^2 \Delta + \pi d_{\mathrm{hc}}^3 + B_0 d_{\mathrm{hc}}\right)\ln\left(\frac{b + d_{\mathrm{hc}}}{b + d_{\mathrm{hc}} + \Delta}\right) b \\
& \left. - 2\pi \ln\left(\frac{b + d_{\mathrm{hc}}}{b}\right) b^3 \right\}
\end{aligned}
\qquad (2.79)
$$

This expression is shown in Fig. 2.10 and discussed in section 2.4. In the limits $b \gg d_{\mathrm{hyd}}$ and $b \ll d_{\mathrm{hyd}}$ it reduces to the asymptotic expressions (2.45) and (2.48), respectively.

Bibliography

[1] Y. Burak and D. Andelman, *Phys. Rev. E.* **62** (2000) 5296.

[2] G. Gouy, *J. Phys. (France)* **9** (1910) 457.

[3] D. L. Chapman, *Philos. Mag.* **25** (1913) 475.

[4] P. Debye and E. Hückel, *Phyzik* **24** (1923) 185.

[5] P. Debye and E. Hückel, *Phyzik* **25** (1924) 97.

[6] J. Israelachvili, *Intermolecular and Surface Forces*, 2nd ed., Academic Press: New York, 1991.

[7] D. Andelman, in *Handbook of Physics of Biological Systems*, R. Lipowsky and E. Sackmann (eds.), Elsevier Science: Amsterdam, 1994, Vol. I, Chap. 12, p. 603.

[8] B. Honig and A. Nicholls, *Science* **268** (1995) 1144.

[9] E. J. W. Verwey and J. T. G. Overbeek, *Theory of the Stability of Lyophobic Colloids*, Elsevier: Amsterdam, 1948.

[10] S. Alexander *et al.*, *J. Chem. Phys* **80** (1984) 5776.

[11] J. L. Barrat and J. F. Joanny, *Adv. Chem. Phys.* **XCIV** (1996) 1.

[12] D. Harries, S. May, W. M. Gelbart, and A. Ben-Shaul, *Biophys. J.* **75** (1998) 159.

[13] I. Borukhov, D. Andelman, and H. Orland, *Macromolecules* **31** (1998) 1665.

[14] G. J. Fleer *et al.*, *Polymers at Interfaces*, Chapman & Hall: London, 1993.

[15] R. Kjellander and S. Marčelja, *J. Chem. Phys.* **82** (1985) 2122.

[16] R. Kjellander, *J. Chem. Phys.* **88** (1988) 7129.

[17] S. Levine, C. W. Outhwaite, and L. B. Bhuiyan, *J. Electroanal. Chem.* **123** (1981) 105.

[18] C. W. Outhwaite and L. B. Bhuiyan, *J. Chem. Soc. Faraday Trans. 2* **79** (1983) 707.

[19] L. Blum and D. Henderson, in *Fundamentals of Inhomogeneous Fluids*, D. Henderson (ed.), Marcel Dekker: New York, 1992, Chap. 6, pp. 239–276, and references therein.

[20] R. R. Netz and H. Orland, *Europhys. Lett.* **45** (1999) 726.

[21] R. R. Netz and H. Orland, *Europhys. J. E.* **1** (2000) 203.

[22] L. Guldbrand, B. Jönsson, H. Wennerström, and P. Linse, *J. Chem. Phys.* **80** (1984) 2221.

[23] R. Kjellander, T. Åkesson, B. Jönsson, and S. Marčelja, *J. Chem. Phys.* **97** (1992) 1424.

[24] H. Greberg, R. Kjellander, and T. Åkesson, *Mol. Phys.* **92** (1997) 35.

[25] M. J. Stevens and M. O. Robbins, *Europhys. Lett.* **12** (1990) 81.

[26] I. Borukhov, D. Andelman, and H. Orland, *Phys. Rev. Lett.* **79** (1997) 435.

[27] I. Borukhov, D. Andelman, and H. Orland, *Electrochim. Acta* **46** (2000) 221.

[28] D. B. Lukatsky and S. A. Safran, *Phys. Rev. E.* **60** (1999) 5848.

[29] G. M. Torrie and G. N. Patey, *Electrochim. Acta* **36** (1991) 1677.

[30] J. Israelachvili and H. Wennerström, *Nature* **379** (1996) 219.

[31] F. Otto and G. N. Patey, *Phys. Rev. Lett.* **60** (1999) 4416.

[32] R. M. Pashley, *J. Colloid Interface Sci.* **80** (1981) 153.

[33] R. M. Pashley and J. N. Israelachvili, *J. Colloid Interface Sci.* **101** (1984) 511.

[34] B. V. Derjaguin and L. D. Landau, *Acta Phys. Chem. USSR* **XIV** (1941) 633.

[35] S. Marčelja, *Nature* **385** (1997) 689.

[36] S. Marčelja, *Langmuir* **16** (2000) 6081.

[37] E. Guàrdia, R. Rey, and J. A. Padró, *J. Chem. Phys.* **95** (1991) 2823.

[38] E. Guàrdia, R. Rey, and J. A. Padró, *Chem. Phys.* **155** (1991) 187.

[39] D. E. Smith and L. X. Dang, *J. Chem. Phys.* **100** (1994) 3757.

[40] A. P. Lyubartsev and A. Laaksonen, *Phys. Rev. Lett.* **55** (1997) 5689.

[41] A. P. Lyubartsev and A. Laaksonen, *Phys. Rev. Lett.* **52** (1995) 3730.

[42] S. Marčelja, *Period. Biol.* **100** (1998) 7.

[43] S. Marčelja, *Colloid Surface A* **130** (1997) 321.

[44] S. Marčelja, private communication.

[45] L. Lue, N. Zoeller, and D. Blankschtein, *Langmuir* **15** (1999) 3726.

[46] J. K. Percus, *J. Stat. Phys.* **42** (1986) 921.

[47] L. D. Landau and E. M. Lifshitz, *Statistical Physics, 3rd edition, Part 1*, Pergamon Press: New York, 1980.

[48] We are indebted to R. Netz for raising this point.

[49] An ion-surface interaction is treated on a mean-field level in: M. N. Tamashiro and P. Pincus, *Phys. Rev. E* **60** (1999) 6549.

[50] S. L. Carnie and D. Y. C. Chan, *J. Chem. Phys.* **74** (1981) 1293.

[51] R. Kjellander, *Ber. Bunsenges. Phys. Chem.* **100** (1996) 894.

[52] G. S. Manning, *J. Chem. Phys.* **51** (1969) 954.

[53] T. Morita and K. Hiroike, *Prog. Theor. Phys.* **25** (1961) 537.

Chapter 3

Hydration interactions: Inter-plate interactions

The following chapter deals with discrete solvent effects on the interaction of two parallel charged surfaces in ionic aqueous solution.[1] These effects are taken into account using the theoretical formalism introduced in chapter 2. We study numerically the density profile of ions between the two plates, and the resulting inter-plate pressure. At large plate separations the two plates are decoupled and the ion distribution can be characterized by an effective Poisson-Boltzmann charge that is smaller than the nominal charge, as was found in chapter 2. The pressure is thus reduced relative to Poisson-Boltzmann predictions. At plate separations below ~ 20 Å the pressure is modified considerably, due to the solvent mediated short-range attraction between ions in the system. For high surface charges this contribution can overcome the mean-field repulsion giving rise to a net attraction between the plates.

3.1   Introduction

Aqueous ionic solutions are abundant in biological and chemical systems. Often they play a prominent role in determining the properties of charged macromolecules that are immersed in them [2]. The mean field theory of electrolytes, known as Poisson-Boltzmann (PB) theory and its linearized version, Debye-Hückel theory [2–7], are known for many decades and have proved to be useful and important tools. PB theory was applied in the study of colloidal dispersions [8, 9], biological membranes [7], synthetic and biological polyelectrolytes [10, 11], and complex systems such as DNA-lipid complexes [12]. Nevertheless, PB theory is known to have important limitations. Being a mean field theory, ion-ion correlations are ignored.

---

[1]The material presented in this chapter was published in Ref. [1].

In addition, the finite size of ions is neglected. These effects have been studied extensively using various approaches [13] such as liquid state [14–17] and density functional [18] theories, simulations [19–21], field theory [22, 23] and other modifications to the PB theory [24–27].

Most of the studies of corrections to PB have concentrated on the so-called primitive model, where ions are assumed to interact with each other through the electrostatic interaction and a hard core steric repulsion. Although this model can describe many effects that are neglected in PB theory, it still neglects some physical features that are present in real systems. Most notably, the aqueous solvent is treated as a continuous medium, whereas in reality ions interact with discrete solvent molecules.

Solvent effects are strong especially in water, because the polar water molecules interact very strongly with ions. The most significant result is that the electrostatic ion-ion interaction is reduced by a factor $\varepsilon \simeq 78$ at room temperature, due to screening by the dielectric environment. However the discreteness of the solvent results in a more complicated picture. When ions approach each other at separations of a few water molecular diameters, the effective interaction between them is modified considerably. Fig. 2.2 shows the correction to the $1/\varepsilon r$ potential between two Na^+ ions in water. This effective potential was calculated, using a simulation scheme [28], for a bulk NaCl solution of concentration 0.55 M, at room temperature. Note that the short-range potential, remaining after the subtraction of the Coulomb interaction, is oscillatory and predominantly attractive.

The possibility to calculate the effective potential between ions in water leads naturally to the model depicted schematically in Fig. 3.1. The water is treated as a continuous medium, with a dielectric constant ε. In addition to the electrostatic interaction a short-range interaction is included between ion pairs. The short-range potential, denoted as $u_{ij}(r)$, is taken as an input to the model (from simulation), and can in general depend on the ion species i and j. For example, the potential shown in Fig. 2.2 is used between Na^+-Na^+ pairs. The effective potential is calculated in a bulk solution and thus depends only on the ion-ion separation. However, systems containing charged surfaces can lead to inhomogeneity or anisotropy in the ion distribution.

The model described above was suggested in Ref. [29], and was studied in planar geometry using the Anisotropic Hyper-Netted Chain (AHNC) approximation [15] in Refs. [30–33]. In chapter 2 we presented a simplified approach to the same model. In this latter approach, a term accounting for the short-range solvent-mediated ion-ion interaction is added to the PB free energy. The formalism obtained in this way is simple although less accurate than
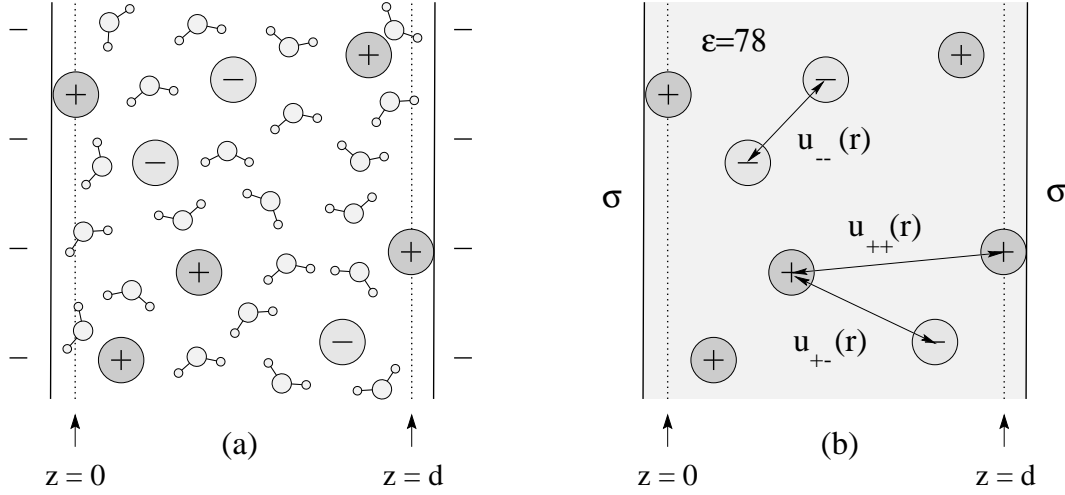
Figure 3.1: Schematic description of the pair potential model. An aqueous ionic solution confined between two charged plates in (a) is replaced by ions in a continuum dielectric medium with electrostatic and short-range interactions $u_{ij}(r) = u_{ij}(|\mathbf{r}|)$ in (b). The coordinates $z = 0$ and $z = d$ designate the contact positions of the ions with the plates. The distance of closest approach is equal to $d_{\mathrm{hc}}/2$, where d_{hc} is the hard-core diameter of the ions.

the AHNC approximation, and in particular neglects ion-ion correlations. On the other hand numerical calculations can be done fairly easily, and are feasible in non-planar geometries. In addition, various analytical results can be obtained, and the discrete solvent effects can be readily understood in terms of basic physical principles. In the present chapter we use the same formalism to study discrete solvent effects on interacting charged and planar plates.

In the present work, following Refs. [30–33] and chapter 2, we do not take into account an effective ion-surface potential. A numerical calculation of such a potential, using a realistic model for the water molecules, is currently not available. Moreover, we neglect the dependence of the effective ion-ion potentials on the ion positions relative to the surface. Other limitations of the current model are discussed in chapter 2. Despite these approximations, the model is a good starting point for studying qualitative effects of the discrete solvent.

The outline of the paper is as follows. Section 3.2 reviews the model and discusses its application to two charged and planar plates. In Sec. 3.3 we discuss the corrections to the PB density profile. In section 3.4 we obtain expressions for the inter-plate pressure and derive a generalized contact theorem. The resulting pressure curves are studied numerically and analytically in section 3.5. Finally, section 3.6 offers some concluding remarks. The technical details in the derivation of the pressure are presented in the Appendix.

3.2   The Model

3.2.1   Free energy

The free energy of the system can be written as a functional of the local ion densities, consisting of the usual PB term and a hydration correction term. Assuming that the boundary conditions are of fixed charges, the following approximated form for the free energy can be obtained (chapter 2):

$$
\begin{aligned}
\Omega \;=\; & \frac{\varepsilon}{8\pi}\int(\nabla\Psi)^2\mathrm{d}^3\mathbf{r} + k_BT\int\sum_i c_i\left(\ln\frac{c_i}{\zeta_i}-1\right)\mathrm{d}^3\mathbf{r} \\
& +\int\Lambda(\mathbf{r})\left(\nabla^2\Psi+\frac{4\pi}{\varepsilon}\sum_i c_ie_i\right)\mathrm{d}^3\mathbf{r} \\
& +\frac{k_BT}{2}\sum_{i,j}\int c_i(\mathbf{r})c_j(\mathbf{r}')U_{ij}(\mathbf{r}-\mathbf{r}')\,\mathrm{d}^3\mathbf{r}\mathrm{d}^3\mathbf{r}'
\end{aligned}
\tag{3.1}
$$

where Ψ is the electrostatic potential, c_i are the ion densities, e_i are their respective charges, ε is the dielectric constant, k_BT is the thermal energy and the potential U_{ij} is defined below. The bulk ion densities $c_{b,i}$ are determined by the fugacities $\zeta_i = \exp(\beta\mu_i)/\lambda_T^3$, where μ_i are the chemical potentials, λ_T is the de Broglie thermal wave length and $\beta = 1/k_BT$. Note that the simple PB relation $c_{b,i} = \zeta_i$ is altered with the inclusion of hydration interactions, as will be explained below (Sec. 3.2.2). A detailed discussion of the various approximations involved in Eq. (3.1) is given in chapter 2. Here we shall briefly discuss each of the terms, and outline the way in which Eq. (3.1) is obtained.

The first three terms in Eq. (3.1) form the usual PB expression for the free energy. The first term is the electrostatic free energy and the second term is the entropy of the ions. The electrostatic potential Ψ is a functional of the ion densities c_i, and is determined by the Poisson equation and the boundary conditions imposed by the surface charges. Instead of writing this dependence explicitly in the free energy, it is convenient to add a third term to Ω, containing a Lagrange multiplier $\Lambda(\mathbf{r})$.

The fourth term in Eq. (3.1) accounts for the hydration interaction, and is quadratic in the ion densities. The weighted potential U_{ij} is defined as:

$$
U_{ij} = 1 - \mathrm{e}^{-\beta u_{ij}(|\mathbf{r}-\mathbf{r}'|)}
\tag{3.2}
$$

where u_{ij} is the nominal short-range hydration interaction between ions of species i and j (Fig. 2.2). To obtain Eq. (3.1) we first treat the short-range interaction u_{ij} using a virial

expansion of the grand canonical potential, keeping terms up to the quadratic order. The electrostatic interaction is then treated exactly as in PB theory, using a mean field approximation for the electrostatic potential Ψ. As an alternative approach Eq. (3.1) can be obtained from a field theory expansion of the grand partition function [34].

3.2.2 Density equations

The density profiles are obtained by minimizing the free energy Ω with respect to the ion densities c_i. The third term in Eq. (3.1), containing the Lagrange multiplier $\Lambda(\mathbf{r})$ allows us to regard the densities $c_i(\mathbf{r})$ and the electrostatic potential $\Psi(\mathbf{r})$ as independent fields, and require that Ω has an extremum with respect to the three fields c_i, Ψ and Λ. Requiring that Ω has an extremum with respect to Ψ gives:

$$\Lambda = \frac{\varepsilon}{4\pi}\Psi \tag{3.3}$$

and the extremum condition with respect to c_i then gives:

$$\ln\frac{c_i(\mathbf{r})}{\zeta_i} + \sum_j \int c_j(\mathbf{r}')U_{ij}(\mathbf{r}-\mathbf{r}')\,\mathrm{d}^3\mathbf{r}' + \beta e_i\Psi(\mathbf{r}) = 0 \tag{3.4}$$

where relation (3.3) has been substituted to express Λ in terms of Ψ. This equation is supplemented by the Poisson equation:

$$\nabla^2\Psi = -\frac{4\pi}{\varepsilon}\sum_i e_i c_i \tag{3.5}$$

Since Eq. (3.4) is an integral equation, the c_i cannot be written as a simple function of Ψ. Therefore, a single equation for Ψ, analogous to the PB equation, cannot be obtained, and we are left with the two coupled equations (3.4) and (3.5). These equations should be solved together to obtain the electrostatic potential and density profiles. For $U \to 0$, Eq. (3.4) reduces to the Boltzmann equation $c_i = \zeta_i \exp(-\beta e_i\Psi)$. In the bulk $\Psi = 0$, leading to the relation $c_{b,i} = \zeta_i$. Combining these relations with Eq. (3.5) reproduces the PB equation:

$$\nabla^2\Psi = -\frac{4\pi}{\varepsilon}\sum_i c_{b,i}e_i\mathrm{e}^{-\beta e_i\Psi} \qquad \text{(PB)} \tag{3.6}$$

Equations (3.4) and (3.5) were solved for a single charged and planar plate in chapter 2. The treatment of two parallel plates is very similar, and is outlined below for completeness. The system is shown schematically in Fig. 3.1 (b). The plate positions are designated by $z = 0$ and $z = d$, using the convention that these are the coordinates of closest approach of the ions to the

plates (while the potentials $u_{ij}(r)$ are measured from the *centers* of the ions). The two plates are negatively charged, each one with a uniform surface charge σ. No discreteness of surface charge is taken into account in the present work. We assume an electrolyte of valency $z_+{:}z_-$, *i.e.*, a solution of positive and negative ions of charges $e_\pm = \pm z_\pm e$, where e is the electron charge.

In order to simplify the equations further, the interactions between the different pairs of ion species can be taken to be equal, *i.e.*, $U_{ij}(\mathbf{r}) = U_{++}(\mathbf{r}) \equiv U(\mathbf{r})$ where U_{++} is the weighted potential between the (positive) counterions. The exact choice of U_{+-} and U_{--} is expected to be of only minor significance, as the co-ions are repelled from the surface neighborhood and only the positive counterions reach high densities there. From charge neutrality we have $c_b \equiv c_{b,+} = (z_-/z_+)c_{b,-}$ and similarly $\zeta \equiv \zeta_+ = (z_-/z_+)\zeta_-$, where the relation between c_b and ζ will be determined later.

Due to the one-dimensional symmetry imposed by the charged and planar planes, the integration in Eq. (3.4) can be performed over the $x - y$ plane to obtain:

$$c_\pm(z) = \zeta_\pm e^{\mp\beta e z_\pm \Psi} \exp\left[-\int_0^d c(z')B(z-z')\,\mathrm{d}z'\right] \tag{3.7}$$

where $c = c_+ + c_-$ is the total ion density and $B(z)$ is the effective interaction between two layers of ions, expressed as an integral of $U(\mathbf{r})$ in the plane of constant z. Using cylindrical coordinates:

$$B(z) = 2\pi \int_0^\infty \rho\,\mathrm{d}\rho\, U(\sqrt{z^2 + \rho^2}) \tag{3.8}$$

The Poisson equation (3.5) reads:

$$\begin{aligned}
\frac{\mathrm{d}^2\Psi}{\mathrm{d}z^2} &= \frac{4\pi e}{\varepsilon}\zeta z_+ \left(e^{\beta e z_- \Psi} - e^{-\beta e z_+ \Psi}\right) \\
&\quad \times \exp\left[-\int_0^d c(z')B(z-z')\,\mathrm{d}z'\right]
\end{aligned} \tag{3.9}$$

Equations (3.7) and (3.9) are supplemented by the following boundary conditions:

$$\left.\frac{\mathrm{d}\Psi}{\mathrm{d}z}\right|_{z=0} = -\frac{4\pi}{\varepsilon}\sigma \ ; \ \left.\frac{\mathrm{d}\Psi}{\mathrm{d}z}\right|_{z=d/2} = 0 \tag{3.10}$$

since the problem with two plates of equal charge at $z = 0$ and $z = d$ is symmetric about the mid-plane $z = d/2$.

Finally, the relation between ζ and the bulk density c_b can be obtained from Eq. (3.7). We imagine that the two plates are immersed in a bath of electrolyte. In the region outside the plates an equation similar to Eq. (3.7) holds, where the integration inside the exponent is performed in the external region. Far away from the plates, as Ψ becomes zero, c_+ and c_- assume their asymptotic constant, bulk values. The integrand inside the exponential can be replaced by $-(1 + z_+/z_-)c_b B(z - z')$ leading to the result:

$$c_b = \zeta \exp\left[-\left(1 + \frac{z_+}{z_-}\right) B_t c_b\right] \tag{3.11}$$

where:

$$B_t \equiv \int_{-\infty}^{\infty} \mathrm{d}z\, B(z) = \int \mathrm{d}^3\mathbf{r}\, U(\mathbf{r}) \tag{3.12}$$

is also equal to $2B_2$, the second virial coefficient. The limit $B_t c_b \to 0$ is the limit in which the short-range interaction becomes negligible in the bulk. In this limit the relation between the bulk density and fugacity of Eq. (3.11) tends to the ideal gas relation $c_b = \zeta = \exp(\beta\mu)/\lambda_T^3$.

In the next section we will concentrate on a symmetric $1:1$ electrolyte, where the equations (3.7) and (3.9) take the form:

$$\begin{aligned}
c_\pm(z) &= \zeta \mathrm{e}^{\mp\beta e\Psi} \exp\left[-\int_0^d c(z')B(z - z')\,\mathrm{d}z'\right]\\
\frac{\mathrm{d}^2\Psi}{\mathrm{d}z^2} &= \frac{8\pi e}{\varepsilon}\zeta \sinh\left(\beta e\Psi\right)\\
&\quad\times \exp\left[-\int_0^d c(z')B(z - z')\,\mathrm{d}z'\right]
\end{aligned} \tag{3.13}$$

and:

$$c_b = \zeta \exp\left(-2B_t c_b\right) \tag{3.14}$$

3.2.3 Definitions and parameters

For the short-range ion-ion potential $u(\mathbf{r})$ we use the effective potential between Na^+ - Na^+ ion pairs, shown in Fig. 2.2. For ion-ion separations below 2.9Å a hard core interaction is assumed. Fig. 2.3 shows the effective layer-layer interaction $B(z)$, as was derived from this potential using Eq. (3.8). This effective interaction is mostly attractive, as $B(z)$ is negative on most of its range, and has a characteristic range of approximately 7 Å. The structure of $B(z)$ reflects the oscillatory behavior of $u(\mathbf{r})$.

It is useful to introduce the length scales characterizing the PB density profiles [7]. The *Gouy-Chapman length*, defined as $b = \varepsilon k_B T/(2\pi e|\sigma|)$, characterizes the width of the diffusive counterion layer close to a single charged plate with a surface charge density σ, in the absence of added salt. The *Debye-Hückel screening length*, $\lambda_{\mathrm{D}} = (8\pi c_b e^2/\varepsilon k_B T)^{-1/2}$, equal to $19.6\,\text{Å}$ for $c_b = 0.025\,\text{M}$ at room temperature characterizes the decay of the screened electrostatic interaction in a solution with added salt. The strength of the electrostatic interaction can also be expressed using the *Bjerrum length*, $l_{\mathrm{B}} = e^2/(\varepsilon k_B T)$. This is the distance at which the electrostatic interaction between two unit charges in a dielectric medium becomes equal to the thermal energy. It is equal to about 7Å in water at room temperature. In terms of the Bjerrum length $b = e/2\pi l_B|\sigma|$ and $\lambda_D = (8\pi c_b l_B)^{-1/2}$.

The inclusion of the hydration interaction introduces additional length scales in the system. For the interaction of Figs. 2.2 and 2.3, the range of the interaction d_{hyd} is approximately 7Å, over twice the hard core diameter $d_{\mathrm{hc}} = 2.9\text{Å}$. The strength of the hydration interaction is characterized by the second virial coefficient $B_t/2$, with $B_t \simeq -(7.9\text{Å})^3$ as is calculated from Eq. (3.12).

3.3   Density profiles

Equations (3.7) and (3.9) are a set of three nonlinear integrodifferential equations. We treat them numerically using an iterative scheme, based on the assumption that the positive ion density profile is dominated by the electrostatic interaction. We start with the PB profile and calculate iteratively corrections to this profile, as result from Eqs. (3.7) and (3.9). For a 1:1 electrolyte we iteratively solve the equation:

$$
\begin{aligned}
\frac{\mathrm{d}^2\Psi^{(n)}}{\mathrm{d}z^2} &= \frac{8\pi e}{\varepsilon}\zeta\sinh\left(\beta e\Psi^{(n)}\right) \\
&\quad \times \exp\left[-\int_0^d c^{(n-1)}(z')B(z-z')\,\mathrm{d}z'\right]
\end{aligned}
\tag{3.15}
$$

where the superscript n stands for the nth iteration,

$$
\begin{aligned}
c_{\pm}^{(n)}(z) &\equiv \zeta e^{\mp\beta e\Psi^{(n)}} \\
&\quad \times \exp\left[-\int_0^d c^{(n-1)}(z')B(z-z')\,\mathrm{d}z'\right]
\end{aligned}
\tag{3.16}
$$

and the zeroth order densities $c_{\pm}^{(0)}$ are taken as the density profiles generated by the PB equation (3.6). The boundary conditions (3.10) are satisfied by the electrostatic potential in all iterations.
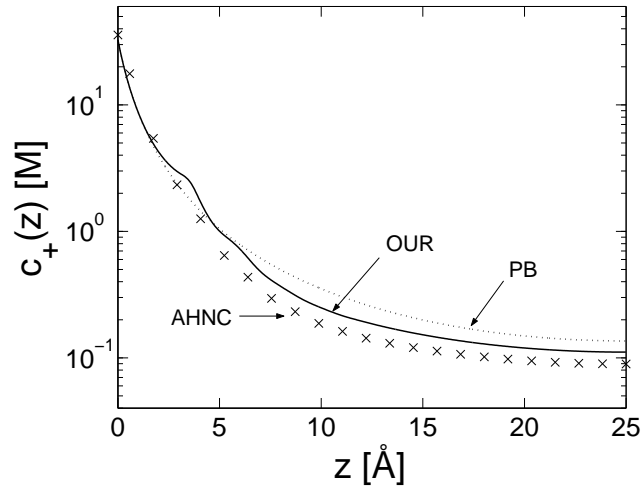
Figure 3.2: Counterion density profile (solid line) obtained from numerical solution of Eq. 3.7 with the hydration interaction as of Fig. 2.3, plotted on a semi-log plot. The bulk ion density is $c_b = 0.025M$ and the surface charge is $|\sigma| = 0.333 C/m^2 \simeq 1\,e/48\,Å^2$ The dielectric constant is $\varepsilon = 78$ and the temperature is 298K. The distance between the plates is $d = 50Å$. The density profile is symmetric about the mid-plane at $z = 25\,Å$. The dotted line shows the corresponding density profile obtained from the PB equation. The symbols ('x') show the density profile obtained in the AHNC approximation, using the same parameters [35].

The solution converges after several iterations. It is interesting to note that the first iteration captures most of the effect. This observation can lead to various analytical results, as shown in chapter 2 for a single plate.

In the following sections we will concentrate on the pressure between the plates. First we discuss briefly the modification to the PB density profiles. Let us begin by considering a large plate separation d. In this case the results are similar to the single-plate case, since d is larger than all other length scales in the system, and we present them for completeness.

Fig. 3.2 shows the density profile of the positively charged counterions (solid line) between two charged plates, with $d = 50\,Å$. Only one half of the system is shown, since the profile is symmetric around the mid-plane. The surface charge, $|\sigma| = 0.333 C/m^2$ corresponds to approximately $48Å^2$ per unit charge. This is a typical high surface charge obtained for mica plates. It corresponds to a Gouy-Chapman length $b = 1.06Å$, at a temperature of 298K, with $\varepsilon = 78$. The electrolyte bulk concentration is 0.025M, corresponding to a Debye-Hückel screening length $\lambda_D = 19.58Å$. The density profile is compared to the result of PB theory (dotted line).

The main effect is that the short-range attraction draws additional counterions to the vicinity
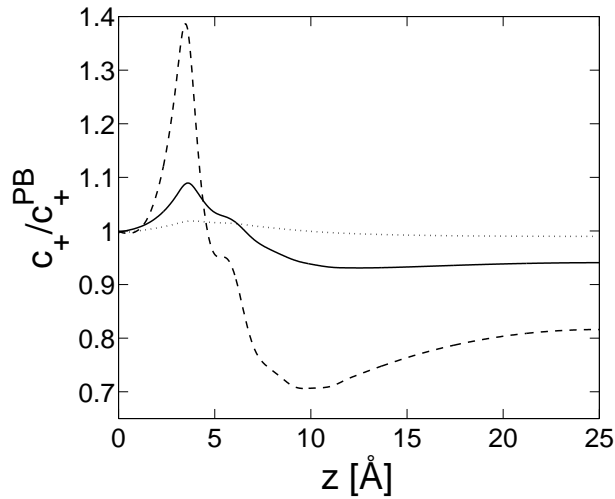
Figure 3.3: The ratio of the positive ion density obtained from Eq. (3.7) and the value obtained from PB theory, for surface charges $|\sigma| = 0.333\text{C/m}^2 \simeq 1\,e/48\,\text{Å}^2$ (dashed line), $0.1\text{C/m}^2 \simeq 1\,e/144\,\text{Å}^2$ (solid line) and $0.0333\text{C/m}^2 \simeq 1\,e/480\,\text{Å}^2$ (dotted line). All other parameters are as in Fig. 3.2.

of the charged plate. Note, however, that the contact density remains very close to the PB density, as will be explained later. The increase of the counterion density near the plate is followed by a depletion further away. This can be understood in the no-salt case since the total number of counterions is fixed. In our case the salt concentration is low. The Debye-Hückel screening length is large compared to the Gouy-Chapman length and compared to the range of the short-range interaction, so the salt has a minor effect.

The counterion density profile is also compared with results of the AHNC approximation [35] that were obtained using the same short-range hydration potential ('x' symbols). The qualitative effect is similar in our model and in the AHNC. Specifically, both density profiles follow the PB density curve for the first few Ångströms from the plate and show a considerable decrease in the positive ion density, relative to PB, starting at a distance of about $5\,\text{Å}$ from the plate. The maximal decrease in the density is approximately 30% in our model and almost 50% in the AHNC profile, both relative to the PB profile.

The effect of the short-range ion-ion interaction strongly depends on the surface charge. This is demonstrated in Fig. 3.3. The ratio of the counterion density and its PB value, c/c^{PB}, is shown for three values of σ. The effect of the hydration potential is very minor for small surface charge ($|\sigma| = 0.0333\,\text{C/m}^2 \simeq 1\,e/480\,\text{Å}^2$), where the ratio c/c^{PB} is approximately 2% at its maximum, and considerable for a surface charge of $0.333\,\text{C/m}^2 = 1\,e/48\,\text{Å}^2$, where it reaches approximately 40%.
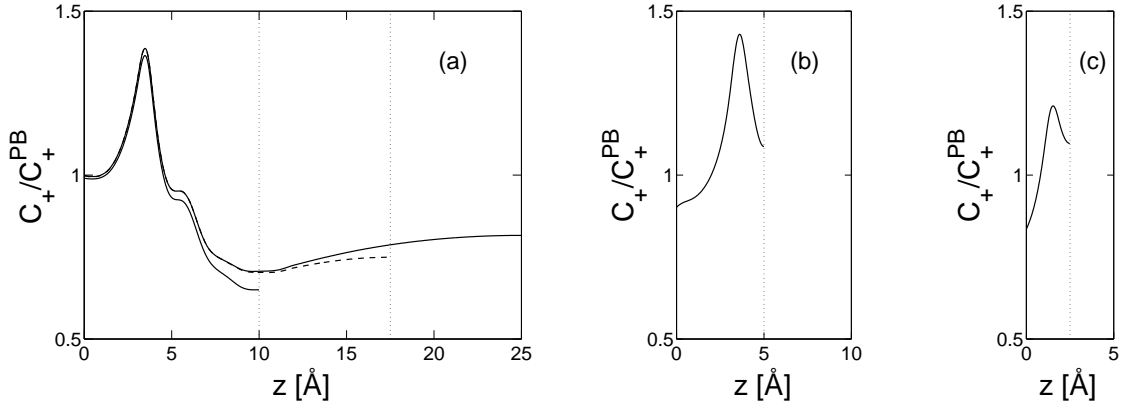
Figure 3.4: The ratio between the positive ion density obtained from Eq. (3.7) and its PB value, for plate separations d equal to (a) $50\,\text{Å}$ (solid line), $35\,\text{Å}$ (dashed line), $20\,\text{Å}$ (solid line), (b) $10\,\text{Å}$ and (c) $5\,\text{Å}$. All other parameters are as in Fig. 3.2. Each curve is shown between the plate at $z = 0$ and the mid-plane $z = d/2$.

As the plate separation decreases, the modification to c^{PB} is expected to remain similar to the single plate case as long as $d/2$ is large compared to b and to d_{hyd}. This can indeed be seen in Fig. 3.4, where a high surface charge, as in Fig. 3.2, is considered. In this case $b \simeq 1\,\text{Å} \ll d_{\text{hyd}} \simeq 7\,\text{Å}$, so a deviation from the single plate curve is expected when $d/2 \lesssim d_{\text{hyd}} \simeq 7\,\text{Å}$. The ratio c/c_{PB} is shown for several plate separations between 5 and $50\,\text{Å}$. The results are very similar for $d = 50, 35$ and $20\,\text{Å}$ (Fig. 3.4 (a)). In particular, note that the contact density remains very close to the PB value in all three separations. This is a result of the generalized contact theorem, derived in section 3.4. For smaller d, equal to 5 and $10\,\text{Å}$ (Figures 3.4 (b) and (c), respectively) the behavior is different, and in particular the contact density deviates from the PB value. The effect of decreasing d was found to be similar for smaller surface charge (*e.g.*, $0.1\,\text{C/m}^2$,) and for salt concentration up to $0.1\,\text{M}$.

The most important effect on the density profile is that the ion density is depleted far away from the charged plates. When the two plates are highly separated from each other the ion density can be described, far away from the plates, using an effective PB surface charge. This effective charge was calculated in chapter 2, and is smaller than the nominal charge (for example, for the surface charge used in Fig. 3.2 it is smaller by a factor of ~ 3.8). The reduced density leads to a reduced pressure, relative to PB, as will be explained in the following sections.

3.4   Pressure equation and contact theorem

The pressure P_{in} in the region between the two plates can be obtained by differentiating the free energy Ω with respect to the plate separation d:

$$P_{\text{in}} = -\frac{\delta\Omega}{\delta d} \tag{3.17}$$

To compute $\delta\Omega$ we can imagine that a 'slice' of width δd is inserted at some position z_0 between the two plates. Adding up all the contributions to $\delta\Omega$, and using Eq. (3.7) and the boundary conditions (3.10) we obtain:

$$\begin{aligned}
P_{\text{in}} = k_B T \sum_i c_i(z_0) - \frac{\varepsilon}{8\pi} \left(\frac{d\Psi}{dz}\right)^2 \bigg|_{z_0} \\
- k_B T \sum_{ij} \int_0^{z_0} dz \int_{z_0}^d dz' \, c_i(z) c_j(z') \frac{dB}{dz}(z'-z)
\end{aligned} \tag{3.18}$$

This result is correct for any combination of ion species i, assuming the same short-range interaction u_{ij} between different ion pairs. The full derivation is given in the Appendix. The pressure is equal throughout the plate spacing and, therefore, independent on the choice of z_0.

The net pressure P between the plates is the difference between the pressure inside and outside the plates. The latter is equal throughout the region outside the plates. In particular, it is equal to the bulk pressure P_{bulk}, so we have:

$$P = P_{\text{in}} - P_{\text{bulk}} \tag{3.19}$$

To obtain P_{bulk}, we note that an equation similar to Eq. (3.18) holds in the bulk, with constant electrostatic potential and with c_i constant and being equal to the bulk densities. For the case of a 1:1 electrolyte, we find:

$$P_{\text{bulk}} = 2k_B T c_b \left(1 + B_t c_b\right) \tag{3.20}$$

Since B_t is negative the bulk pressure is lower than its PB value. Note that in the case of no added salt $P_{\text{bulk}} = 0$.

The expression (3.18) assumes a particularly simple form if we set z_0 to zero, namely on one of the plates. Then the third term in (3.18) vanishes and the second term is fixed by the boundary conditions, giving:

$$P = k_B T \sum_i c_i(0) - \frac{2\pi}{\varepsilon}\sigma^2 - P_{\text{bulk}} \tag{3.21}$$

Alternatively, if we choose z_0 at the mid-plane, $z = d/2$, by symmetry the second term in (3.18) vanishes and the pressure is expressed as:

$$
\begin{aligned}
P &= k_B T \sum_i c_i(d/2) \\
&- k_B T \sum_{ij} \int_0^{d/2} dz \int_{d/2}^d dz'\, c_i(z)c_j(z') \frac{dB}{dz}(z'-z) \\
&- P_{\text{bulk}}
\end{aligned}
\tag{3.22}
$$

The equality of these two expressions for the pressure results in the generalized contact theorem [2, 36]:

$$
\begin{aligned}
\sum_i c_i(0) &= \frac{2\pi\beta}{\varepsilon}\sigma^2 + \sum_i c_i(d/2) \\
&- \sum_{ij} \int_0^{d/2} dz \int_{d/2}^d dz'\, c_i(z)c_j(z') \frac{dB}{dz}(z'-z)
\end{aligned}
\tag{3.23}
$$

The very small relative change of the contact density, compared to PB theory, at large plate separations can be understood from this result. We consider first the case of high surface charge, where the Gouy-Chapman length is small compared to the Debye-Hückel screening length, $b \ll \lambda_D$. In this case the second and third terms on the right hand side of Eq. (3.23) become negligible compared to the first term when $d \gg b, d_{\text{hyd}}$, where d_{hyd} is the range of the hydration interaction. The contact ion density is then dominated by the positive ion density, and is very close to the PB value. When there are only counterions in the solution and $d \to \infty$ (or equivalently, in the case of one isolated plate), we have exactly, as in PB theory :

$$c_+(0) = \frac{2\pi\beta}{\varepsilon}\sigma^2 \qquad \text{(one plate, no salt)} \tag{3.24}$$

If b is not small compared to λ_D, the correction to the contact density is still small for large enough plate separations, assuming that the hydration interaction is negligible in the bulk, *i.e.* $-B_t c_b = -B_t/(8\pi l_B \lambda_D^2) \ll 1$. When $d \gg \lambda_D$ and $d > d_{\text{hyd}}$, the coupling between the two plates is negligible and Eq. (3.23) becomes:

$$\sum_i c_i(0) \simeq \frac{2\pi\beta}{\varepsilon}\sigma^2 + P_{\text{bulk}} \tag{3.25}$$

The only difference in this expression relative to the PB contact density is the change in the bulk pressure. This change is negligible if the hydration interaction is small enough in the bulk.

For smaller d, the integral in (3.23) can contribute to a significant change in the contact density relative to PB theory. This can be seen in Fig. 3.4, where $b \ll \lambda_{\mathrm{D}}$, at plate separations below $\sim 10\,\text{Å}$.

3.5   Pressure curves

3.5.1   Pressure beyond Poisson-Boltzmann

We would like to compare the pressure from our model with the PB pressure, which can be written as follows:

$$P_{\mathrm{PB}} = k_B T \sum_i \left[c_{\mathrm{PB},i}(d/2) - c_{b,i} \right] \tag{3.26}$$

where $c_{\mathrm{PB},i}(d/2)$ is the PB density of the ith ion species at the mid-plane. Using equations (3.22) and (3.20) the pressure in our model can be written as the sum of the following three terms:

$$
\begin{aligned}
P &= P_m + P_{\mathrm{hyd}} - 2k_B T B_t c_b \\
&= k_B T \sum_i \left[c_i(d/2) - c_{b,i} \right] \\
&\quad - k_B T \sum_{ij} \int_0^{d/2} \mathrm{d}z \int_{d/2}^d \mathrm{d}z'\, c_i(z) c_j(z') \frac{\mathrm{d}B}{\mathrm{d}z}(z'-z) \\
&\quad - 2k_B T B_t c_b^2
\end{aligned}
\tag{3.27}
$$

A symmetric 1:1 electrolyte is assumed for simplicity throughout this section. The first term in Eq. (3.27),

$$P_m = k_B T \sum_i \left[c_i(d/2) - c_{b,i} \right] \tag{3.28}$$

is similar in form to the PB pressure (3.26), but the mid-plane density in equations (3.28) and (3.26) can be different. The second term in Eq. (3.27), which we denote as the hydration pressure:

$$P_{\mathrm{hyd}} = -k_B T \sum_{ij} \int_0^{d/2} \mathrm{d}z \int_{d/2}^d \mathrm{d}z'\, c_i(z) c_j(z') \frac{\mathrm{d}B}{\mathrm{d}z}(z'-z) \tag{3.29}$$
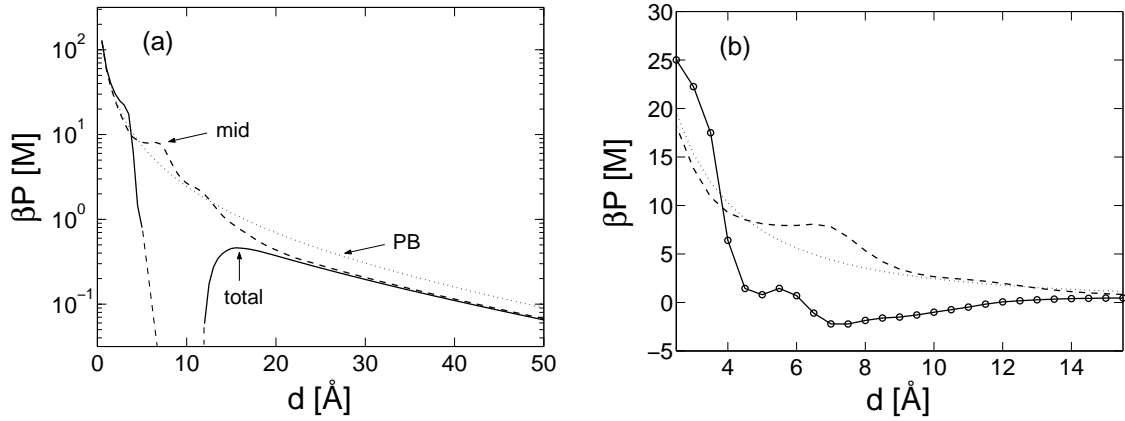
Figure 3.5: (a) Pressure between two plates with surface charge $|\sigma| = 0.333\,\mathrm{C/m^2} \simeq 1\,e/48\,\text{Å}^2$, as a function of the plate separation d, on a semi-log plot. All the parameters are as in Fig. 3.2. The solid line shows the overall pressure P obtained from Eq. (3.22). The dashed line shows the contribution P_m resulting from the mid-plane density and the dotted line shows the PB pressure. (b) The same curves on a linear scale, in the region where the overall pressure becomes negative, *i.e.*, attractive.

is the integrated short-range force acting between ion pairs in the two halves of the system. The third term is the change in the bulk pressure relative to PB theory, due to the inclusion of a 2nd virial coefficient in the bulk equation of state.

Some simple observations can be made immediately from Eq. (3.27). These observations will be useful in the next subsection, where the numerically calculated pressure curves are presented (Figs. 3.5 and 3.6). For now let us assume that the third term in Eq. (3.27) is negligible as compared to the first two. Of these two terms, the first, P_m, is linear in the density whereas the second term, P_{hyd}, is quadratic. As a result, the relative importance of P_m and P_{hyd} depends on the plate separation d. At large d the density in the mid-plane region is small, so that $P_{\mathrm{hyd}} \ll P_m$. The main correction to the PB pressure (3.26) then comes from the change of the mid-plane density, $c(d/2) - c_{\mathrm{PB}}(d/2)$. Far away from the two plates the system behaves as predicted by PB theory with a modified, effective surface charge. The mid-plane density is depleted relative to PB, since counterions are attracted to the vicinity of the charged plates. Hence the pressure is smaller than in PB theory. As the plate separation decreases and the mid-plane density increases, P_{hyd} can become important.

3.5.2 Numerical results

The general arguments of the previous section can be verified by calculating numerically the pressure using Eq. (3.27). Fig. 3.5 shows the pressure as a function of the plate separation d for
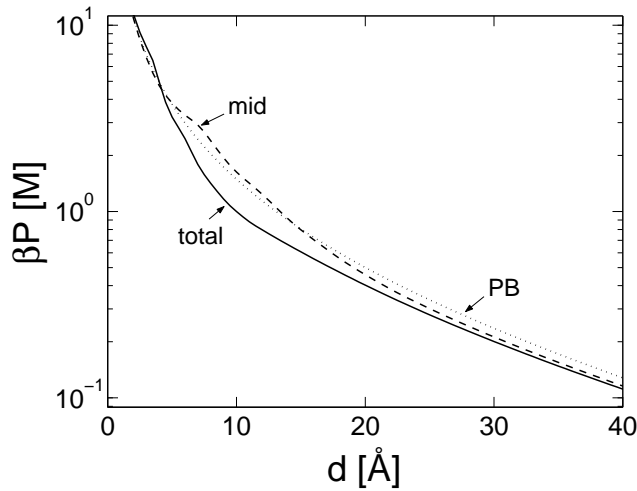
Figure 3.6: The repulsive pressure between two plates with surface charge $|\sigma| = 0.119\,\mathrm{C/m^2} \simeq 1\,e/135\,\text{Å}^2$, as a function of the plate separation d. All other parameters are as in Fig. 3.2. The solid line shows the overall pressure P, the dashed line shows the contribution P_m of the mid-plane density, and the dotted line shows the results of PB theory.

a large surface charge $|\sigma| = 0.333\,\mathrm{C/m^2} \simeq 1\,e/48\,\text{Å}^2$ and bulk ion density $c_b = 0.025$M (solid line). The pressure is compared with P_{PB} (dotted line). The contribution of P_m, the first term in Eq. (3.27), is also shown (dashed line).

The behavior of the pressure at a large range of plate separations is shown in Fig. 3.5 (a) on a semi-logarithmic plot. At large d, the pressure is dominated by P_m, as expected. It is considerably smaller than the PB pressure, due to the reduced effective charge on the plates. At lower d the second term in Eq. (3.27), P_{hyd}, becomes dominant, and the overall interaction is attractive at plate separations between 6 and 12 Å. Note that the apparent sharp decrease in the pressure at a separation of approximately 13Å is artificial, and results from the divergence of the logarithmic scale as the pressure approaches zero. Fig. 3.5 (b) shows the same pressure using a linear scale, in the region in which it becomes negative (attractive). The net pressure crosses smoothly from positive to negative values due to a steady increase in the magnitude of the (negative) P_{hyd}. At very short separations P_m dominates again, and the pressure coincides with the predictions of PB theory.

Fig. 3.6 shows the effect of the hydration potential for a smaller surface charge, $|\sigma| = 0.119\mathrm{C/m^2} \simeq 1\,e/135\,\text{Å}^2$. In this case and for all surface charge, $|\sigma| \lesssim 0.25\,\mathrm{C/m^2}$, the pressure is repulsive at all plate separations. The correction over the PB result is much smaller than in Fig. 3.5, but still significant. At plate separations of approximately 5 to 20Å P_{hyd} is the dominant contribution to the deviation from PB, and results in a considerably reduced pressure.
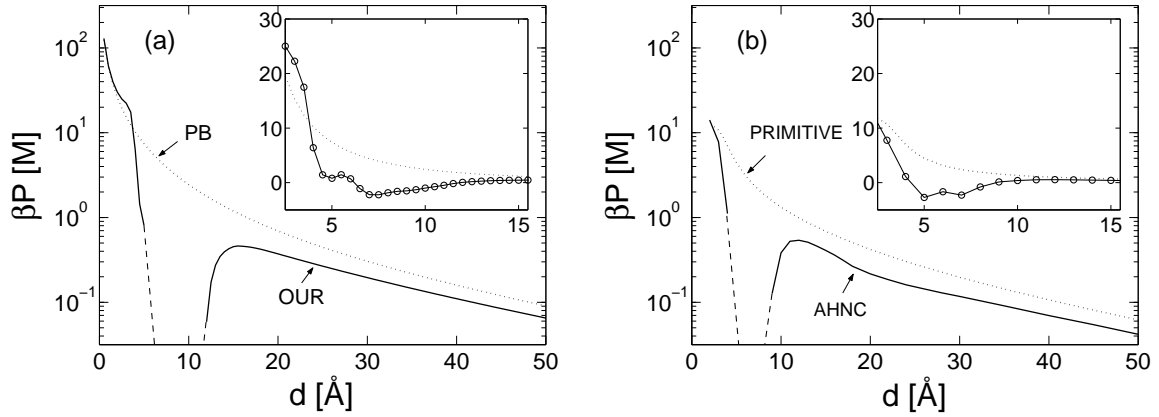
Figure 3.7: Comparison between the pressure obtained (a) in our model and (b) in the AHNC approximation [35], using the same short-range hydration potential (solid lines). All the parameters are as in Fig. 3.5 ($|\sigma| = 0.333\,\mathrm{C/m}^2 \simeq 1\,e/48\,\mathrm{Å}^2$). The pressure is shown as a function of the plate separation d. A semi-logarithmic scale is used in the main plots and a linear scale is used in the insets. In (a) the dotted line shows the PB pressure. In (b) the dotted line shows the pressure obtained in the AHNC approximation when the ion-ion interaction includes only the hard core and the electrostatic interactions.

At larger d the pressure is reduced mainly because of the change in the mid-plane density.

3.5.3 Comparison with AHNC

Fig. 3.7 shows a side by side comparison of the pressure obtained in our model (a) and in the AHNC approximation (b).[2] The same surface charge $|\sigma| = 0.333\,\mathrm{C/m}^2 \simeq 1\,e/48\,\mathrm{Å}^2$ and short-range hydration potential are used in the two calculations. The main plots show the pressure using a logarithmic scale. The insets show the pressure on a linear scale in the region where it becomes attractive. The full pressure (solid line) is compared in Fig. 3.7 (a) with the PB pressure (dotted line). In Fig 3.7 (b) the AHNC pressure (solid line) is compared with the pressure obtained using an electrostatic and hard core interaction only (dotted line). Since the AHNC approximation accounts for ion-ion correlations, there are differences between the pressure curves in our model as compared to the AHNC approximation. However a comparison of Figs. 3.7 (a) and (b) shows that very similar qualitative and even semi-quantitative effects of the hydration interaction are found in the two calculations.

A comparison for smaller $|\sigma| = 0.119\mathrm{C/m}^2 \simeq 1\,e/135\,\mathrm{Å}^2$ is shown in Fig. 3.8. The solid line is the pressure in our model and the dashed line is the AHNC pressure. The dotted line shows

---

[2]In Refs. [29–31] there was an error in the inclusion of the hydration pressure, making it much smaller than its real value. The corrected data, kindly provided to us by S. Marčelja, is used in the comparison of the present work with the AHNC results. See also similar data presented in Ref. 31.
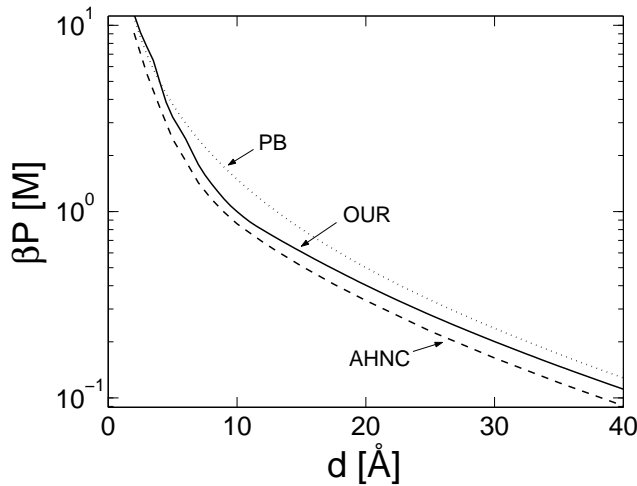
Figure 3.8: Comparison between the pressure obtained in our model (solid line) and the AHNC approximation (dashed line), for a surface charge $|\sigma| = 0.119\,\mathrm{C/m^2} \simeq 1\,e/135\,\mathrm{\mathring{A}}^2$. All the parameters are as in Fig. 3.6. The pressure is shown as a function of the inter-plate separation d using a semi-logarithmic plot. The dotted line shows the PB pressure.

the PB pressure. As in Fig. 3.7, the qualitative effect is similar in the two calculations.

Since the AHNC approximation takes into account ion-ion correlations, the comparison allows us to assess the relative importance of correlations and discrete solvent effects. The results shown in Figs. 3.5 and 3.7 indicate that for large σ discrete solvent effects can be much larger than correlation effects induced by the electrostatic interaction. For smaller surface charge, as in Figs. 3.6 and 3.8, these effects are of similar order of magnitude. In the AHNC approximation the pressure includes an electrostatic term due to correlations between ions in the two halves of the system, in addition to the hydration and mid-plane density contributions. In Fig. 3.8 this term is of similar order of magnitude as P_{hyd}, and is the main source for the difference between the solid line (our model) and dashed line (AHNC). For larger surface charge, as in Fig. 3.7, P_{hyd} becomes much larger than the electrostatic contribution.

3.5.4   Further analysis

Large plate separations

As discussed above, the hydration term becomes small at large d, compared to the change in the mid-plane density. In order to study the contribution of the mid-plane density to the pressure, let us assume that the plate separation d is much larger than all other length scales in the system: $b, d_{\mathrm{hyd}}, \lambda_D$. The two plates are then decoupled and the mid-plane potential can be written as $\Psi(d/2) \simeq 2\Psi_1(d/2)$ where $\Psi_1(d/2)$ is the electrostatic potential at a distance $d/2$

from a *single* plate. We assume also that $\lambda_D \gg b$, which is usually the case when the surface charge density is large. At a large distance from the plate the single plate profile is a PB profile, corresponding to a renormalized surface charge σ_{eff} (chapter 2). The contribution P_m to the pressure can then be written as follows [7]:

$$P_{\text{m}} \simeq \frac{8k_BT}{\pi l_B \lambda_D^2} \left(1 - \frac{2b_{\text{eff}}}{\lambda_D}\right) e^{-d/\lambda_D} \tag{3.30}$$

where $b_{\text{eff}} = 1/2\pi l_B|\sigma_{\text{eff}}|$ is the effective Gouy-Chapman length. A similar expression holds for the PB pressure, with the nominal Gouy-Chapman length b used instead of b_{eff}. We thus find that:

$$\frac{P_m}{P_{\text{PB}}} \simeq \frac{1 - 2b_{\text{eff}}/\lambda_D}{1 - 2b/\lambda_D} \simeq 1 - 2\frac{b_{\text{eff}} - b}{\lambda_D} \tag{3.31}$$

In chapter 2 an analytical expression for $b_{\text{eff}} - b$ is found. Its general behavior is:

$$b_{\text{eff}} - b \sim -\frac{B_t}{l_B b} \tag{3.32}$$

with a numerical prefactor of $1/12\pi$ in the limit $b \ll d_{\text{hyd}}$ and a numerical prefactor $1/4\pi$ in the limit $b \gg d_{\text{hyd}}$. The parameters of the hydration interaction $d_{\text{hyd}} \simeq 7\,\text{Å}$ and $B_t \simeq -500\,\text{Å}^3$ are as defined in Sec. 3.2.3.

A careful treatment of Eq. (3.27) shows that the second and third terms also add a contribution to the pressure that should be regarded as linear in the density, although this contribution is small. For large enough d the integration range in the second term of Eq. (3.27) can be extended to be between $-\infty$ and $+\infty$ because dB/dz has a finite range. In addition all quantities can be replaced by their mid-plane values. We then find that the second term (P_{hyd}) and third term of Eq. (3.27) give:

$$\begin{aligned}
P_{\text{hyd}} &- 2k_BTB_tc_b^2 \\
&\simeq \frac{1}{2}k_BTB_t \sum_{ij}[c_i(d/2) - c_b][c_j(d/2) - c_b] \\
&+ 2k_BTB_tc_b \sum_i[c_i(d/2) - c_b]
\end{aligned} \tag{3.33}$$

The first term is quadratic in $[c_i(d/2) - c_b]$ and can be neglected relative to P_m at large d. The second term is linear, although small because $B_tc_b \ll 1$. It accounts for the small difference between the dashed and solid lines at large d in Fig. 3.5 (a).
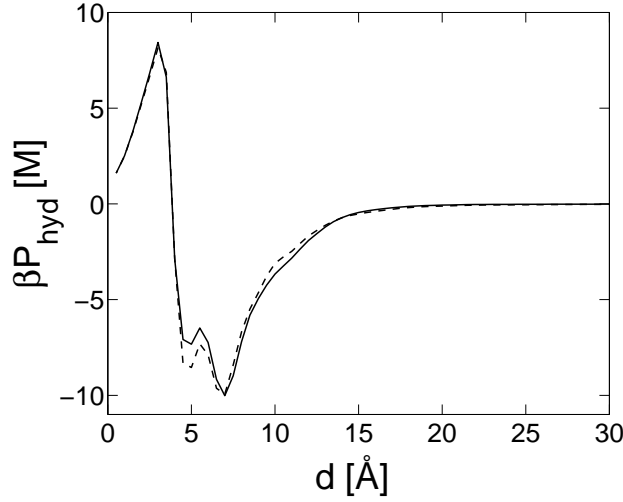
Figure 3.9: The hydration pressure P_{hyd} as a function of the plate separation d (solid line). All the parameters are as in Fig. 3.2. The dashed line shows the approximation to P_{hyd} obtained by replacing the ion density in the integral of Eq. (3.29) by the PB ion density.

Hydration pressure

The behavior of P_{hyd}, the hydration pressure term, can be understood as follows. As a zero-th order approximation, the ion density is dominated by electrostatics and can be replaced in Eq. (3.29) by its PB value. Fig. 3.9 shows that this gives a very good approximation. Hence we can write:

$$P_{\mathrm{hyd}} \simeq \sum_{ij} \int_0^{d/2} \mathrm{d}z \int_{d/2}^d \mathrm{d}z' \, c_{\mathrm{PB},i}(z) F(z'-z) c_{\mathrm{PB},j}(z') \tag{3.34}$$

where

$$F(z) \equiv -k_B T \frac{\mathrm{d}B(z)}{\mathrm{d}z} \tag{3.35}$$

represents the force between two planar ion layers separated by a distance z. The following behavior of $F(z)$ can be inferred from Fig. 2.3. At inter-layer separations $z < d_{\mathrm{hc}} = 2.9\,\text{Å}$ $F(z)$ is positive (repulsive). At larger z the value of $B(z)$ increases from its large negative value at $z = d_{\mathrm{hc}}$ to zero over a few Angströms, leading to a strongly attractive (negative) $F(z)$. A closer inspection of Fig. 2.3 shows that $F(z)$ is oscillatory, due to the local maxima and minima of $B(z)$. As we shall see below these fine details are smoothed away when two diffusive layers of finite thickness interact.

The behavior of P_{hyd} in Fig. 3.9 can now be understood as follows. Most of the counterions

are concentrated near the two plates, in layers whose thickness is of order $b = 1.06\,\text{Å}$. Note that b is small compared to $d_{\text{hyd}} \simeq 7\,\text{Å}$. When $d > d_{\text{hyd}}$ these two layers do not interact directly with each other through the short-range interaction. Ions in the two sides of the mid-plane interact with each other, leading to a negative (attractive) P_{hyd}. As d is decreased towards d_{hyd}, larger and larger ion densities come into contact through $F(z)$ and the magnitude of the negative P_{hyd} increases accordingly. The gradual increase in the magnitude of P_{hyd} reflects the algebraic decay of the density profile near each layer. When d decreases below $\sim 2d_{\text{hyd}} \simeq 14\,\text{Å}$, the magnitude of P_{hyd} increases more rapidly, as the ions in the two layers interact with ions in the mid-plane region.

The behavior of P_{hyd} changes when d decreases below d_{hyd}. Most of the contribution to P_{hyd} now comes from the interaction between the dense counterion layers near the two plates. As d decreases these layers are separated by correspondingly decreasing distances. The hydration pressure follows roughly the structure of $F(z)$. It is strongly attractive for $d \gtrsim d_{\text{hc}}$ and repulsive for $d < d_{\text{hc}}$. The fine details of $F(z)$ are smoothed due to the thickness of the diffusive ion layers.

As the plate separation decreases below d_{hc} towards contact P_{hyd} tends to zero, as it should since $F(0) = -k_B T \left. \frac{\mathrm{d}B}{\mathrm{d}z} \right|_{z=0} = 0$. One implication of this result is that P_m returns to be the dominant contribution to the pressure, even for high surface charges. Another implication is that the short-range interaction becomes unimportant. As in PB theory, the ions in the region between the two plates become essentially a confined ideal gas, and their total number is determined by charge neutrality. Thus P_m coincides with the PB pressure matching the *nominal* surface charge density σ. This is seen clearly in Fig. 3.5.

Small plate separations

In experiments the actual surface charge is usually not exactly known, because the number of ions dissociating from the surface is uncontrolled. The PB charge is then fitted to the large separation behavior. This charge can be significantly smaller than the actual surface charge, as discussed above. The interpretation of our results is then as follows. At plate separations below approximately $20\,\text{Å}$, an attractive force appears, due to P_{hyd}. This force can reduce the net repulsion, or even induce a net attraction, depending on the surface charge on the plates. As the plate separation decreases below the range of the hydration interaction $d_{\text{hyd}} \simeq 7\,\text{Å}$, P_{hyd} decreases and eventually tends to zero. The pressure then coincides with the PB pressure matching the *nominal* surface charge. As was pointed out in Ref. [29] this leads to an apparent strong repulsive force when compared with the PB curve fitted to the large separation behavior.
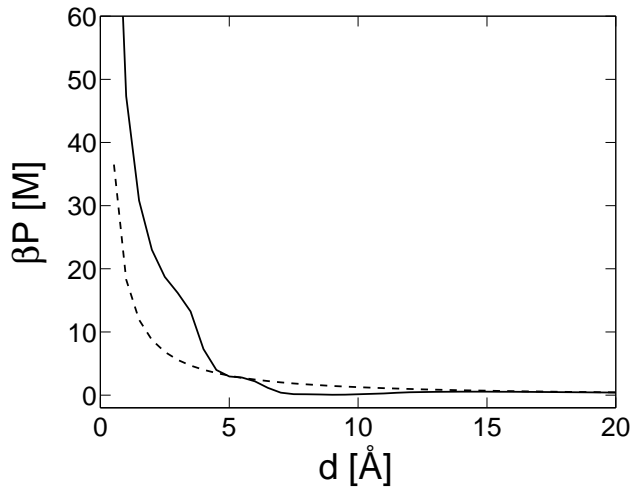
Figure 3.10: The total (repulsive) pressure between two plates with surface charge $|\sigma| = 0.25\,\mathrm{C/m^2} \simeq 1\,e/64\,\mathrm{\AA}^2$, as a function of the plate separation d, using a linear plot (solid line). All other parameters are as in Fig. 3.2. The pressure is compared with the PB pressure curve fitted to the large separation behavior, with $|\sigma_{\mathrm{eff}}| \simeq 0.09\,\mathrm{C/m^2} \simeq 1\,e/180\,\mathrm{\AA}^2$ (dashed line).

As an example, the pressure corresponding to $\sigma = 0.25\,\mathrm{C/m^2} \simeq 1\,e/64\,\mathrm{\AA}^2$ is shown in Fig. 3.10 as a function of d (solid line) using a linear scale. The dashed line shows the PB pressure curve using an effective surface charge chosen to match the large d behavior of the solid line. When the two lines are compared a strong (apparent) repulsive contribution is seen in the solid line below $d \simeq 5\,\mathrm{\AA}$, and an attractive contribution is seen for $5\,\mathrm{\AA} \lesssim d \lesssim 15\,\mathrm{\AA}$.

Divalent ions

When divalent ions are present in the solution, correlation effects become much larger than in the monovalent case [19, 20] and can lead in some cases to attraction between the plates. Discrete solvent effects are also modified, since the effective short-range interaction mediated by the solvent is different in the two cases. A numerical calculation of these potentials is currently not available, but some general observations can be made.

When the charge on the ions is doubled, the electrostatic interaction between two ions increases by a factor of 4. The ion-ion separation where the electrostatic interaction is equal to $k_B T$ increases from $l_B \simeq 7\,\mathrm{\AA}$ to almost $30\,\mathrm{\AA}$. On this electrostatic scale, the water molecular size ($\sim 3\,\mathrm{\AA}$) is much smaller than in the monovalent case. Hence we can expect the solvent to be more similar to a continuous dielectric medium. Indeed, the correction to the $1/\varepsilon r$ potential between two (artificial) $\mathrm{Na^{2+}}$ ions in water [37] is found to be purely repulsive, and is significant only at separations below $\sim 10\,\mathrm{\AA}$, where the electrostatic interaction is considerably larger than

k_BT. Thus we expect discrete solvent effects, resulting from effective ion-ion potentials, to reduce in the divalent case, whereas correlation effects, which are not included in our model, increase.

Let us now comment on the effective ion-surface potential, which is not taken into account in the present work. The distance from the charged plate, where the electrostatic ion-surface interaction is equal to $k_\mathrm{B}T$, decreases from b in the monovalent case to $b/2$ in the divalent case. On this smaller scale the discreteness of the solvent becomes more pronounced. Hence we expect the importance of the effective ion-surface potential to increase in the divalent case, as opposed to that of the effective ion-ion potential. This effect lies outside the scope of the present work and merits a separate study.

3.6 Concluding remarks

Summarizing our results on the pressure, we find that hydration effects can be understood as arising from two contributions. The first contribution is the change in the mid-plane ion density. This contribution dominates at large plate separations and can be understood in terms of an effective PB surface charge in our model. The effective PB charge is smaller than the nominal charge due to the accumulation of counterions in the vicinity of the charged plates. Thus the pressure is reduced relative to PB theory, using the same surface charge.

As an alternative viewpoint, the PB surface charge can be chosen to match the large plate separation of the pressure in our model. When this is done, an apparent repulsive force appears in our model at very small plate separations ($\lesssim 5\,\text{Å}$), as compared with the fitted PB pressure.

The second contribution to the pressure is the direct solvent mediated attraction between ion pairs in the two halves of the system. This latter term can become dominant at plate separations between $\sim 5\,\text{Å}$ and $\sim 20\,\text{Å}$. It can induce a net attractive interaction between the two plates when the surface charge is high.

Attraction between like-charged surfaces is never predicted by PB theory [38, 39]. On the other hand, mechanisms involving correlations can lead to attraction. Several approaches have shown that ion-ion correlations can have this effect, in the framework of the primitive model [18–20]. In practice, this attraction can be strong enough to overcome the mean field repulsion when divalent ions are present in the solution. When there are only monovalent ions in the solution, ion-ion correlations have a much smaller effect. Another mechanism that can lead to attraction is the van der Waals force, arising from correlations between the polarizations on the two surfaces. As we find in this work, solvent mediated forces, related to ion-solvent

correlations, are another mechanism that can induce inter-surface attraction. In some cases (monovalent ions, small separation, large surface charge) they are the leading mechanism for attraction.

A strong deviation from PB predictions is indeed measured [40,41] between charged surfaces in aqueous solution at separation below $\sim 20\,\text{Å}$. The force includes an oscillatory contribution, with a period corresponding to the water molecular size. This force is due to the structuring of water in layers between the surfaces. In addition to this oscillatory contribution, an additional strong contribution is seen, which is often referred to as the hydration force [2,40]. The aqueous pair potential model of Ref. [29] was a first step towards the understanding of this force. A more realistic picture will probably emerge if a proper effective ion-surface interaction will be included, in addition to the effective ion-ion interaction. Furthermore, the modification to the ion-ion effective potential in a confined geometry may also be important. In order to assess the importance of these effects, further simulation results are needed as an input to the model.

The aqueous pair potential and the free energy (3.1) involve various approximations, which are discussed extensively in chapter 2 and in Ref. [42]. Nevertheless, the large modification to the PB pressure, as obtained also using the AHNC approximation [32,33,35] , indicates that the solvent effects on the ion distribution are a crucial ingredient in the origin of hydration forces [29,43]. The semi-quantitative agreement of our results with the AHNC approximation indicates that our formalism captures the important effects and suggests its further application in non-planar geometries, where the AHNC approximation is too difficult to apply.

3.A   Derivation of the pressure

The free energy of the system is given by the sum: $\Omega = \Omega_{\text{PB}} + \Delta\Omega$ with Ω_{PB} and $\Delta\Omega$ defined as follows:

$$
\begin{aligned}
\Omega_{\text{PB}} &= \frac{\varepsilon}{8\pi} \int_0^d \left(\frac{\mathrm{d}\Psi}{\mathrm{d}z}\right)^2 \mathrm{d}z + k_B T \int_0^d \sum_i c_i \left(\ln\frac{c_i}{\zeta} - 1\right) \mathrm{d}z \\
\Delta\Omega &= \frac{1}{2} k_B T \sum_{i,j} \int_0^d \mathrm{d}z \int_0^d \mathrm{d}z'\, c_i(z) c_j(z') B_{ij}(z'-z)
\end{aligned}
\tag{3.36}
$$

We now imagine that the separation between the two plates is increased from d to $d + \delta z$ by adding a 'slice' of width δz between the planes z_0 and $z_0 + \delta z$. We map the regions $0 \le z \le z_0$ and $z_0 \le z \le d$ in the original system to the regions $0 \le z \le z_0$ and $z_0 + \delta z \le z \le d + \delta z$ in the modified system, respectively. We then have:

$$\delta\Omega_{\mathrm{PB}} \quad = \quad \frac{\varepsilon}{4\pi}\int_0^d \mathrm{d}z\,\left(\frac{\mathrm{d}\Psi}{\mathrm{d}z}\right)\delta\left(\frac{\mathrm{d}\Psi}{\mathrm{d}z}\right) + k_B T\int_0^d \mathrm{d}z\,\sum_i \delta c_i \ln\frac{c_i}{\zeta}$$

$$+\delta z\left[\frac{\varepsilon}{8\pi}\left(\frac{\mathrm{d}\Psi}{\mathrm{d}z}\right)^2 + k_B T\sum_i c_i\left(\ln\frac{c_i}{\zeta}-1\right)\right]_{z=z_0} \tag{3.37}$$

The first term can be integrated by parts. With the conventions described above, the boundary terms can be written as follows:

$$\Psi\delta\left.\frac{\mathrm{d}\Psi}{\mathrm{d}z}\right|_0^{z_0} + \Psi\delta\left.\frac{\mathrm{d}\Psi}{\mathrm{d}z}\right|_{z_0}^d =$$

$$= \Psi(z_0)\left[\frac{\mathrm{d}\Psi_{\mathrm{new}}}{\mathrm{d}z}(z_0) - \frac{\mathrm{d}\Psi}{\mathrm{d}z}(z_0) - \frac{\mathrm{d}\Psi_{\mathrm{new}}}{\mathrm{d}z}(z_0+\delta z) + \frac{\mathrm{d}\Psi}{\mathrm{d}z}(z_0)\right]$$

$$= -\Psi(z_0)\frac{\mathrm{d}^2\Psi}{\mathrm{d}z^2}(z_0)\delta z \tag{3.38}$$

where use of the boundary conditions at $z = 0$ and $z = d$ has been made. Using this relation and the Poisson equation (3.5), we obtain:

$$\delta\Omega_{\mathrm{PB}} \quad = \quad \delta z\left[\sum_i e_i\Psi c_i + \frac{\varepsilon}{8\pi}\left(\frac{\mathrm{d}\Psi}{\mathrm{d}z}\right)^2 + k_B T\sum_i c_i\left(\ln\frac{c_i}{\zeta}-1\right)\right]_{z_0}$$

$$+ \int_0^d \mathrm{d}z\,\sum_i \delta c_i\left[e_i\Psi + k_B T\ln\frac{c_i}{\zeta}\right] \tag{3.39}$$

To compute $\delta\Delta\Omega$, $\Delta\Omega$ can be separated to the following three terms:

$$\Delta\Omega \quad = \quad \frac{1}{2}k_B T\sum_{i,j}\int_0^{z_0}\mathrm{d}z\int_0^{z_0}\mathrm{d}z'\,c_i(z)c_j(z')B_{ij}(z'-z)$$

$$+\frac{1}{2}k_B T\sum_{i,j}\int_{z_0}^d \mathrm{d}z\int_{z_0}^d \mathrm{d}z'\,c_i(z)c_j(z')B_{ij}(z'-z)$$

$$+k_B T\sum_{i,j}\int_0^{z_0}\mathrm{d}z\int_{z_0}^d \mathrm{d}z'\,c_i(z)c_j(z')B_{ij}(z'-z) \tag{3.40}$$

The variation of c_i in these three terms gives:

$$\delta\Delta\Omega_1 = k_B T\sum_{i,j}\int_0^d \mathrm{d}z\int_0^d \mathrm{d}z'\,c_i(z)\delta c_j(z')B_{ij}(z'-z) \tag{3.41}$$

The variation of the third term in Eq. (3.40) gives two additional contributions, one from the variation of $B(z'-z)$ under the insertion of the 'slice' at z_0:

$$\delta \Delta \Omega_2 = \delta z \cdot k_B T \sum_{i,j} \int_0^{z_0} \mathrm{d}z \int_{z_0}^d \mathrm{d}z' \, c_i(z) c_j(z') \frac{\mathrm{d}B_{ij}}{\mathrm{d}z}(z' - z) \tag{3.42}$$

and the other from the integration over the 'slice' itself:

$$\delta \Delta \Omega_3 = \delta z \cdot k_B T \sum_{i,j} \int_0^d \mathrm{d}z \, c_i(z_0) c_j(z) B_{ij}(z - z_0) \tag{3.43}$$

Summing up all the contributions to $\delta \Omega$ we have:

$$
\begin{aligned}
\delta \Omega \;=\; & \delta \Omega_{\mathrm{PB}} + \delta \Delta \Omega_1 + \delta \Delta \Omega_2 + \delta \Delta \Omega_3 \\
\;=\; & \delta z \sum_i c_i(z_0) \times \left\{ \frac{\varepsilon}{8\pi} \left(\frac{\mathrm{d}\Psi}{\mathrm{d}z} \right)^2 (z_0) + e_i \Psi(z_0) + k_B T \left[\ln \frac{c_i(z_0)}{\zeta} - 1 \right] \right. \\
& \left. + k_B T \sum_j \int_0^d \mathrm{d}z \, c_j(z) B_{ij}(z - z_0) \right\} \\
& + \int_0^d \mathrm{d}z \sum_i \delta c_i(z) \times \left\{ e_i \Psi(z) + k_B T \ln \frac{c_i(z)}{\zeta} + k_B T \sum_j \int_0^d \mathrm{d}z' \, c_j(z') B_{ij}(z' - z) \right\} \\
& + \delta z \, k_B T \sum_{ij} \int_0^{z_0} \mathrm{d}z \int_{z_0}^d \mathrm{d}z' \, c_i(z) c_j(z') \frac{\mathrm{d}B_{ij}}{\mathrm{d}z}(z' - z) \tag{3.44}
\end{aligned}
$$

Using the equilibrium equation (3.7) this reduces to:

$$
\begin{aligned}
-\frac{\delta \Omega}{\delta z} \;=\; & k_B T \sum_i c_i(z_0) - \left. \frac{\varepsilon}{8\pi} \left(\frac{\mathrm{d}\Psi}{\mathrm{d}z} \right)^2 \right|_{z_0} \\
& - k_B T \sum_{ij} \int_0^{z_0} \mathrm{d}z \int_{z_0}^d \mathrm{d}z' \, c_i(z) c_j(z') \frac{\mathrm{d}B_{ij}}{\mathrm{d}z}(z' - z) \tag{3.45}
\end{aligned}
$$

This result can be readily generalized to the case of several ion species, as in Eq. (3.18).

Bibliography

[1] Y. Burak and D. Andelman, *J. Chem. Phys.* **114** (2001) 3271.

[2] J. Israelachvili, *Intermolecular and Surface Forces*, 2nd ed., Academic Press: New York, 1991.

[3] G. Gouy, *J. Phys. (France)* **9** (1910) 457.

[4] D. L. Chapman, *Philos. Mag.* **25** (1913) 475.

[5] P. Debye and E. Hückel, *Phyzik* **24** (1923) 185.

[6] P. Debye and E. Hückel, *Phyzik* **25** (1924) 97.

[7] D. Andelman, in *Handbook of Physics of Biological Systems*, R. Lipowsky and E. Sackmann (eds.), Elsevier Science: Amsterdam, 1994, Vol. I, Chap. 12, p. 603.

[8] E. J. W. Verwey and J. T. G. Overbeek, *Theory of the Stability of Lyophobic Colloids*, Elsevier: Amsterdam, 1948.

[9] S. Alexander *et al.*, *J. Chem. Phys* **80** (1984) 5776.

[10] F. Oosawa, *Polyelectrolytes*, Marcel Dekker: New York, 1971.

[11] J. L. Barrat and J. F. Joanny, *Adv. Chem. Phys.* **XCIV** (1996) 1.

[12] D. Harries, S. May, W. M. Gelbart, and A. Ben-Shaul, *Biophys. J.* **75** (1998) 159.

[13] L. Blum and D. Henderson, in *Fundamentals of Inhomogeneous Fluids*, D. Henderson (ed.), Marcel Dekker: New York, 1992, Chap. 6, pp. 239–276, and references therein.

[14] R. Kjellander and S. Marčelja, *J. Chem. Phys.* **82** (1985) 2122.

[15] R. Kjellander, *J. Chem. Phys.* **88** (1988) 7129.

[16] S. Levine, C. W. Outhwaite, and L. B. Bhuiyan, *J. Electroanal. Chem.* **123** (1981) 105.

[17] C. W. Outhwaite and L. B. Bhuiyan, *J. Chem. Soc. Faraday Trans. 2* **79** (1983) 707.

[18] M. J. Stevens and M. O. Robbins, *Europhys. Lett.* **12** (1990) 81.

[19] L. Guldbrand, B. Jönsson, H. Wennerström, and P. Linse, *J. Chem. Phys.* **80** (1984) 2221.

[20] R. Kjellander, T. Åkesson, B. Jönsson, and S. Marčelja, *J. Chem. Phys.* **97** (1992) 1424.

[21] H. Greberg, R. Kjellander, and T. Åkesson, *Mol. Phys.* **92** (1997) 35.

[22] R. R. Netz and H. Orland, *Europhys. Lett.* **45** (1999) 726.

[23] R. R. Netz and H. Orland, *Europhys. J. E.* **1** (2000) 203.

[24] I. Borukhov, D. Andelman, and H. Orland, *Phys. Rev. Lett.* **79**, (1997) 435.

[25] I. Borukhov, D. Andelman, and H. Orland, *Electrochim. Acta* **46** (2000) 221.

[26] D. B. Lukatsky and S. A. Safran, *Phys. Rev. E.* **60** (1999) 5848.

[27] L. Lue, N. Zoeller, and D. Blankschtein, *Langmuir* **15** (1999) 3726.

[28] A. P. Lyubartsev and A. Laaksonen, *Phys. Rev. E.* **55** (1997) 5689.

[29] S. Marčelja, *Nature* **385** (1997) 689.

[30] S. Marčelja, *Period. Biol.* **100** (1998) 7.

[31] S. Marčelja, *Colloid Surface A* **130** (1997) 321.

[32] R. Kjellander, A. P. Lyubartsev, and S. Marčelja, *J. Chem. Phys.* **114** (2001) 9565.

[33] F. Otto and G. N. Patey, *J. Chem. Phys.* **112** (2000) 8939.

[34] R. R. Netz, private communication.

[35] This data was provided to us by S. Marčelja.

[36] S. L. Carnie and D. Y. C. Chan, *J. Chem. Phys.* **74** (1981) 1293.

[37] E. Guàrdia and J. A. Padró, *J. Chem. Phys.* **104** (1996) 7219.

[38] J. C. Neu, *Phys. Rev. Lett.* **82** (1999) 1072.

[39] J. E. Sader and D. Y. C. Chan, *J. Colloid Interface Sci.* **213** (1999) 268.

[40] R. M. Pashley, *J. Colloid Interface Sci.* **80** (1981) 153.

[41] R. M. Pashley and J. N. Israelachvili, *J. Colloid Interface Sci.* **101** (1984) 511.

[42] S. Marčelja, *Langmuir* **16** (2000) 6081.

[43] J. Israelachvili and H. Wennerström, *Nature* **379** (1996) 219.

Symbol Legend (Chapters 2–3)

β	Inverse thermal energy, $1/(k_B T)$.
ε	Dielectric constant.
η	$\ln(c/\zeta 0)$.
$\lambda(\mathbf{r})$	Lagrange multiplier relating Ψ and c_i.
λ_D	Debye length, $\lambda_D = (8\pi l_B c_b)^{-1/2}$.
μ_i	Chemical potential of ion species i.
Ω	Free energy [Energy].
Ψ	Electrostatic potential.
$\sigma(\mathbf{r})$	Fixed charge distribution of immobile charges [charge/unit volume].
σ	Surface charge density of charged plate [charge/unit area].
σ_{eff}	Effective surface charge.
ζ_i	Fugacity of ion species i.
ζ	Fugacity of 1:1 salt.
$B(z)$	Eq. (2.24).
B_t	Eq. (2.28).
b	Gouy-Chapman length, $b = \varepsilon k_B T/(2\pi e|\sigma|)$.
b_{eff}	Effective Gouy-Chapman length.
$c_i(\mathbf{r})$	Local concentration of ion species i.
$c_{b,i}$	Bulk concentration of ion species i.
c_b	Bulk concentration of 1:1 salt.
d	Separation between charged plates.
d_{hyd}	Range of hydration interaction.
e_i	Charge of ion species i.
e	Electron (unit) charge.
H	Hamiltonian.
l_B	Bjerrum length, $l_B = e^2/(\varepsilon k_B T)$.
M	Molar (Mol/Liter).
P	Pressure.
u_{ij}	Short-range interaction between ion species i,j
U_{ij}	Weighted ion-ion interaction, Eq. (2.17).
w	$\ln(c/c_{\mathrm{PB}})$.
z_i	Valency ion species i.
z	normal coordinate to charged plane.

Chapter 4

Test charge model for the electric double layer

The following chapter deals with ion-ion correlation effects in the planar electric double layer.[1] We present a model for the ion distribution near a charged surface, based on the response of the ions to the presence of a single test particle. Near an infinite planar surface this model produces the exact density profile in the limits of weak and strong coupling, which correspond to zero and infinite values of the dimensionless coupling parameter. At intermediate values of the coupling parameter our approach leads to approximate density profiles that agree qualitatively with Monte-Carlo simulation. For large values of the coupling parameter our model predicts a crossover from exponential to algebraic decay at large distance from the charged plate. Based on the test charge approach we argue that the exact density profile is described, in this regime, by a modified mean field equation, which takes into account the interaction of an ion with the ions close to the charged plate.

4.1 Introduction

Interactions between charged objects in solution are determined by the distribution of ions around them. Understanding these distributions is thus of fundamental importance for theoretical treatment of water soluble macromolecules such as polyelectrolytes, charged membranes, and colloids [2,3]. In recent years, much interest has been devoted to correlation effects in ionic solutions and to attempts to go beyond mean field theory in their treatment. In particular it has been realized that such effects can lead to attractive interactions between similarly charged objects, as was demonstrated in theoretical models [4–11], simulation [6, 12–15] and experi-

---

[1]The material presented in this chapter was published in Ref. [1].

Figure 4.1: Schematic description of the double layer model considered in this work. An infinite charged plate having a uniform surface charged density σ is immersed in a dielectric medium having dielectric constant ε on both sides of the plate. The charge of the plate is neutralized by point-like counterions, carrying each a charge e. These ions are confined to the positive z half space, where $z = 0$ is the plane occupied by the plate. In thermal ($k_B T$) units the interaction between two ions is given by l_B/r, where r is the distance between the ions and $l_B = e^2/(\varepsilon k_B T)$ is the Bjerrum length.

ment [16–20].

Despite the theoretical interest in ion correlation effects, they are not fully understood even in the most simple model for a charged object surrounded by its counterions, shown schematically in Fig. 4.1. The charged object in this model is an infinite planar surface localized at the plane $z = 0$, having a uniform charge density σ. The charged plate is immersed in a solution of dielectric contact ε and is neutralized by a single species of mobile counterions (there is no salt in the solution). These counterions are confined to the half space $z > 0$ and each one of them carries a charge e, which is a multiple of the unit charge for multivalent ions. The ions are considered as point-like, *i.e.*, the only interactions in the system, apart from the excluded volume at $z < 0$, are electrostatic.

The system described above is characterized by a single dimensionless coupling parameter [21][2]

$$\Xi = \frac{2\pi e^3 \sigma}{(\varepsilon k_B T)^2} \tag{4.1}$$

where $k_B T$ is the thermal energy. At small values of this coupling parameter the electrostatic interaction between ions is weak. As a result, in the limit $\Xi \to 0$ mean field theory is exact, as can be formally proved using a field-theory formulation of the problem [21]. Correlations

---

[2]A related dimensionless parameter is Γ, conventionally defined for the two dimensional one component plasma (see Ref. [10]). This parameter is related to Ξ as follows: $\Xi = 2\Gamma^2$.

between ions close to the charged plate play a progressively more important role with increase of the coupling parameter. From Eq. (4.1) one sees that this happens with an increase of the surface charge, with decrease of the temperature or dielectric constant, and with increase of the charge or, equivalently, the valency of counterions. The model of Fig. 4.1 thus provides an elementary theoretical framework for studying ion correlation effects near charged objects, with no free parameters other than Ξ, which tunes and controls the importance of ion correlations.

In recent years two theoretical approaches were proposed for treatment of the strong coupling limit $\Xi \to \infty$. The first approach [10] is based on properties of the strongly coupled, two dimensional one component plasma, and emphasizes the possibility of Wigner crystal like ordering parallel to the charged plane. The second approach [11] is formally an exact, virial type expansion applied to a field-theory formulation of the partition function. Both of these approaches predict an exponential decay of the ion density distribution in the strong coupling limit, leading to a more compact counterion layer than in mean field theory.

Although the form of the density profile is established in the two limits $\Xi \to 0$ and $\Xi \to \infty$, its behavior at intermediate values of the coupling parameter is still not clear. Liquid-state theory approaches such as the AHNC approximation [22] can probably be used in this regime, but in practice they were applied in the literature only to relatively small values of the coupling parameter, usually also including ingredients other than those in the model of Fig. 4.1 – such as finite ion size, added salt, or an interaction between two charged planar surfaces. The infinite planar double layer with no added salt (Fig. 4.1) was recently studied using Monte-Carlo computer simulation [14], providing detailed results on the counterion distribution in a wide range of coupling parameter values. These results validate the expected behavior in the weak and strong coupling limits. In addition they provide new data at intermediate values of the coupling parameter, to which theoretical approaches can be compared.

We propose, in the present work, a new theoretical approach for treating the distribution of counterions near the charged plate. This approach is based on an approximate evaluation of the response of the ionic layer, to the presence of a single test particle. While an exact evaluation of this response would, in principle, allow the distribution of ions to be obtained exactly, we show that even its approximate calculation provides meaningful and useful results. In the limits of small and large Ξ the exact density profile is recovered. At intermediate values of the coupling parameter our approach agrees semi-quantitatively with all the currently available simulation data.

The outline of this work is as follows. In Sec. 4.2 we present the model and discuss why

it produces the exact density profile in the weak and strong coupling limits. In Sec. 4.3 we present numerical results for the density profile close to the charged plate, and compare them with simulation results of Ref. [14]. Numerical results of our model, further away from the charged plate, where there is currently no data from simulation, are presented in Sec. 4.4, and scaling results are obtained for the behavior of our model in this regime. Finally, in Sec. 4.5 we discuss the relevance of our model's predictions, at small and large z, to the exact theory. Many of the technical details and derivations appear in the appendices at the end of this work.

4.2 Model

4.2.1 Scaling

Consider the system shown in Fig. 4.1, with the parameters σ, e, ε defined in the introduction. We will first express the free energy using the dimensionless coupling parameter Ξ. In the canonical ensemble the partition function can be written as follows (z_i is the z coordinate of the i-th ion):

$$\exp(-F_N) = \frac{1}{N!} \int \prod_{i=1}^{N} d^3 \mathbf{r}_i \exp\left[-\sum_{i=1}^{N} \frac{z_i}{\mu} - \sum_{j>i} \frac{l_B}{|\mathbf{r}_i - \mathbf{r}_j|} \right] \tag{4.2}$$

where $l_B = e^2/\varepsilon k_B T$ is the distance at which the Coulomb energy of two ions is equal to the thermal energy $k_B T$, and $\mu = e/(2\pi l_B \sigma)$ characterizes the bare interaction of an ion with the charged plane. These quantities, the only two independent length scales in the problem, are known as the Bjerrum length and Gouy-Chapman length, respectively. We rescale the coordinates by the Gouy-Chapman length:

$$\tilde{\mathbf{r}}_i = \frac{\mathbf{r}_i}{\mu}, \tag{4.3}$$

yielding $\exp(-F_N) = (\mu)^{3N} \exp(-\tilde{F}_N)$, where

$$\exp(-\tilde{F}_N) = \frac{1}{N!} \int \prod_{i=1}^{N} d^3 \tilde{\mathbf{r}}_i \exp\left[-\sum_{i=1}^{N} \tilde{z}_i - \sum_{j>i} \frac{\Xi}{|\tilde{\mathbf{r}}_i - \tilde{\mathbf{r}}_j|} \right] \tag{4.4}$$

and the ratio

$$\Xi = \frac{l_B}{\mu} \tag{4.5}$$

is the coupling parameter that was previously defined in Eq. (4.1). The requirement of charge neutrality is: $N/A = \sigma/e$, where A is the planar area. Hence the number of ions per rescaled unit area is equal to:

$$\frac{N}{\tilde{A}} = \frac{1}{2\pi\Xi} \tag{4.6}$$

where $\tilde{A} = A/\mu^2$. The local density of ions in the rescaled coordinates is equal to $\tilde{\rho}(\mathbf{r}) = \mu^3 \tilde{\rho}(\mathbf{r})$. Due to symmetry this density depends only on $\tilde{z}$ and it is convenient to define a normalized, dimensionless, density per unit length:

$$\tilde{n}(\tilde{z}) = 2\pi l_B \mu^2 \rho = 2\pi \Xi \tilde{\rho} \qquad (4.7)$$

having the property:

$$\int_0^\infty \mathrm{d}\tilde{z}\, \tilde{n}(\tilde{z}) = 1 \qquad (4.8)$$

as seen from Eqs. (4.6) and (4.7). From here on we will omit the tilde symbol ($\sim$) from all quantities, in order to simplify the notations. In order to express physical quantities in the original, non-scaled units, the following substitutions can be used:

$$\mathbf{r} \quad \rightarrow \quad \mathbf{r}/\mu \qquad (4.9)$$

$$n \quad \rightarrow \quad 2\pi l_B \mu^2 \rho \qquad (4.10)$$

We will also omit the subscript N from the free energy $\tilde{F}_N$, implying that N is determined by charge neutrality.

4.2.2   Known results in the limits of small and large Ξ

We briefly review some known properties of the ion distribution in the limits of small and large Ξ (for a more complete discussion, see Ref. [11]). In the limit of $\Xi \to 0$ mean field theory becomes exact. The density profile is obtained from the Poisson-Boltzmann (PB) equation and decays algebraically, having the form [23]

$$n_{\mathrm{PB}}(z) = \frac{1}{(z+1)^2} \qquad (4.11)$$

Within the adsorbed layer ions form a three dimensional, weakly correlated gas: the electrostatic interaction between neighboring ions is small compared to the thermal energy. This last statement can be verified by considering the density of ions at contact with the plane, $\rho_{\mathrm{PB}}(0) = 1/(2\pi\Xi)$ [see Eqs. (4.7) and (4.11)]. The typical distance between neighboring ions is thus of order $\Xi^{1/3}$. In the non-scaled units this distance is much larger than l_B, which validates the statement that ions are weakly correlated: $\Xi^{1/3}\mu = \Xi^{-2/3}l_B \gg l_B$. Note also that this typical distance is small compared to the width of the adsorbed layer (Gouy-Chapman length): $\Xi^{1/3}\mu \ll \mu$.

In the opposite, strong coupling (SC) limit of $\Xi \gg 1$, the density profile decays exponentially,

$$n_{\mathrm{SC}}(z) = \exp(-z) \qquad (4.12)$$

The width of the adsorbed layer is still of order μ in the non-scaled units, but is now small compared to l_B. Equation (4.6) indicates that the average lateral distance between ions is then of order $\Xi^{1/2}$. This distance is large compared to the width of the ionic layer, $\Xi^{1/2}\mu \gg \mu$. On the other hand it is small in units of the Bjerrum length: $\Xi^{1/2}\mu = \Xi^{-1/2}l_B \ll l_B$. The ions form, roughly speaking, a two-dimensional sheet and are highly correlated within this adsorbed layer. The typical lateral separation between ions, $\Xi^{1/2}$, is an important length scale in the strong coupling limit, and will play an important role also in our approximated model.

At sufficiently large values of Ξ it has been conjectured (but not proved) that ions form a two-dimensional, triangular close-packed Wigner crystal parallel to the charged plate. Based on the melting temperature of a two dimensional, one component plasma, one can estimate that this transition occurs at $\Xi \gtrsim 31,000$ [10,14]. Furthermore, the ion-ion correlation function is expected to display short range order similar to that of the Wigner crystal even far below this transition threshold. The exponential decay of Eq. (4.12) was predicted, based on these notions, in Ref. [10]. The same result can be obtained also in a formal virial expansion [11], which is valid for large Ξ but does not involve long range order parallel to the charged plate at any value of Ξ.

Finally we note two general properties of the density profile that are valid at any value of Ξ. First, the normalized contact density $n(0)$ is always equal to unity – a consequence of the contact theorem [24] (see also Appendix 4.D). Second, the characteristic width of the adsorbed layer is always of order unity in the rescaled units. These two properties restrict the form of the density distribution quite severely and indeed the two profiles (4.11) and (4.12) are similar to each other close to the charged plane. Far away from the plate, however, they are very different from each other: at $z \gg 1$ the probability to find an ion is exponentially small in the SC limit, while in the weak coupling limit it decays only algebraically and is thus much larger. Furthermore, in the weak coupling case, moments of the density, including the average distance of an ion from the plate, diverge.

Although the form of the density profile is known in the limits of small and large Ξ, two important issues remain open. The first issue is the form of the density profile at intermediate values of Ξ. At coupling parameter values such as 10 or 100 perturbative expansions around the limits of small or large Ξ [11,21] are of little use, because they tend to give meaningful results only at small values of their expansion parameter. Such intermediate values are common in experimental systems with multivalent ions, as demonstrated in Table 4.1. Second, even at very small or very large Ξ the respective asymptotic form of $n(z)$ may be valid within a limited

	$\sigma(e/\text{Å}^2)$	$\mu(\text{Å})$	$\Xi(1\text{-}e)$	$\Xi(4\text{-}e)$
Cell membrane	0.002	10	0.6	40
DNA	0.01	2	3	200
Mica	0.02	1	6	400

Table 4.1: Characteristic values of σ, μ and Ξ for several representative macromolecules. Values of Ξ are shown for two cases: monovalent counterions (1-e) and 4-valent ones (4-e). The Gouy-Chapman length μ corresponds to monovalent ions. The cell membrane charge density is estimated assuming that 10% of the lipids in the membrane are charged. The surface charge of DNA is estimated from the linear charge density along the DNA contour, equal to $1/1.7\,e/\text{Å}$, and assuming a radius of $10\,\text{Å}$. For Mica full dissociation of charged groups is assumed. In all three cases the Bjerrum length is taken as $l_B = 7\,\text{Å}$, which corresponds to water at room temperature.

range of z values. In particular, for large Ξ it is natural to suppose that sufficiently far away from the charged plate the density profile crosses over from SC to PB behavior. Indeed, far away from the plate the ion density is small, resembling the situation near a weakly charged surface. The main objective of this work is to investigate these issues, both of which necessitate going beyond the formal limits of vanishing and infinite Ξ.

4.2.3 Test-charge mean field model

Our model is based on the following observation: the normalized density $n(z)$ is proportional to the partition function of a system where a single ion is fixed at the coordinate z:

$$n(z) = \frac{1}{Z}\exp[-F(z)] \tag{4.13}$$

where

$$\exp[-F(z_0)] = \frac{1}{(N-1)!}\int \prod_{i=1}^{N-1}\mathrm{d}^3\mathbf{r}_i \ \times$$
$$\exp\left(-z_0 - \sum_{i=1}^{N-1}z_i - \sum_{i=1}^{N-1}\frac{\Xi}{|\mathbf{r}_i - z_0\hat{\mathbf{z}}|}\right.$$
$$\left. - \sum_{j>i}\frac{\Xi}{|\mathbf{r}_i - \mathbf{r}_j|}\right) \tag{4.14}$$

and

$$Z = \int_0^\infty \mathrm{d}z\,\exp[-F(z)] \tag{4.15}$$

where the coordinate of the fixed (N-th) ion in Eq. (4.14) is $z_0\hat{\mathbf{z}}$. Equations (4.13)-(4.15) are exact and can be readily formulated also in the grand canonical ensemble.

In the original coordinates $F(z_0)$ is the free energy of ions in the external potential:

$$\frac{z}{\mu} + \frac{l_B}{|\mathbf{r} - z_0\hat{\mathbf{z}}|} \tag{4.16}$$

exerted by the charged plane and fixed ion. Examination of Eq. (4.14) shows that in the rescaled coordinates these are ions of charge $\sqrt{\Xi}$ in the external potential:

$$\frac{1}{\sqrt{\Xi}}\left[z + \frac{\Xi}{|\mathbf{r} - z_0\hat{\mathbf{z}}|}\right] \tag{4.17}$$

Our starting point for evaluating $n(z)$ is the exact relation expressed by Eq.(4.13) but we will use a mean field approximation in order to evaluate $F(z_0)$. In this approximation the free energy is expressed as an extremum of the following functional of φ:

$$\begin{aligned}
F_{\text{PB}}(z_0) &= \frac{1}{\Xi}\int \mathrm{d}^3\mathbf{r}\left\{-\frac{1}{8\pi}(\nabla\varphi)^2 - \lambda\theta(z)\mathrm{e}^{-\varphi}\right.\\
&+ (\varphi - \ln\lambda)\left[-\frac{1}{2\pi}\delta(z) + \Xi\delta(\mathbf{r} - z_0\hat{\mathbf{z}})\right]\right\}\\
&- F_{\text{self}}
\end{aligned} \tag{4.18}$$

where φ is the reduced electrostatic potential, $\theta(z)$ is the Heaviside function, and F_{self} is an infinite self energy which does not depend on z_0. The derivation of Eq.(4.18) is given in Appendix 4.A.

The mean field equation for φ is found from the requirement $\delta F_{\text{PB}}/\delta\varphi(\mathbf{r}) = 0$:

$$-\frac{1}{4\pi}\nabla^2\varphi = \lambda\theta(z)\mathrm{e}^{-\varphi} - \frac{1}{2\pi}\delta(z) + \Xi\delta(\mathbf{r} - z_0\hat{\mathbf{z}}) \tag{4.19}$$

This equation describes the mean field distribution of ions in the presence of a charged plane of uniform charge density $-1/(2\pi)$ (second term in Eq. (4.19)) and a point charge Ξ located at $\mathbf{r} = z_0\hat{\mathbf{z}}$ (third term in Eq. (4.19)). In cylindrical coordinates the solution φ can be written as a function only of the radial coordinate r and of z, due to the symmetry of rotation around the z axis.

It is easy to show that at the extremum of F_{PB} the overall charge of the system, including the charged surface, test charge and mobile counterions, is zero. The fugacity λ has no effect on the extremal value of F_{PB}; changing its value only shifts $\varphi(\mathbf{r})$ by a constant.

Equations (4.13) and (4.15), together with the mean-field approximation for $F(z_0)$ given by Eqs. (4.18) and (4.19) constitute the approximation used in this work:

$$n(z) = \frac{1}{Z}\exp[-F_{\text{PB}}(z)] \tag{4.20}$$

where

$$Z = \int_0^\infty \mathrm{d}z \exp[-F_{\text{PB}}(z)] \tag{4.21}$$

We will refer to this approximation as the test-charge mean field (TCMF) model.
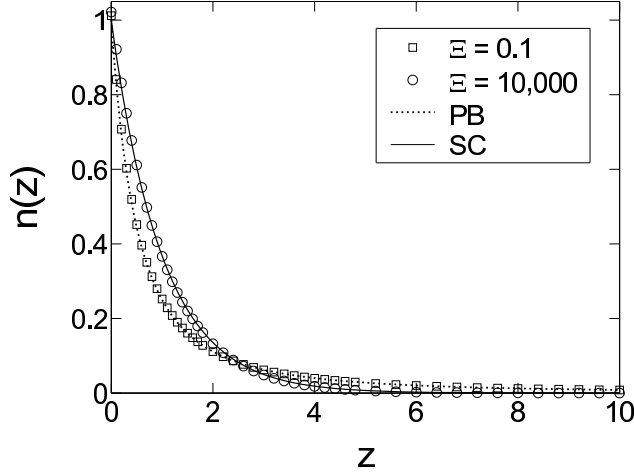
Figure 4.2: Density profiles, $n(z)$, numerically calculated using the TCMF model of Eqs. (4.19)-(4.21), with $\Xi = 0.1$ (squares) and $\Xi = 10{,}000$ (circles). The solid lines show the exact asymptotic profiles in the low coupling, $n_{\mathrm{PB}}(z) = 1/(z+1)^2$, and in the strong coupling limit, $n_{\mathrm{SC}} = \exp(-z)$.

4.2.4   Limits of small and large Ξ

As a first example we present, in Fig. 4.2, density profiles obtained numerically from Eqs. (4.20)-(4.21) at $\Xi = 0.1$ (circles) and at $\Xi = 10000$ (squares). The continuous lines are the theoretically predicted profiles at $\Xi \to 0$, $n_{\mathrm{PB}}(z) = 1/(z+1)^2$, and at $\Xi \to \infty$, $n_{\mathrm{SC}}(z) = \exp(-z)$. The figure demonstrates that the weak coupling and strong coupling limits are reproduced correctly in our approximation. Before presenting further numerical results, we discuss the behavior of our model in the two limits of small and large Ξ.

Our discussion is based on the following exact identity:

$$\frac{\mathrm{d}}{\mathrm{d}z_0}\ln\left[n(z_0)\right] = -\frac{\mathrm{d}}{\mathrm{d}z_0}F(z_0) = -\left.\frac{\partial}{\partial z}\left\langle\varphi(\mathbf{r};z_0)\right\rangle\right|_{\mathbf{r}\,=\,z_0\hat{\mathbf{z}}} \tag{4.22}$$

where $\langle\varphi(\mathbf{r};z_0)\rangle$ is the thermally averaged electrostatic potential at $\mathbf{r}$, when a test charge is *fixed* at $z_0\hat{\mathbf{z}}$ (the first argument of $\langle\varphi(\mathbf{r};z_0)\rangle$ designates the position $\mathbf{r}$ where the potential is evaluated, while the second argument designates the position of the test charge, $z_0\hat{\mathbf{z}}$). In other words, the gradient of $\ln[n(z_0)]$ is equal to the electrostatic force acting on a test charge positioned at $\mathbf{r} = z_0\hat{\mathbf{z}}$. This equation does not involve any approximations and is proved in Appendix 4.B.

Within our approximation, where $F(z_0)$ is replaced by $F_{\mathrm{PB}}(z_0)$, a similar equation holds (also proved in the Appendix):

$$\frac{\mathrm{d}}{\mathrm{d}z_0}\ln\left[n(z_0)\right] = -\frac{\mathrm{d}}{\mathrm{d}z_0}F_{\mathrm{PB}}(z_0) = -\left.\frac{\partial}{\partial z}\varphi(\mathbf{r};z_0)\right|_{\mathbf{r}\,=\,z_0\hat{\mathbf{z}}} \tag{4.23}$$

where $\varphi(\mathbf{r}; z_0)$ is now the solution of Eq. (4.19). In other words, the gradient of $\ln[n(z_0)]$ is equal to the electrostatic force experienced by a test charge positioned at $\mathbf{r} = z_0\hat{\mathbf{z}}$, evaluated using the mean field equation (4.19). This quantity,

$$f(z_0) \equiv \left.\frac{\partial}{\partial z}\varphi(\mathbf{r}; z_0)\right|_{\mathbf{r}\,=\,z_0\hat{\mathbf{z}}} \tag{4.24}$$

will be studied in detail below because of its important role within our model. With this notation the relation between $f(z)$ and $n(z)$ reads:

$$\frac{\mathrm{d}}{\mathrm{d}z}\ln[n(z)] = -f(z) \tag{4.25}$$

Using Eq. (4.25) we can understand why both the weak and strong coupling limits are reproduced correctly in our model:

Weak coupling

In the limit $\Xi \to 0$,

$$\frac{\partial}{\partial z}\varphi(\mathbf{r}; z_0) \to \frac{\mathrm{d}}{\mathrm{d}z}\varphi_{\mathrm{PB}}(z). \tag{4.26}$$

where $\varphi_{\mathrm{PB}}(z)$ is the solution of Eq. (4.19) without a test charge, *i.e.*, setting $\Xi = 0$. We note that the potential φ (Eq. 4.19) has three sources: the charge of mobile counterions, $\lambda\theta(z)\mathrm{e}^{-\varphi}$, the uniformly charged plane, and the test charge. Although the potential due to the test charge is infinite at $\mathbf{r} = z_0\hat{\mathbf{z}}$, its derivative with respect to z is zero and has no contribution in Eq. (4.26). Using Eq. (4.25) we find:

$$\frac{\mathrm{d}}{\mathrm{d}z}\ln[n(z)] = -\frac{\mathrm{d}}{\mathrm{d}z}\varphi_{\mathrm{PB}}(z) \tag{4.27}$$

This equation, together with the normalization requirement for $n(z)$ leads to the result:

$$n(z) = \frac{1}{Z_0}\exp[-\varphi_{\mathrm{PB}}(z)] = n_{\mathrm{PB}}(z) \tag{4.28}$$

Strong coupling

In the strong coupling limit, $\Xi \to \infty$, a correlation hole forms in the distribution of mobile counterions around the test charge at $\mathbf{r} = z_0\hat{\mathbf{z}}$. The structure and size of this hole, as obtained from Eq. (4.19), will be discussed in detail later. For now it is sufficient to note that the correlation hole gets bigger with increasing Ξ. As $\Xi \to \infty$ the force at $z_0\hat{\mathbf{z}}$ due to the mobile counterions vanishes, leaving only the contribution of the charged plane: $(\partial/\partial z)\varphi(\mathbf{r}; z_0, \Xi) \to 1$. Hence in this limit

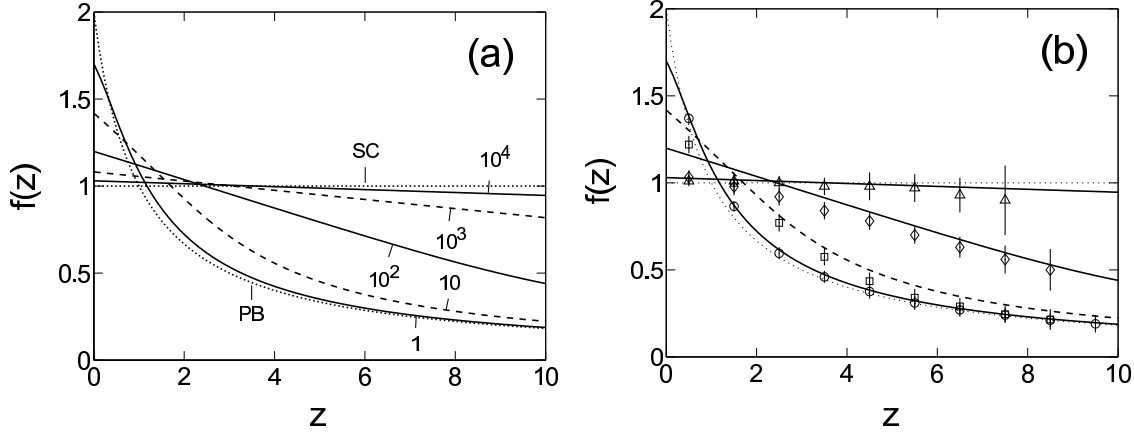$$\frac{\mathrm{d}}{\mathrm{d}z}\ln[n(z)] = -1 \tag{4.29}$$

Figure 4.3:   (a) Electrostatic force acting on a test charge, $f(z)$, numerically calculated using the mean field equation (4.19). Alternating solid and dashed lines show $f(z)$ for $\Xi = 1$, 10, 10^2, 10^3, and 10^4. The dotted lines show the PB and SC forms of $f(z)$, $f_{\mathrm{PB}}(z) = 1/(z+1)$ and $f_{\mathrm{SC}}(z) = \exp(-z)$. (b) Comparison of $f(z)$, calculated from Eq. (4.19) (solid and dashed lines, same as in part (a)), with results from Monte-Carlo simulation [25], adapted from Ref. [14] ($\Xi = 1$, circles; $\Xi = 10$, squares; $\Xi = 10^2$, diamonds; $\Xi = 10^4$, triangles). Values of $f(z)$ are obtained from simulation results for $n(z)$ using the exact relation $\mathrm{d}\ln n(z)/\mathrm{d}z = -f(z)$. Numerical estimation of the derivative of $\ln[n(z)]$ results in relatively large error bars, which are shown as vertical lines.

leading to the strong coupling result:

$$n(z) = \exp(-z) \tag{4.30}$$

where the prefactor of the exponent follows from the normalization condition, Eq. (4.8).

In the rest of this work we will explore predictions of the TCMF model at intermediate coupling, where neither of the two limits presented above is valid. Before proceeding we note that a similar discussion as above, of the weak and strong coupling limits, applies also to the exact theory, because of Eq. (4.22).

4.3   Numerical Results and Comparison with Simulation

Results for $f(z)$

We consider first the behavior of $f(z)$, defined in Eq. (4.24), close to the charged plate. Figure 4.3 (a) shows this behavior for $\Xi = 1$, 10, 10^2, 10^3 and 10^4 (alternating solid and dashed lines). The curves were obtained from a numerical solution of the partial differential equation (PDE), Eq. (4.19) (see Appendix 4.C for details of the numerical scheme). For comparison the weak coupling (PB) and strong coupling (SC) limits are shown using dotted lines:

$$f_{\mathrm{PB}}(z) = \frac{2}{z+1} \quad ; \quad f_{\mathrm{SC}}(z) = 1 \tag{4.31}$$

As Ξ increases $f(z)$ gradually shifts from PB to SC behavior. At $\Xi = 10^4$, $f(z)$ is very close to 1 within the range of z shown in the plot, although there is still a noticeable small deviation from unity.

In Fig. 4.3 (b) these results are compared with simulation data (symbols), adapted from Ref. [14]. The value of $f(z)$ was obtained from the simulation results for $n(z)$ using the relation $\mathrm{d}\ln[n(z)]/\mathrm{d}z = -f(z)$.[3] Qualitatively our results agree very well with simulation. Note especially the gradual decrease of $f(z)$ with increasing z for $\Xi = 100$ (diamonds): this value of Ξ is far away from both the weak coupling and the strong coupling limits. The regime where $f(z)$ decreases linearly with z will be further discussed in Sec. 4.4.1.

It was previously conjectured [11] that for all values of Ξ the SC limit is valid close enough to the charged plane. We note, however, that at contact with the plane $f(z)$ is different from unity at small and intermediate values of Ξ. Hence it is not very meaningful to define a region close to the plane where the SC limit is valid, unless Ξ is very large. Values of $f(z)$, extracted from simulation data in Fig. 4.3 (b), suggest the same conclusion, *i.e.*, $f(z)$ does not approach unity at contact with the plane. A more accurate measurement of $f(z)$ in the simulation is desirable because the error bars, as obtained in Fig. 4.3 (b), are quite large.

Results for $n(z)$

The density profile $n(z)$ can be found numerically by integrating Eq. (4.25) and use of the normalization condition (4.8).[4] Figure 4.2 already demonstrated that $n(z)$ coincides with the exact profiles, $n_{\mathrm{PB}}(z)$ and $n_{\mathrm{SC}}(z)$, in the limits of small and large Ξ. Figure 4.4 (a) shows the difference between $n(z)$ and $n_{\mathrm{PB}}(z)$ for $\Xi = 1$, 10, 10^2, and 10^4, as calculated numerically in the TCMF model (continuous lines). These results are compared with simulation data (symbols) [14, 25].

We first observe that the contact theorem is not obeyed in our approximation: $n(0) - n_{\mathrm{PB}}(0) = n(0) - 1$ is different from zero. This is an undesirable property, because the contact theorem is an exact relation. The contact theorem is obeyed in the TCMF model only in the limits of small and large Ξ, where the density profile as a whole agrees with the exact form, and the normalization condition (4.8) enforces $n(0)$ to be correct. The violation at intermediate values of Ξ is finite, small compared to unity, and peaks at Ξ between 10 and 100. At these values of Ξ the overall correction to PB is quite inaccurate at the immediate vicinity of the

---

[3]The numerical differentiation of $\ln[n(z)]$ leads to large error bars because $n(z)$, as obtained from the simulation, is noisy. In principle $f(z)$ could be evaluated more accurately during the simulation run by direct use of Eq. (4.24), *i.e.* by averaging the electrostatic force acting on ions as function of their distance from the plane.

[4]It is also possible to find $n(z)$ using Eqs. (4.20)-(4.21), but integrating Eq. (4.25) is numerically more accurate.
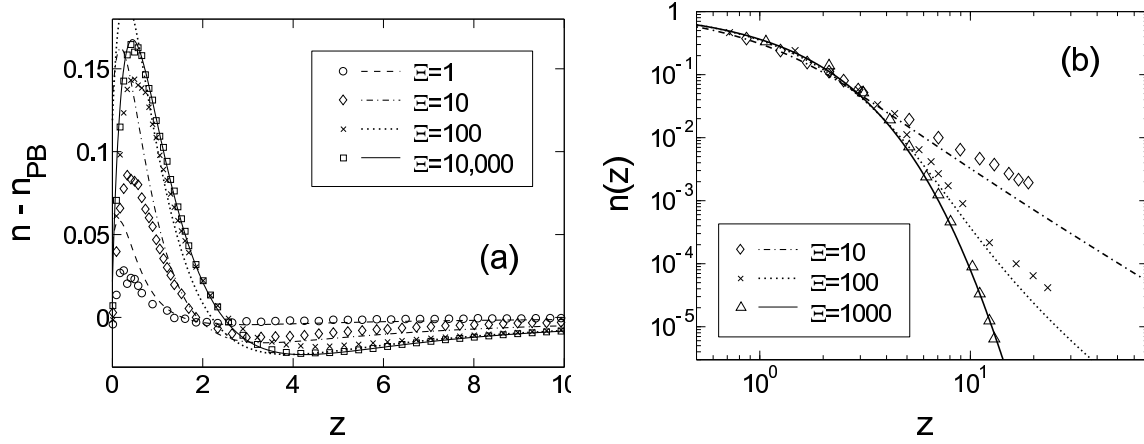
Figure 4.4:   (a) Correction to the PB density profile, $n(z) - n_{\mathrm{PB}}(z)$, calculated numerically using the TCMF model, as function of z (lines). For comparison, symbols show the correction obtained from Monte-Carlo simulation [14, 25]. Four values of Ξ are shown (see legend), 1, 10, 10^2, and 10^4. (b) The density profile itself, $n(z)$, on a wider range of z than in part (a) and using logarithmic scales in both axes (lines - TCMF; symbols - MC simulation).

charged plate. On the other hand, at z larger than 1 our approximated results agree quite well with simulation for all the values of Ξ, as seen in Fig. 4.4 (a).

The violation of the contact theorem in the TCMF model can be traced to a non-zero net force exerted by the ionic solution on itself (see Appendix 4.D). This inconsistency results from the use of a mean field approximation for the distribution of ions around the test charge, while the probability distribution of the test charge itself is given by Eq. (4.20).

It is possible to evaluate exactly the first order correction in Ξ to the PB density profile in the TCMF model, the details of which are given in Appendix 4.E. This correction turns out to be different from the exact first order correction, which was calculated in Ref. [21] using a loop expansion up to one loop order (also shown in the Appendix). It is important to note, however, that the latter correction provides a useful result only for relatively small values of Ξ. At Ξ of order 10 and larger TCMF results are much closer to simulation than those of the loop expansion.

Further comparison with simulation is shown in Fig. 4.4 (b). Here we show the density $n(z)$ itself, rather than the difference with respect to $n_{\mathrm{PB}}(z)$. The data is shown on a larger range of z than in part (a) and a logarithmic scale is used in order to allow small values of $n(z)$ to be observed far away from the plate. In the range shown the TCMF model agrees semi-quantitatively with simulation.

As a summary of this section we can say that the test charge mean field (TCMF) model

captures the essential behavior of the ion distribution at close and moderate distances from the charged plate. Furthermore, all the available data from simulation agrees qualitatively with our approximation's predictions.

4.4 TCMF results far away from the charged plate

Our analysis of the ion distribution far away from the charged plate is done, at first, strictly within the context of the TCMF model, while a discussion of its relevance to the exact theory is deferred to Sec. 4.5. The main question of interest is whether a transition to PB behavior occurs at sufficiently large z, even for large values of Ξ.

As a first step we will identify the important length scales characterizing the density distribution. Let us concentrate first on the size of the correlation hole around a test charge. Naively we may expect this size to be of order Ξ, due to the form of the bare potential, $\Xi/|\mathbf{r} - z_0\hat{\mathbf{z}}|$. A simple argument shows, however, that when the test charge is close to the charged plane the size of the correlation hole is much smaller than Ξ. Assume, roughly, that the mobile ion density is zero within a cylindrical shell of radius R around the test charge. The amount of charge depleted from this cylinder is then equal to $R^2/2$, since the surface charge per unit area is equal to $1/2\pi$ (see Eq. (4.19)). This depleted charge must balance exactly the charge of the test particle, equal to Ξ, yielding a cylinder radius that scales as $\sqrt{\Xi}$ rather than as Ξ.

In order to put this argument to test, Fig. 4.5 (a) shows the density of mobile ions calculated from Eq. (4.19) with a test charge at $z_0 = 1$, having $\Xi = 1,000$. The shape of the correlation hole is roughly cylindrical and its radius is indeed of order $\sqrt{\Xi} \simeq 30$. The influence of the test charge on its surroundings is very non-linear, with a sharp spatial transition from the region close to the test charge, where the density is nearly zero, to the region further away, where the effect of the test charge is very small. At larger separations from the plate the qualitative picture remains the same, as long as z_0 is small compared to $\sqrt{\Xi}$ and provided that $\Xi \gg 1$.

A very different distribution of mobile ions is found when z_0 is of order Ξ, as shown in Fig. 4.5 (b). The coupling parameter is the same as in part (a), $\Xi = 1,000$, but the test charge is now at $z_0 = 1,000$. Instead of showing directly the density of mobile ions as in part (a), the figure shows the ratio between this density and $n_{\mathrm{PB}}(z) = 1/(z + 1)^2$. This ratio is now very close to unity near the charged plane, where most of the ions are present. It is small compared to unity only within a spherical correlation hole around the test charge, whose size is of order Ξ.

The above examples lead us to divide our discussion of the z dependence into two regimes:
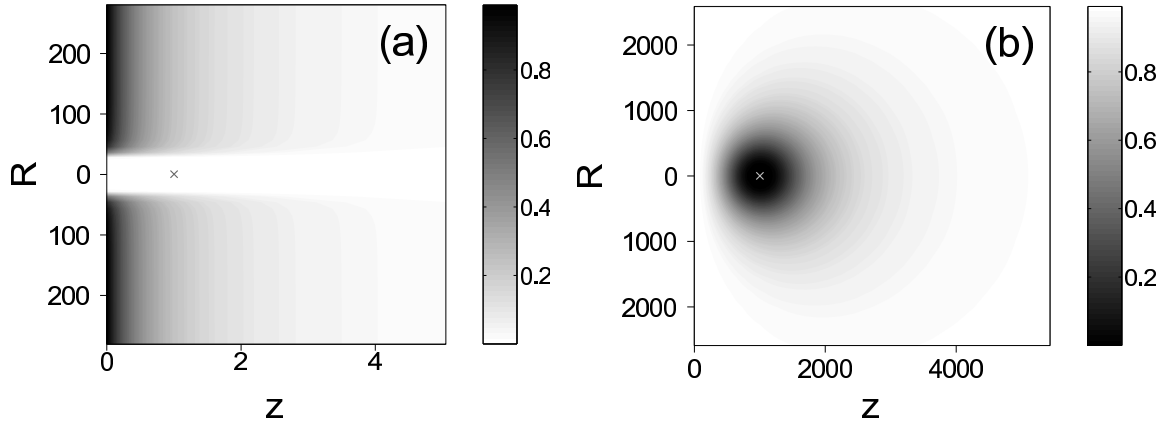
Figure 4.5:   (a) Scaled density of ions around a test charge, positioned at $z_0 = 1$, as obtained from Eq. (4.19). The cross designates the position of the test charge. In cylindrical coordinates the density is a function only of z (horizontal axis) and r (vertical axis). Darker shading in the plot means larger density (see also the legend on the right). The coupling constant is $\Xi = 1{,}000$. For r larger than $\sqrt{\Xi}$ the profile, as function of z, quickly converges to the PB profile, $n_{\mathrm{PB}}(z)$ (b) A similar plot as in part (a), but the test charge is now at $z_0 = \Xi = 1{,}000$. Here the ratio between the density and the PB profile is shown, rather than the density itself. This ratio is everywhere a number between zero (black) and one (white). The effect of the test charge on the ion distribution is large only within a correlation hole around the test charge, having approximately a spherical shape and a radius of order Ξ.

4.4.1 $z < \sqrt{\Xi}$

In order to justify use of the cylindrical correlation hole approximation within this range, let us assume such a correlation hole and calculate the force acting on the test charge:

$$f(z) \simeq \int_0^\infty \mathrm{d}z'\, n_{\mathrm{PB}}(z') \frac{z' - z}{\sqrt{\Xi + (z' - z)^2}} \tag{4.32}$$

where $n_{\mathrm{PB}}(z')$ is given by Eq. (4.11), the radius of the cylindrical region from which ions are depleted is taken as $\sqrt{\Xi}$, and the expression multiplying $n_{\mathrm{PB}}(z')$ is the force exerted by a charged sheet having a circular hole of radius $\sqrt{\Xi}$ and positioned in the plane z'. Figures 4.6 (a) and (b) show a comparison of this approximation (dashed lines) with that obtained from a full numerical solution of Eq. (4.19) (solid lines). The coupling parameter is equal to 10,000 in (a) and to 100 in (b). In both cases the approximation works well up to $z_0 \simeq \sqrt{\Xi}$. In Fig. 4.6 (c) the force acting on a test charge at contact with the plane, $f(0)$, is shown for five values of Ξ between 1 and 10,000 (symbols), and compared with the approximation of Eq. (4.32) (solid line). Note that Eq. (4.32) is not a good approximation when Ξ is of order unity or smaller, since the correlation hole is then small compared to the width of the ion layer.
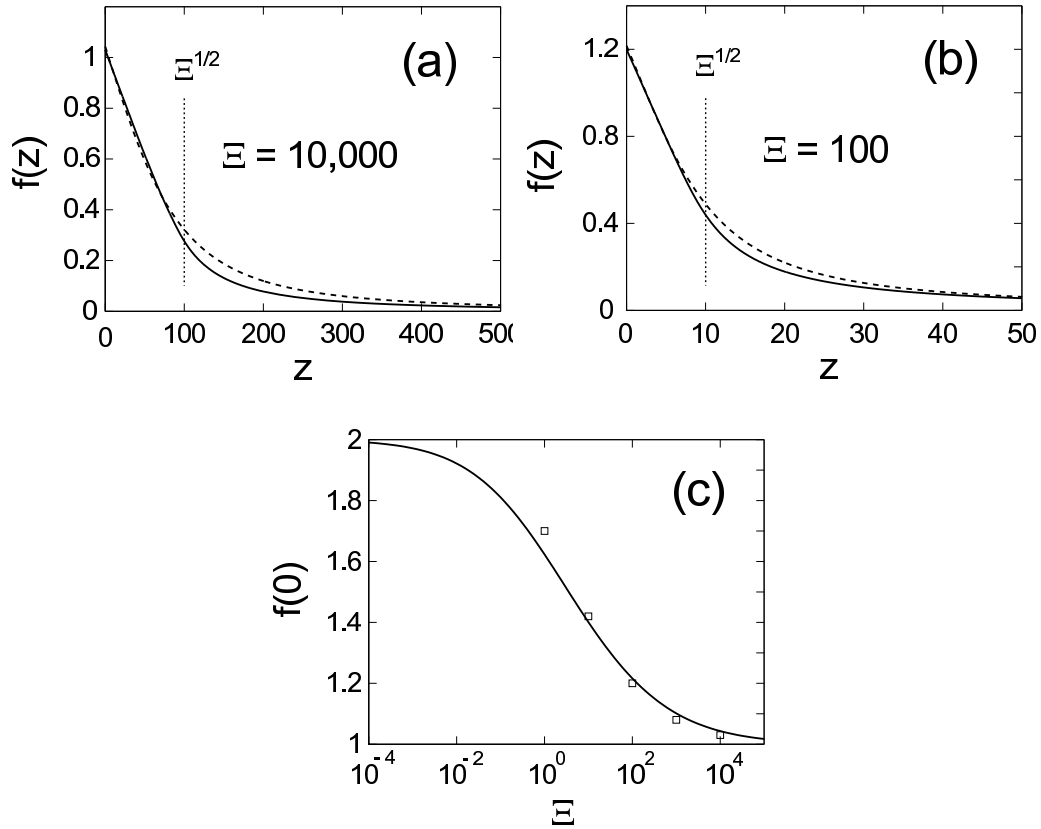
Figure 4.6: (a), (b) Comparison of the approximation to $f(z)$ given by Eq. (4.32) (dashed line), with a full numerical solution of the PDE (solid line). The coupling parameter Ξ is equal to 10,000 in (a) and to 100 in (b). Note that the approximation shown in the dashed line is good up to a distance from the plate equal to about $\sqrt{\Xi}$ in both cases. A distance of $\sqrt{\Xi}$ from the charged plate is designated by the vertical dotted lines. Part (c) shows a comparison of $f(0)$ in the approximation given by Eq. (4.32) (symbols) and in the exact PDE solution (solid line) for a wide range of Ξ values.

4.4.2 $z > \sqrt{\Xi}$

When the test charge is far away from the plane, its effect close to the charged plate is small, suggesting that a linear response calculation may be applicable:

$$f(z) = f_{\text{PB}}(z) + \Xi f_1(z) \tag{4.33}$$

The first term in this equation is the PB value of $f(z)$, while $f_1(z)$ can be calculated using previous results of Ref. [21]:

$$\begin{aligned}
f_1(z) & = \frac{1}{2}\frac{\mathrm{d}g(z)}{\mathrm{d}z} = \frac{1}{4(z+1)^3} \times \Big\{ 8z \\
& - (1+i)\mathrm{e}^{(1-i)z}\left[1 - z + (1-2i)z^2 + z^3\right] \\
& \times E_1\left[(1-i)z\right] \\
& - (1-i)\mathrm{e}^{(1+i)z}\left[1 - z + (1+2i)z^2 + z^3\right] \\
& \times E_1\left[(1+i)z\right] \Big\}
\end{aligned} \tag{4.34}$$

where $g(z)$ was defined in Ref. [21] and is given by Eq. (4.79), and $E_1(z)$ is the exponential-integral function [26]. We prove the first equality of Eq. (4.34) in Appendix 4.E. Figure 4.7 shows $f_1(z)$ (solid line) together with its asymptotic form for large z (dashed line),

$$f_1(z) \simeq \frac{3}{4z^2} \quad , \quad z \gg 1 \tag{4.35}$$

Note that the asymptotic form of $\Xi f_1(z)$ has the same z dependence as the electrostatic force exerted by a metallic surface, equal to $\Xi/(4z^2)$ in our notation, but the numerical prefactor is different.

Although the influence of the test charge is small near the surface, its influence on ions in its close vicinity is highly non-linear and definitely not small. Hence the applicability of Eq. (4.33) is far from being obvious when Ξ is large. We check this numerically by calculating $f(z) - f_{\text{PB}}(z)$ and comparing with $\Xi f_1(z)$. The results are shown in Fig. 4.8 (a), for 5 values of Ξ: 1, 10, 10^2, 10^3, and 10^4.

For each value of Ξ the ratio $(f - f_{\text{PB}})/(\Xi f_1)$ (shown in the plot) approaches unity as z is increased, showing that Eq. (4.33) does become valid at sufficiently large z. The approach is, however, rather slow: a value close to unity is reached only when $z \gg \Xi$. At $z = \Xi$ the ratio is approximately equal to 0.6 in all five cases. We conclude that the linear approximation of Eq. (4.33) is applicable only for $z \gg \Xi$. Note that at these distances from the charged plate the linear correction itself is very small compared to the PB term,

$$\frac{\Xi f_1(z)}{f_{\text{PB}}(z)} \simeq \frac{3\Xi}{4z^2}\frac{z+1}{2} \simeq \frac{3}{8}\frac{\Xi}{z} \ll 1 \tag{4.36}$$
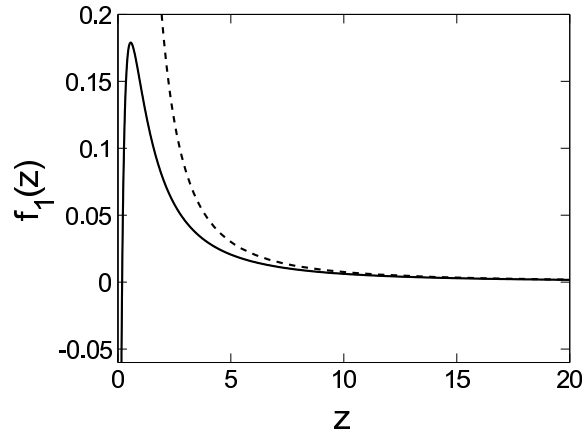
Figure 4.7: First order (linear) term in an expansion of $f(z)$: $f(z) = f_{\mathrm{PB}}(z) + \Xi f_1(z) + \ldots$, Eq. (4.34), as obtained from the loop expansion of Ref. [21]. The dashed line shows the asymptotic form of $f_1(z)$ at large z, $f_1(z) \simeq 3/(4z^2)$.
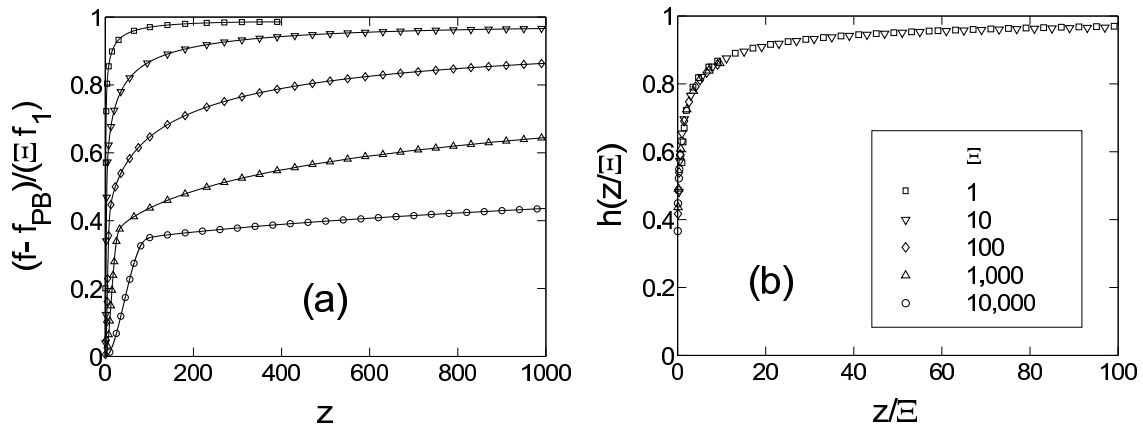
Figure 4.8: Comparison between the correction to $f(z)$ relative to $f_{\mathrm{PB}}(z)$, with the linearized expression $\Xi f_1(z)$. In (a) the ratio $[f(z) - f_{\mathrm{PB}}(z)]/[\Xi f_1(z)]$ is shown as function of z for five different values of Ξ: 1, 10, 10^2, 10^3, and 10^4 (see legend in part (b); symbols show the same quantity as the solid line and are displayed in order to distinguish between the five lines). The ratio approaches unity at z much larger than Ξ. In (b) the same data as in (a) is shown as function of z/Ξ, leading to an almost perfect collapse of the five data sets on a single curve.

Figure 4.9: Same data as in Fig. 9 (b), shown using a logarithmic scale in the horizontal (z/Ξ) axis. The approximated collapse of the different data sets, corresponding to different values of Ξ, is seen to be valid only in the regime $z \gtrsim \sqrt{\Xi}$. The vertical arrows mark $z = 1.5\sqrt{\Xi}$ for $\Xi = 1$, 10, 10^2, and 10^3, above which the scaling (4.3) is approximately valid.

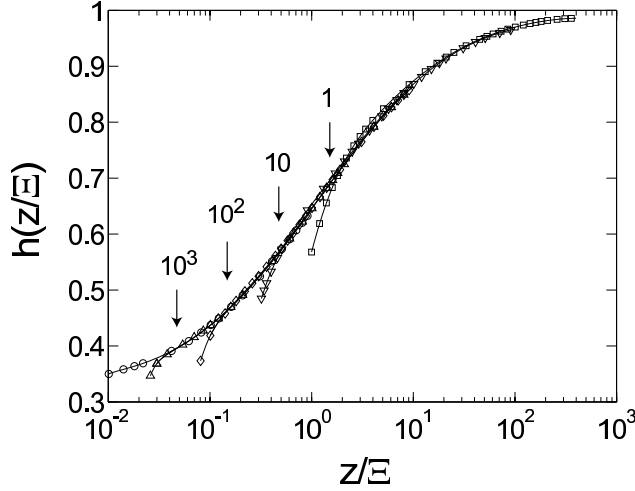where we also assumed that $z \gg 1$ and used Eq. (4.35).

Further insight on the results shown in Fig. 4.8 (a) is obtained by noting that all of them approximately collapse on a single curve after scaling the z coordinate by Ξ. This curve, denoted by $h(z/\Xi)$, is shown in Fig. 4.8 (b):

$$f(z) - f_{\mathrm{PB}}(z) \simeq \Xi f_1(z) \times h\left(\frac{z}{\Xi}\right) \tag{4.37}$$

In order to demonstrate at what range of z values this scaling result is valid the same data is shown in Fig. 4.9 using a logarithmic scale in the horizontal (z/Ξ) axis. It is then seen clearly that (4.37) holds for z/Ξ larger than a minimal value, which is proportional to $\Xi^{-1/2}$. The vertical arrows designate $z/\Xi = 1.5/\sqrt{\Xi}$ for each value of Ξ, approximately the point where the scaling becomes valid. Returning to consider z itself, we conclude that (4.37) holds for $z \gtrsim 1.5\sqrt{\Xi}$. This result justifies the separation of the z dependence into two regimes, $z < \sqrt{\Xi}$ and $z > \sqrt{\Xi}$.

We finally turn to consider the ion density $n(z)$. Using Eqs. (4.35) and (4.37) we can write

$$-\frac{\mathrm{d}}{\mathrm{d}z}n(z) = f(z) \simeq f_{\mathrm{PB}}(z) + \frac{1}{\Xi} \cdot \frac{3}{4}\left(\frac{z}{\Xi}\right)^{-2} h\left(\frac{z}{\Xi}\right) \tag{4.38}$$

which leads, upon integration, to the approximate scaling result,

$$n(z) \simeq c_0(\Xi)\frac{1}{(z+1)^2}\eta\left(\frac{z}{\Xi}\right) \tag{4.39}$$
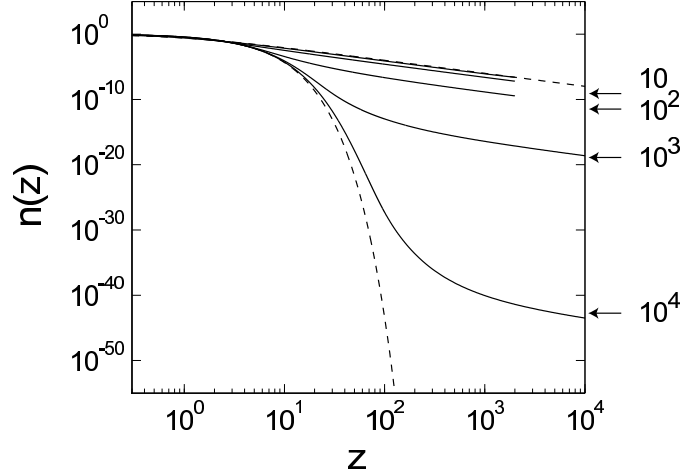
Figure 4.10: Scaled ion density, $n(z)$ calculated using the TCMF model, shown for five different values of Ξ (solid lines, top to bottom): 1, 10, 10^2, 10^3, and 10^4. A logarithmic scale is used on both axis, allowing the behavior far away from the charged plate to be seen. The dashed lines show $n_{\mathrm{PB}}(z)$ (upper dashed line) and $n_{\mathrm{SC}}(z)$ (lower dashed line). At $z \gg \Xi$ the density profile is proportional to $n_{\mathrm{PB}}(z)$, with a prefactor whose logarithm scales as $\sqrt{\Xi}$. To demonstrate this the horizontal arrows mark the value of $\exp(-0.8\sqrt{\Xi}) \times n_{\mathrm{PB}}(10^4)$ for $\Xi = 10$, 10^2, 10^3, and 10^4. The prefactor 0.8 is an approximate fitting parameter.

where

$$\ln[\eta(u)] = -\frac{3}{4} \int_u^\infty \mathrm{d}u' \, \frac{h(u')}{u'^2} \tag{4.40}$$

The prefactor $c_0(\Xi)$ depends, through the normalization condition, on the behavior of $n(z)$ close to the charged plane where the scaling form of Eq. (4.39) is not valid. Equation (4.39) is indeed validated by the numerical data and applies for $z \gtrsim \sqrt{\Xi}$ and $\Xi \gg 1$.

The density itself, $n(z)$, is plotted in Fig. 4.10 using a semi-logarithmic scale, for $\Xi = 1$, 10, 10^2, 10^3, and 10^4. At $z \gg \Xi$ $n(z)$ is proportional to $n_{\mathrm{PB}}(z)$, as expected from Eq. (4.39). The prefactor c_0 is extremely small for large Ξ. We recall that c_0 is mainly determined by the behavior close to the charged plane, where $f(z)$ is of order unity up to $z \lesssim \sqrt{\Xi}$. Following this observation we can expect $\ln[c_0(\Xi)]$ to scale roughly as $\sqrt{\Xi}$. This estimate is validated by the numerical results and is demonstrated in the figure using the horizontal arrows. For $\Xi = 10$, 10^2, 10^3, and 10^4 these arrows show an estimate for $n(z)$ at $z = 10^4$, given by

$$n_{\mathrm{PB}}(z) \times \exp(-0.8\sqrt{\Xi})$$

in very good agreement with the actual value of n.

4.5   Further Discussion

At this point we may ask to what extent our results represent the behavior of $n(z)$ in the exact theory. Before discussing this question we turn our attention for a moment to the system that our problem was mapped into in Eq. (4.19) – that of a single ion of valence Ξ in contact with a charged plane and its monovalent counterions. The results of Sections 4.3 and 4.4 can be regarded as exact for such a system, provided that the monovalent ions are weakly correlated (having, by themselves, a small coupling parameter as determined from their charge and that of the planar surface). These results are thus of direct relevance to the interaction of a large multivalent macroion with a charged surface that is immersed in a weakly correlated solution of counterions.

Returning to the original question, we separate our discussion according to the scaling results of the numerical analysis:

4.5.1 $z < \sqrt{\Xi}$

When Ξ is very large a test charge at $z < \sqrt{\Xi}$ is essentially decoupled from the rest of the ionic solution, feeling only the force exerted by the charged plane. This is the reason why an exponential decay, $n(z) \sim \exp(-z)$, is obtained in our model, as well as in simulation and in the perturbative strong coupling expansion of Ref. [11]. However, at intermediate values of Ξ such as 10, 100, or 1000 our results show that this exponential decay is only a rough approximation. The decoupling of a test charge from the rest of the ions is only partial, even at $z = 0$, leading to a value of $f(z)$ that is (*i*) larger than unity at $z = 0$ and (*ii*) considerably smaller than unity at $z = \sqrt{\Xi}$. Both of these predictions are validated by simulation, as shown in Fig. 4.3 (b).

The quantitative agreement in $f(z)$ between our model and simulation is surprisingly good, considering that the ionic environment surrounding the test charge is different in our approximation, compared to the exact theory. This good agreement can be attributed to the correct length scales that characterize the approximate ionic environment: $\sqrt{\Xi}$ in the lateral direction, and 1 in the transverse direction. Indeed, in the lateral direction our results can be compared with pair distributions that were obtained in Monte-Carlo simulation [14]. The pair distributions found in the simulation are characterized by a strong depletion within a correlation hole having diameter of order $\sqrt{\Xi}$, in great similarity to Fig. 4.5 (a). What is not captured by our approach is that multiple maxima and minima exist at $\Xi \gtrsim 100$.[5] Nevertheless, even at the very large coupling parameter value $\Xi = 10^4$ these oscillations decay quite rapidly with lateral

---

[5]In principle, a more accurate evaluation of the pair distribution function, possibly capturing its oscillatory nature, may be obtained from an approach similar to the TCMF with two test charges instead of one.

distance, and we can still say that the TCMF model captures the most significant feature of the pair distribution (namely, the structure of the correlation hole).

4.5.2 $z > \sqrt{\Xi}$

Throughout most of this section we concentrate on the case $z > \Xi$, while a short discussion of the range $\sqrt{\Xi} < z < \Xi$ is presented at the end of this section.

Our model predicts a transition to algebraic decay of $n(z)$ at $z \gtrsim \Xi$. Similar predictions were made in Ref. [10] and in Ref. [14], where it was estimated that mean field results are valid for $z > \Xi \ln \Xi$ based on a perturbative expansion around mean field. There are currently no available results from simulation in this regime.

A mean field behavior is obtained in our model in the sense that

$$f(z) \simeq f_{\mathrm{PB}}(z) = \frac{1}{z+1} \tag{4.41}$$

decays as $1/z$ for large z. Nevertheless the finer details in our results do not match the form predicted by PB theory. The starting point for the following discussion is an hypothesis that sufficiently far from the plate the exact density follows a PB form,

$$n_{\mathrm{asym}}(z) = \frac{1}{(z+b)^2} \tag{4.42}$$

where b (or μb in the original, non-scaled coordinates) is an effective Gouy-Chapman length, characterizing the ionic solution far away from the plate.

The asymptotic density profile found in our approximation, $n(z) = c(\Xi)/(z+1)^2$, is different from Eq. (4.42). To understand this difference let us explain first the asymptotic behavior of $f(z)$: it decays in the TCMF model as $1/(z+1)$ because beyond the correlation hole the test charge is surrounded by an ion density of the form $n_{\mathrm{PB}} = 1/(z+1)^2$. This form is different from the profile $n(z)$ that is eventually obtained by integrating $f(z)$ – an inconsistency which is the source of the difference between $f(z)$ in our approximation and the hypothesized form $f(z) \sim 1/(z+b)$ (see also the discussion in Appendix 4.D).

The behavior of our approximate $f(z)$ leads to a decay of $n(z)$ of the form $1/(z+1)^2$. The normalization condition for $n(z)$ is then enforced through a small prefactor $c(\Xi)$. In comparison, in the hypothesized form (4.42) the prefactor must be 1 and the normalization is achieved by a large value of b. Note that b must be an extremely large number for large values of Ξ: due to the exponential decay of $n(z)$ at $z \lesssim \sqrt{\Xi}$ the logarithm of b must be at least of order $\sqrt{\Xi}$.

Further insight on the behavior at $z > \Xi$ can be obtained using the exact equation (4.22):

$$\frac{\mathrm{d}}{\mathrm{d}z} \ln [n(z)] = -f(z) \tag{4.43}$$

where $f(z)$ is now the mean (thermally averaged) electrostatic force acting on a test charge at distance z from the plate, in the exact theory.

For the mean field form $n_{\mathrm{asym}}(z)$ to be correct, the contribution to $f(z)$ coming from the influence of the test charge on its environment must be small compared to the mean field force, which is given by $1/(z+b)$. Following our results from the previous section, the former quantity is given by $\alpha\Xi/z^2$, where α is of order unity. Using the mean field equation (4.19) we obtained $\alpha = 3/4$; in the exact theory, and for large Ξ, where ions form a much more localized layer close to the plane than in mean field, it is plausible that $\alpha = 1/4$, as in the force acting on a test charge next to a conducting surface [10, 14]. In any case, for Eq. (4.42) to represent correctly the decay of $n(z)$ we must have

$$\frac{\alpha\Xi}{z^2} < \frac{1}{z+b} \tag{4.44}$$

leading to the result $z \gtrsim (\Xi b)^{1/2}$ which is exponentially large due to b. Up to this crossover distance the decay of $n(z)$ is dominated by the correlation-induced interaction with the ions close to the plate.

We conclude that for a very large range of z values the decay of $n(z)$ must be different from Eq. (4.42). At the same time, a mean field argument is probably applicable, because the density of ions is very small in this regime: we may presume that the contribution to $f(z)$ can be divided into two parts – one part, coming from ions far away from the plate, which is hardly influenced by the test charge; and a second part, coming from ions close to the charged plate, where the test charge influence on $f(z)$ is given by $\alpha\Xi/z^2$. This reasoning leads to the following differential equation for $n(z)$:

$$\frac{\mathrm{d}^2}{\mathrm{d}z^2}\ln[n(z)] = 2n(z) + \frac{2\alpha\Xi}{z^3} \tag{4.45}$$

whose detailed derivation is given in Appendix 4.F. By defining $n(z) = \exp(-\phi + \alpha\Xi/z)$ Eq. (4.45) is recast in the form:

$$\frac{\mathrm{d}^2\phi}{\mathrm{d}z^2} = -2\exp\left(-\phi + \frac{\alpha\Xi}{z}\right) = -2n(z) \tag{4.46}$$

showing that mean field theory is applicable, but an external potential $-\alpha\Xi/z$, coming from the ions close to the plate, must be included in the PB equation. In practice, for large Ξ this equation will lead to a decay of the form $n(z) \sim \exp(\alpha\Xi/z)$ as suggested also in Refs. [10, 14], while a crossover to an algebraic decay will occur only at a distance of at least $\left[\Xi\exp(\sqrt{\Xi})\right]^{1/2}$ where Eq. (4.44) has been used and prefactors of order unity, inside and outside the exponential, are omitted. A numerical solution of Eq. (4.46) may be useful in order to describe the ionic

layer at intermediate values of Ξ (of order 10 - 100), where both mean field and correlation-induced forces are of importance at moderate distances from the plate. In order to test this idea quantitatively more data from simulation is required.

Finally we discuss the case where $z > \sqrt{\Xi}$ but z is not large compared to Ξ. Let us also assume that Ξ is very large, so that most of the ions are much closer to the plate than a test charge fixed at $z\hat{\mathbf{z}}$. Within the TCMF model the effect of the test charge on ions close to the plate is nonlinear, leading to the scaling result of Eq. (4.37). Similarly, in the exact theory it is not clear whether the correlation-induced force acting on the test charge is of the form $\alpha\Xi/z^2$, since the effect of the test charge on ions close to the plate is not a small perturbation. Hence we believe that the relevance of Eq. (4.46) for $z < \Xi$, and the behavior of $f(z)$ in this regime, merit further investigation.[6]

4.6 Conclusion

In this work we showed how ion correlation effects can be studied by evaluating the response of the ionic solution to the presence of a single test particle. Although we calculated this response using a mean field approximation, we obtained exact results in the limits of small and large Ξ, and qualitative agreement with simulation at intermediate values.

The approach taken in this work demonstrates that for highly correlated ionic liquids it is essential to treat the particle charge in a non-perturbative manner. Once a single ion is singled out, even a mean field approximation applied to the other ions provides useful results. This scheme, called the test-charge mean field (TCMF) model, provides a relatively simple approximation, capturing the essential effects of strong correlations – to which more sophisticated treatments can be compared.

Technically what is evaluated in this work is the ion-surface correlation function. Consideration of correlation functions of various orders leads naturally to liquid state theory approximations [27], some of which are very successful in describing ionic liquids [22]. In particular these approximations usually treat the ion-ion correlation function in a more consistent manner than the approximation used in this work, thus possibly alleviating some of the undesirable features of the TCMF model presented here, such as the violation of the contact theorem. The main advantage of the TCMF model is its simplicity, allowing the behavior of $n(z)$ to be understood in all the range of coupling parameter values in terms of $f(z)$, the force acting on a test charge.

---

[6]In order to improve over TCMF results it may by useful to treat mobile ions close to the plane as a two dimensional layer, while going beyond the mean field approximation of the TCMF model in their treatment. The response to the test charge at $\mathbf{r} = z_0\hat{\mathbf{z}}$ may then help understand the decay of $n(z)$ in the full three dimensional problem, through Eq. (4.25). Such a calculation is beyond the scope of the present work.

Furthermore, the exact equation (4.22), which does not involve any approximation, is a useful tool in assessing correlation effects – as was done, for example, in this work in the end of Sec. 4.5.

It will be useful to summarize the main results obtained in this work. First, the exact equation (4.22) provides a simple explanation of the exponential decay of the density profile in the strong coupling limit. In light of this equation, exponential decay is expected as long as the test charge is decoupled from the rest of the ionic solution. Note that there is no necessity for long range order to exist in order for the exponential decay to occur, as was emphasized also in Ref. [10]. Indeed, within our TCMF model the ion distribution around a test charge does not display any long range order (see Fig. 4.5 (a)) and yet simulation results, in particular in the strong coupling limit, are recovered very successfully.

Second, the characteristic size of the correlation hole around an ion close to the plane, $\sqrt{\Xi}$, plays an important role in determining the density profile. For very large Ξ the profile decays exponentially up to $z \lesssim \sqrt{\Xi}$, beyond which a crossover to a less rapid decay occurs. For intermediate values of the coupling parameter $z = \sqrt{\Xi}$ is still an approximate boundary between regimes of different behavior of $n(z)$, but the density profile at $z < \sqrt{\Xi}$ does not decay in the simple exponential form $\exp(-z)$. In this sense one cannot speak of a region close to the plate where strong coupling results are valid.

For $z \gtrsim \Xi$ our approximation predicts a transition to an algebraic decay of $n(z)$, of the form $c(z)/(z+1)^2$, where the prefactor $c(z)$ is exponentially small for large Ξ. A different asymptotic behavior of the form $1/(z+b)^2$ is probably valid at very large z, but is not predicted by the TCMF model. Arguments presented in Sec. 4.5, based on the exact equation (4.22), lead to the conclusion that for large Ξ the latter form (with a constant value of b) can only be valid at extremely large values of z, while suggesting that at all distances from the plate larger than Ξ a modified mean field equation, Eq. (4.46), is valid. This equation, matched with the behavior of the ion distribution close to the charged plate, ultimately determines the value of the effective Gouy-Chapman length b.

Finally, as a by-product of the analysis of Sec. 4.4, we obtain scaling results for the interaction of a high-valent counterion with a charged plane immersed in a weakly correlated ionic liquid. All the results of Sec. 4.4 and in particular the scaling form (4.37), valid for $z \gtrsim \sqrt{\Xi}$, can be regarded as exact in such a system.

Our approach can be easily generalized to more complicated geometries than the planar one, although the practical solution of the PB equation with a test charge may be more difficult in

these cases. Other natural generalizations are to consider non-uniformly charged surfaces and charged objects in contact with a salt solution. Beyond the TCMF approximation of Eqs. (4.19), (4.20), and (4.21), the exact equation (4.22) always applies and can be a very useful tool for assessing correlation effects near charged macromolecules of various geometries.

We conclude by noting that important questions remain open regarding the infinite planar double layer, which is the most simple model of a charged macroion in solution. One such issue, on which the present work sheds light, is the crossover from a strongly coupled liquid close to the charged plate to a weakly correlated liquid further away. In particular, the precise functional dependence of the effective Gouy-Chapman length b on Ξ is still not known. More simulation results, in particular at large distances from the charged plate, and a direct evaluation of $f(z)$ from simulation, may be useful in order to gain further understanding and to test some of the ideas presented in this work. Another important issue, which has not been addressed at all in the present work, is the possible emergence of a crystalline long range order parallel to the plane at sufficiently large values of the coupling parameter. Although plausible arguments have been presented for the occurrence of such a phase transition at $\Xi \gtrsim 3 \times 10^4$ [10], its existence has not been proved.

4.A Mean field free energy

In this appendix we show how the mean field free energy (4.18) is obtained as an approximation to $F(z_0)$, Eq. (4.14). We start from a general expression for the grand canonical potential of an ionic solution interacting with an external and fixed charge distribution $\sigma(\mathbf{r})$. In the mean field approximation [21, 28],

$$
\begin{aligned}
\Omega \;=\; & \int \mathrm{d}^3\mathbf{r} \left\{ -\frac{1}{8\pi l_B q^2} \left[\nabla \phi(\mathbf{r}) \right]^2 + \frac{\sigma(\mathbf{r})\phi(\mathbf{r})}{q} \right. \\
& \left. - \lambda \Theta(\mathbf{r}) \mathrm{e}^{-\phi(\mathbf{r})} \right\}
\end{aligned}
\tag{4.47}
$$

where q is the valency of the ions, λ is the fugacity, $\Theta(\mathbf{r})$ is equal to 1 in the region accessible to the ions and to zero elsewhere (equal in our case to $\theta(z)$, the Heaviside function), and Ω is given in units of $k_B T$. Requiring an extremum with respect to φ, the reduced electrostatic potential, yields the PB equation which determines the electrostatic potential and the actual value of Ω. We use equation (4.47), which is given in the grand-canonical ensemble, because it is widely used in the literature [21, 28]. In Ref. [21] Eq. (4.47) is derived systematically as the zero-th order term in a loop expansion of the exact partition function.

Inspection of Eq. (4.14) shows that it describes the free energy of an ionic solution interacting

with an external charge distribution having the following parameters,

$$
\begin{aligned}
\text{valency} \qquad & q && = && \sqrt{\Xi} \\
\text{Ext. potential} \qquad & \sigma(\mathbf{r}) && = && \frac{1}{\sqrt{\Xi}}\left[-\frac{1}{2\pi}\delta(z) + \Xi\delta(\mathbf{r} - z_0\hat{\mathbf{z}})\right] \\
\text{Bjerrum length} \qquad & l_B && = && 1
\end{aligned}
\tag{4.48}
$$

In the second line (external potential) the first term comes from the uniformly charged plate and the second term comes from the fixed test charge. Plugging these values in Eq. (4.47) yields,

$$
\begin{aligned}
\Omega \;=\; & \frac{1}{\Xi}\int d^3\mathbf{r}\left\{-\frac{1}{8\pi}(\nabla\varphi)^2 - \lambda\theta(z)e^{-\varphi}\right. \\
& +\; \left.\varphi\left[-\frac{1}{2\pi}\delta(z) + \Xi\delta(\mathbf{r} - z_0\mathbf{z})\right]\right\}
\end{aligned}
\tag{4.49}
$$

In order to obtain Eq. (4.18) two modifications are required. First, we need to return to the canonical ensemble by adding μN to Ω, where N is the total number of ions. Noting that $\mu = \ln\lambda$ and that from charge neutrality $qN = -\int d^3\mathbf{r}\sigma(\mathbf{r})$, this modification yields the extra term that is proportional to $\ln\lambda$ in Eq. (4.18). Second, we note that Ω includes the Coulomb self-energy of the charged plane and of the test charge. This infinite term does not depend on z_0 and should be subtracted from Ω since it is not included in the definition of $F(z_0)$, Eq. (4.14).

We finally note that the results of this Appendix can also be obtained directly from the canonical partition function, as expressed by Eq. (4.14).

4.B   Derivation of Identity (4.23)

We would like to evaluate the variation $\delta F_{\text{PB}}(z_0)/\delta z_0$, where F_{PB} is given by Eq. (4.18). Note that φ itself depends on z_0. However the first derivative of F_{PB} with respect to $\varphi(\mathbf{r})$ is zero. Hence the only contribution to $\delta F_{\text{PB}}/\delta z_0$ comes from the explicit dependence on z_0:

$$
\begin{aligned}
\frac{\delta F_{\text{PB}}[z_0]}{\delta z_0} \;=\; & \frac{1}{\Xi}\int d^3\mathbf{r}\,(\varphi - \ln\lambda)\Xi\frac{\partial}{\partial z_0}\delta(\mathbf{r} - z_0\hat{\mathbf{z}}) \\
\;=\; & -\left.\frac{\partial\varphi}{\partial z}\right|_{\mathbf{r}\,=\,z_0\hat{\mathbf{z}}}
\end{aligned}
\tag{4.50}
$$

It is also instructive to derive this identity within the exact theory. Equation (4.14) can be written as follows:

$$
\exp[-F(z_0)] = \frac{1}{(N-1)!}\int\prod_{i=1}^{N-1} d^3\mathbf{r}_i\exp\left(-H_{z_0}\{\mathbf{r}_i\}\right)
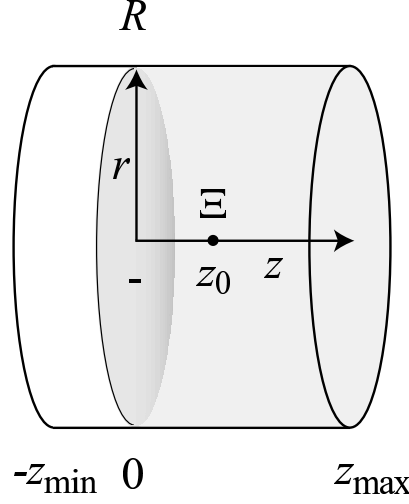\tag{4.51}
$$

Figure 4.11: Schematic illustration of the setup used to solve numerically the PDE (4.19). The equation is solved in a finite cylindrical cell, extending from $-z_{\min}$ to $z_{\max}$ in the z axis and from 0 to R in the r axis. The charged plane is at $z = 0$ and ions are only present for $z > 0$. Neumann boundary conditions ($\nabla\varphi \cdot \hat{\mathbf{n}} = 0$) are imposed at the cell boundaries. The test charge is at $\mathbf{r} = z_0\hat{\mathbf{z}}$

where the N-th charge is fixed at $\mathbf{r} = z_0\hat{\mathbf{z}}$:

$$H_{z_0}\{\mathbf{r}_i\} = -z_0 - \sum_{i=1}^{N-1} z_i - \sum_{i=1}^{N-1} \frac{\Xi}{|\mathbf{r}_i - z_0\hat{\mathbf{z}}|} - \sum_{j>i} \frac{\Xi}{|\mathbf{r}_i - \mathbf{r}_j|} \tag{4.52}$$

Differentiating with respect to z_0 yields:

$$\frac{\delta F(z_0)}{\delta z_0} = -\left\langle \frac{\partial H_{z_0}}{\partial z_0} \right\rangle = -\left\langle -1 + \sum_{i=1}^{N-1} \frac{\Xi(z_0 - z_i)}{|\mathbf{r}_i - z_0\hat{\mathbf{z}}|^3} \right\rangle \tag{4.53}$$

where the averaging is performed over all configurations of the $N - 1$ ions with the weight $\exp(-H_{z_0}\{\mathbf{r}_i\})$. This quantity is the mean electrostatic field acting on a test charge at $z_0\hat{\mathbf{z}}$.

4.C Numerical scheme

Numerically solving a non-linear PDE such as (4.19) requires careful examination of the solution behavior. The purpose of this section is to explain the numerical scheme used in this work, and in particular the parameters required to obtain a reliable solution.

Finite cell

We solve Eq. (4.19) as a two dimensional problem in the coordinates r and z, making use of the symmetry of rotation around the z axis. The problem is defined within a finite cell of cylindrical

shape, shown schematically in Fig. 4.11. The negatively charged plate is at $z = 0$ and ions are only allowed in the region $z > 0$, marked as the gray-shaded region in the plot.

We impose a boundary condition of zero electrostatic field,

$$\nabla\varphi \cdot \hat{\mathbf{n}} = 0, \tag{4.54}$$

at the cell boundaries: $z = -z_{\min}$, $z = z_{\max}$, and $r = R$. The cell size, as determined by these boundaries, must be sufficiently large, as will be further discussed below.

In the numerical solution it is necessary to solve φ for the electrostatic potential at positive as well as negative z.[7] Note that a boundary condition such as (4.54) at $z = 0$ would correspond to zero dielectric constant at $z < 0$, while we are interested in the case of continuous dielectric constant across the plate.

Differential equation

The source term in Eq. (4.19) diverges at $z = 0$ and at $\mathbf{r} = z_0\hat{\mathbf{z}}$. We avoid this difficulty by shifting the potential:

$$\varphi = \psi + |z| + \frac{\Xi}{|\mathbf{r} - z_0\hat{\mathbf{z}}|} \tag{4.55}$$

and solving for ψ, which is the potential due only to the mobile ions. The equation for ψ,

$$\nabla^2\psi = -4\pi\lambda\theta(z)\exp\left(-\psi - z - \frac{\Xi}{|\mathbf{r} - z_0\hat{\mathbf{z}}|}\right) \tag{4.56}$$

is solved with a Neumann boundary condition for ψ, derived from Eqs. (4.54) and (4.55). Note that, unlike φ, ψ is well behaved at $z_0\hat{\mathbf{z}}$. The nonlinear equation (4.56) can be solved by iterative solution of a linear equation (see, for example, [29, 30]),

$$\begin{aligned}
\nabla^2\psi_n &= -4\pi\lambda\theta(z)\exp\left(-\psi_{n-1} - z - \frac{\Xi}{|\mathbf{r} - z_0\hat{\mathbf{z}}|}\right) \\
&\times \; [1 - (\psi_n - \psi_{n-1})]
\end{aligned} \tag{4.57}$$

where ψ_n represents the n-th iteration.

Grid and solution method

In the coordinates r,z the cylindrical cell is a rectangular domain,

$$[0, R] \times [-z_{\min}, z_{\max}].$$

---

[7]This situation is different from that of the PB equation with no test charge, in which the electrostatic potential depends only on z. The boundary condition at $z = 0$, for the case of zero dielectric constant at $z < 0$, is then sufficient in order to solve for the potential at $z > 0$.

We use bi-cubic Hermite collocation [31] in this domain in order to translate the PDE into a set of linear algebraic equations on a grid. These equations are then solved using Gauss elimination with scaled partial pivoting. Storing the band matrix representing the linear equations requires approximately $48 \times N_r^2 \times N_z$ memory cells, where N_r and N_z are the number of grid points in the r and z directions, respectively [31]. Because this number can be very large, it is essential to use a variably spaced grid in both of the coordinates. We use the following scheme:

r coordinate: In the absence of a test charge, an arbitrarily coarse grid can be used in the r direction, due to the translational symmetry parallel to the charged plane. In our case (where a test charge is present) the grid spacing is determined by the distance from the test charge, as follows,

$$\frac{\mathrm{d}n}{\mathrm{d}r} = \frac{n_r}{r + r_{\mathrm{grid}}}, \tag{4.58}$$

where n_r and r_{grid} are two fixed parameters, while n stands for the grid point index and $\mathrm{d}n/\mathrm{d}r$ is the number of grid points per unit increment of the radial coordinate. This spacing is approximately uniform up to the threshold r_{grid}, whereas for $r \gg r_{\mathrm{grid}}$ it is proportional to $1/r$. The grid points are then of the form

$$r_n = r_{\mathrm{grid}} \times \left[\exp\left(\frac{n}{n_r} \right) - 1 \right] \tag{4.59}$$

In practice r_{grid} is chosen approximately proportional to $\sqrt{\Xi}$, in order to allow the structure of the correlation hole to be represented faithfully.

z coordinate: In this coordinate the grid spacing is influenced by the distance from the charged plate as well as the distance from the test charge. We describe separately the spacing determined from each of these two criteria; the actual grid is obtained by using the smaller of the two spacings at each point.

(i) Distance from the plate: we use a grid spacing proportional to the derivative of $\varphi_{\mathrm{PB}}(z)$:

$$\frac{\mathrm{d}n}{\mathrm{d}z} \propto \frac{2}{z + 1} \tag{4.60}$$

Ignoring, for the moment, the distance from the test charge, Eq. (4.60) leads to grid points of the form

$$z_n = \exp(n \cdot D) - 1 \tag{4.61}$$

where the parameter D is the grid spacing close to the charged plate. A similar scheme is used in the negative z half-space.

(ii) Distance from the test charge: we use a form similar to (4.58),

$$\frac{\mathrm{d}n}{\mathrm{d}z} = \frac{n_z}{|z - z_0| + z_{\mathrm{grid}}}, \tag{4.62}$$

Ξ	$z_{\min}$	$z_{\max}$	R	D	z_{grid}	n_z	r_{grid}	n_r
10^4	10^4	10^5	10^5	0.2	5000	5	100	5
10^3	10^4	10^5	10^5	0.2	500	4	33	4
10^2	10^3	10^4	10^4	0.2	50	4	10	4
10	10^3	10^4	10^4	0.2	5	4	3	4
1	4×10^2	4×10^3	4×10^3	0.2	0.5	4	1	4
0.1	80	800	800	0.2	0.05	4	0.2	4

Table 4.2: Parameters used in numerical solution of the PDE.

In practice, the threshold z_{grid} is chosen proportional to Ξ, in contrast to r_{grid} which is chosen proportional to $\sqrt{\Xi}$.

Parameters

The parameters that were used to obtain the numerical results presented in this work are summarized in Table 4.2. We compared our results with those obtained with (a) Increasing $z_{\min}$, $z_{\max}$, and R by a factor of 10; and (b) decreasing the grid spacing by a factor of 2, both in the r and in the z coordinates. The influence of these changes was found to be negligible on all the data presented in this work.

4.D   Contact theorem

In this appendix we derive the contact theorem [24] in a way that highlights the reason why it is not obeyed in our approximation. We start from an exact expression for the free energy,

$$F = -\ln \int_a^\infty \mathrm{d}z' \exp[-F(z')] \tag{4.63}$$

where the charged plate is at $z = a$. This plate position can be chosen arbitrarily, hence $\partial F / \partial a = 0$:

$$0 = \left. \frac{\partial F}{\partial a} \right|_{a=0} = n(0) - \int_a^\infty \mathrm{d}z'\, n(z') \frac{\partial F}{\partial z}(z') \tag{4.64}$$

where we used the relations

$$n(z) = \frac{\exp[-F(z)]}{\int_0^\infty \mathrm{d}z' \exp[-F(z')]} \tag{4.65}$$

and

$$\left. \frac{\partial F(z)}{\partial a} \right|_z = - \left. \frac{\partial F(z)}{\partial z} \right|_a \tag{4.66}$$

We now use Eq. (4.22) to obtain,

$$n(0) - \int_0^\infty n(z) \frac{\partial}{\partial z} \langle \varphi(\mathbf{r}; z) \rangle \bigg|_{\mathbf{r} = z_0 \hat{\mathbf{z}}} = 0 \qquad (4.67)$$

The second term in this equation is the average electrostatic force acting on the ions per unit area. This force can be separated into two contributions. The first one, exerted by the charged plane, is equal to $-\int \mathrm{d}z'\, n(z') = -1$ because the plane applies an electrostatic force which does not depend on z' and is equal to unity in our rescaled coordinates. The remaining contribution to the force, exerted by the ions on themselves, must be zero due to Newton's third law, leading to the result $n(0) = 1$.

The discussion up to now was exact. It also applies to PB theory, where the self consistency of the mean field approximation ensures that Newton's third law is obeyed. On the other hand, within our approximation the force exerted by the ions on themselves,

$$\int_0^\infty n(z)\, [f(z) - 1]$$

is not zero. This inconsistency can be traced to a more fundamental inconsistency which is briefly described below.

The probability to find the test charge at $\mathbf{r} = z\hat{\mathbf{z}}$ and a mobile ion at $\mathbf{r}'$ is proportional, in our approximation, to

$$n(z)n(z')g(\mathbf{r}, \mathbf{r}') \equiv n(z)\exp\left[-\varphi(\mathbf{r}'; z)\right] \qquad (4.68)$$

In the exact theory the probability to find two ions at $\mathbf{r}$ and $\mathbf{r}'$ must be symmetric with respect to exchange of $\mathbf{r}$ and $\mathbf{r}'$. On the other hand the correlation function $g(\mathbf{r}, \mathbf{r}')$, as defined above, is not symmetric. In other words, the ion-ion correlation function in the TCMF model is not symmetric.

4.E   Small Ξ expansion

The recovery of mean field results at small Ξ was demonstrated and explained in Sec. 4.2. Here we derive this result formally as an expansion in powers of Ξ. The advantage of this formal expansion is that it allows us to find also the first order correction to the PB profile within our model.

We expand ΞF_{PB}, Eq. (4.18), up to second order in Ξ:

$$\Xi F_{\mathrm{PB}}(z_0) = F_0 + \Xi F_1(z_0) + \Xi^2 F_2(z_0) + \cdots \qquad (4.69)$$

The zero-th order term, F_0, does not depend on z_0 and is the PB free energy of a charged plane in contact with its counterions, without a test charge. In order to evaluate the following terms,

we also expand φ in powers of Ξ:

$$\varphi(\mathbf{r}; z_0) = \varphi_0(\mathbf{r}) + \Xi\varphi_1(\mathbf{r}; z_0) + \Xi^2\varphi_2(\mathbf{r}; z_0) + \cdots \tag{4.70}$$

To zero-th order we have from Eqs. (4.18) and (4.19):

$$F_0 = \int d^3\mathbf{r} \left\{ -\frac{1}{8\pi}(\nabla\varphi_0)^2 - \lambda\theta(z)e^{-\varphi_0(z)} \right\} \tag{4.71}$$

where

$$\nabla^2\varphi_0 = \frac{d^2\varphi_0}{dz^2} = -4\pi\lambda\theta(z)e^{-\varphi_0} \tag{4.72}$$

is the potential due to counterions in the PB approximation. The first order term in the free energy, F_1, is found by expanding equation (4.18) in Ξ. This expansion includes two contributions, the first from φ_1 and the second from the explicit dependence on Ξ in Eq. (4.18). The first contribution vanishes because φ_0 is an extremum of the zero-th order free energy, leaving only the second contribution:

$$F_1(z_0) \quad = \quad \int d^3\mathbf{r}\, \varphi_0(\mathbf{r})\delta(\mathbf{r} - z_0\hat{\mathbf{z}}) = \varphi_0(z_0) \tag{4.73}$$

Returning to our approximation for $n(z)$, given by Eq. (4.20), we find that:

$$n(z) \quad = \quad \frac{1}{Z}\exp\left[-F_{\mathrm{PB}}(z)\right] = \frac{1}{Z}\exp\left[-\frac{F_0}{\Xi} - \varphi_0(z)\right]$$

$$= \quad \frac{1}{Z_0}\exp\left[-\varphi_0(z)\right], \tag{4.74}$$

where Z_0 is found from the normalization condition (4.21). To leading order in Ξ, $n(z)$ is equal to the PB density profile, as expected:

$$n(z) = n_{\mathrm{PB}}(z) = \frac{1}{Z_0}\exp[-\varphi_0(z)] = \frac{1}{(z+1)^2} \tag{4.75}$$

where Z_0 is a normalization constant. The next order term in the expansion of f can be found on similar lines as $F_1(z)$, and is equal to

$$F_2(z_0) = \frac{1}{2}\delta\varphi_1(z_0\hat{\mathbf{z}}; z_0) \tag{4.76}$$

where $\delta\varphi$ is the difference between the first order correction to φ and the bare potential of the test charge:

$$\delta\varphi_1(\mathbf{r}) = \varphi_1(\mathbf{r}) - \frac{1}{|\mathbf{r} - z_0\hat{\mathbf{z}}|} \tag{4.77}$$

The first order term in the expansion of φ, $\varphi_1(\mathbf{r}; z_0)$ is the solution of the differential equation:

$$\left[\nabla^2 - 4\pi\lambda e^{-\varphi_0}\right]\varphi_1 = -4\pi\delta(\mathbf{r} - z_0\hat{\mathbf{z}}) \tag{4.78}$$

The function $\delta\varphi_1(\mathbf{r})$ arises also in the systematic loop expansion of the free energy around the mean field solution [21]. Its value at $\mathbf{r} = z_0\hat{\mathbf{z}}$ is given by [21]:

$$\delta\varphi_1(z_0\hat{\mathbf{z}}; z_0) \equiv g(z_0) = \frac{1}{2(z_0 + 1)^2} \times$$
$$\left\{ ie^{(1-i)z_0} E_1\left[(1 - i)z_0\right](1 + iz_0)^2 \right.$$
$$\left. -ie^{(1+i)z_0} E_1\left[(1 + i)z_0\right](1 - iz_0)^2 - 4z_0 \right\} \tag{4.79}$$

where $E_1[x]$ is the exponential-integral function [26]. Using Eqs. (4.20) and (4.76) we find that up to first order in Ξ the density profile is given by:

$$n(z) = n_{\text{PB}}(z) + \Xi n_1(z) \tag{4.80}$$

where

$$n_1(z) = \left[N_1 - \frac{1}{2}g(z).\right] n_{\text{PB}}(z) \tag{4.81}$$

In this expression $g(z)$ is given by Eq. (4.79) and N_1 is obtained from the normalization condition (4.21):

$$N_1 = \frac{1}{2}\int \mathrm{d}z\, n_{\text{PB}}(z)g(z) \simeq -0.3104 \tag{4.82}$$

Note that this is different from the exact expression for the first order correction in Ξ,[8] which is obtained in the loop expansion and is not reproduced here, but is shown in Fig. 4.12.

Figure 4.12 shows $n_1(z)$ as defined by Eq. (4.81) (solid line). The symbols show the correction to n_{PB} calculated numerically from TCMF for $\Xi = 0.1$ and scaled by $1/\Xi = 10$. At this small value of Ξ the linearization provides a very good approximation for the correction to $n_{\text{PB}}(z)$.

The dashed line shows the exact first order correction in Ξ to the ion density, obtained from the loop expansion. Comparison of the solid and dashed lines shows that the TCMF model does not capture correctly the exact first order correction. In particular, $n_1(0)$ is different from zero in our approximation; in the exact correction $n_1(0) = 0$ as it must be due to the contact theorem. It is important to realize that although the exact first order correction is useful for values of Ξ of order unity and smaller, the TCMF has a much wider range of validity for $\Xi \gtrsim 1$.

Proof of Equation (4.34)

Our purpose here is to prove the first equality of Eq. (4.34),

$$f_1(z) = \frac{1}{2}\frac{\mathrm{d}g(z)}{\mathrm{d}z} \tag{4.83}$$

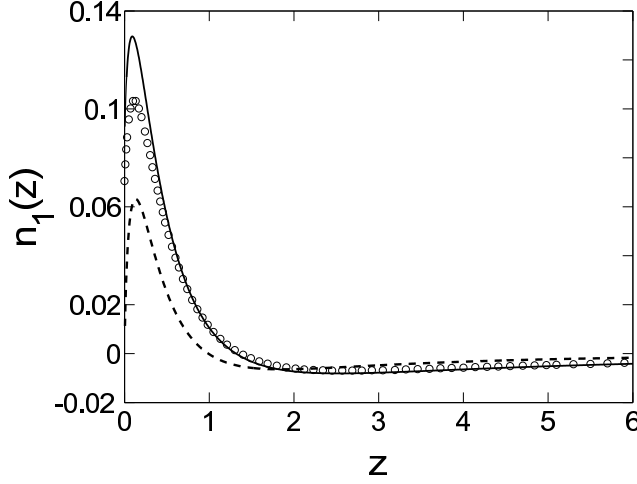[8]See Eq. (64) and Fig. 4 in Ref. [21].

Figure 4.12:   First order (linear) correction in Ξ to $n(z)$, as obtained from the test charge mean field approximation, Eq. (4.81) (solid line), compared to the exact first order correction calculated using a loop expansion [21] (dashed line). The symbols show $[n(z) - n_{\mathrm{PB}}(z)]/\Xi$ calculated numerically in the test charge mean field approximation with $\Xi = 0.1$.

where the electrostatic field acting on a test charge is $-(f_{\mathrm{PB}}(z) + \Xi f_1(z) + \ldots)$, *i.e.*, $f_1(z)$ is the first order term in Ξ. In order to do this, let us consider the correction to the mean field potential due to an infinitesimal point charge of magnitude Ξ that is placed at $\mathbf{r} = z\hat{\mathbf{z}}$. We designate this correction, evaluated at the point $\mathbf{r}'$, as $G(\mathbf{r}, \mathbf{r}')$. This Green's function is found by solving Eq. (4.78) which reads, with a slight change of notation:

$$\left[\nabla_{\mathbf{r}'}^2 - 4\pi\lambda e^{-\varphi_0(\mathbf{r}')}\right] G(\mathbf{r}, \mathbf{r}') = -4\pi\delta(\mathbf{r} - \mathbf{r}') \tag{4.84}$$

The electrostatic field acting on the test charge is then $-f_{\mathrm{PB}}(z) - \Xi f_1(z)$, where

$$f_1(z) = \left.\frac{\partial}{\partial z'}G(\mathbf{r}, \mathbf{r}')\right|_{\mathbf{r}' = \mathbf{r}} = \frac{1}{2}\frac{\partial}{\partial z}G(\mathbf{r}, \mathbf{r}) = \frac{1}{2}\frac{\mathrm{d}g(z)}{\mathrm{d}z} \tag{4.85}$$

and $g(z)$ is defined in Eq. (4.79). In the second step we used the symmetry of $G(\mathbf{r}, \mathbf{r}')$ to exchange of $\mathbf{r}$ and $\mathbf{r}'$, which follows from the fact that the operator acting on $G(\mathbf{r}, \mathbf{r}')$ in Eq. (4.84), as well as the right hand side of that equation, are symmetric with respect to exchange of $\mathbf{r}$ and $\mathbf{r}'$.

4.F   Mean field equation at large z

We start from the exact identity (4.43) and would like to evaluate $f(z)$ for a test particle placed at sufficiently large z, assuming also that Ξ is large. The mean field electrostatic force acting

on the particle is given by

$$f_{\mathrm{MF}}(z) = 1 - \int_0^z \mathrm{d}z' \, n(z') + \int_z^\infty \mathrm{d}z' \, n(z') \tag{4.86}$$

where the first term on the right hand side is the contribution of the charged plane, the second term is the contribution of ions between the plane and the test particle, and the third term is the contribution of the other ions. Eq. (4.86) would describe the exact force acting on the test particle had it not had any effect on the distribution of the other ions in the system. We need to add to this force the contribution due to the influence of the test charge on the other ions.

Due to the exponential decay close to the plate the ion layer further than $z = \sqrt{\Xi}$ is very dilute. Hence it makes sense to include in the correlation-induced force only a contribution from the ions close to the plate. Estimating this contribution as $\alpha\Xi/z^2$ we conclude that

$$\frac{\mathrm{d}\ln n(z)}{\mathrm{d}z} = -f(z) = -f_{\mathrm{MF}}(z) - \frac{\alpha\Xi}{z^2} \tag{4.87}$$

Differentiation of this equation with respect to z yields Eq. (4.45):

$$\frac{\mathrm{d}^2 \ln n(z)}{\mathrm{d}z^2} = 2n(z) + \frac{2\alpha\Xi}{z^3} \tag{4.88}$$

Symbol Legend (Chapter 4)

ε Dielectric constant.

μ Gouy-Chapman length, $\mu = e/(2\pi l_B \sigma)$.

φ Reduced electrostatic potential.

σ Surface charge density [charge/unit area].

Ξ Coupling parameter, $\Xi = l_B/\mu$.

b Effective Gouy-Chapman length, Eq. (4.42).

e Counterion charge (an integer multiple of the unit charge).

$f(z_0)$ Electrostatic field acting on a test charge at $z_0\hat{z}$, Eq. ().

$F[z_0]$ Restricted free energy with a test charge at $z_0\hat{z}$.

l_B Bjerrum length, $l_B = e^2/(\varepsilon k_B T)$. Note that in this chapter e is the counterion charge, and therefore l_B depends on the counterion valency.

$n(z)$ Local counterion density.

z Normal coordinate to the charged plane.

Bibliography

[1] Y. Burak, H. Orland, and D. Andelman, *Phys. Rev. E.* **70** (2004) 016102.

[2] C. Holm, P. Kékicheff, and R. Podgornik (eds.), *Electrostatic Effects in Soft Matter and Biophysics*, Kluwer Academic: Dordrecht, 2001.

[3] W.M. Gelbart, R.F. Bruinsma, P.A. Pincus, and V.A. Parsegian, *Phys. Today* **53** (2000) 38.

[4] R. Podgornik and B. Žekš, *J. Chem. Soc. Faraday Trans. 2* **84** (1988) 611.

[5] M.J. Stevens and M. O. Robbins, *Europhys. Lett.* **12** (1990) 81.

[6] R. Kjellander, T. Åkesson, B. Jönsson, and S. Marčelja, *J. Chem. Phys.* **97** (1992) 1424.

[7] B.Y. Ha and A.J. Liu, *Phys. Rev. Lett.* **79** (1997) 1289.

[8] R.R. Netz and H. Orland, *Europhys. Lett.* **45** (1999) 726.

[9] D. B. Lukatsky and S. A. Safran, *Phys. Rev. E.* **60** (1999) 5848.

[10] V.I. Perel and B.I. Shklovskii, *Physica A* **274** (1999) 446; B.I. Shklovskii, *Phys. Rev. E.* **60** (1999) 5802.

[11] R.R. Netz, *Eur. Phys. J. E.* **5** (2001) 557.

[12] L. Guldbrand, B. Jönsson, H. Wennerström, and P. Linse, *J. Chem. Phys.* **80** (1984) 2221.

[13] N. Grønbech-Jensen, R.J. Mashl, R.F. Bruinsma, and W.M. Gelbart, *Phys. Rev. Lett.* **78** (1997) 2477.

[14] A.G. Moreira and R.R. Netz, *Eur. Phys. J. E.* **8** (2002) 33; A.G. Moreira and R.R. Netz, *Europhys. Lett.* **52** (2000) 705.

[15] M. Deserno, A. Arnold, and C. Holm, *Macromol.* **36** (2003) 249.

[16] R. Kjellander, S. Marčelja, and J.P. Quirk, *J. Colloid Int. Sci.* **126** (1988) 194.

[17] V.A. Bloomfield, *Biopolymers* **31** (1991) 1471.

[18] D.C. Rau and A. Parsegian, *Biophys. J.* **61** (1992) 246; D.C. Rau and A. Parsegian, *Biophys. J.* **61** (1992) 260.

[19] P. Kékicheff, S. Marčelja, T.J. Senden, and V.E. Shubin, *J. Chem. Phys.* **99** (1993) 6098.

[20] E. Raspaud, M.O. de la Cruz, J.L. Sikorav, and F. Livolant, *Biophys. J.* **74** (1998) 381.

[21] R.R. Netz and H. Orland, *Eur. Phys. J. E.* **1** (2000) 203.

[22] R. Kjellander and S. Marčelja, *J. Chem. Phys.* **82** (1985) 2122; R. Kjellander, *J. Chem. Phys.* **88** (1988) 7129; R. Kjellander and S. Marčelja, *J. Chem. Phys.* **88** (1988) 7138.

[23] For a review, see D. Andelman, in *Handbook of Physics of Biological Systems*, R. Lipowsky and E. Sackmann (eds.), Elsevier Science: Amsterdam, 1994, Vol. I, Chap. 12, p. 603.

[24] S.L. Carnie and D.Y.C. Chan, *J. Chem. Phys.* **74** (1981) 1293.

[25] A.G. Moreira and R.R. Netz, private communication.

[26] M. Abramowitz and I.A. Stegun, *Handbook of Mathematical Functions*, Dover: New York, 1972.

[27] L. Blum and D. Henderson, in *Fundamentals of Inhomogeneous Fluids*, D. Henderson (ed.), Marcel Dekker: New York, 1992, Chap. 6, pp. 239–276, and references therein.

[28] Y. Burak and D. Andelman, *Phys. Rev. E.* **62** (2000) 5296.

[29] D.L. Harries, S. May, W.M. Gelbart, and A. Ben-Shaul, *Biophys. J.* **75** (1998) 159.

[30] S.L. Carnie, D.Y.C. Chan, and J. Stankovich, *J. Colloid Interface Sci.* **165** (1994) 116.

[31] E.N. Houstis, W.F. Mitchell, and J.R. Rice, *ACM Trans. Math. Soft.* **11** (1985) 379.

Chapter 5

Onset of DNA Aggregation in Presence of Monovalent and Multivalent Counterions

In the following chapter, we address theoretically aggregation of DNA segments by multivalent polyamines such as spermine and spermidine.[1] In experiments, the aggregation occurs above a certain threshold concentration of multivalent ions. We demonstrate that the dependence of this threshold on the concentration of DNA has a simple form. When the DNA concentration c_{DNA} is smaller than the monovalent salt concentration, the threshold multivalent ion concentration depends linearly on c_{DNA}, having the form $\alpha c_{\mathrm{DNA}} + \beta$. The coefficients α and β are related to the density profile of multivalent counterions around isolated DNA chains, at the onset of their aggregation. This analysis agrees extremely well with recent detailed measurements on DNA aggregation in the presence of spermine. From the fit to the experimental data, the number of condensed multivalent counterions per DNA chain can be deduced. A few other conclusions can then be reached: *i*) the number of condensed spermine ions at the onset of aggregation decreases with the addition of monovalent salt; *ii*) the Poisson-Boltzmann theory over-estimates the number of condensed multivalent ions at high monovalent salt concentrations; *iii*) our analysis of the data indicates that the DNA charge is not over-compensated by spermine at the onset of aggregation.

5.1   Introduction

Condensation and aggregation of DNA, induced by multivalent counterions, have been extensively studied in the past two decades (for a review, see Ref. [3] and references therein). The

---

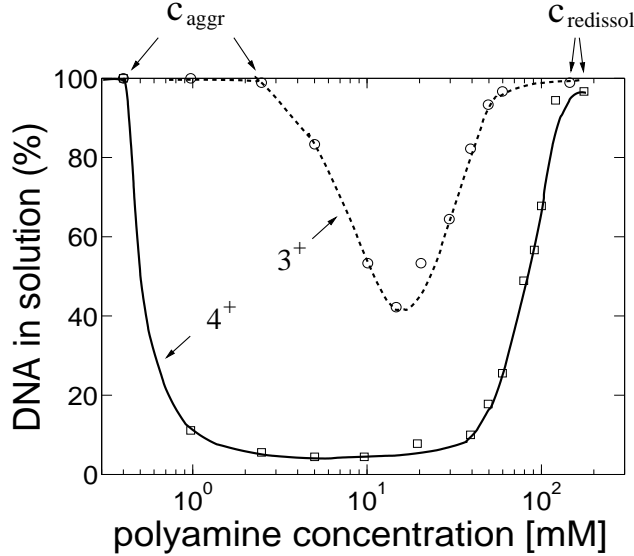[1]The material presented in this chapter was published in Refs. [1, 2].

Figure 5.1: Percent of solubilized DNA, as function of polyamine concentration: square symbols - spermine, circles - spermidine. The solid and dashed lines are guides for the eye. DNA and NaCl concentrations are $3\,\mathrm{mM}$ and $25\,\mathrm{mM}$, respectively. Below the aggregation threshold, c_{aggr}, and above the re-dissolution threshold, c_{redissol}, all the DNA is dissolved. The data is adapted from Ref. [5].

term condensation usually refers to the collapse of a single, long DNA chain. Condensation plays an important role in storage and packing of DNA; for example, in viral capsids [4]. Aggregation of DNA is a closely related phenomenon, where multiple chains attract each other and form a variety of condensed mesophases of complex structure [5, 6]. In both phenomena multivalent counterions play a crucial role, screening the electrostatic repulsion between charged strands of DNA and mediating an effective attraction.

A variety of tri- and tetra-valent ions can induce aggregation and condensation, among them the polyamines spermidine (3^+) and spermine (4^+) [7–9], as well as cobalt-hexamine [10, 11]. In typical experiments on aggregation [5, 12, 13] multivalent ions are gradually added to a solution with fixed concentration of DNA segments and monovalent salt. Two such examples for spermine and spermidine are reproduced in Fig. 5.1 [5]. As the multivalent ion concentration is raised above a certain threshold, DNA segments begin to aggregate, and precipitate from the solution. Above the aggregation threshold, the DNA concentration decreases gradually or abruptly, depending on various parameters such as the monovalent salt concentration and total DNA concentration. Further addition of multivalent ions at higher concentrations reverses the aggregation. Above a second, re-dissolution threshold, all the DNA is re-dissolved in the solution (Fig. 5.1). The re-dissolution threshold (above which all the DNA re-dissolves) is
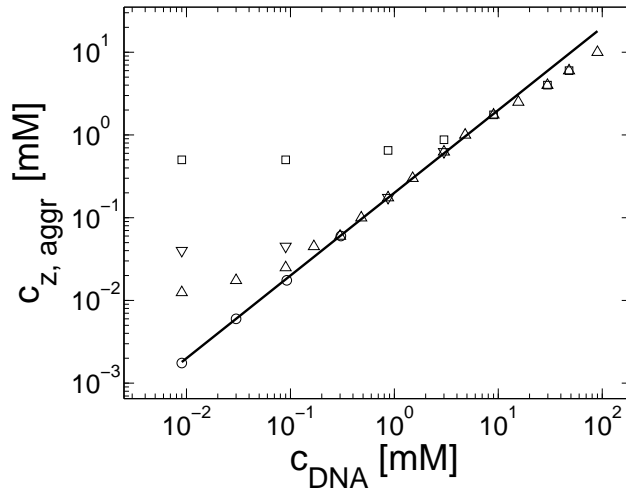
Figure 5.2: Spermine concentration $c_{z,\mathrm{aggr}}$ at the onset aggregation, as a function of DNA monomer concentration c_{DNA}. Data is shown for four monovalent salt concentrations: $2\,\mathrm{mM}$ ($\circ$), $13\,\mathrm{mM}$ ($\triangle$), $23\,\mathrm{mM}$ ($\triangledown$), and $88\,\mathrm{mM}$ ($\square$). The solid line corresponds to a fixed ratio: $c_{z,\mathrm{aggr}}/c_{\mathrm{DNA}} = 0.20$. The data is adapted from [12].

almost independent on the DNA concentration. Its value can be attributed to screening of electrostatic interactions by multivalent ions [12].

The aggregation threshold, where the onset of aggregation occurs, is the main experimental phenomenon addressed in this chapter. The multivalent ion concentration at the onset depends strongly on the monovalent salt and DNA concentrations. This dependence has been recently measured in detail for short (150 base pair) DNA segments in presence of spermine [12], and is reproduced in Fig. 5.2. The figure shows measurements of spermine concentrations at the onset of aggregation, for DNA concentrations ranging over four orders of magnitude and for four different monovalent salt concentrations: 2, 13, 23 and 88 mM. At very low DNA concentration, the spermine concentration depends strongly on the monovalent salt concentration. At higher DNA concentration it has only a weak dependence on the monovalent ion concentration but the spermine concentration is proportional to the DNA concentration, indicating that a certain number of spermine counterions are required, per DNA base, in order to induce aggregation. The solid line in Fig. 5.2, adapted from [12], corresponds to a ratio: $c_{z,\mathrm{aggr}}/c_{\mathrm{DNA}} = 0.20$, where $c_{z,\mathrm{aggr}}$ is the spermine concentration at the aggregation onset and c_{DNA} is the DNA concentration. This linear relation fits a large number of the experimental points in the intermediate DNA concentration range. It has been suggested in Refs. [12, 14] that the deviations from this line, at low and high DNA concentrations, represent two distinct physical regimes that need to be analyzed separately from the intermediate regime, where the linear fit works well.

In this work we focus on the onset of aggregation, and specifically on its dependence on the DNA concentration. We show that this dependence is simple for *all the range* of DNA concentration. Furthermore, for c_{DNA} smaller than the monovalent salt concentration we show that this dependence is linear: $c_{z,\mathrm{aggr}} = \alpha c_{\mathrm{DNA}} + \beta$. The coefficient β is the multivalent counterion concentration far away from the DNA chains, while α accounts for the excess of multivalent ions around each chain. These quantities can be extracted, *e.g.,* from the four experimental curves of Fig. 5.2. Several further conclusions are then drawn on the onset of DNA aggregation and on the counterion distribution around each double-stranded DNA.

5.2   Theoretical considerations

Consider an aqueous solution containing monovalent (1:1) salt, multivalent (z:1) salt and DNA segments below their threshold for aggregation. Throughout this chapter, the DNA solution is assumed to be dilute enough such that the DNA segments do not overlap. We also assume that these DNA segments can be regarded as rigid rods. The concentrations of added monovalent salt, multivalent salt and DNA monomers are denoted by c_s, c_z and c_{DNA}, respectively. These are the solute concentrations per unit volume as controlled and adjusted in experiments. We will assume that the monovalent and multivalent salts have the same type of co-ion, so that altogether there are three ion species in the solution:

1. A multivalent counterion contributed from the z:1 multivalent salt, of concentration c_z.

2. A monovalent counterion contributed by monovalent salt of concentration c_s, and by counterions dissociated from the DNA, of concentration c_{DNA}: in total, $c_s + c_{\mathrm{DNA}}$.

3. Co-ions coming from both z:1 and 1:1 salts, of concentration $c_s + zc_z$.

Each DNA segment attracts a layer of oppositely charged counterions referred to as the condensed counterions. As long as the typical distance between segments is large compared to the electrostatic screening length κ^{-1}, the electrostatic potential decays exponentially to zero far away from the DNA segments. In turn, the concentrations of the three ion species decay to well defined *bulk* values denoted by c_1^∞ for the monovalent ions and c_z^∞ for the z-valent ones. These concentrations should be distinguished from the concentrations c_s and c_z introduced above, which are the average concentrations of added salts regulated experimentally.

The Debye screening length, κ^{-1}, characterizing the exponential decay of the electrostatic potential, is determined by the bulk concentrations of all three ionic species:

$$\kappa^2 = 4\pi l_B \left[c_1^\infty + z^2 c_z^\infty + (c_1^\infty + z c_z^\infty) \right]. \tag{5.1}$$
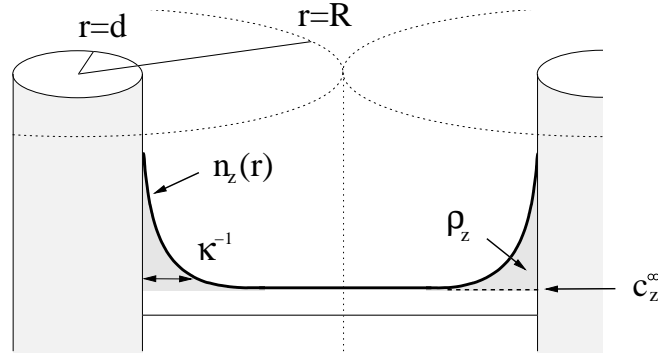
Figure 5.3: Schematic representation of the multivalent density profile, $n_z(r)$ between two neighboring DNA segments, each modeled as a cylinder of radius d. Here r is the distance from the axis of the left DNA strand. The radius $r = R$ corresponds to the inter-strand mid-distance and is the unit cell radius. The density decays to its bulk value c_z^∞ on distances larger than κ^{-1}, where κ^{-1} is the Debye length defined in Eq. (5.1). The excess density of multivalent ions ρ_z is indicated by the shaded areas.

where the third term is the co-ion concentration. It is equal to $c_1^\infty + zc_z^\infty$ due to charge neutrality far from the DNA where the potential decays to zero. The above equation makes use of the Bjerrum length, $l_B = e^2/(\varepsilon k_B T)$, equal to about $7\,\text{Å}$ in aqueous solution at room temperature, $k_B T$ is the thermal energy , e is the electron charge and $\varepsilon = 80$ is the dielectric constant of water. The Debye length as well as c_z^∞ are shown schematically in Fig. 5.3. Other quantities that will be defined below are also indicated in this figure.

In dilute solutions different DNA segments do not overlap. Following previous works, we introduce a cell model also shown schematically in Fig. 5.3. Note that the model serves to illustrate the subsequent derivations but is not essential for the validity of our main results. In the cell model, each segment, of a cylindrical cross-section, is at the center of a cylindrical cell of radius R and area $A = \pi R^2$ such that

$$c_{\text{DNA}} = 1/(aA). \tag{5.2}$$

Namely, each DNA monomer occupies a specific volume aA, where $a \simeq 1.7\text{Å}$ is the average charge separation on the chain taken hereafter as the monomer length.

We will assume below that the DNA solution is dilute enough so that R is large compared to the Debye length κ^{-1}. This assumption is essential for our derivation and can be verified for all the experimental data considered in this chapter. Density profiles of the three ion species are then practically identical to those near an isolated DNA segment with the same bulk concentrations c_1^∞, c_z^∞. In other words, the profiles are determined uniquely by c_1^∞ and
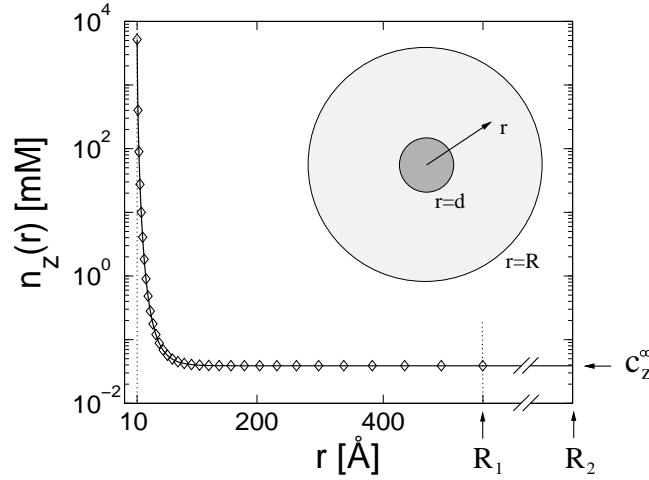
Figure 5.4: Density profile $n_z(r)$ of 4-valent ions as function of r, the distance from the DNA axis, on a semi-log plot, calculated using the Poisson-Boltzmann equation in a cell model, where the DNA segment is modeled as a uniformly charged cylinder. The cell model is shown schematically in the inset. Two cell sizes are shown, with outer radii $R_1 = 560\,\text{Å}$ $(c_{\text{DNA}} = 1\,\text{mM})$ and $R_2 = 1.8 \times 10^4\,\text{Å}$ $(c_{\text{DNA}} = 10^{-3}\,\text{mM})$, indicated by arrows. In both cases the radius of closest approach of ions to the charged chain is at $r = d$, where $d = 10\,\text{Å}$ as indicated by a dotted vertical line. The boundary condition at the inner cylinder matches the linear charge density of DNA $(1e/1.7\text{Å})$. The bulk densities of monovalent and multivalent ions, c_1^∞ and c_z^∞, are chosen to be the same in the two cells, leading to practically identical density profiles. The solid line represents the larger cell (R_2), and diamonds are used for the smaller cell (R_1). Density profiles of monovalent counterions and co-ions are not shown but are also practically identical in the two cells. Average salt concentrations are $c_s = 22\,\text{mM}$ and $c_z = 0.21\,\text{mM}$ in the smaller cell, and $c_s = 23\,\text{mM}$, $c_z = 0.039\,\text{mM}$ in the larger cell. Bulk concentrations are $c_1^\infty = 23\,\text{mM}$ and $c_z^\infty = 0.039\,\text{mM}$. Note that these bulk concentrations are practically identical to the salt concentrations in the larger cell. Note also that $c_1^\infty > c_s$ in the smaller cell reflecting the contribution of the counterions released by the DNA.

c_z^∞, with practically no dependence (or, more precisely, an exponentially small dependence) on the DNA monomer concentration. A demonstration of this claim is presented in Fig. 5.4, using the Poisson-Boltzmann theory in a cell model. For two very different values of R corresponding to different c_{DNA}, the counterion profiles match perfectly when the values of c_1^∞ and c_z^∞ are the same. Note that the average concentrations of added salts, c_s and c_z, have different values in the two cells because of the contribution of condensed ions.

The total number of z-valent counterions, per cell unit length, is given by:

$$Ac_z = Ac_z^\infty + \rho_z(c_1^\infty, c_z^\infty) \tag{5.3}$$

where ρ_z is the excess number of z-valent ions per unit length near the DNA. Throughout the chapter we use the symbol c to denote concentrations per unit volume and ρ for concentrations per DNA unit length. The excess ρ_z can be evaluated in the limit of infinite cell radius,

corresponding to an isolated chain:

$$\rho_z = 2\pi \int_0^\infty r \mathrm{d}r \left[n_z(r) - c_z^\infty \right],\tag{5.4}$$

where $n_z(r)$ is the z-valent *local* counterion concentration at distance r from the axis of symmetry, and $n_z(\infty) = c_z^\infty$. Following the discussion in the previous paragraph, the excess ρ_z is determined uniquely by c_1^∞ and c_z^∞. Its exact functional dependence on these variables is generally not known, although it can be evaluated approximately, *e.g.*, using the Poisson-Boltzmann equation or in computer simulations.

For monovalent counterions we have, in a similar fashion:

$$Ac_s + Ac_{\mathrm{DNA}} = Ac_1^\infty + \rho_1(c_1^\infty, c_z^\infty),\tag{5.5}$$

where ρ_1, the excess of monovalent counterions per unit length, is defined as in Eq. (5.4), and $Ac_{\mathrm{DNA}} = 1/a$ is the DNA charge density per unit length. The extra term in the left-hand-side of Eq. (5.5) originates from monovalent counterions contributed by the DNA monomers. Using Eq. (5.2) we can rewrite Eqs. (5.3) and (5.5) as:

$$c_z = c_z^\infty + a\rho_z \left(c_1^\infty, c_z^\infty \right) c_{\mathrm{DNA}}\tag{5.6}$$

and

$$c_s = c_1^\infty + \left[a\rho_1 \left(c_1^\infty, c_z^\infty \right) - 1 \right] c_{\mathrm{DNA}}.\tag{5.7}$$

These two equations relate the experimentally adjustable c_s, c_z and c_{DNA} to the bulk densities c_1^∞, c_z^∞ that in turn, are important because they determine the ion density profiles.

In the limit of infinite DNA dilution, $c_{\mathrm{DNA}} = 0$, and therefore $c_z = c_z^\infty$ and $c_s = c_1^\infty$. At any finite DNA concentration c_z and c_s are not equal to c_z^∞ and c_1^∞, respectively, because each segment captures some of the multivalent ions and releases a number of monovalent ones. Equations 5.6 and 5.7 express the correction to c_s, c_z at given c_1^∞, c_z^∞ for both mono- and multivalent counterion species. The dimensionless quantities $a\rho_1, a\rho_z$ are the excess of the mono- and multi-valent counterion species, respectively, per DNA monomer.

We would like to emphasize the generality of Eqs. (5.6) and (5.7). They do not depend on the assumption of parallel DNA residing in the middle of oriented cylindrical unit cells, or on any mean-field approximation for the distribution of counterions. The only assumption required to derive Eqs. (5.6) and (5.7) is that the average distance between DNA segments is large compared with the Debye length. Although Eqs. (5.6) and (5.7) are correct for any c_s, c_z

and c_{DNA} below the onset of DNA aggregation, we will be interested below specifically in the aggregation onset.

Onset of aggregation

Our aim now is to find how the value of c_z at the onset of aggregation, $c_{z,\mathrm{aggr}}$, depends on c_{DNA}. We will assume that this aggregation onset depends on c_1^∞ and c_z^∞, but not on the average distance between DNA chains. We motivate this assumption by the fact that c_1^∞ and c_z^∞ determine the density profile of multivalent counterions around the DNA chains, which, in turn, mediate the attraction necessary for aggregation. Before discussing this assumption in more detail, let us first consider its consequences. We can imagine an experiment where c_z^∞ is gradually increased while c_1^∞ is kept fixed. Aggregation will start, in this experiment, above a certain threshold value of c_z^∞. Our assumption is that this threshold does not depend on c_{DNA}. In real experiments, however, c_z is adjusted rather than c_z^∞, and c_s is kept fixed rather than c_1^∞. In order to find the threshold value in terms of the experimentally available c_z we need to map c_1^∞, c_z^∞ onto c_s, c_z. This mapping is described by Eqs. (5.6)–(5.7), and involves c_{DNA}. It is only through this mapping that c_{DNA} will affect the threshold of aggregation.

The limit of $c_{\mathrm{DNA}} \ll c_s$:

The limit $c_{\mathrm{DNA}} \ll c_s$ offers a particularly simple dependence of $c_{z,\mathrm{aggr}}$ on c_{DNA} and is considered first. Most models and experiments indicate that monovalent counterions cannot overcharge DNA segments. Hence the monovalent excess, $a\rho_1$, in Eq. (5.7), is a number between zero and one, because the excess monovalent charge is smaller than that of DNA. From Eq. (5.7) $|c_s - c_1^\infty| \ll c_s$ as long as $c_{\mathrm{DNA}} \ll c_s$. It is then possible to replace c_1^∞ by c_s, leading to a simplification of Eq. (5.6):

$$c_z = c_z^\infty + a\rho_z \left(c_s, c_z^\infty\right) c_{\mathrm{DNA}}. \tag{5.8}$$

Note that c_{DNA} is indeed smaller than c_s in most of the experimental points in Fig. 5.2. However a similar simplification cannot be applied for c_z because it is typically much smaller than c_s, and often smaller than c_{DNA}.

According to our principal assumption, aggregation starts at a threshold value $c_z^\infty = c_z^*$, which does not depend on c_{DNA} [while $c_{z,\mathrm{aggr}}$, the average multivalent salt concentration does

depend on c_{DNA} through Eq. (5.8)]. Similarly, the density profile at the threshold does not depend on c_{DNA}, because it is determined by $c_1^\infty = c_s$ and c_z^*. The excess of z-valent counterions, as determined from this profile, is equal to:

$$\rho_z^* = \rho_z\left(c_s, c_z^*\right), \tag{5.9}$$

with no dependence on c_{DNA}. Using the threshold values c_z^* and ρ_z^* in Eq. (5.8), we find that the average concentration of z-valent ions at the onset of aggregation is:

$$c_{z,\mathrm{aggr}}(c_{DNA}) = c_z^* + a\rho_z^* c_{DNA}. \tag{5.10}$$

This is the threshold concentration that was measured experimentally in [12]. Note that in (Eq. 5.10) c_z^* as well as ρ_z^* depend on the monovalent salt concentration, c_s, but the explicit dependence is omitted for clarity.

The simple relationship expressed by Eq. (5.10) is one of our main results. As a visualization of this result we refer again to Fig. 5.3. The quantities ρ_z, c_z^∞ and the density profile $n_z(r)$ are indicated in this figure. At the onset of aggregation c_z^∞ is equal to c_z^* and does not depend on c_{DNA} (or equivalently, on the spacing between DNA segments, R). As c_{DNA} is increased the distance between DNA strands decreases. The onset values of c_z^∞ and ρ_z do not change, but the contribution of ρ_z to the average concentration increases, leading to an increase in $c_{z,\mathrm{aggr}}$.

The coefficients $a\rho_z^*$ and c_z^* of the linear dependence in Eq. (5.10) are the coefficients α and β defined in the introduction section. They can be easily found from the experimental data: c_z^* is the value of $c_{z,\mathrm{aggr}}$ in the limit of infinite DNA dilution, $c_{DNA} \to 0$, since in this limit $c_z = c_z^\infty = c_z^*$. The excess at the onset, ρ_z^*, can be found from the slope of $c_{z,\mathrm{aggr}}$ as function of c_{DNA}. Before presenting a detailed comparison with experiments, we generalize the treatment for small c_{DNA} to arbitrary values.

The case of $c_{DNA} \geq c_s$:

When c_{DNA} is of the same order as c_s or larger, corrections to c_1^∞ must be taken into account, as expressed by Eq. (5.7), and the linear relation of Eq. (5.10) no longer holds. The ion density profiles as well as c_s and c_z are now determined by the two variables c_1^∞ and c_z^∞. The relation between c_1^∞ and c_z^∞ and the experimentally controlled c_s, c_z, c_{DNA} is given by Eqs. (5.6)–(5.7). In terms of c_1^∞, c_z^∞ the criterion for aggregation remains the same as in the previous case:

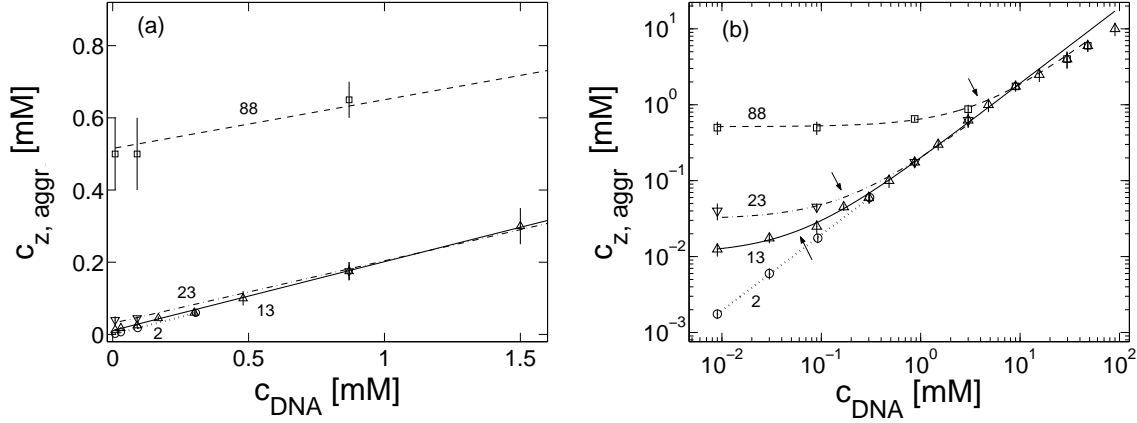$$c_z^\infty = c_z^*(c_1^\infty). \tag{5.11}$$

Figure 5.5: Spermine concentration at the onset of aggregation $c_{z,aggr}$ as a function of c_{DNA}, fitted to the form derived in Eq. (5.10) (different line types are used for different salt concentrations). Value of c_s (in mM) is indicated next to each curve. Experimental data is adapted from [12] and shown in the following symbols: $c_s = 2\,mM$ (∘), $13\,mM$ (△), $23\,mM$ (▽), and $88\,mM$ (□). Experimental error bars (E. Raspaud, private communication) are indicated by vertical lines. The fitted lines and experimental points are shown using a linear scale in (a) up to $c_{DNA} = 1.5\,mM$, and a log-log scale in (b) up to $c_{DNA} = 100\,mM$, allowing all data points to be shown on the same plot. Only the data up to $c_{DNA} = 10\,mM$ was used for the linear fit. The crossover values of c_{DNA}, as defined by Eq. (5.14), are indicated by arrows in (b).

The three equations 5.6, 5.7 and 5.11, with the three unknowns c_1^∞, c_z^∞ and c_z lead to a unique solution for $c_{z,aggr}$. Note that c_1^∞ is larger than c_s because of counterions coming from the DNA as can be seen in Eq. (5.7), where $a\rho_1 - 1$ is negative. In Eq. (5.10), c_s is replaced by c_1^∞, which is larger than c_s for large c_{DNA}. Hence, increasing c_{DNA} has an effect similar to addition of monovalent salt. As noted above, this effect is significant only for $c_{DNA} > c_s$.

5.3   Comparison with experiment

Raspaud et al [12] measured the spermine ($z = 4$) concentration c_z at the onset of aggregation as a function of c_{DNA} for four values of c_s and with c_{DNA} ranging over four orders of magnitude — from 10^{-2} to $10^2\,mM$. We fitted the data (E. Raspaud and J.-L. Sikorav, private communication) for each c_s to a straight line according to Eq. (5.10). The least square fit presented in Fig. 5.5 takes into account the experimental error bars and data points up to $c_{DNA} = 10\,mM$. In Fig. 5.5 (a) the fit is shown using a linear scale which covers the range of c_{DNA} only up to $c_{DNA} = 1.5\,mM$ for clarity purposes. Due to the large range of c_{DNA} it is impossible to show all the data on the linear scale of Fig. 5.5 (a). Instead, the same data and linear lines are shown in Fig. 5.5 (b) on a log-log scale over the full experimental range of c_{DNA}.

The linear fit is very good for all four values of monovalent salt concentration c_s. Note that for $c_s = 88\,\text{mM}$ the fit is very good up to the largest value of $c_{\text{DNA}} = 48\,\text{mM}$ reported in the experiment, although our fit takes into account only data points up to $c_{\text{DNA}} = 10\,\text{mM}$. It was previously suggested [12] that a separate regime exists for $c_{\text{DNA}} \gtrsim 10\,\text{mM}$, characterized by a power law relation between c_z and c_{DNA} with an exponent smaller than unity. Our analysis suggests a different conclusion. The fit clearly demonstrates that the relation is linear all the way up to $c_{\text{DNA}} = 48\,\text{mM}$, as predicted by Eq. (5.10). Note also that even at $c_{\text{DNA}} = 48\,\text{mM}$ we have $c_{\text{DNA}} < c_s$ so the assumptions leading to Eq. (5.10) are still valid.

The only points in Fig. 5.5 (b) that deviate significantly from the fit are the three points where $c_s = 13\,\text{mM}$ (triangles) and $c_{\text{DNA}} > 20\,\text{mM}$ (two of these points coincide with points having $c_s = 88\,\text{mM}$, shown using square symbols.) This deviation is easily explained by the fact that $c_{\text{DNA}} \gg c_s$ so that corrections to c_1^∞ must be taken into account. For example, at $c_{\text{DNA}} = 90\,\text{mM}$ the nominal monovalent counterion concentration is $103\,\text{mM}$, taking into account counterions contributed by the DNA. In order to find c_1^∞ we need to subtract the condensed counterions, as determined by ρ_1. We can estimate ρ_1 at this point by solving the Poisson-Boltzmann equation in a unit cell with the appropriate radius. The chemical potentials of the three ion species are tuned such that their concentrations match the known values of c_z and c_s. This leads to an estimate: $c_1^\infty \simeq 68\,\text{mM}$. Hence, c_z at the onset of aggregation should lie a little below the continuation of the $c_s = 88\,\text{mM}$ line which is, indeed, where it is found. The trend for $c_s = 13\,\text{mM}$ can probably be seen already at the point $c_{\text{DNA}} = 15\,\text{mM}$, although the deviation at this point is still within the range of experimental error. The few other experimental points with $c_{\text{DNA}} \approx c_s$ deviate slightly from the straight line as well (still within experimental error bars). In all these cases the deviation is in the direction corresponding to a higher value of c_s, as expected.

A linear relation of the form $c_{z,\text{aggr}} = \alpha c_{\text{DNA}} + \beta$, was previously suggested on empirical basis for aggregation induced by spermidine (3^+), on a smaller range of DNA concentrations [5, 15]. Although this result looks similar to our prediction on the onset of aggregation, it is not directly related to our analysis because $c_{z,\text{aggr}}$ was taken in those works to be the transition midpoint. This is the point where half of the maximal precipitation of DNA is reached. Our analysis does not apply at the transition midpoint since it requires all the DNA segments to be well separated from each other. Indeed, the coefficient α, related to the transition midpoint, was found in [15] and [5] to be of order 10^2, much larger than unity. Such a value of α cannot be interpreted as the excess of spermidine ions per monomer near isolated chains.

c_s[mM]	c_z^*[mM]	$a\rho_z^*$
2	0 ± 0.0003	0.194 ± 0.020
13	0.011 ± 0.002	0.191 ± 0.013
23	0.031 ± 0.005	0.173 ± 0.025
88	0.52 ± 0.05	0.135 ± 0.026

Table 5.1: Fit parameters used in Fig. 5.5.

The parameters of the linear fit in Fig. 5.5 are summarized in Table 5.1 for the four experimentally used values of c_s.

5.3.1 Crossover in the log-log plot

For presentation purposes we plot in Fig 5.5 (b), $c_{z,\text{aggr}}$ vs. c_{DNA} on a log-log scale, as appeared in Ref. [12]. The linear relation that was found between these two quantities is not clearly manifested on the log-log plot, because a linear dependence of the form $y = \alpha x + \beta$ is not easily recognized in such a plot. Furthermore, such a linear relation appears on a log-log plot to be *artificially* characterized by two distinct behaviors, at low and high values of the independent variable. These two behaviors were mentioned in [12] and can be seen in Fig. 5.5 (b). However, they do not represent in our opinion two real physical regimes and can be understood by taking the logarithm of Eq. (5.10). For small c_{DNA} (large R):

$$\log c_z \simeq \log c_z^* \tag{5.12}$$

i.e, c_z does not depend on c_{DNA} as is seen in Fig. 5.5 (b) in the small c_{DNA} limit. In the opposite limit of large c_{DNA} (small R):

$$\log c_z \simeq \log c_{\text{DNA}} + \log a\rho_z^* \tag{5.13}$$

Here, the linear dependence of c_z on c_{DNA} yields a line of slope 1 in the same figure.

The crossover between these apparent behaviors occurs when the number of bulk and excess ions are the same:

$$c_{\text{DNA}} = \frac{c_z^*}{a\rho_z^*} \tag{5.14}$$

When c_{DNA} is much smaller than this crossover value, the number of excess multivalent ions near DNA segments is negligible compared to their total number. In the other extreme of c_{DNA} much larger than the crossover value, the number of free multivalent ions is negligible compared to the excess ions, and nearly all multivalent ions are bound to the DNA.

For the experimental data in Fig. 5.5 the crossover value is equal to 0.06, 0.18 and $3.9\,\mathrm{mM}$ for $c_s = 13$, 23 and $88\,\mathrm{mM}$, respectively, and smaller than $1.5 \times 10^{-3}\,\mathrm{mM}$ for $c_s = 2\,\mathrm{mM}$. The first three crossover points are indicated by arrows in Fig. 5.5 (b).

5.4 DNA aggregation and counterion condensation

We separate the discussion following our results in three parts. The first addresses the conditions required for DNA aggregation. The coefficients of the linear relation in Eq. (5.10), c_z^* and ρ_z^*, have a definite physical meaning. Their values, as extracted from the experimental data provide insight on these conditions. The second part deals with condensation of counterions on DNA (to be distinguished from condensation of DNA chains). The general relation $\rho_z = \rho_z(c_1^\infty, c_z^\infty)$ that was introduced in Eqs. (5.3)–(5.4) is a property of counterion condensation on isolated chains. By extracting the values of ρ_z, c_1^∞ and c_z^∞ at the onset of DNA aggregation, we can learn about exact density profiles of spermine around DNA, and compare our findings with approximations such as Poisson-Boltzmann theory. Finally, we comment on our main assumption, which was used in the theoretical considerations section.

5.4.1 Conditions at the onset of aggregation

Most of the proposed theoretical models for inter-chain attraction and aggregation (see, for example, [12,16–22]) regard the charged chain as surrounded by a layer of condensed ions which is usually modeled as a one-dimensional gas. This layer mediates an inter-chain attraction, and the models predict the number of condensed ions required to initiate aggregation of the chains. In the current work we do not address this theoretical problem, but rather concentrate on what can be inferred from the experimental results using the analysis presented in the previous section. This analysis provides insight on the conditions prevailing at the onset of aggregation. In particular, the excess ρ_z^* characterizes the number of condensed multivalent counterions that are present near each chain at the onset. Although in general the notion of condensed counterions is somewhat ill-defined, as it depends on which ions are regarded as bound to the DNA, we show in Appendix 5.A that in our case it does have a reasonably well defined meaning. Furthermore, the number of condensed multivalent ions per monomer is practically the same as $a\rho_z^*$.

The excess of multivalent counterions per monomer, $a\rho_z^*$, is shown in Fig. 5.6 as function of c_s. All values are taken from Table 5.1, as extracted from the experimental data. The dashed line is a linear fit. Two different axis scales are used on the left and right of the plot. The left
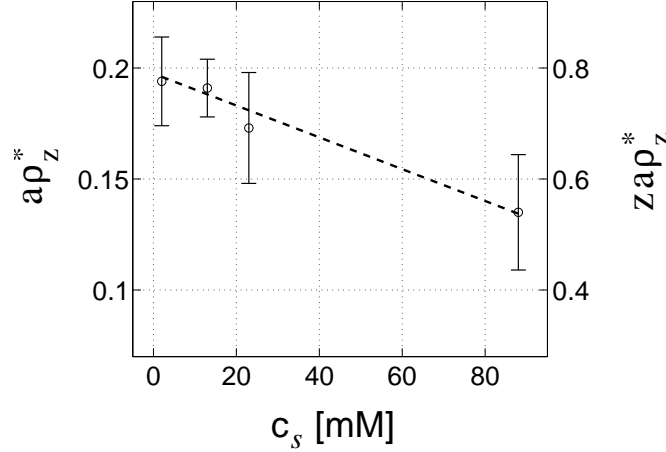
Figure 5.6: Excess of multivalent counterions per monomer at the onset of aggregation, $a\rho_z^*$, as function of c_s. All values are taken from Table 5.1, as extracted from the experimental data of [12]. Error bars are indicated by vertical bars and the dashed line is a linear fit to be used as a guide to the eye. On the right axis $za\rho_z^*$ is shown, where $z = 4$ for spermine. This value is equal to the fraction of DNA charge compensated by the condensed multivalent ions. Note that according to the Manning condensation theory the same quantity is equal to 0.94, for tetravalent ions and no added salt.

axis shows the value of $a\rho_z^*$. The right one shows the part of DNA charge that is compensated by condensed multivalent ions, $za\rho_z^*$, where $z = 4$ for spermine. From the plot we deduce the following two conclusions:

1. The number of condensed multivalent ions (per DNA monomer) $a\rho_z^*$ at the onset decreases as the monovalent salt concentration increases, with variation between 0.19 and 0.14. A possible reason for this trend may be that the bare electrostatic repulsion between chains is decreased due to increased screening. Hence a smaller number of multivalent ions is required in order to overcome this repulsion. The change in ρ_z^* may also be related to the competition between monovalent and multivalent ions in the aggregated DNA state.

2. The data indicates that there is no over-charging of the DNA by spermine at the onset (see also [20]) since $za\rho_z^* < 1$. At higher concentration of spermine, beyond the threshold, we do not rule out the possibility of DNA over-charging, as was suggested by [20].

Although ρ_z^* decreases with increase of c_s, it is of the same order of magnitude for all the c_s values in Table 5.1. In contrast, c_z^* varies in Table 5.1 over more than three orders of magnitude. As was previously suggested [12,16], this large variation in c_z^* is a result of competition between monovalent and multivalent counterions. We discuss the relation between ρ_z^* and c_z^* to some

c_1^∞ [mM]	c_z^∞ [mM]	$a\rho_z$ (exp)	$a\rho_z$ (PB)
2	0 ± 0.0003	0.194 ± 0.020	0.186 ± 0.005
13	0.011 ± 0.002	0.191 ± 0.013	0.178 ± 0.002
23	0.031 ± 0.005	0.173 ± 0.025	0.172 ± 0.002
88	0.52 ± 0.05	0.135 ± 0.026	0.164 ± 0.002

Table 5.2: Excess of 4-valent ions near DNA compared with PB theory.

extent in the following subsection. A more detailed analysis of this relation, emphasizing the role of competition between the two counterion species, is presented in Appendix 5.B (see also, Refs. [23–25]).

5.4.2 Counterion condensation

We now turn to analyze the condensation of monovalent and multivalent ions around DNA. Each line in Table 5.1 provides a measurement of the excess ρ_z at certain values of c_1^∞ and c_z^∞. The general relation $\rho_z(c_1^\infty, c_z^\infty)$ is a property of counterion density profiles around isolated DNA segments. Hence, the data in Table 5.1 can be used to test any particular theory used to calculate such ion distributions.

The most simple model to consider is the Poisson-Boltzmann (PB) theory [26–29]. In Table 5.2 we compare the excess predicted by PB theory with the experimental result, by solving the PB equation such that c_1^∞ and c_z^∞ match the experimental values of c_s and c_z^* from Table 5.1. The excess is then calculated from the PB density profile, and compared with the experimental value of $a\rho_z$ (equal to $a\rho_z^*$ of Table 5.1). The DNA is modeled as a uniformly charged cylinder of radius $d = 10\,\text{Å}$.

Inspection of the results in Table 5.2 shows that there is a reasonable agreement with experiment (within the error bars) for the three smaller values of $c_s = 2, 13, 23\,\text{mM}$. However, for $c_s = 88\,\text{mM}$ there is a 30% deviation. The two data points with $c_{\text{DNA}} > 10\,\text{mM}$ that were not taken into account in the linear fit of Fig. 5.5 suggest that ρ_z is closer to the lower bound of the experimental error range, whereas the PB value is larger than the upper bound.

Overall, the agreement with PB theory (Table 5.2) is surprisingly good considering that PB theory does not work so well for bulky multivalent ions. Deviations from PB theory have several sources. One of these sources is specific molecular details such as the geometrical shape of ions, DNA structure and short–range interactions. Another source for deviations are ion-ion correlations between spermine molecules, computed in theories which go beyond the
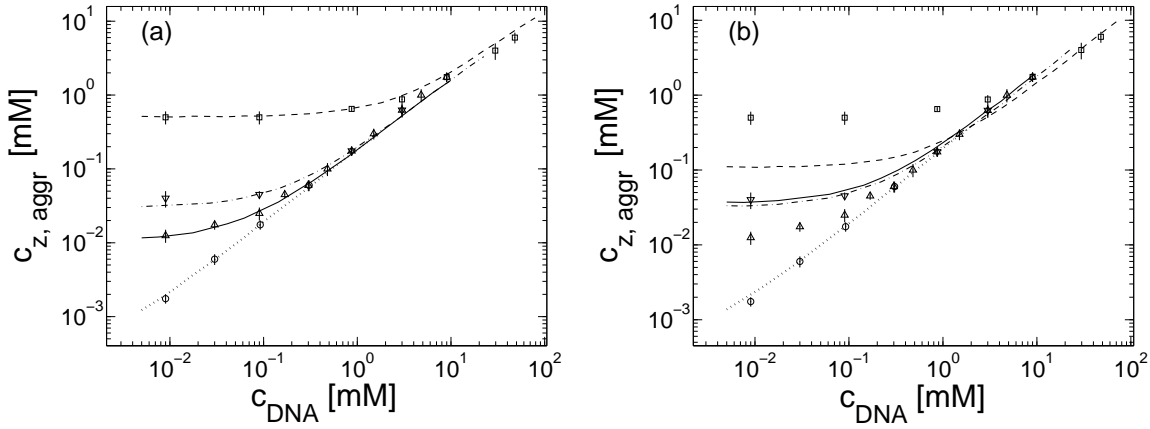
Figure 5.7: Spermine concentration (in mM) as a function of DNA monomer concentration (mM) at the onset of aggregation, calculated using the PB equation. Two different criteria are used in parts (a) and (b) to determine the onset: in (a) c_z^∞, as calculated using the PB equation, is equal to the experimental value of c_z^* from Table 5.1. In (b) ρ_z of PB theory is equal to ρ_z^* from Table 5.1. The radius of DNA is taken as $d = 10\,\text{Å}$. Log-log plot is used in order to show the five decades of DNA concentrations. For each c_s the plot covers experimental data up to $c_{\text{DNA}} = c_s$. For larger c_{DNA}, corrections due to changes in c_1^∞ should be taken into account, as was discussed in the preceding section. All notations are the same as in Fig. 5.5.

mean-field approximation. However, these correlations tend to increase the number of bound multivalent counterions [30], while for $c_s = 88\,\text{mM}$, the number of bound multivalent counterions is decreased. We conclude that correlation effects by themselves are not the main source of the deviations seen in Table 5.2. In addition the data analysis does not indicate over-charging of the DNA. Such an effect may be expected if correlation effects are strong [20].

In Fig. 5.7 we compare the DNA aggregation data with PB predictions at finite DNA concentrations. For each DNA concentration the PB equation is solved in a cylindrical cell of the appropriate radius. The multivalent counterion concentration c_z is gradually increased until the onset is reached, and its onset value, $c_{z,\text{aggr}}$ is plotted as function of c_{DNA}. Two different criteria are used to determine the onset $c_{z,\text{aggr}}$. In Fig. 5.7 (a) it is chosen as the point where c_z^∞ is equal to the experimental value c_z^* of Table 5.1; whereas in Fig. 5.7 (b) the onset is chosen the point where $\rho_z = \rho_z^*$. In order to span all the data range we use for convenience a log-log plot, as in Fig. 5.5 (b).

On a linear scale all the lines in Fig. 5.7 (a) and (b) are straight lines. This fact serves as additional confirmation of our general analysis in the theoretical considerations section. In accordance with our analysis, both c_z^* and ρ_z are constant along each line, and the slope of each line is equal to $a\rho_z$. Note that the relation between c_z^* and ρ_z is determined in Fig. 5.7

within the PB approximation, while in Fig. 5.5 both of these coefficients are related to the actual counterion density profiles in the experimental system. The use of the PB equation is the source of deviations from experimental data in Fig. 5.7.

On first inspection the match with experiment in Fig. 5.7 (a) is very good, whereas the match in Fig. 5.7 (b) is not as good. On closer inspection it is seen that the fit in Fig. 5.7 (b) is not good for small values of c_{DNA}, while it is actually better than in Fig. 5.7 (a) for large c_{DNA}. With the PB equation it is not possible to obtain a perfect fit for both small and large c_{DNA} because the values of c_z and ρ_z are not independent. Fixing $c_z^\infty = c_z^*$ [as in Fig. 5.7 (a)] sets a value of ρ_z that is different from ρ_z^*; and the opposite happens in Fig. 5.7 (b). The fit in Fig. 5.7 (a) is quite good even for large c_{DNA} because the values of ρ_z^* are of similar order of magnitude for all four lines.

Deviations as in Fig. 5.7 are inevitable if any approximations are used to model the distribution of counterions around DNA. Note however that within such approximate models our general theoretical considerations should apply, as long as the total number of ions in the system is counted properly. Such a model that goes beyond PB was proposed in [31]. Indeed, within this model a linear relationship similar to Eq. (5.10) was found.

The experimental results analyzed in this section may be influenced, to a certain degree, by the fact that there was more than one type of monovalent counterion in the system. For the three higher salt concentrations, except for $c_s = 2\,\mathrm{mM}$, the solution contained $10\,\mathrm{mM}$ of TrisH$^+$ ions in addition to Na$^+$ [12]. For the largest salt concentration, $88\,\mathrm{mM}$, where significant deviations from PB theory are found, this effect is probably negligible. Another detail regarding the TE buffer is that the Tris ions may be only partly ionized. If only 80% of Tris is ionized, as suggested in [32], the concentrations $c_s = 13\,\mathrm{mM}$, $23\,\mathrm{mM}$ and $88\,\mathrm{mM}$ should be reduced by $2\,\mathrm{mM}$. Although this will have only a small effect on our results, it will improve both the comparison with PB and the fit with the dashed line in Fig. 5.6, for the point $c_s = 13$ mM. For the two other concentrations of $23\,\mathrm{mM}$ and $88\,\mathrm{mM}$ the effect will be negligible.

5.4.3 Further comments on underlying model assumption

Our underlying assumption, that the onset of aggregation depends uniquely on c_1^∞ and c_z^∞ (but not on c_{DNA}), is an approximation that can be justified on several different levels but deserves further and more thorough investigation. The most simple motivation for this assumption is that multivalent ions, in the vicinity of the chains, mediate the attraction necessary for aggregation. In turn, the number of condensed multivalent ions near each chain is determined by c_1^∞ and c_z^∞.

Let us first suppose that aggregation starts when a net attraction appears between two chains. This assumption may be justified if chains are sufficiently long and their translational entropy can be neglected. In order to find the onset of two-chain attraction the free energy of a two-chain complex should be calculated as a function of the distance between the two chains. This free energy represents the effective interaction between the two chains, mediated by the ionic solution. The counterion distribution near each chain will not be the same for close-by and for isolated chains. However in both cases the concentrations must decay to their bulk values throughout the solution, c_1^∞ and c_z^∞. This requirement serves as a boundary condition, imposed at a large distance from the two chains. It will determine uniquely the counterion distribution between the chains, as well as the free energy associated with the two-chain complex. Hence c_1^∞ and c_z^∞ determine the effective interaction between chains, and in particular whether an attraction occurs at a certain range of inter-chain separations; in terms of these variables the onset of two-chain attraction does not depend on c_{DNA}.

Strictly speaking, the onset of aggregation and the onset of two-chain attraction are not the same. The aggregate phase involves interactions between multiple chains, whereas chains in the dilute phase interact very weakly with each other. Aggregation starts when the free energy per chain is equal in the dilute and aggregate phases. Note that the chemical potential of each ion species must be the same in the two phases, and that in the dilute phase these chemical potentials are directly related to c_1^∞ and c_z^∞. Hence c_1^∞ and c_z^∞ determine the free energy per chain in the two phases. The approximation of independence on c_{DNA} neglects the translational entropy of DNA segments, which can be justified for long enough and rigid segments. It also neglects contributions from interactions between chains in the dilute phase, which are assumed to be small compared to the free energy of the single DNA-counterion complexes.

5.5   Summary

We have shown that the onset of aggregation at finite (non-zero) DNA concentration, $c_{z,\text{aggr}}$, is determined by the onset in the limit of infinite DNA dilution. For DNA monomer concentration smaller than that of monovalent salt, $c_{DNA} \lesssim c_s$, the multivalent counterion concentration at the onset, $c_{z,\text{aggr}}$, depends linearly on c_{DNA}. The coefficients of this linear dependence are the bulk concentration of multivalent counterions and their excess relative to the bulk near each DNA segment. Both of these coefficients are of theoretical interest and can be extracted from the available experimental data.

Our main assumption is that the onset of aggregation can be related to the ion density

profiles around each chain. Hence, it is uniquely determined by c_1^∞ and c_z^∞, the bulk concentrations of the two counterion species, respectively. Our results and fit to experiment strongly support this assumption. Nevertheless, we believe that more detailed theoretical and experimental investigations are needed in order to fully understand its range of validity. For example, it will be of interest to test experimentally the equilibration of a DNA solution through a dialysis membrane, with a cell containing only counterions [33–35]. This procedure allows a direct control of the ionic bulk concentrations.

In order to predict precisely the onset of aggregation, the structure of the aggregated phase must be considered. Nevertheless, it is instructive to focus only on single chains at the onset, as is often done. At the aggregation onset the electrostatic repulsion between isolated chains in solution must be overcome by a sufficiently strong attraction mediated by multivalent counterions. This number of counterions is expected to depend only weakly on physical parameters such as the monovalent salt concentration. Our analysis does not address directly the question of the onset origin, but merely supports the fact that the number of condensed multivalent ions at the onset, $a\rho_z^*$, is of the same order of magnitude, regardless of the c_s value. A more refined result of our analysis is that $a\rho_z^*$ is not constant but decreases with increase of c_s. On the other hand c_z^*, the value of c_z^∞ at the onset, depends strongly on c_s. This is mainly a result of the competition between monovalent and multivalent ions, as discussed in Appendix 5.B.

Our analysis also sheds light on counterion condensation on DNA, which is independent on the criterion for DNA aggregation. The experimental data indicates that for high c_s the number of spermine ions in the vicinity of DNA is smaller than the prediction of Poisson-Boltzmann theory. A similar trend was observed in computer simulations [30] of spermidine (3^+) and NaCl in contact with DNA. Spermidine binding was affected by addition of monovalent salt more strongly than the Poisson-Boltzmann prediction. For high salt concentrations spermidine binding was considerably smaller. In the computer simulations both molecular specific interactions, the geometrical shape of the constituents and inter-ion correlations were taken into account. All these effects, and in particular the geometry of the spermidine molecule, which is similar to that of spermine, were found to play an important role.

The above analysis demonstrates that specific interactions play an important role in determining the threshold of aggregation. In the dilute phase these interactions strongly influence the competition between monovalent and multivalent ions and the free energy of DNA-counterion complexes. Similarly, specific interactions play a prominent role in the dense phase [36]. Force measurements under osmotic stress [37–39] provide a wealth of information on these interac-

tions.

In conclusion, the physical parameters extracted here from experiment on the onset of DNA aggregation provide insight on the conditions required for aggregation, and on condensation of ions around DNA. These parameters may turn out to be of great value in assessment of various theoretical models. Additional detailed experiments may further deepen our understanding of these complex phenomena.

5.A   Relation between excess and condensed ions

In this appendix we discuss the relation between the excess and the number of condensed ions. The latter quantity is not as well defined as the former, but relates more naturally to the aggregation mechanism. The notion of condensed ions suggests that some ions are bound to the charged chain while others are free. In reality there is a density profile that extends all the way from $r = d$ to $r = R$ with no definite separation between condensed and free ions. In the following we define condensed ions rather loosely as the number of ions up to a certain characteristic distance from the chain [23, 25]. We show that for multivalent ions this number does not depend strongly on the choice of this characteristic distance. Hence, the number of condensed ions is reasonably well defined. Moreover, the excess number of multivalent counterions, which can be directly calculated from the experimental data, is nearly identical to this quantity. This point will be further explained below.

Fig. 5.8 shows the excess of 4-valent counterions $\delta\rho_z(r)$ up to a distance r from the DNA axis, as a function of r:

$$\delta\rho_z(r) = 2\pi \int_0^r r' \mathrm{d}r' \; [n_z(r') - c_z^\infty] \tag{5.15}$$

with the limit $\delta\rho_z(\infty) = \rho_z$ of Eq. (5.4). The density profile was calculated using the Poisson-Boltzmann equation, with the radius of DNA taken as $d = 10\,\text{Å}$ and with bulk densities of ions as in the last line of Table 5.1: $c_s = c_1^\infty = 88\,\text{mM}$, $c_z^\infty = 0.52\,\text{mM}$.

Three observations can be made. First, most but not all of the excess z-valent ions are localized very close to the DNA, at a distance of order μ/z, where μ is the Gouy-Chapman length (see [26]):

$$\mu = \frac{1}{2\pi l_B \sigma} = \frac{d}{l_B \rho_{\text{DNA}}} \tag{5.16}$$

where σ is the average charge per unit area on the cylinder surface, $\sigma = \rho_{\text{DNA}}/2\pi d$, and $\rho_{\text{DNA}} = 1/a$ is the DNA charge per unit length. At room temperature the Bjerrum length $l_B \simeq 7\,\text{Å}$ and for DNA with 4-valent counterions $\mu/z \simeq 0.6\,\text{Å}$. Second, the counterions within a layer of few times the Debye length ($\kappa^{-1} = 10.0\,\text{Å}$ in Fig. 5.8) neutralize the DNA charge.
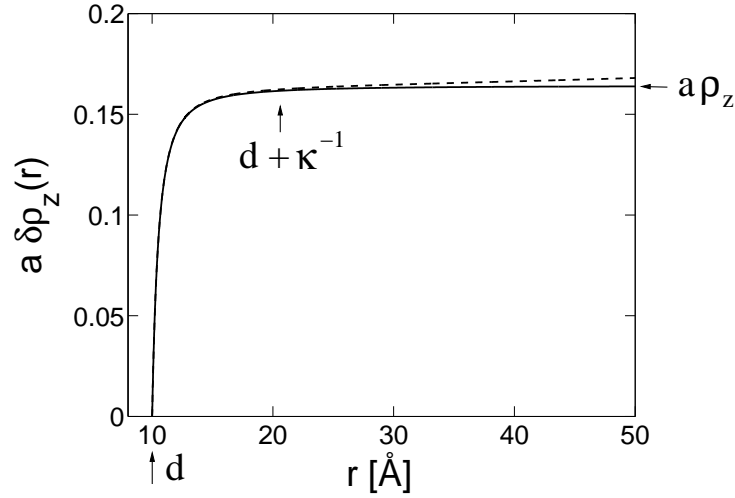
Figure 5.8: Excess of 4-valent ions per DNA monomer, up to a distance r from the axis of a charged cylinder of radius $d = 10$Å (modeling the DNA) as obtained using the Poisson-Boltzmann equation (solid line). The excess $\delta\rho_z(r)$ is defined in Eq. (5.15). The number of charges per unit length on the cylinder is $1/a$ where $a = 1.7$ Å to fit DNA values. The bulk densities of monovalent and multivalent ions are $c_1^\infty = 88$ mM, $c_z^\infty = 0.52$ mM, yielding $\kappa^{-1} = 10.0$ Å. The quantity $\delta\rho_z$ (solid line) can be compared with the total number of 4-valent ions (dashed line) up to a distance r from the cylinder. The distance $d + \kappa^{-1}$ from the DNA axis is indicated by a vertical arrow, and characterizes the decay of the density profile far away from the DNA.

Nearly all the excess distribution is in this layer. Third, in order to estimate the total amount of counterions in the condensed layer of thickness $\alpha\kappa^{-1}$, where α is a number of order unity, we need to add $\delta\rho_z$ to the bulk contribution, $\pi\alpha^2\kappa^{-2}c_z^\infty$. Using κ from Eq. (5.1), the latter is equal to:

$$\left(\frac{\alpha^2}{4l_B}\right)\frac{c_z^\infty}{2c_1^\infty + z(z+1)c_z^\infty} \tag{5.17}$$

In experiment, c_z^∞ is much smaller than c_1^∞ at the onset, and the bulk contribution of Eq. (5.17) can be neglected relative to ρ_z, for α of order unity. This can be seen specifically in Fig. 5.8 by comparing the solid and dashed lines.

The outcome of the above discussion is that ρ_z, defined in Eq. (5.4) as the excess of counterions throughout the cell, can be regarded, to a good approximation, as the total number of counterions within a condensation layer whose thickness is approximately the Debye length. For typical concentration ranges as considered here we do not expect that this outcome will change, even for models going beyond Poisson-Boltzmann theory.

As a further demonstration, the number of multivalent counterions up to several different distances from the DNA is shown in Table 5.3, as calculated in a unit cell using the Poisson-Boltzmann equation. For each c_s in Table 5.1 we find the Poisson-Boltzmann density profile

c_s[mM]	d + 10 Å	d + 20 Å	d + κ^{-1}	d + $2\kappa^{-1}$	$a\rho_z$
2	0.191	0.193	0.194	0.194	0.194
13	0.187	0.190	0.190	0.191	0.191
23	0.171	0.172	0.172	0.173	0.173
88	0.134	0.135	0.134	0.135	0.135

Table 5.3: Number of z-valent counterions, per DNA monomer, up to several different distances from the DNA axis, compared with $a\rho_z$.

such that $c_1^\infty = c_s$ and $\rho_z = \rho_z^*$, and then calculate the number of multivalent ions (per DNA monomer) up to the following distances from the DNA radius: 10 Å, 20 Å, κ^{-1} and $2\kappa^{-1}$. The values of κ^{-1}, as obtained from Eq. (5.1) are equal to 68, 26, 20 and 10 Å for c_s = 2, 13, 23 and 88 mM, respectively. These numbers are compared with $a\rho_z^*$. All the different measures in Table 5.3 yield results that are very close to each other.

5.B   Competition between monovalent and multivalent ions

As discussed in the previous sections, the three quantities c_s, c_z^* and ρ_z^* are not independent. The bulk densities c_s and c_z^* enforce a certain density profile near isolated DNA chains, and in particular determine the excess value ρ_z^*. In this appendix we study the relation between c_s, c_z^*, and ρ_z^* in more detail. Since ρ_z^* is of the same order of magnitude for different values of c_s, we study how the value of c_z^* depends on c_s and ρ_z^*, which are considered as the two independent variables.

We first apply a simplified two-phase model, in the absence of short-range interactions, in order to gain some insight on the dependence of c_z^* on ρ_z^* and c_s. Then, we consider the effects of short range interactions on this relation, within the framework of mean–field theory. Other theoretical and experimental studies of competition between monovalent and multivalent ions can be found in Refs. [23, 25, 30, 40–43].

5.B.1   Two-phase model

Two-phase models have been widely used to describe the distribution of counterions around cylindrical macromolecules [27, 44]. In these models ions are considered as either condensed or free. The condensed ions gain electrostatic energy due to their proximity to the negatively charged chain but lose entropy, since they are bound at a small cylindrical shell around it. For systems with more than one type of counterion Manning introduced the so-called two-variable

theory [45], which is an extension of his previous model [44, 46]. This model has been used to analyze condensation of DNA molecules by spermine and spermidine [24, 47]. In this section we present a similar model, which differs from Manning's two-variable theory in some details. As a by-product of our analysis we compare our two-phase model with PB theory and Manning's two-variable theory.

Model details and main equations

We assume that the PE is confined within a finite cylindrical cell of radius R and area $A = \pi R^2$, defined as in Eq. (5.2).

The free energy, per unit length within a cell, is then written as follows:

$$
\begin{aligned}
F &= \rho_z \ln\left(\lambda^3 \frac{\rho_z}{A_c}\right) + \rho_1 \ln\left(\lambda^3 \frac{\rho_1}{A_c}\right) \\
&+ \rho_z^f \ln\left(\lambda^3 \frac{\rho_z^f}{A - A_c}\right) + \rho_1^f \ln\left(\lambda^3 \frac{\rho_1^f}{A - A_c}\right) \\
&+ \frac{1}{2}(-\rho_{\text{DNA}} + z\rho_z + \rho_1)\phi
\end{aligned}
\tag{5.18}
$$

where $\rho_{\text{DNA}} = 1/a$ is the number of unit charges per unit length of DNA. The first two terms are the entropy of condensed multivalent and monovalent counterions, where ρ_z and ρ_1 are the number of condensed ions per unit length of the DNA. We assume that condensed ions are bound on a cylindrical shell around the DNA and take its area, for simplicity, to be:

$$
A_c = \pi d^2
\tag{5.19}
$$

where d is the DNA radius (Fig. 5.9). The length λ is included in order to have a dimensionless argument inside the logarithms, and can be chosen arbitrarily.

The next two terms are the entropy of free counterions. The numbers per unit length of free multivalent ions, ρ_z^f, and of free monovalent ions, ρ_1^f, are related to the number of condensed ions since the total number of ions within the cell is fixed:

$$
\begin{aligned}
\rho_z^f \equiv (A - A_c)c_z^f &= Ac_z - \rho_z, \\
\rho_1^f \equiv (A - A_c)c_1^f &= Ac_s + \rho_{\text{DNA}} - \rho_1.
\end{aligned}
\tag{5.20}
$$

where we introduced the concentrations of free counterions c_z^f and c_1^f.

Finally, the electrostatic energy is evaluated as if all the bound ions are exactly at the cylinder rim, $r = d$, and the linearized Debye-Hückel approximation is used for the electrostatic
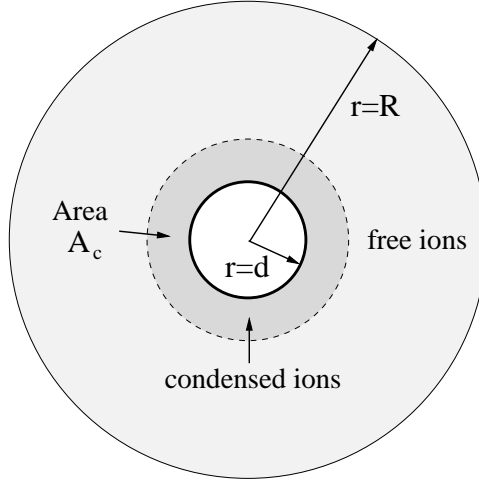
Figure 5.9: Schematic representation of the two-phase model, applied in a cell of radius R. Bound ions are assumed to occupy a cylindrical shell of area A_c around the DNA. The free ions occupy the rest of the space up to radius R. The electrostatic energy is evaluated as if all condensed ions are exactly at the inner (DNA) radius, $r = d$.

potential at $r > d$. This leads to the last term in Eq. (5.18), where ϕ is the reduced electrostatic potential at $r = d$, given by:

$$\phi = -2l_B(\rho_{\text{DNA}} - z\rho_z - \rho_1)\frac{K_0(\kappa d)}{\kappa d K_1(\kappa d)} \tag{5.21}$$

where we assume that the outer cell radius is much larger than d and κ^{-1}, K_0 and K_1 are zeroth and first order modified Bessel functions of the first kind, and κ^{-1} is the Debye length, defined similarly to Eq. (5.1):

$$\kappa^2 = 4\pi l_B \left[2c_1^f + z(z+1)c_z^f \right] \tag{5.22}$$

We neglect in Eq. (5.18) the contribution from the entropy of monovalent co-ions.

The number of condensed monovalent and z-valent counterions is found by minimizing the free energy with respect to ρ_1 and ρ_z [taking into account Eq. (5.20)], yielding:

$$\ln\left(\frac{\rho_z}{c_z^f A_c}\right) = -z\phi \;\; ; \;\; \ln\left(\frac{\rho_1}{c_1^f A_c}\right) = -\phi. \tag{5.23}$$

In this minimization we neglect contributions due to the dependence of κ on ρ_1 and ρ_z. This is justified by the fact that:

$$\frac{\partial \kappa}{\partial \rho_1} = -\frac{4\pi l_B}{\kappa(A - A_c)} \;\; ; \;\; \frac{\partial \kappa}{\partial \rho_z} = -\frac{2\pi l_B z(z+1)}{\kappa(A - A_c)}. \tag{5.24}$$

As long as $A - A_c \gg l_B \kappa^{-1}$ these contributions are indeed negligible.

c_s	$a\rho_z^*$	c_z^* (two-phase)	c_z^* (PB)	c_z^* (Manning)
2	0.194	4.1×10^{-4}	4.3×10^{-4}	7.5×10^{-7}
13	0.191	1.0×10^{-2}	3.7×10^{-2}	3.4×10^{-4}
23	0.173	7.4×10^{-2}	3.3×10^{-2}	4.1×10^{-4}
88	0.135	3.9×10^{-1}	1.1×10^{-1}	4.8×10^{-3}

Table 5.4: Comparison of c_z^∞ corresponding to the threshold value of $a\rho_z$, as predicted by our two-phase model (two-phase), Poisson-Boltzmann theory (PB) and two-variable theory (Manning).

Consequences for DNA aggregation

We are interested in the qualitative dependence of c_z^* on c_s. Note that c_z^∞ of the previous sections has the same role as c_z^f in the two-phase model, while ρ_z and ρ_1 in the two-phase model play a similar role as the excess (designated in the previous sections using the same symbols, ρ_z and ρ_1). The approximations made in the two-phase model manifest themselves in the relation between c_z^f, c_1^f and ρ_z, which is different from the analog relationship in PB theory.

For the monovalent salt, assuming that $c_s > c_{\text{DNA}}$, c_1^f can be replaced by c_s. Equation (5.24) then yields the following relation:

$$c_z^* = \frac{\rho_z^*}{A_c} \left(\frac{c_s A_c}{\rho_1^*} \right)^z \tag{5.25}$$

where ρ_1^* is the linear density of bound monovalent ions at the onset of aggregation, and ρ_z^* is the linear density of bound multivalent ions (a more elaborate discussion, leading to a similar conclusion, is found in Ref. [40]). Qualitatively ρ_1^* is the only ingredient that needs to be estimated in this equation, since c_s is controlled experimentally and $z\rho_z^*$ is of order one.

The main outcome of Eq. (5.25) is that c_z^* scales roughly as $(c_s)^z$. This explains the large variation of c_z^* at different monovalent salt concentrations since $z = 4$. There are several sources for corrections to this scaling. The first one is the dependence of ρ_1^* on c_s and ρ_z^*. A second source of corrections is the effect of short-range interactions, which is discussed below within PB theory (Sec. 5.B.2). In addition, Eq. (5.25) involves all the approximations of the two-phase model.

Comparison with other models

We conclude this section by comparing the predictions of the two-phase model with those of PB theory and Manning's two-variable theory (see also Refs. [23,25]). This is instructive due to the wide use of the two-phase model in the literature. Table 5.4 lists the value of c_z^* calculated

with the two-phase model, using the values of c_s and ρ_z^* of Table 5.1. The two-phase model can be seen to agree qualitatively with PB theory. Quantitatively, their predictions differ by a factor of up to four in the table.

Our two-phase model differs from Manning's model in some details. First, the area used in the expression for the entropy of bound counterions is different. Second, the expression for the electrostatic energy of bound ions is given in Manning's theory by:

$$\phi = 2l_B \left(\rho_{\mathrm{DNA}} - z\rho_z - \rho_1\right) \ln\left(1 - \mathrm{e}^{-\kappa a}\right). \tag{5.26}$$

Note that for small κd the two forms in Eqs. (5.26) and (5.21) are similar if a is replaced by d, since:

$$\frac{K_0(\kappa d)}{\kappa d K_1(\kappa d)} \simeq -\ln\left(1 - \mathrm{e}^{-\kappa d}\right) \tag{5.27}$$

In the last column of Table 5.4 we present the results of Manning's two-variable theory, in the version that was used in Refs. [24, 25, 47] (with different areas of condensation for monovalent and multivalent counterions). Compared to our two-phase model, deviations from PB theory are larger, typically of approximately two orders of magnitude. Since both two-phase models are quite similar to each other, their different predictions demonstrate the large sensitivity of c_z^* to model-dependent parameters. In our opinion such models are useful for obtaining qualitative predictions, but should be used with great care when quantitative predictions are required.

5.B.2   Short-range interactions

Spermine is a long, relatively narrow molecule. Because of this geometry spermine can approach DNA at close proximity. It can even penetrate the grooves at certain sites and orientations [48, 49]. Configurations that are close enough to the DNA are accompanied by a loss of orientational entropy. There are many additional factors that modify the interaction of spermine with DNA, compared to simplified electrostatic models. Among them are short-range interactions, specific ordering of charges on the spermine and DNA, and arrangement of the surrounding water molecules.

Using PB theory it is not possible to take all these effects into account. In this section we will demonstrate, within the framework of PB theory, that short-range interaction parameters can strongly affect the competition between monovalent and multivalent ions [41, 42, 50], and thereby affect the onset of aggregation in a similar way to that seen in Table 5.2.

As a simple example (with somewhat arbitrary parameters chosen to demonstrate our point) two short-range effects are added to the PB model. We consider 4-valent ions that are larger than the monovalent ones. Hence the distance of closest approach to the DNA is different for

c_s[mM]	c_z^∞[mM]	$a\rho_z^*$	$a\rho_z$ (PB)	$a\rho_z$ (SR)
2	0 ± 0.0003	0.194 ± 0.020	0.186 ± 0.005	0.191 ± 0.006
13	0.011 ± 0.002	0.191 ± 0.013	0.178 ± 0.002	0.172 ± 0.003
23	0.031 ± 0.005	0.173 ± 0.025	0.172 ± 0.002	0.163 ± 0.003
88	0.52 ± 0.05	0.135 ± 0.026	0.164 ± 0.002	0.149 ± 0.003

Table 5.5: Excess of 4-valent ions near DNA, $a\rho_z^*$, extracted from DNA aggregation experiments (as in Table 5.1), compared with calculated values using Poisson-Boltzmann theory (PB), and Poisson-Boltzmann theory with short range interactions (SR).

the two species. In this example these distances (smallest allowed distances between an ion center and the DNA axis) are taken as $9\,\text{Å}$ for the monovalent counterions and $12\,\text{Å}$ for the multivalent ones. In addition, we include a short-range attraction between the multivalent ions and DNA: multivalent ions gain $3\,k_BT$ if their distance from the DNA is smaller than $15\,\text{Å}$. Qualitatively these are two competing effects. The first one (closer approach of monovalent ions) slows down replacement of monovalent ions by multivalent ions, while the second (short-range attraction) has the opposite effect. The balance between the two effects is different for different c_s and c_z^∞.

Table 5.5 shows values of $a\rho_z$ calculated using the above modified model. These values (SR) are shown next to the results of the usual Poisson-Boltzmann theory (PB) and compared with the experimental values of $a\rho_z^*$. For $c_s = 2\,\text{mM}$, ρ_z is almost the same in the two calculations. For $c_s = 88\,\text{mM}$ and $c_z^\infty = 0.52\,\text{mM}$ ρ_z is considerably decreased with the inclusion of short-range interactions, and is closer to the experimental value. Any one of the two short-range effects, by itself, results in a large discrepancy with experimental data at low salt concentration.

We believe that the importance of competing mechanisms for a long, multivalent ion such as spermine [30] go beyond the simple modifications to PB described above. More refined modifications include the loss of orientational entropy at close proximity to the DNA. This effect creates a short-range repulsion, whereas the correlation effect beyond mean-field is similar to a short-range attraction. We stress, however, that the improvement found in Table 5.5 over simple PB theory does not imply that our short-range interaction parameters are realistic for spermine and DNA. It only demonstrates that such effects can account for the discrepancy with PB predictions.

As a second example we consider multivalent ions that are bulkier than monovalent ones, so that their distance of closest approach to DNA is larger from the monovalent one by $4\,\text{Å}$. No short-range attraction is included. Figure 5.10 shows the onset of aggregation using the same
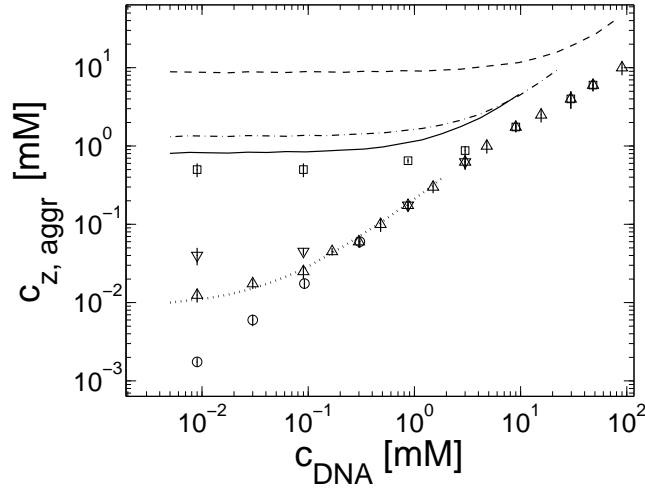
Figure 5.10: Multivalent ion concentration [mM], as function of DNA monomer concentration [mM] at the onset of aggregation, calculated using the PB equation, with different radii of closest approach for monovalent ions ($9\,\text{Å}$) and multivalent ions ($13\,\text{Å}$). The criteria for the onset is that $\rho_z = \rho_z^*$ of Table 5.1, as in Fig. 5.7 (b). A log-log plot is used in order to show the five decades of DNA concentrations.

criterion as in Fig. 5.7 (b), *i.e.*, $\rho_z = \rho_z^*$ of Table. 5.1. Compared to Fig. 5.5 (b), a much larger value of c_z is needed to reach the same value of ρ_z. Such an effect may be found for large and bulky counterions.

To summarize this appendix, the large variation of c_z^* in Table 5.1, for different values of c_s, is the result of competition between monovalent and multivalent counterions. Due to this competition, c_z^* is highly sensitive to short-range, ion-specific effects, as well as to model-dependent approximations. Simplified models that include only electrostatic interactions are thus inherently limited in their capability to predict the conditions required for DNA aggregation in a quantitative manner.

Symbol Legend (Chapter 5)

κ^{-1}	Debye length.
μ	Gouy-Chapman length, Eq. (5.16).
ρ_1, ρ_z	Excess of monovalent/multivalent ions per unit length, Eq. (5.4).
	Number of condensed ions per unit length in the two-phase model (Appendix 5.B).
ρ_1^f, ρ_z^f	Number of free counterions per unit length of the cell (Appendix 5.B).
ρ_{DNA}	Number of unit charges per unit length of the DNA axis.
a	Monomer length, taken as $1/\rho_{\mathrm{DNA}}$.
A	Cell area.
A_f	Area available to condensed ions (Appendix 5.B).
c_1^∞, c_z^∞	Bulk concentrations.
c_1^f, c_z^f	Concentrations of free counterions (Appendix 5.B).
c_{DNA}	DNA (monomer) concentration.
c_s	Concentration of added monovalent salt.
c_z	Concentration of added multivalent salt.
c_z^*	Threshold value of c_z^∞ at the onset of aggregation.
ρ_z^*	Value of ρ_z at the onset of aggregation.
$c_{z,\mathrm{aggr}}$	Average multivalent salt concentration at the onset of aggregation.
d	DNA radius (10 Å).
l_B	Bjerrum length.
$n_z(r)$	Local concentration of multivalent counterions.
R	Cell radius.
z	Valency of multivalent counterions.

Bibliography

[1] Y. Burak, G. Ariel, and D. Andelman, *Biophys. J.* **85** (2003) 2100.

[2] Y. Burak, G. Ariel, and D. Andelman, *Curr. Opin. Colloid Int. Sci.* **9** (2004) 53.

[3] V.A. Bloomfield, D.M. Crothers, and I. Tinoco, *Nucleic Acids: Structures, Properties, and Functions*, University Science Books: Sausalito, CA, 2000.

[4] W.M. Gelbart, R.F. Bruinsma, P.A. Pincus, and V.A. Parsegian, *Physics Today* **53** (2000) 38.

[5] J. Pelta, F. Livolant, and J.-L. Sikorav, *J. Bio. Chem.* **271** (1996) 5656.

[6] J. Pelta, D. Durand, J. Doucet, and F. Livolant, *Biophys. J.* **71** (1996) 48.

[7] C.W. Tabor, and H. Tabor, *Ann. Rev. Biochem.* **53** (1984) 749.

[8] L.C. Gosule and J.A. Schellman, *J. Mol. Biol.* **121** (1978) 311.

[9] D.K. Chattoraj, L.C. Gosule, and J.A. Schellman, *J. Mol. Biol.* **121** (1978) 327.

[10] J. Widom and R.L. Baldwin, *J. Mol. Biol.* **144** (1980) 431.

[11] J. Widom and R.L. Baldwin, *Biopolymers.* **22** (1983) 1595.

[12] E. Raspaud, M. Olvera de la Cruz, J.-L. Sikorav, and F. Livolant, *Biophys. J.* **74** (1998) 381.

[13] M. Saminathan, T. Antony, A. Shirahata, L.H. Sigal, T. Thomas, and T.J. Thomas, *Biochemistry.* **38** (1999) 3821.

[14] E. Raspaud, I. Chaperon, A. Leforestier, and F. Livolant, *Biophys. J.* **77** (1999) 1547.

[15] A. Osland and K. Kleppe, *Nucleic Acids Res.* **4** (1977) 685.

[16] M. Olvera de la Cruz, L. Belloni, M. Delsanti, J.P. Dalbiez, O. Spalla, and M. Drifford, *J. Chem. Phys.* **103** (1995) 5781.

[17] I. Borukhov, K.-C. Lee, R.F. Bruinsma, W.M. Gelbart, A.J. Liu, and M. Stevens, *J. Chem. Phys.* **117** (2002) 462.

[18] I. Borukhov, R.F. Bruinsma, W.M. Gelbart, and A.J. Liu, *Phys. Rev. Let.* **86** (2001) 2182.

[19] J. Wittmer, A. Johner, and J.F. Joanny, *J. Phys. II France.* **5** (1995) 635.

[20] T.T. Nguyen, I. Rouzina, and B.I. Shklovskii, *J. Chem. Phys.* **112** (2000) 2562.

[21] B.Y. Ha and A.J. Liu, *Phys. Rev. Lett.* **79** (1997) 1289.

[22] J.J. Arenzon, J.F. Stilck, and Y. Levin, *Eur. Phys. J. B.* **12** (1999) 79.

[23] L. Belloni, M. Drifford, and P. Turq, *Chem. Phys.* **83** (1984) 147.

[24] R.W. Wilson and V.A. Bloomfield, *Biochemistry* **79** (1979) 2192.

[25] R.W. Wilson, D.C. Rau, and V.A. Bloomfield, *Biophys. J.* **30** (1980) 317.

[26] D. Andelman, in *Handbook of Physics of Biological Systems*, I. R. Lipowsky and E. Sackmann (eds.), Elsevier Science: Amsterdam, 1984, Vol. I, Chap. 12, p. 603.

[27] F. Oosawa, *Polyelectrolytes*, Marcel Dekker: New York, 1971.

[28] M. Le Bret and H. Zimm *Biopolymers* **23** (1984) 287.

[29] M. Guéron and G. Weisbuch *Biopolymers* **19** (1980) 353.

[30] A.P. Lyubartsev and L. Nordenskiöld, *J. Phys. Chem. B* **101** (1997) 4335.

[31] T.T. Nguyen and B.I. Shklovskii, *J. Chem. Phys.* **115** (2001) 7298.

[32] J.X. Tang, T. Ito, T. Tau, P. Traub, and P.A. Janmey, *Biochemistry* **36** (1997) 12600.

[33] W.H. Braunlin, T.J. Strick, and M.T. Record, Jr., *Biopolymers.* **21** (1982) 1301.

[34] G.E. Plum and V.A. Bloomfield, *Biopolymers* **27** (1988) 1045.

[35] J.A. Subirana and J.L. Vives, *Biopolymers* **20** (1981) 2281.

[36] H.H. Strey, R. Podgornik, D.C. Rau, and V.A. Parsegian, *Curr. Opin. Struct. Biol.* **8** (1998) 309.

[37] D.C. Rau, B. Lee, and V.A. Parsegian, *Proc. Natl. Acad. Sci. USA.* **81** (1984) 2621.

[38] D.C. Rau and V.A. Parsegian, *Biophys. J.* **61** (1992) 246.

[39] D.C. Rau and V.A. Parsegian, *Biophys. J.* **61** (1992) 260.

[40] I. Rouzina and V.A. Bloomfield, *J. Phys. Chem. B* **100** (1995) 4292.

[41] I. Rouzina and V.A. Bloomfield, *J. Phys. Chem. B* **100** (1996) 4305.

[42] I. Rouzina and V.A. Bloomfield, *Biophys. Chem.* **64** (1997) 139.

[43] H. Magdelénat, P. Turq, P. Tivant, M. Chemla, R. Menez, and M. Drifford, *Biopolymers* **18** (1979) 187.

[44] G.S. Manning, *J. Chem. Phys.* **51** (1969) 924.

[45] G.S. Manning, *Quart. Rev. Biophys. II* **2** (1978) 179.

[46] G.S. Manning, *Biophys. Chem.* **7** (1977) 95.

[47] V.A. Bloomfield, R.W. Wilson, and D.C. Rau, *Biophys. Chem.* **11** (1980) 339.

[48] N. Korolev, A.P. Lyubartsev, L. Nordensiköld, and A. Laaksonen, *J. Mol. Biol.* **308** (2001) 907.

[49] N. Korolev, A.P. Lyubartsev, A. Laaksonen, and L. Nordenskiöld, *Biophys. J.* **82** (2002) 2860.

[50] H. Deng and V.A. Bloomfield, *Biophys. J.* **77** (1999) 1556.

Chapter 6

Charge regulation of interacting weak polyelectrolytes

In the following chapter we study the pH-regulated dissociation of weak rod-like polyelectrolytes (PEs).[1] We introduce a generalized non-uniform mean-field formalism to describe the dissociation. Our formalism allows for two-sublattice symmetry breaking, which in titration curves is associated with a plateau for intermediate dissociation degrees. We first test our method in the case of a single weak PE by comparison with exact enumeration studies and show that it gives quantitatively accurate results for the dissociation degree in the full range of pH values, and in specific performs much better than the nearest-neighbor approximation (where exact solutions are possible). We then study charge regulation of the coupled system of a weak polyacid and a weak polybase as a function of their mutual distance, which has some relevance for PE-multilayer formation and for PE complexation. An intricate interplay of the degree of dissociation and the effective interaction between the PEs as a function of their mutual distance is found.

6.1   Introduction

The charge of weak polyacids and polybases is determined by the probability of each functional group to dissociate and expose a charged residue. This probability depends on a chemical equilibrium which can be tuned by varying the pH of the solution. In contrast to dilute solutions of monoacids or monobases, in weak polyelectrolytes (PEs) each functional group is influenced by all other groups along the polymer, via their mutual electrostatic interaction. As a result of the repulsion between charged groups, even strong PEs become weak at low salt concentrations.

---

[1]The material presented in this chapter was published in Ref. [1].

Furthermore, when two or more polymers interact with each other, their degree of ionization is modified, compared to their isolated state, and depends on parameters such as the distance between the polymers and their relative spatial configuration. Due to the many-body nature of this problem, and the long range of the electrostatic interactions, an exact solution for the average charge as function of pH is generally not known.

In this chapter we consider stiff PEs, where there is no coupling between the dissociation degree of freedom and the polymer conformation (for treatment of such coupling in flexible PEs see, for example, [2–4]). We consider first a single PE in salt solution and discuss some of the approximations commonly used to characterize its charge regulation. It was previously shown that a uniform mean field approach cannot adequately describe charge regulation when the coupling between charges along the polymer is strong [5]. In these cases ionizable groups dissociate in a two-step process, characterized by a plateau in the charge *vs.* pH curve. This process results from a spatially inhomogeneous charging pattern and is not predicted by a uniform mean field approach. We introduce a mean field theory with explicit symmetry breaking between two sublattices. Such an approximation is shown to be semi-quantitatively accurate and performs better than previous calculations where the range of interactions is restricted [5], as we demonstrate by comparison with exact enumeration over all configurations for finite chain lengths.

In the second part of the chapter we apply our non-uniform mean-field scheme to the interaction of two stiff PEs. We restrict ourselves to the simple case of polymers aligned parallel to each other and calculate the average charging and free energy as function of their distance. Our model reveals some of the intricate effects that can occur in interacting weak PEs. In a broader context, these interactions are of interest in the formation of PE multilayers, composed of alternating layers of positively and negatively charged polymers [6–8]. In particular weak polyacids and polybases can be used to form multilayers [9, 10]. In this case properties such as the layer thickness and density depend strongly on the dissociation degree of the functional groups, and can be tuned sensitively by varying the pH of the solution [10].

6.2   Single Polyelectrolyte

The free energy for a weak PE, immersed in an aqueous ionic solution, can be written as follows:

$$F = -\ln \sum_{\{s_i = 0,1\}} \exp(-\mathcal{H}) \qquad (6.1)$$

The Hamiltonian $\mathcal{H}$ is given by:

$$\mathcal{H} = \mu \sum_i s_i + \sum_{i>j} s_i s_j v_{\mathrm{DH}}(\mathbf{r}_i, \mathbf{r}_j) \tag{6.2}$$

where r_i is the position of the ith monomer and s_i can be either zero (for an uncharged monomer) or one (charged monomer). The sum in Eq. (6.1) goes over all different configurations of dissociated groups. Note that F and $\mathcal{H}$ are given in units of the thermal energy $k_B T$. The chemical potential μ is related to the pH of the solution [11]:

$$\mu = -2.303(\mathrm{pH} - \mathrm{pK_a}) - l_B \kappa \qquad \text{(Acid)}$$

$$\mu = 2.303(\mathrm{pH} - \mathrm{pK_b}) - l_B \kappa \qquad \text{(Base)} \tag{6.3}$$

where κ is the Debye screening length, $l_B = e^2/(\varepsilon k_B T)$ is the Bjerrum length, equal to about $7\,\text{Å}$ in water at room temperature, $k_B T$ is the thermal energy, ε_w is the dielectric constant of water and e is the unit charge. The last term in Eq. (6.3) is the self-energy of the two charges created in the dissociation process. We assume throughout this chapter that the ionic solution can be described using the linearized Debye-Hückel theory, so that electrostatic interactions between charges are pairwise additive, as in Eq. (6.2). The exact form of v_{DH} depends on the salt concentration, and also on the dielectric properties of the polymer backbone, as will be discussed below. In the most simple case of dielectric continuity between the polymer and solution, v_{DH} is equal to:

$$v_{\mathrm{DH}}(\mathbf{r}_1, \mathbf{r}_2) = l_B \frac{\mathrm{e}^{-\kappa|\mathbf{r}_1 - \mathbf{r}_2|}}{|\mathbf{r}_1 - \mathbf{r}_2|} \tag{6.4}$$

The linear Debye-Hückel approach neglects non-linear effects that are associated with counterion condensation and which are contained in the non-linear Poisson-Boltzmann formalism. The main reason for resorting to linear theory is that only at that level can the complicated problem of spatially inhomogeneous charge distributions on the PE backbone be calculated. One justification is that weak polyelectrolytes as studied in this chapter are typically not strongly charged, so that non-linear effects are less important than for strong polyelectrolytes, as will be discussed in more detail in the concluding section.

For the following calculations, it is convenient to use symmetric variables $\tilde{s}_i$ having the values $-1, 1$ instead of $0, 1$:

$$s_i = \frac{1 + \tilde{s}_i}{2} \tag{6.5}$$

In terms of these variables the partition function is:

$$Z = \sum_{\{\tilde{s}_i = -1, 1\}} \exp\left\{ -\tilde{c} - \tilde{\mu} \sum_i \tilde{s}_i - \sum_{i>j} \tilde{s}_i \tilde{s}_j \tilde{v}_{\mathrm{DH}}\left[a(i-j)\right] \right\} \tag{6.6}$$

where:

$$\tilde{c} = \frac{1}{2}N\mu + \frac{1}{4}N\sum_{j>0} v_{\text{DH}}[aj]$$

$$\tilde{\mu} = \frac{\mu}{2} + \frac{1}{2}\sum_{j>0} v_{\text{DH}}[aj]$$

$$\tilde{v}_{\text{DH}} = \frac{1}{4}v_{\text{DH}} \tag{6.7}$$

and a is the nearest-neighbor distance between dissociable groups on a straight line.

6.2.1   Non-uniform mean-field approach with two sublattices

Mean-field equations

In principle, the above statistical one-dimensional problem can be solved using transfer-matrix techniques which take the long-ranged interactions into account via a multiple-time integration with a suitably chosen kernel. In order to obtain a simple, tractable solution we use mean-field methods, which are implemented in the following way. The Gibbs variational principle can be used to obtain an upper bound for the free energy $F = -\ln Z$,

$$F \leq F_0 + \langle \mathcal{H} \rangle_0 - \langle \mathcal{H}_0 \rangle_0 \tag{6.8}$$

In this inequality $\mathcal{H}_0$ is a trial Hamiltonian (to be specified below) and $F_0 = -\ln Z_0$, where Z_0 is the partition function obtained from $\mathcal{H}_0$; The thermal averages in Eq. (6.8) are evaluated using $\mathcal{H}_0$. We introduce the trial Hamiltonian

$$\mathcal{H}_0 = h_0 \sum_i \tilde{s}_{2i} + h_1 \sum_i \tilde{s}_{2i+1} \tag{6.9}$$

which separates the polymer into two sublattices. The variational parameters h_0, h_1 are fields which act on the charges in the two sublattices. By minimizing the right hand side of Eq. (6.8) with respect to h_0 and h_1, the following equations are obtained,

$$h_0 = \tilde{\mu} + J\langle\tilde{s}_0\rangle_0 + K\langle\tilde{s}_1\rangle_0$$

$$h_1 = \tilde{\mu} + J\langle\tilde{s}_1\rangle_0 + K\langle\tilde{s}_0\rangle_0 \tag{6.10}$$

where

$$\langle\tilde{s}_0\rangle_0 = -\tanh(h_0) \quad ; \quad \langle\tilde{s}_1\rangle_0 = -\tanh(h_1), \tag{6.11}$$

and

$$J = \frac{1}{2}\sum_{j>0} v_{\text{DH}}[2ja] \quad ; \quad K = \frac{1}{2}\sum_{j\geq0} v_{\text{DH}}[(2j+1)a] \tag{6.12}$$

The choice of two sublattices (as opposed to more sublattices with a larger period) is related to the strong anti-correlation that can exist between adjacent monomers, and will be further motivated below.

Main properties of mean-field equations

Equations (6.10) and (6.11) always have a symmetric solution for which $h_0 = h_1$. However, the symmetric solution is not always the minimum of the free energy but can be, instead, a saddle point in the 2D plane spanned by h_0 and h_1. In these cases two other solutions exist, both of which break the symmetry between the two sublattices, *i.e.*, $h_0 \neq h_1$. One solution can be obtained from the other by exchanging h_0 and h_1. The average charging degree of the polymer is then equal to:

$$\langle s \rangle_0 = \frac{\langle \tilde{s} \rangle_0 + 1}{2} = \frac{\langle \tilde{s}_0 \rangle_0 + \langle \tilde{s}_1 \rangle_0 + 2}{4} \tag{6.13}$$

In order to understand for which parameters symmetry breaking occurs, let us consider first the case $\tilde{\mu} = 0$. In this case the Hamiltonian exhibits the symmetry $\tilde{s}_i \rightarrow -\tilde{s}_i$ in addition to the symmetry of exchanging the two sublattices. Even if the latter symmetry is broken, we have $\langle \tilde{s} \rangle_0 = 0$, or equivalently $\langle s \rangle_0 = 1/2$, *i.e.*, exactly half of the monomers are dissociated. Using the fact that $h_0 = -h_1$, Eqs. (6.10) and (6.11) reduce in this case to one transcendental equation,

$$h_0 = (K - J) \tanh(h_0) \tag{6.14}$$

This equation has a non-zero solution (where $h_0 \neq h_1$) only if:

$$K - J > 1 \tag{6.15}$$

If this condition is met, a sublattice symmetry breaking solution also exists within a certain range of $\tilde{\mu}$ values around zero. Outside the range $|\tilde{\mu}| < \tilde{\mu}_c$ there is no symmetry breaking, *i.e.*, $\langle \tilde{s}_0 \rangle_0 = \langle \tilde{s}_1 \rangle_0$. If condition (6.15) is not met, there is no symmetry breaking solution for any value of $\tilde{\mu}$.

The solution with $h_0 = h_1$ (no sublattice symmetry breaking) can be found by substituting this equality in Eqs.(6.10) and (6.11), leading to the transcendental equation

$$h_0 = (K + J) \tanh(h_0) \tag{6.16}$$

In a uniform mean-field approximation this solution is found for all values of $\tilde{\mu}$, whereas in our case it applies only for $|\tilde{\mu}| \geq \tilde{\mu}_c$.

Before considering concrete examples we comment on the nature of the transition at $\tilde{\mu} = \pm\tilde{\mu}_c$. This transition is second order, *i.e.*, $\langle \tilde{s}_1 \rangle_0 - \langle \tilde{s}_0 \rangle_0 \rightarrow 0$ as $\tilde{\mu} \rightarrow \pm\tilde{\mu}_c$. Note that a non-zero

$\tilde{\mu}$ does not break the symmetry of exchanging the two sublattices in the Hamiltonian. This is why the order parameter is continuous at the transition. However the derivative of the order parameter with respect to $\tilde{\mu}$ is discontinuous and diverges when approaching the transition from the side where symmetry breaking occurs. Similarly, the derivative of the average dissociation degree with respect to $\tilde{\mu}$ has a discontinuity at the transition. These are artifacts of the mean-field approach, since the exact solution for a one dimensional system with short-ranged interactions cannot exhibit a real phase transition [12]. However, our non-uniform mean-field scheme still predicts the average charge very accurately, as will be demonstrated below.

6.2.2   Uniform dielectric constant

In the case of a uniform dielectric constant, in which the screened interaction is given by Eq. (6.4), the summations in Eq. (6.12) can be performed explicitly, yielding

$$
\begin{aligned}
J &= -\frac{l_B}{4a} \left[\ln\left(1 - \mathrm{e}^{-\kappa a}\right) + \ln\left(1 + \mathrm{e}^{-\kappa a}\right) \right] \\
K &= -\frac{l_B}{4a} \left[\ln\left(1 - \mathrm{e}^{-\kappa a}\right) - \ln\left(1 + \mathrm{e}^{-\kappa a}\right) \right] \tag{6.17} \\
\tilde{\mu} &= \frac{\mu}{2} - \frac{l_B}{2a} \ln\left(1 - \mathrm{e}^{-\kappa a}\right) \tag{6.18}
\end{aligned}
$$

The condition for sublattice symmetry breaking, Eq. (6.15), translates to

$$
K - J = \frac{l_B}{2a} \ln\left(1 + \mathrm{e}^{-\kappa a}\right) > 1 \tag{6.19}
$$

Increasing κ decreases $K - J$ and thus the possibility for sublattice symmetry breaking. Symmetry breaking can occur for a finite range of κ and pH only if the condition

$$
\frac{l_B}{a} > \frac{2}{\ln 2} \simeq 2.9 \tag{6.20}
$$

is met. For $l_B = 7.0\,\text{Å}$ this condition leads to $a \lesssim 2.4\,\text{Å}$. Hence vinyl-based polymers with an acid group on every second Carbon atom such as poly-styrene-sulfonate or poly-acrylic-acid with a charge-distance of $a \approx 2.5$ Å are marginally close to symmetry breaking within the present model. However, a dielectric discontinuity due to the polymer backbone can increase $K - J$ considerably, as will be discussed in the following sub-section.

Examples with symmetry breaking will be shown in the following sub-section, while here we restrict ourselves to the case of dielectric continuity and no symmetry breaking. In the case of no symmetry breaking all the dependence on κ enters through the quantity

$$
K + J = -(l_B/2a) \ln\left(1 - \mathrm{e}^{-\kappa a}\right), \tag{6.21}
$$

which increases with increasing Debye length κ^{-1}.
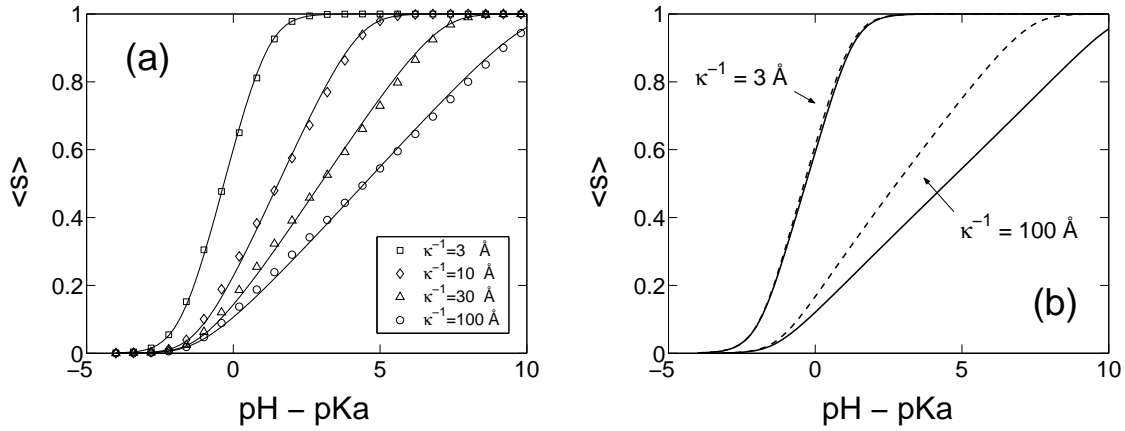
Figure 6.1: (a) Average degree of dissociation of a polyacid as function of pH-pKa, calculated using a mean-field approximation (solid lines). For comparison an exact enumeration over all configurations is also shown (symbols) with $N = 20$ and using periodic boundary conditions. Results for four different values of the Debye length are shown, $\kappa^{-1} = 3\,\text{Å}$ (squares), $10\,\text{Å}$ (diamonds), $30\,\text{Å}$ (triangles) and $100\,\text{Å}$ (circles). The separation between charged groups is $a = 2.5\,\text{Å}$. (b) Average degree of dissociation as function of pH-pKa, calculated using an exact enumeration for a chain length $Na = 50\,\text{Å}$. The solid lines show enumeration results with periodic boundary conditions (as shown using symbols in part (a)). These results are compared with enumeration without periodic boundary conditions (dashed lines). Two different values of the Debye length are shown in the plot, $\kappa^{-1} = 3\,\text{Å}$ (to the left) and $100\,\text{Å}$ (to the right).

Results

In Fig. 6.1 (a) we show the average degree of charge dissociation following from our mean-field equation for a polyacid with $a = 2.5$ Å, for four different salt concentrations, corresponding to $\kappa^{-1} = 3$, 10, 30 and 100 Å (solid lines). These results are compared with an exact calculation of the free energy for a finite chain with $N = 20$ dissociable groups (symbols), by enumeration over all 2^N states. For the exact enumeration, periodic boundary conditions are imposed by setting the interaction between monomers i and j to be

$$v_{\text{DH}}^p(i,j) = \sum_{n=-\infty}^{\infty} v_{\text{DH}}(i, j + nN). \tag{6.22}$$

The comparison between mean-field and the exact enumeration is very good for all four values of κ^{-1} shown in the figure. Note that in all these cases there is no symmetry breaking in the mean-field solution, as expected since the charge distance of $a = 2.5$ Å does not satisfy the condition Eq. (6.20). Comparison of the four curves shows that κ^{-1} has a large effect on the degree of charging. As κ^{-1} is increased each monomer interacts more strongly with the other monomers. This increased repulsion reduces the charging, or, as one might put it, the long-ranged repulsion between charged groups makes even strong PEs weak.

Throughout this work we will assume that the polymer is long compared to the Debye length. However, it is important to realize that for shorter polymers the average degree of dissociation depends on the polymer length. In order to demonstrate this point we show in Fig. 6.1 (b) the average degree of dissociation as function of pH for a finite chain of length Na, where $N = 20$ and $a = 2.5\,\text{Å}$. In the calculation an exact enumeration over all configurations is performed, without periodic boundary conditions (dashed lines). The results are compared with an enumeration with periodic boundary conditions (solid lines), as was done in Fig. 6.1 (a). For $\kappa^{-1} = 3\,\text{Å}$, the polymer length is larger than the screening length, $Na \gg \kappa^{-1}$ and the two calculations yield nearly identical results. In the second case shown in the plot, $\kappa^{-1} = 100\,\text{Å}$, κ^{-1} and Na are of the same order of magnitude and there are significant finite size effects. These results may be important for the interaction of short DNA oligomers with substrates, as they show that the polymer length affects adsorption behavior also via the effective charge of PEs.

Restriction to nearest-neighbor interactions

A common approximation that was previously applied for the charge regulation of PEs is to consider only nearest-neighbor (NN) interactions [13–15]. The reason is that exact closed-form solutions are available in this case. Within the non-uniform mean-field approach, this approximation corresponds to setting $K = (l_B/2a)\exp(-\kappa a)$ and $J = 0$. Note that the combination $K + J$, which determines the solution without symmetry breaking, is smaller in the NN case than in the full interaction case. On the other hand the combination $K - J$, which affects the symmetry breaking (see Eq. (6.15)), is larger in the NN case.

In Fig. 6.2 we compare the NN predictions (dashed lines and open symbols) with those obtained using the full long-range interaction (solid lines and filled symbols), for two different values of the Debye length. The symbols show exact enumeration results, obtained using periodic boundary conditions and are thus representative of an infinitely long system, while the lines show mean-field results. For both values of the Debye length there are significant deviations between the NN result and the full interaction. As can be expected, these deviations are larger for the larger screening length, $\kappa^{-1} = 100\,\text{Å}$, since in this case the interaction between further-nearest neighbors contributes significantly to the total interaction. Note that for $\kappa^{-1} = 100\,\text{Å}$ and NN interactions (open square symbols and dashed line) there is also a small effect of symmetry breaking in the mean-field solution, resulting in a non-monotonous slope near $\langle s \rangle = 0.5$. A similar effect is seen in the exact enumeration. As a main result of this section, we see that the restriction to nearest-neighbor interactions is in general not a good approximation,
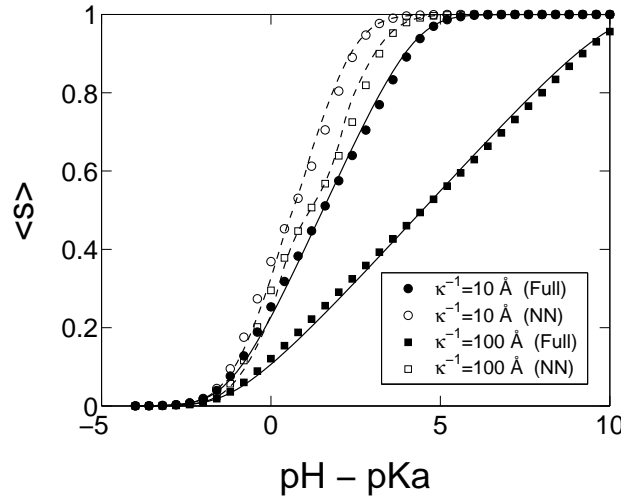
Figure 6.2: Comparison of a nearest neighbor mean-field approximation (dashed lines) with a mean-field calculation taking into account all long range interactions (solid lines) for a polyacid having $a = 2.5 \, \text{Å}$, as function of pH-pKa. Results for two values of the Debye length are shown. They can be distinguished in the plot according to the type of symbols (circles, $\kappa^{-1} = 10 \, \text{Å}$; squares, $\kappa^{-1} = 100 \, \text{Å}$). The symbols show exact enumeration results with $N = 20$ and periodic boundary conditions (empty symbols - only nearest neighbor interactions; full symbols - full long range interaction). In the enumeration with NN interactions results are nearly identical to the analytical expression for an infinite chain.

while the mean-field approach reproduces the exact enumeration results very accurately.

6.2.3 Non-uniform dielectric constant

So far we neglected effects of the dielectric discontinuity between the polymer and its surroundings. As these effects tend to increase the electrostatic interactions, they are expected to be important for the dissociation process. They were estimated in Ref. [5] using a simple model, shown in Fig. 6.3. The PE is modeled as a cylinder of radius d and dielectric constant $\varepsilon_d < \varepsilon_w$, where $\varepsilon_w \simeq 80$ is the dielectric constant of water. Charged groups are assumed to be equally spaced along the cylinder axis, with separation a. Here we generalize this model to some extent by placing these charged groups at a distance $0 \leq b \leq d$ from the axis, as shown in Fig. 6.3. The electrostatic potential exerted by one such charge on another one was calculated in Ref. [5] and is given by

$$\psi = \frac{\varepsilon_w}{\varepsilon_d} \frac{l_B}{z} + \frac{1}{2\pi} \sum_{n=-\infty}^{\infty} W_p(z, n) \tag{6.23}$$

where z is the distance between the charges. The first term is equal to the electrostatic interaction within a medium of dielectric constant ε_d, with no screening by salt. In the second term,
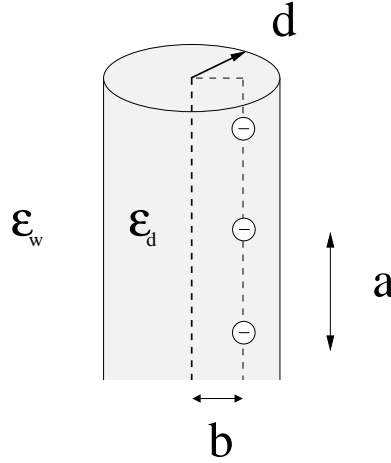
Figure 6.3: Schematic representation of a simple model taking into account the difference between the dielectric properties of water and a polymer's backbone. A PE is modeled as a cylinder of radius d with a dielectric constant ε_d, while the dielectric constant outside the cylinder is equal to ε_w. Charged groups that can dissociate from the polymer are located at regular intervals a from each other, at a distance b from the cylinder axis.

W_p is equal to

$$W_p(z,n) = 4\frac{\varepsilon_w}{\varepsilon_d}l_B \int_0^\infty \mathrm{d}k \cos(kz)\left[I_n(kb)\right]^2 R(k,n) \qquad (6.24)$$

where

$$R(k,n) = \frac{k\varepsilon_d\left[K_{n-1}(kd) + K_{n+1}(kd)\right]K_n(pd) - p\varepsilon_w\left[K_{n-1}(pd) + K_{n+1}(pd)\right]K_n(kd)}{k\varepsilon_d\left[I_{n-1}(kd) + I_{n+1}(kd)\right]K_n(pd) + p\varepsilon_w\left[K_{n-1}(pd) + K_{n+1}(pd)\right]I_n(kd)} \qquad (6.25)$$

$p = \left(k^2 + \kappa^2\right)^{1/2}$ and K_n, I_n are the n-th modified Bessel functions of the first and second kind, respectively.

In Ref. [5] only the case $b = 0$ was considered. For two charges located exactly at the polymer axis, $b = 0$, the electrostatic interaction approaches $(\varepsilon_w/\varepsilon_d)l_B/z$ at short separations, while for larger separations it crosses over to the interaction in the aqueous ionic solution, $l_B\exp(-\kappa z)/z$. The former interaction is typically much larger than the latter, leading to a two-step charging curve and failure of a uniform mean-field approach. On the other hand, only close-by monomers interact strongly with each other, motivating the use of a nearest-neighbor (NN) model [5], where only interactions between neighboring monomers are taken into account. The free energy and average degree of dissociation can then be calculated exactly [13–15], e.g., using the transfer matrix method [12, 16].

The NN approximation indeed predicts the two-step behavior of the charging curve, but it can fail for large values of the Debye screening length, since in this case further-nearest neighbor interactions become important. For large κ^{-1} long-range interactions can be important

although they are much weaker than the interactions between neighboring monomers, as shown in the following numerical examples.

Results for radially symmetric charge distribution

In Fig. 6.4 (a) the NN prediction (dashed line, exact solution) is compared with an enumeration using the full long range interaction (circles). The Debye length is $\kappa^{-1} = 100\,\text{Å}$ and interactions between monomers are calculated using Eq. (6.23) with $b = 0$, $d = 2.5\,\text{Å}$, $\varepsilon_w/\varepsilon_d = 80/3$ and a monomer separation $a = 3.5\,\text{Å}$. In all calculations with dielectric discontinuity we use a monomer separation $a = 3.5\,\text{Å}$ rather than $2.5\,\text{Å}$, which corresponds to a somewhat smaller fraction of dissociable groups.

The exact solution of the NN model in Fig. 6.4 (a) (broken line) deviates significantly from the enumeration results with the full range of interactions included (circles). In contrast, our non-uniform mean-field approach with symmetry breaking (solid line in Fig. 6.4 (a)) is semi-quantitatively correct. The success of our generalized mean-field approximation is one of the main results in the first part of this work. Note that the main difference with respect to enumeration is that the mean-field approximation over-estimates the effects of symmetry breaking, as seen from the exaggerated size of the plateau region.

We also present in Fig. 6.4 (a) a comparison between the NN exact solution (dashed line) and an enumeration taking only nearest-neighbor interactions into account (crosses). This is done in order to test finite size effects in the exact enumeration. The enumeration and exact solution yield almost identical results, demonstrating that an enumeration with $N = 20$ is typically very accurate for a single polymer. We note that periodic boundary conditions are essential in order to obtain this level of accuracy in enumeration, when long range interactions are included [compare Fig. 6.1 (b)]. As another test for the enumeration procedure we increased N to 30 for several different choices of $v_{\text{DH}}(z)$. In all these cases deviations from results with $N = 20$ were insignificant.

Figure 6.4 (b) shows a comparison between the NN exact solution (broken line) and a mean-field calculation with two sublattices (solid line), taking only the NN interaction into account, for $\kappa^{-1} = 100\,\text{Å}$. The NN-mean-field approximation shows an effect similar to the curve in Fig 6.4 (a): two artificial discontinuities in the derivative of $\langle s \rangle$ are seen, corresponding to two erroneous second-order transitions. In addition, the plateau is more pronounced compared to the exact solution. Nevertheless, the overall prediction for $\langle s \rangle$ as function of pH is quite accurate.

Finally, the dependence on the Debye screening length κ^{-1} is investigated in Fig. 6.4 (c),
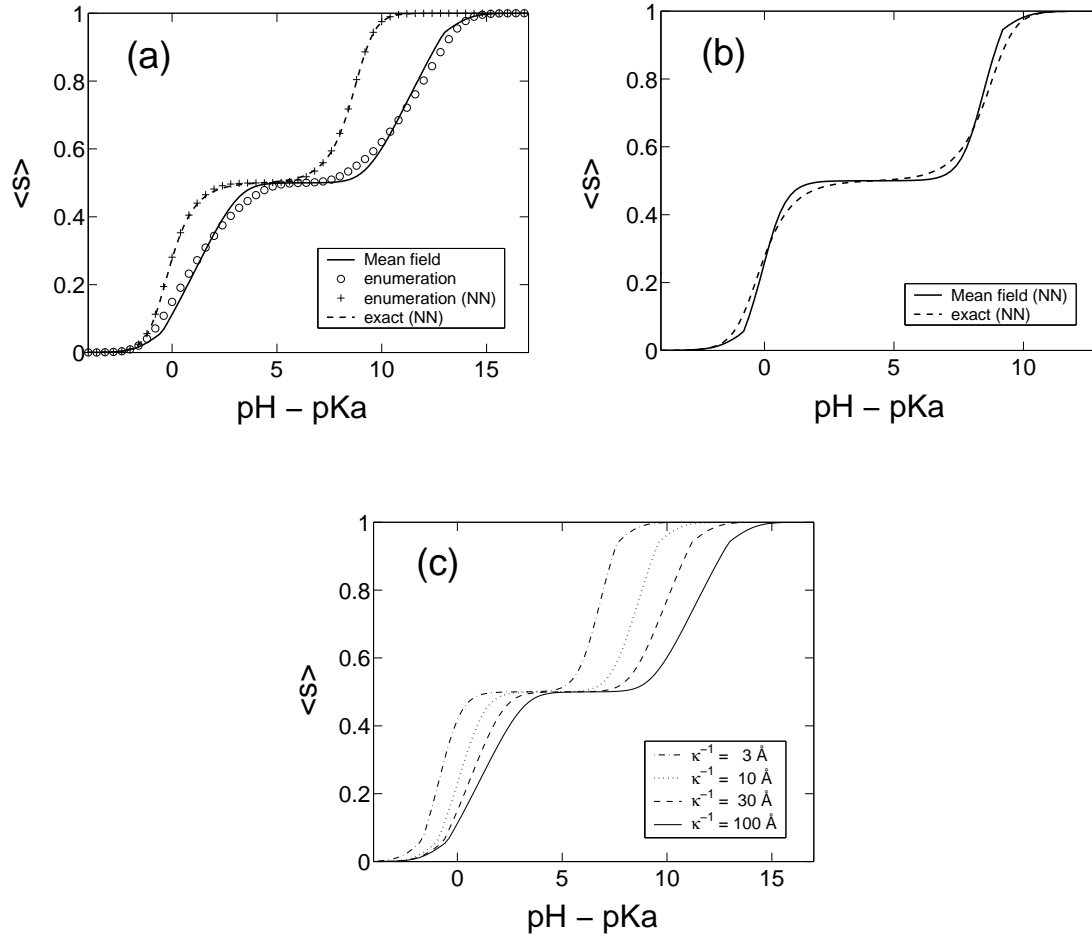
Figure 6.4: Average degree of dissociation of a polymer with strong interactions between close by monomers, characterized by a plateau near $\langle s \rangle = 1/2$. The interactions between monomers are calculated using the cylindrical model shown in Fig. 3, with $\varepsilon_d = 3$, $\varepsilon_w = 80$, $d = 2.5\,\text{Å}$, $a = 3.5\,\text{Å}$, $b = 0$ and a Debye length $\kappa^{-1} = 100\,\text{Å}$. (a) Mean-field results with two sublattices (solid line) are compared with an enumeration over all configurations with $N = 20$ and periodic boundary conditions (circle symbols). The mean-field results show two cusps, where transitions occur between a solution with no symmetry breaking and one with symmetry breaking (the latter occurs for intermediate pH). Results are also compared with an enumeration taking only nearest neighbor (NN) interactions into account (crosses) and the exact solution with NN interactions, calculated using the transfer matrix method (dashed line). (b) Mean-field calculation with two sublattices taking only NN neighbor interactions into account (solid line), compared with the exact solution with NN interactions (dashed line). (c) Dissociation as function of PH for four different values of the Debye screening length: $\kappa^{-1} = 3$, 10, 30 and 100 Å, calculated using the mean-field approximation with two sublattices. All parameters other than κ are as in part (a). The interaction parameters J, K used in the mean-field approximation are equal to $0.21, 4.36$ ($\kappa^{-1}{=}3\,\text{Å}$); $0.46, 4.86$ ($\kappa^{-1}{=}10\,\text{Å}$); $0.87, 5.30$ ($\kappa^{-1}{=}30\,\text{Å}$); and $1.37, 5.84$ ($\kappa^{-1}{=}100\,\text{Å}$).
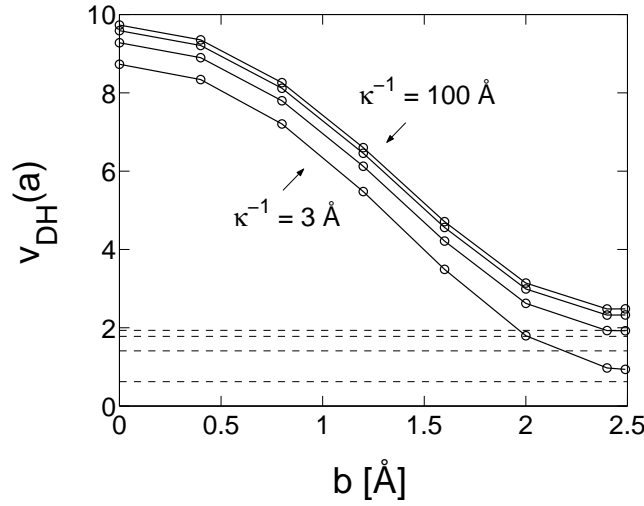
Figure 6.5: Dependence of the electrostatic interaction between two monomers on their distance b from the polymer axis, within the cylindrical model of Fig. 3. The distance between the monomers is $a = 3.5\,\text{Å}$ and the other model parameters are $d = 2.5\,\text{Å}$, $\varepsilon_d = 3$ and $\varepsilon_w = 80$. Results are shown for four values of the Debye length, $\kappa^{-1} =$3, 10, 30, and 100 Å. The electrostatic interaction in an aqueous ionic solution is shown for comparison using dashed lines.

using our non-uniform mean-field approach. The parameters J and K of the sublattice interactions are calculated for each value of κ using Eqs. (6.12) and (6.23). For all the four values of κ^{-1} that are shown, $\kappa^{-1} = 3$, 10, 30 and $100\,\text{Å}$ a pronounced plateau is visible. The cusps that are present in all four cases [for example, at $\langle s \rangle \simeq 0.07$ and $\langle s \rangle \simeq 0.93$ in (a)] are artifacts due to the mean-field approach.

Dependence on the position of charged groups

In most polyacids and polybases the charged units are located in side groups, rather than being close to the polymer axis. This raises the question whether an interaction much larger than the usual Debye-Hückel interaction will occur even if the charges are displaced from the axis. Within the simple cylindrical model presented above, this question can be addressed by calculating the electrostatic interaction between two monomers as a function of b. Such a calculation is shown if Fig. 6.5, for four different values of the screening length κ^{-1}. The monomers are separated by a distance of $a = 3.5\,\text{Å}$, while the polymer radius is taken as $d = 2.5\,\text{Å}$, as in Fig 6.4. In all four cases a very large decrease of v_{DH} occurs with increase of b toward the cylinder boundary, $b = d$. For large d this result is not surprising, since the cylinder becomes similar to a planar interface, separating an aqueous ionic solution and a low dielectric medium. Near such an interface the electrostatic interaction is equal to twice the screened electrostatic interaction in water [17].

For large cylinder radius $d \gg \kappa^{-1}$ we have checked that Eq. (6.23) indeed yields this result. In Fig. 6.5 the cylinder radius is not large compared to the Debye length and the interaction close to the cylinder boundary is even smaller than in the planar limit. The screened interaction in water is shown for comparison using dashed lines.

The above analysis demonstrates that actual electrostatic interactions between near-by monomers depend strongly on the spatial organization of the PE. These interactions probably cannot be estimated reliably using simplified models such as the cylindrical one presented above. The detailed polymer structure, as well as other effects such as the discreteness of the solvent, must be taken into account.

6.2.4   Further discussion of the two-sublattice approximation

Although the comparison with exact enumeration demonstrates that a two-sublattice model is useful, one may ask to what extent the separation into two sublattices has a physical significance. In order to discuss this question we note that within the plateau region of the titration curve there is typically a strong anti-correlation between even and odd monomers. In order to understand this anti-correlation one may think of the ground state of the Hamiltonian in Eq. (6.6), concentrating first on the special case $\tilde{\mu} = 0$. When the interaction between monomers favors opposite dissociation values, the ground state is typically a periodic array of alternating values in the even and odd positions, $s = +1$ and $s = -1$. The long range order of the ground state is not preserved within the exact theory at any finite temperature, due to the entropy associated with domain boundaries in a one dimensional system [12]. Nevertheless, at a certain range of pH values around $\tilde{\mu} = 0$ we may expect a staggered correlation function with strong anti-correlation between even and odd monomers.

As an example, Fig. 6.6 shows the correlation function, $\langle s_i s_0 \rangle - \langle s_i \rangle \langle s_0 \rangle$, for a PE having the same parameters as in Fig. 6.4 (a), calculated by exact enumeration over all states of a PE of length $N = 30$ and using periodic boundary conditions. Results are shown for three different pH values: in the top plot pH = 7, corresponding to $\tilde{\mu} = 0$. The correlation function has a staggered form which persists over the full length of the PE. Nevertheless it is clear that there is no true long range order because the (anti) correlation decreases slightly with monomer separation. In the middle plot, where the pH is equal to 9, the correlation has a shorter range, persisting only up to a distance of about 8 sites from the center monomer. Note that a pH value of 9 is approximately at the right edge of the plateau region seen in Fig. 6.4 (a). With further increase of pH the correlation length continues to decrease and at pH = 13.5 (bottom plot) there is almost no correlation even between adjacent monomers. This pH value is close
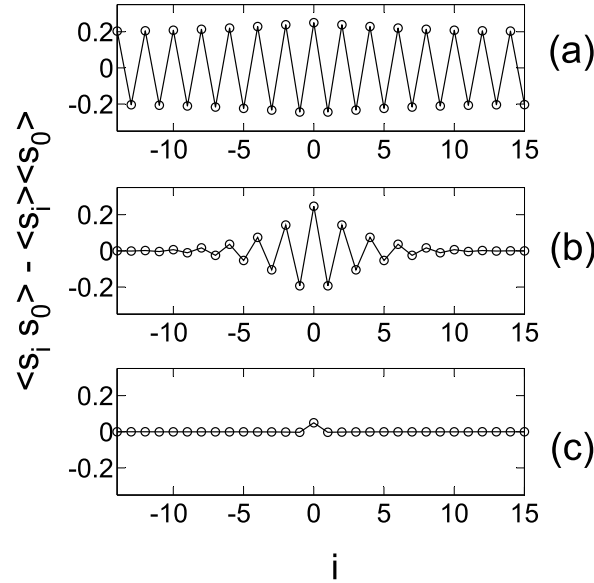
Figure 6.6: Correlation function between the dissociation of a monomer and that of its neighbors, $\langle s_i s_0 \rangle - \langle s_i \rangle \langle s_0 \rangle$, calculated from an exact enumeration over all configurations of a PE having $N = 30$ monomers, with periodic boundary conditions. All physical parameters are as in Fig. 4(a). The pH is equal to 7 in (a), corresponding to $\tilde{\mu} = 0$, to 9 in (b), and to 13.5 in (c).

to the transition point that is found in the two-sublattice model, beyond which there is no symmetry breaking between the two sublattices. In summary, Fig. 6.6 demonstrates that the two-sublattice approximation captures an essential physical property of the dissociation pattern that is absent in the uniform mean field approach, namely a strong anti-correlation between even and odd sites.

In principle, a periodicity other than two may be included in the formulation of the mean field equations, and could lead, for certain parameters, to a lower free energy than the two-fold periodicity. In such cases a plateau would be expected in the titration curve at an average degree of dissociation other than one half. Comparison with the exact enumeration and with typical experimental results indicates that such additional symmetry breaking into structures with more than two sublattices does not occur within the physical parameters considered in this work.

In the second part of this work, where we will look at the interaction between two weak polyelectrolytes, we will employ Debye-Hückel interactions in a uniform dielectric constant, Eq. (6.4), as well as the interaction within a cylindrical dielectric cavity with $b = 0$, which constitute the two extreme cases. In both cases we expect a mean-field approach with two
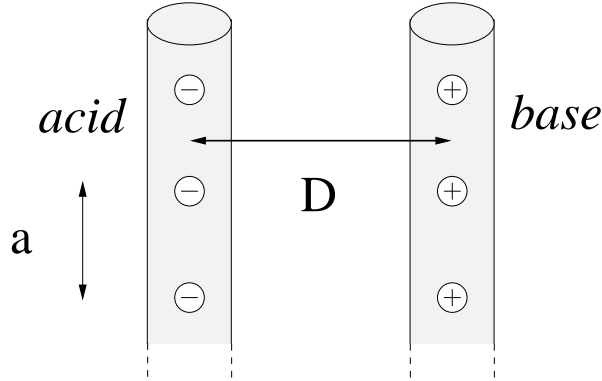
Figure 6.7: Schematic illustration of a model describing the interaction of a polyacid with a parallel polybase, separated by a distance D. The distance between charged groups in both of the PEs is a. For simplicity the charged groups are facing each other.

sublattices to be adequate in order to predict the average charging, as was demonstrated in the preceding discussion.

6.3 Interaction between polyacid and polybase

6.3.1 Uniform mean-field approach

The model we consider is shown schematically in Fig. 6.7. A polyacid (left) and polybase (right) are aligned parallel to each other and separated by a distance D. For simplicity we assume that the distance between charged groups (denoted by a) is identical in the two polymers and that the charge lattices are in phase with each other in the two polymers, as shown in the figure. We would like to calculate the average charge on the two polymers and the free energy as a function of D.

We consider first the case of a uniform dielectric constant, Eq. (6.4), and also assume that for each polymer a uniform mean-field theory (with no symmetry breaking) is adequate. As was shown in the calculations for a single polymer, the latter assumption is justified for monovalent monomers having a nearest neighbor separation $a \gtrsim 2.5\,\text{Å}$.

It is convenient to define for the polyacid

$$s_a = \frac{1 + \tilde{s}_a}{2} \qquad (6.26)$$

and for the polybase

$$s_b = \frac{1 - \tilde{s}_b}{2} \qquad (6.27)$$

where s_a and s_b are zero for an uncharged monomer and one for a charged (dissociated) one. With these definitions both $\tilde{s}_a$ and $\tilde{s}_b$ increase with pH. The mean-field equations are found in a similar way as in the single polymer case, and are given by

$$
\begin{aligned}
h_a &= \tilde{\mu}_a + J\langle \tilde{s}_a \rangle_0 + K\langle \tilde{s}_b \rangle_0 \\
h_b &= \tilde{\mu}_b + J\langle \tilde{s}_b \rangle_0 + K\langle \tilde{s}_a \rangle_0
\end{aligned}
\tag{6.28}
$$

where

$$
\langle \tilde{s}_a \rangle_0 = -\tanh(h_a) \quad ; \quad \langle \tilde{s}_b \rangle_0 = -\tanh(h_b).
\tag{6.29}
$$

The coefficients in these equations are given by:

$$
\begin{aligned}
J &= \frac{1}{4}\sum_{i\neq 0} v_{\mathrm{DH}}(ia) \\
K &= \frac{1}{4}\sum_i v_{\mathrm{DH}}\left[\sqrt{(ia)^2 + D^2}\right] \\
\tilde{\mu}_a &= -\frac{2.303}{2}(\mathrm{pH} - \mathrm{pKa}) + \Delta\tilde{\mu} \\
\tilde{\mu}_b &= -\frac{2.303}{2}(\mathrm{pH} - \mathrm{pKb}) - \Delta\tilde{\mu}
\end{aligned}
\tag{6.30}
$$

where

$$
\Delta\tilde{\mu} = \frac{1}{4}\sum_{i\neq 0} v_{\mathrm{DH}}(ia) - \frac{1}{4}\sum_i v_{\mathrm{DH}}\left(\sqrt{(ia)^2 + D^2}\right) - \frac{l_B\kappa}{2}
\tag{6.31}
$$

Equations (6.28)-(6.29) are very similar to Eqs. (6.10)-(6.11), with a number of important differences. First, the subscripts a and b do not represent two sublattices but instead distinguish between the polyacid and polybase. Another difference is that the chemical potentials $\tilde{\mu}_a$ and $\tilde{\mu}_b$ are usually not equal to each other. Most importantly, J is almost always larger than K, whereas for the two sublattice case J is smaller than K. It is easy to show that for $J > K$ Eqs. (6.28)-(6.29) have a single solution.

Results

The electrostatic interaction between the polyacid and polybase increases dissociation in both polymers (in contrast to the interactions within each PE, which inhibits charged groups from dissociating). Figure 6.8 shows the degree of charging of a polyacid and polybase having $a = 2.5$ Å, as function of pH and for three different values of D. When the polymers are sufficiently far away from each other their dissociation curves are identical to those of a single polymer. For smaller separation the average charge increases. An important case occurs when the pH is tuned such that

$$
(\mathrm{pH} - \mathrm{pKa}) = -(\mathrm{pH} - \mathrm{pKb})
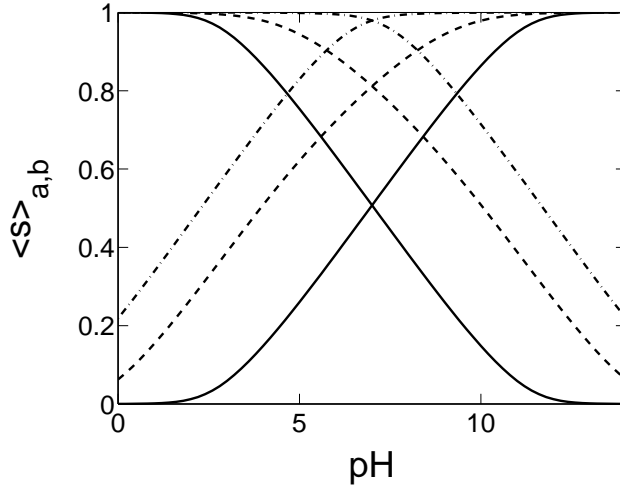\tag{6.32}
$$

Figure 6.8: Average dissociation degree of a polyacid (increasing lines) interacting with a polybase (decreasing lines), as function of pH. The distance between charges is $a = 2.5$ Å; pKa $= 4$, pKb $= 10$ and the Debye length is $\kappa^{-1} = 30$ Å. Results are shown for three values of the inter-polymer separation: $D = 100$ Å (solid lines), 10 Å (dashed lines) and 5 Å (dash-dot lines). The symmetric case where $\mathrm{pH} - \mathrm{pKa} = \mathrm{pKb} - \mathrm{pH}$ occurs at $\mathrm{pH} = 7$.

For example, with the parameters used in Fig. 6.8, pKa $= 4$ (similar to poly-acrylic-acid) and pKb $= 10$ (similar to poly-vinyl-amin), this equality holds at pH $= 7$. In this case, one has $\tilde{\mu}_b = -\tilde{\mu}_a$, as seen from Eq. (6.30), and the solution of Eqs. (6.28)-(6.29) has the properties $h_a = -h_b$ and $\langle \tilde{s}_a \rangle_0 = -\langle \tilde{s}_b \rangle_0$. Using the definitions in Eqs. (6.26)-(6.27), the average charging degrees of the polyacid and polybase are then equal to each other, and the value of h_a is found from the single transcendental equation:

$$h_a = \tilde{\mu}_a + (K - J)\tanh(h_a) \tag{6.33}$$

In the following examples we restrict ourselves to the symmetric case described by Eqs. (6.32) and (6.33). Figure 6.9 (a) shows the average degree of dissociation as function of the polymer separation D (identical for the polyacid and polybase). Results are shown for $a = 2.5$ Å, $\mathrm{pH} - \mathrm{pKa} = \mathrm{pKb} - \mathrm{pH} = 3$ and for four different values of the Debye length, ranging between 3 Å and 100 Å. When D is large compared to κ^{-1} the polymers do not interact, and their average charge is equal to its value in an isolated polymer (compare with Fig. 6.2 at pH-pKa $= 3$). This value depends strongly on κ^{-1}. At separations D of order κ^{-1} and smaller, the average charging increases with decrease of D and approaches unity (full dissociation) at contact.

We turn to the free energy of the two interacting PEs, shown in Fig. 6.9 (b). In this figure the free energy F is divided by N, the number of monomers in each PE. A distinctive feature in
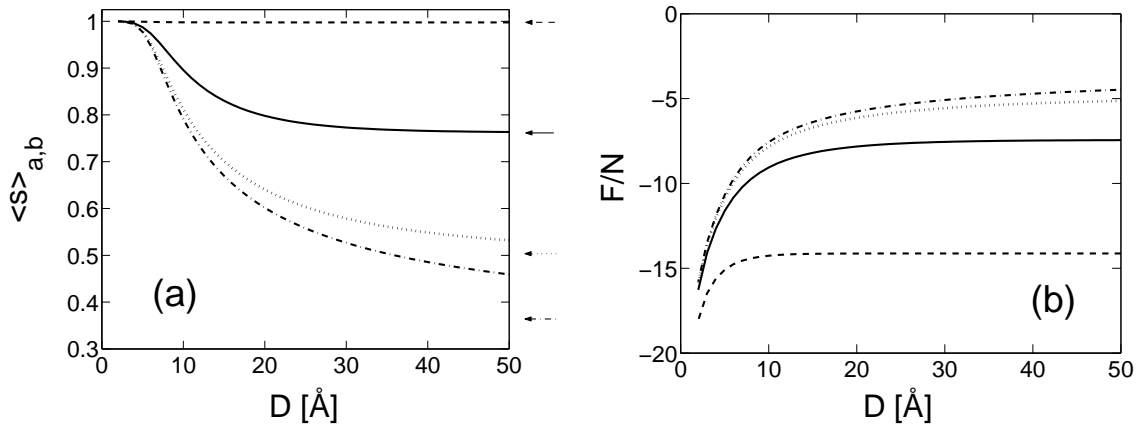
Figure 6.9: Average degree of dissociation (a) and free energy per monomer, F/N (b) as function of the distance D between a polyacid and polybase, with $\mathrm{pH} - \mathrm{pKa} = \mathrm{pKb} - \mathrm{pH} = 3$. Simple Debye-Hückel interactions are used with $\kappa^{-1} = 3\,\text{Å}$ (dashed line), $10\,\text{Å}$ (solid line), $30\,\text{Å}$ (dotted line) and $100\,\text{Å}$ (dash-dot line). All other parameters are as in Fig. 8. The arrows on the right hand side of (a) show the value of $\langle s \rangle$ for an isolated PE.

this figure is that F is almost independent on κ^{-1} at small separations. In contrast to this short separation behavior, F depends strongly on κ^{-1} at large separations. In order to understand these two behaviors we consider each one of the two limits separately:

Small PE distances, $D \ll \kappa^{-1}$

At short separations the average degree of dissociation saturates and is independent on κ^{-1}, as can be seen in Fig. 6.9 (a). The electrostatic interaction energy of the two polymers also becomes nearly independent on κ^{-1}, as can be understood from the following argument. Consider the two polymers as uniformly, oppositely charged and parallel lines. In the limit of no screening, $\kappa = 0$, the electrostatic energy is dominated by interactions at distances of order D and smaller. At distances larger than D opposing positive and negative charges in the two polymers can be regarded as dipoles and the electrostatic interaction between them decays as $1/z^3$ where z is their distance, measured parallel to the polymers. As long as $\kappa^{-1} \gg D$ screening affects only these dipole-dipole interactions, but not the main electrostatic contribution coming from interactions at distances smaller than D. The independence of both $\langle s \rangle$ and the electrostatic energy on κ^{-1} leads to the behavior seen at these small separations.

Large PE distances, $D \gg \kappa^{-1}$

At large separations the free energy approaches the sum of free energies of the two isolated polymers. More precisely, the average degree of dissociation on the two polymers approaches a
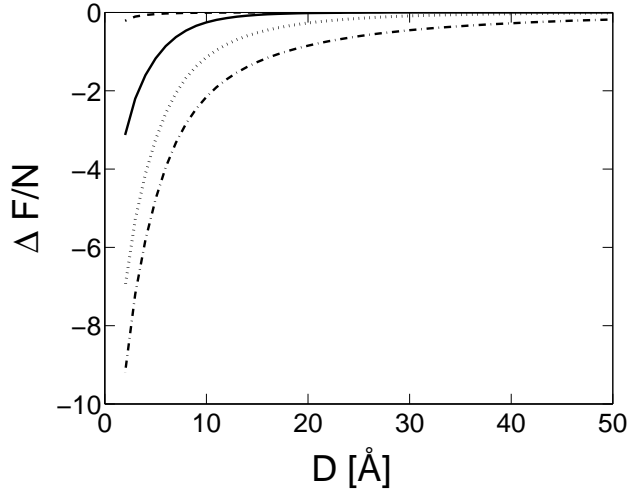
Figure 6.10: The difference ΔF between the free energy F of a polyacid interacting with a polybase, and the asymptotic form of Eq. (6.34). Four values of κ^{-1} are shown. These values, and all other parameters and notations are as in Fig. 9. For each value of κ^{-1} the values of F_0 and s_0 in Eq. (6.34) are equal to the free energy and average degree of dissociation of an isolated PE, respectively.

constant and the free energy can be approximated as follows:

$$\frac{F}{N} \approx \frac{2F_0}{N} - 2l_B \left(\frac{s_0}{a}\right)^2 K_0(\kappa D) \tag{6.34}$$

where F_0 and s_0 are the free energy and average degree of dissociation of a single, isolated PE, respectively. These constants are unrelated to the interaction between the two PEs but depend strongly on κ. The modified Bessel function $K_0(\kappa D)$ characterizes the electrostatic interaction between two parallel and uniformly charged rods:

$$K_0(\kappa D) = \int_0^\infty dz \, \frac{\exp\left(-\kappa\sqrt{z^2 + D^2}\right)}{\sqrt{z^2 + D^2}} = \int_0^\infty du \, \frac{\exp\left(-\sqrt{u^2 + \kappa^2 D^2}\right)}{\sqrt{u^2 + \kappa^2 D^2}} \tag{6.35}$$

Deviations from the asymptotic form (6.34) are expected to occur only when the average degree of dissociation deviates from s_0. This happens approximately when $D \lesssim \kappa^{-1}$ as can be seen in Fig. 6.10, where the difference between F/N and Eq. (6.34) is plotted for the same four values of κ^{-1} as in Fig. 6.9.

6.3.2 Non-uniform mean-field approach

In the case of stronger interactions between monomers within each polymer, the dissociation curve of a single PE is characterized by a plateau. In this case we expect a symmetry breaking transition with two sublattices on each PE. In order to deal with this case the mean-field

Hamiltonian can be generalized to account for sublattices on each one of the two PEs:

$$\mathcal{H}_0 = h_0^a \sum_i \tilde{s}_{2i}^a + h_1^a \sum_i \tilde{s}_{2i+1}^a + h_0^b \sum_i \tilde{s}_{2i}^b + h_1^b \sum_i \tilde{s}_{2i+1}^b \tag{6.36}$$

The mean-field equations and free energy are found using the Gibbs variational principle, in a similar fashion as for the single polymer case. For example, the equation for h_0^a is:

$$h_0^a = \tilde{\mu}^a + J \langle \tilde{s}_0 \rangle_0^a + K \langle \tilde{s}_1 \rangle_0^a + I_0 \langle \tilde{s}_0 \rangle_0^b + I_1 \langle \tilde{s}_1 \rangle_0^b \tag{6.37}$$

where $\langle \tilde{s}_i \rangle_0^\alpha = -\tanh h_i^\alpha$. Similar equations are obtained for h_1^a, h_0^b and h_1^b. The coefficients J,K,I_0 and I_1 in Eq. (6.37) are equal to:

$$
\begin{aligned}
J &= \frac{1}{4} \sum_{i \neq 0} v_{\mathrm{DH}}(2ia) \\
K &= \frac{1}{4} \sum_i v_{\mathrm{DH}}\left[2(i+1)a\right] \\
I_0 &= \frac{1}{4} \sum_i v_{\mathrm{DH}}\left[\sqrt{(2ia)^2 + D^2}\right] \\
I_1 &= \frac{1}{4} \sum_i v_{\mathrm{DH}}\left[\sqrt{(2i+1)^2 a^2 + D^2}\right]
\end{aligned}
\tag{6.38}
$$

and $\tilde{\mu}^a$, $\tilde{\mu}^b$ are given by Eqs. (6.30) and (6.31). The four equations for h_i^α typically have multiple solutions; For example, if symmetry breaking occurs on both polymers the number of solutions is 9. In the limit of non-interacting polymers, $I_0 = I_1 = 0$, four of these solutions are equivalent minima of the free energy, related to each other by exchange of the two sublattices on one or both of the polymers. Interactions between the polymers break the symmetry of exchanging only the sublattices in one of the polymers, and there are two (equivalent) global minima of the free energy.

Results

As a concrete example we consider again the model shown in Fig. 6.3, which accounts for a low dielectric constant of the polymer backbone. Parameters are similar to Fig. 6.4, $b = 0$, $a = 3.5\,\text{Å}$, $d = 2.5\,\text{Å}$ and $\kappa^{-1} = 100\,\text{Å}$. The pH, pKa and pKb values are chosen such that $\mathrm{pH} - \mathrm{pKa} = \mathrm{pKb} - \mathrm{pH} = 3$. The coefficients J and K are set as in Fig. 6.4 with $\kappa^{-1} = 100\,\text{Å}$, $J = 1.4$ and $K = 5.8$. For the coefficients I_0 and I_1 we use Eqs. (6.38) with the screened Debye-Hückel interaction in water, Eq. (6.4). Both of these choices are approximations which become inaccurate when the polymers are very close to each other, since the electrostatic Green's function should then be evaluated in the presence of two dielectric cylinders. However we expect our results to be qualitatively correct as will be further discussed below.
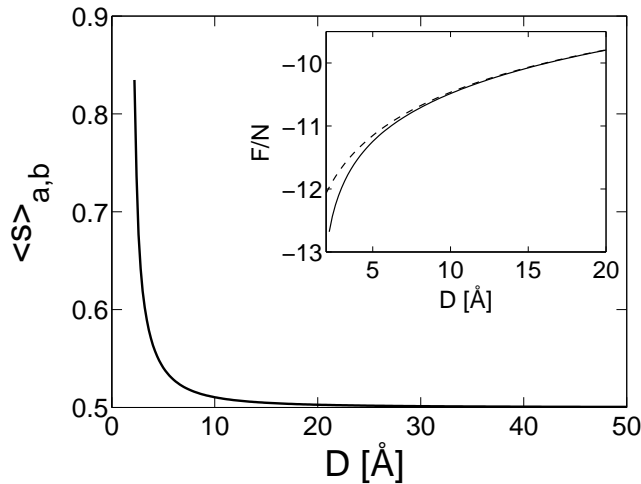
Figure 6.11: Average degree of dissociation of interacting polyacid and polybase, as function of their distance. The interactions between monomers within each PE are calculated assuming a low dielectric backbone, as in Fig. 3. The parameters of the model are as in Fig. 4: $a = 3.5\,\text{Å}$, $d = 2.5\,\text{Å}$, $b = 0$ and $\kappa^{-1} = 100\,\text{Å}$, and $\mathrm{pH} - \mathrm{pKa} = \mathrm{pKb} - \mathrm{pH} = 3$. The inset shows the free energy per monomer, F/N, as function of D (solid line). The dashed line shows the approximation of Eq. (6.34) with $s_0 = 1/2$ and F_0 set to match the value of F at large D.

Figure 6.11 shows the average charging of the two polymers as function of their separation D. Due to the plateau in the dissociation curve of each polymer, $\langle s \rangle$ is close to $1/2$ in most of the separation range. A sharp increase in $\langle s \rangle$ is found at close separations of a few Ångströms. Note that this range, where interactions between the polymers affect the average charging, is much smaller than the Debye length, $\kappa^{-1} = 100\,\text{Å}$.

The inset shows the free energy (solid line) as function of D. For comparison we show (by a broken line) the approximation of Eq. (6.34), with s_0 equal to $1/2$ and F_0 matching the value of F at large D. The two free energies deviate from each other only at very small distances, where $\langle s \rangle$ is larger then $1/2$.

In summary, the symmetry-broken solution is stable for a wide range of distances and gives way to a symmetric solution only at very small distances. Note that in Fig. 6.11 the most significant increase in $\langle s \rangle$ is found for $D < 5\,\text{Å}$, where the two cylinders overlap. However, with the dielectric discontinuity on both polymers taken properly into account (affecting I_0 and I_1 as well as K and J) we can expect a stronger interaction between the polymers for small D. This will lead to an increase of the average charging at larger values of D than in Fig. 6.11.

6.4 Summary

The main result in the first part of this work concerns a generalization of the standard mean-field theory of charge regulation in weak PEs. The polymer is divided into two sublattices, allowing explicitly for correlations between these sublattices to be taken into account. Similar models have been studied in the past in the context of Ising-like models. In the Ising model, interactions are usually assumed to be short-ranged. If only interactions between neighboring monomers are considered, the partition function can be calculated exactly. For PEs the main advantage of using a mean-field approximation is that it allows long-range electrostatic interactions to be taken into account. Simultaneously, one expects mean-field methods to gain in accuracy as the range of interactions increases. Our main result is that a mean-field approach with separation into two sublattices is adequate within a wide range of model parameters. In particular it succeeds in the case of large inter-monomer interactions, where a uniform mean-field theory fails, while also taking into account long range interactions, which may still play an important role.

A motivation for the use of a nearest-neighbor approximation was recently suggested in Ref. [5]. It was pointed out that a low dielectric constant of the polymer backbone can lead to strong enhancement of the coupling between close-by monomers. We show that even within the model of Ref. [5], the nearest neighbor approximation needs improvement for large values of the Debye length, because of the contribution of interactions between non-neighboring monomers. On the other hand, a mean-field approximation with two sublattices is semi-quantitatively accurate. We also demonstrate that effects due to the dielectric discontinuity between the PE interior and the aqueous solvent depend sensitively on the location of the charged groups within the low-dielectric cavity; this is quite relevant, since for most experimental PE architectures, the charged groups are not located centrally but are displaced towards the aqueous interface.

The linearized Debye-Hückel theory is used in this work to evaluate the interaction between monomers. This, of course, is only an approximation, whereas in principle the full non-linear response of the ionic solution must be taken into account. Use of Debye-Hückel interactions is justified as long as the electrostatic potential is small compared to the thermal energy. Hence this approximation is probably reasonably accurate in the plateau region, where the average charge along the polymer is small. Far away from the plateau, and for highly charged PEs, one needs to go beyond Debye-Hückel theory, using the non-linear Poisson-Boltzmann theory. The great advantage of using pairwise interactions is that they allow tractable, analytic solutions to be obtained. In contrast, the nonlinear distribution of ions cannot be calculated analytically

even near a uniformly charged cylinder immersed in a salt solution, let alone an inhomogeneously charged PE. In light of this situation we believe that the results presented in this work provide a useful qualitative treatment of charge regulation even for the case of highly charged PEs, although they may be quantitatively modified by charge renormalization due to nonlinear effects close to the PE [18].

In the second part of this work we studied the interaction between a polyacid and a polybase, using a mean-field approximation. This interaction leads to an increase of the average charging in both polymers as they approach each other. In addition, the interaction energy between a weak polyacid and a weak polybase is stronger than expected in the absence of distance-dependent charge regulation. This means that the effect of charge regulation may be important for the building of stable multilayers, since it decreases the repulsion between similarly charged weak PEs (since the charge regulation in this case decreases the charge strength) and at the same time leads to strongly bound polyacid-polybase pairs. For close-by polymers the electrostatic energy is dominated by interactions between neighboring monomers, and the free energy depends only weakly on the Debye screening length κ^{-1}. On the other hand at large separation between the polymers both the average degree of dissociation and the free energy typically vary strongly with κ^{-1}. The characteristic distance where interactions between the polymers can affect their degree of dissociation is the Debye screening length. However, when there is a plateau in the charge *vs.* pH curve of a single PE, the degree of dissociation may remain close to $1/2$ even at small separations compared to κ^{-1}. In these cases a sharp increase in the average dissociation can occur close to contact.

The increase of charging when weak polyacids and weak polybases come into contact could in principle be observed using infra-red spectroscopy in multilayers. However, one has to keep in mind that in such highly concentrated systems the oppositely charged groups will get very close to each other and form salt bridges.

Symbol Legend (Chapter 6)

ε_d Dielectric constant of PE backbone.

ε_w Dielectric constant of water.

κ Inverse Debye length.

l_B Bjerrum length.

μ Chemical potential.

a Distance between sites along the PE axis.

b Distance of charged sites from the PE axis (Fig. 6.3).

D Distance between PEs.

F Free energy.

h Variational field.

$\mathcal{H}$ Hamiltonian.

J, K Eq. (6.12).

Na PE length.

s_i Dissociation variable of monomer i (0 - uncharged, 1 - charged).

$\tilde{s}_i$ Symmetric dissociation variable (-1 - uncharged, 1 - charged).

Bibliography

[1] Y. Burak and R. R. Netz, *J. Phys. Chem. B* **108** (2003) 4840.

[2] E. Raphael and J.-F. Joanny, *Europhys. Lett.* **13** (1990) 623.

[3] I. Borukhov, D. Andelman, R. Borrega, M. Cloitre, L. Leibler, and H. Orland, *J. Phys. Chem. B* **104** (2000) 11027.

[4] T. Zito and C. Seidel, *Eur. Phys. J. E* **8** (2002) 339.

[5] M. Borkovec, J. Daicic, and G.J. Koper, *Physica A* **298** (2002) 1.

[6] G. Decher, *Science* **277** (1997) 1232.

[7] G.B. Sukhorukov G.B., E. Donath E., S.A. Davis, H. Lichtenfeld, F. Caruso, V.I. Popov, and H. Möhwald, *Polym. Adv. Technol.* **9** (1998) 759.

[8] F. Caruso F., R.A. Caruso R.A., and H. Möhwald, *Science* **282** (1998) 1111.

[9] D. Yoo, S. Shiratori, and M. Rubner, *Macromol.* **31** (1998) 4309.

[10] S. Shiratori and M. Rubner, *Macromol.* **33** (2000) 4213.

[11] R.R. Netz, *J. Phys.: Cond. Matter* **15** (2003) S239.

[12] K. Huang, *Statistical mechanics*, Wiley: New York, 1987, 2nd ed.

[13] R.A. Marcus, *J. Phys. Chem.* **58** (1954) 621.

[14] F.E. Harris and S.A. Rice, *J. Phys. Chem.* **58** (1954) 725.

[15] S. Lifson, *J. Chem. Phys.* **26** (1956) 727.

[16] R.J. Baxter, *Exactly solved models in statistical mechanics*, Academic Press: London, 1982.

[17] R.R. Netz, *Phys. Rev. E.* **60** (1999) 3174.

[18] R.R. Netz and H. Orland, *Eur. Phys. J. E.* **11** (2003) 301.

Chapter 7

Summary and future prospects

In this thesis several problems, involving charged objects in contact with ionic solutions, were investigated. In chapters 2–4 two types of modifications to Poisson-Boltzmann (PB) were considered: discrete solvent effects in aqueous solution, beyond the primitive model, and ion-ion correlation effects, which are not taken into account by the mean-field approach of PB theory.

The main outcome of chapters 2–3 is that discrete solvent effects can be very significant near highly charged surfaces. With sodium counterions, considered specifically in this work, these effects are important when the surface charge is in the order of $0.1 \, \text{C/m}^2 \simeq 6 \times 10^{-3} \, \text{e/Å}^2$ or larger. Counterions accumulate close to the surface more than predicted by the primitive model. Consequently the effective surface charge, far away from a charged surface is reduced relative to the nominal charge.

The effective surface charge can be used in order to evaluate the pressure between two plates at large separations, using the usual PB theory. However, at small inter-surface separations, comparable to the range of the short-range, solvent mediated ion-ion interaction, inter-surface forces behave very differently from the PB prediction, and in particular can be attractive. Such fundamentally different behavior from PB theory is found with highly charged plates, at separations smaller than about $20 \, \text{Å}$. The existence of strong deviations from PB theory at these separations is in agreement with surface-force apparatus measurements [1].

The third chapter's results may explain the apparent repulsion seen experimentally at very small inter-surface separations, referred to as the hydration force [1,2]. On the other hand, the model does not account for oscillatory forces that were observed experimentally [2]. In order to account for these oscillatory forces the free energy of the solvent itself must be considered and, of no less importance, the ion-surface, solvent mediated interaction must be included in

the theory.

The results of chapters 2–3 are qualitative, and mainly point at the importance of solvent-mediated interactions. I believe that further refinement of the model is required in order to make contact with experimental data. In addition to the ion-solvent mediated interaction, a refinement is also required in the ion-ion interaction, which was taken in this work from simulations in a bulk solution. These modifications require evaluation, in simulation, of effective potentials in a confined or anisotropic geometry, which are not available at this time.

The formalism developed in chapters 2–3 can be used to study ion-ion interactions, other than the solvent-mediated ones. In particular, much interest has been devoted lately to the consequences of dispersion interactions, acting on the ions. In this context ion-surface dispersion forces were considered [3,4] but the ion-ion dispersion forces were not taken into account. The formalism of chapters 2–3 may be a valuable tool in assessing their effect.

In chapter 4 ion-ion correlation effects are considered in the most simple possible model for a macroion in ionic solution, namely, an infinite, uniformly charged surface neutralized by counterions. A formalism similar in spirit to Debye and Hückel's theory for bulk electrolytes (Sec. 1.1 and Ref. [5], Sec. 78) is developed, in which a test charge is singled out. The other ions's response is then evaluated, treating the ion charge in a non-linear manner. The emerging theory coincides, in its prediction for the ion density profile, with known asymptotic limits, of very small or very large coupling parameter values.

At intermediate coupling parameters, in which an exact analytic theory is not available, the theory of chapter 4 provides useful results, showing semi quantitative agreement with Monte-Carlo simulation [6]. Further results from simulation are desirable in order to test the predictions on the ion density profile far away from the charged plates and, in particular, the predicted distance-dependent crossover from exponential to algebraic decay. It is argued, in chapter 4, that when the coupling parameter is large a modified mean-field equation describes the ion distribution in a large range of distances from the plate. This prediction awaits comparison with simulation as well.

Many interesting generalizations of chapter 4's formalism are possible, among them consideration of a salt solution, and geometries other than the planar one (technically, the spherical geometry involves the same computational complexity as the planar one since there is one axis of symmetry, the line connecting the sphere's center and the test charge, whereas the cylindrical case is computationally more demanding since there is no axis of symmetry once a test charge is introduced). It is also of great interest to generalize the theory to study the interaction

of two charged surfaces. Such a generalization may yield a relatively simple theory that will interpolate between mean-field theory and strong-coupling theory [7, 8], in its prediction for inter-surface forces.

The works presented in chapters 2–3 and in chapter 4 demonstrate that PB theory is inaccurate close to highly charged objects. Its relative success, in analysis of experimental data, is often due to the use of renormalized surface charges, which are taken as fit parameters. Ideally, it should be possible to calculate these renormalized charges from first principles. From the works presented here, together with others [3, 4, 6, 9–14], it becomes evident that this goal can be achieved only with a unified treatment of solvent-mediated interactions, dispersion forces, detailed surface geometry, and ion-ion correlations.

In contrast to chapters 2–4, chapter 5 deals with a specific experimental system, namely a solution of short, rod-like DNA segments in a solution that contains both monovalent and multivalent counterions. Two quantities, characterizing the ion density profile near isolated segments in the dilute (non-aggregate) phase are extracted from the experimental data: the bulk density c_z^* and the excess ρ_z^* of multivalent ions, at the onset of aggregation. It is argued that these quantities are independent on c_{DNA}, the DNA concentration (in contrast to previous theoretical treatments), whereas the amount of multivalent salt, required to induce aggregation, depends linearly on c_{DNA}. This linear dependence is due only to the contribution of the excess.

Models for the ion distribution near a single DNA segment, such as PB theory, enforce a certain relation between c_s, the monovalent salt concentration, c_z^*, and ρ_z^*. Because this relation is different from the actual one in the experimental system, such models are inherently limited in their capability to describe boundaries in the aggregation phase diagram. Furthermore, as shown in chapter 5, competition between monovalent and multivalent ions amplifies the importance of specific ion effects (not taken into account by PB theory), such as the counterion size and other short-range interactions [15]. Comparison of the extracted c_z^*, ρ_z^* values with PB theory supports this conclusion.

The main assumption made in chapter 5 (that c_z^* is independent on c_{DNA}) relies on the neglect of direct DNA-DNA interactions, and on neglect of the DNA segments's translational entropy. The latter assumption is currently under theoretical investigation [16]. According to our results, taking the DNA translational entropy into account shifts the extracted values of c_z^* and ρ_z^* by a small degree, but does not affect any of chapter 5's qualitative conclusions. In very dilute DNA solutions, smaller than the ones considered in the experiments of Ref. [20], the DNA entropy does affect the onset curve, as will be addressed in a future publication [16].

Chapter 5 sheds light on one aspect of the phase diagram, namely the onset of aggregation. The nature of this boundary in the phase space is not yet clear, neither theoretically or experimentally. Current theoretical approaches treat this boundary as the coexistence line of a dilute phase involving single DNA chains, and a concentrated, liquid crystalline phase [16–20]. However, some measured quantities, such as the amount of DNA remaining in the dilute phase beyond the onset, do not seem to agree with such a picture. In particular, the minimal amount of DNA, at the point where redissolution begins, depends on the initial concentration of DNA (Ref. [20], Fig. 6). I believe that the approach taken in this theoretical work, in which emphasis is placed on analysis of the experimental data, can contribute greatly to further understanding of the phase diagram.

Finally, in chapter 6 charge regulation of weak, rod-like polyelectrolytes (PEs) is considered. This chapter introduces a simple, analytically tractable method, taking into account the anti-correlation between neighboring sites. This anti-correlation is associated with a plateau at intermediate pH values in titration curves, which is reproduced quite accurately using the method introduced in chapter 6. In addition to the introduction of this method, recent results on dielectric discontinuity effects [21] are re-examined. The main conclusion on this issue is that the effect depends strongly on the position of charged groups within the low-dielectric backbone.

Another important conclusion of chapter 6 involves the interaction of two PE chains. The average degree of dissociation is found to depend on the separation between PEs, increasing when two oppositely charged PEs approach each other. The increase can be gradual or abrupt, depending on the strength of interactions between sub-lattices within each PE. A similar conclusion probably applies to multi-layers of weak, oppositely charged PEs [22, 23], and may be important for the building of stable multilayer complexes.

The model of chapter 6 relies on the use of the linearized Debye-Hückel theory to treat all interactions between dissociation sites along the PE backbone. For highly charged PEs it is no longer possible to trace over ionic degrees of freedom in this manner. Treating the full non-linear theory remains an intriguing, open challenge.

All the works presented in this thesis share a common attempt to introduce a theoretical formalism that (i) captures the essential physical effects, (ii) is sufficiently simple to allow some level of analytical treatment and, of no less importance, provides physical insight into the problem under study, and (iii) is rooted in the methods of statistical mechanics. I hope that these works will contribute to the understanding of inhomogeneous ionic solutions, and that they will prove to be useful for the study of other charged macromolecular systems.

Bibliography

[1] R. M. Pashley, *J. Colloid Interface Sci.* **80** (1981) 153.

[2] R. M. Pashley and J. N. Israelachvili, *J. Colloid Interface Sci.* **101** (1984) 511.

[3] B. W. Ninham and V. Yaminsky, *Langmuir* **13** (1997) 2097.

[4] S. A. Edwards and D. R. M. Williams, *Phys. Rev. Lett.* **92** (2004) 248303 and references therein.

[5] L. D. Landau and E. M. Lifshitz, *Statistical Physics, 3rd edition, Part 1*, Pergamon Press: New York, 1980.

[6] A.G. Moreira and R.R. Netz, *Eur. Phys. J. E.* **8** (2002).

[7] R. R. Netz, *Eur. Phys. J. E* **5** (2001) 557.

[8] A. Naji and R. Netz, *Eur. Phys. J. E* **13** (2004) 43.

[9] S. Marčelja, *Nature* **385** (1997) 689.

[10] I. Borukhov, D. Andelman, and H. Orland, *Phys. Rev. Lett.* **79** (1997) 435.

[11] D. B. Lukatsky, S. A. Safran, A. W. C. Lau, and P. Pincus, *Europhys. Lett.* **58** (2002) 785.

[12] L. Guldbrand, B. Jönsson, H. Wennerström, and P. Linse, *J. Chem. Phys.* **80** (1984) 2221.

[13] R. Kjellander and S. Marčelja, *J. Chem. Phys.* **82** (1985) 2122.

[14] A. Y. Grosberg, T. T. Nguyen, and B. Shklovskii, *Rev. Mod. Phys.* **74** (2002) 329.

[15] See also, Y. Burak, G. Ariel, and D. Andelman, *Curr. Opin. Colloid Int. Sci.* **9** (2004) 53.

[16] Y. Schwarzkopf, Y. Burak, and D. Andelman, *manuscript in preparation*.

[17] J. Wittmer, A. Johner, and J.F. Joanny, *J. Phys. II France.* **5** (1995) 635.

[18] T. T. Nguyen, I. Rouzina, and B.I. Shklovskii, *J. Chem. Phys.* **112** (2000) 2562.

[19] F. J. Solis, *J. Chem. Phys.* **117** (2002) 9009.

[20] E. Raspaud, M. Olvera de la Cruz, J.-L. Sikorav, and F. Livolant, *Biophys. J.* **74** (1998) 381.

[21] M. Borkovec, J. Daicic, and G.J. Koper, *Physica A* **298** (2002) 1.

[22] G. Decher, *Science* **277** (1997) 1232.

[23] D. Yoo, S. Shiratori, and M. Rubner, *Macromol.* **31** (1998) 4309.